

A Thesis Submitted for the Degree of PhD at the University of Warwick

Permanent WRAP URL:

<http://wrap.warwick.ac.uk/125819>

Copyright and reuse:

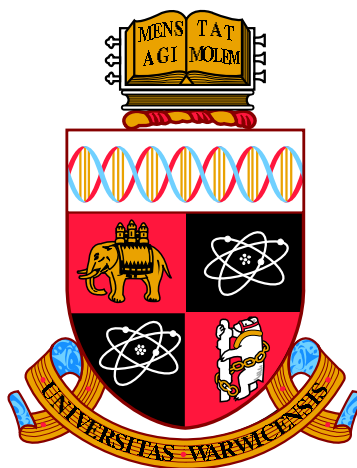
This thesis is made available online and is protected by original copyright.

Please scroll down to view the document itself.

Please refer to the repository record for this item for information to help you to cite it.

Our policy information is available from the repository home page.

For more information, please contact the WRAP Team at: wrap@warwick.ac.uk



Anisotropic Colloids: from Synthesis to Transport Phenomena

by

Brooke W. Longbottom

Thesis

Submitted to the University of Warwick

for the degree of

Doctor of Philosophy

Department of Chemistry

December 2018



Contents

List of Tables	v
List of Figures	vi
Acknowledgments	ix
Declarations	x
Publications List	xi
Abstract	xii
Abbreviations	xiii
Chapter 1 Introduction	1
1.1 Colloids: a general introduction	1
1.2 Transport of microscopic objects – Brownian motion and beyond	2
1.2.1 Motion by external gradient fields	4
1.2.2 Overcoming Brownian motion: propulsion and the requirement of symmetry breaking	7
1.3 Design & synthesis of self-phoretic anisotropic colloids	10
1.4 Methods to analyse colloid dynamics	13
1.4.1 2D particle tracking	14
1.4.2 Trajectory analysis	19
1.5 Thesis outline	24
Chapter 2 Roughening up Polymer Microspheres and their Brownian Mo- tion	32
2.1 Introduction	33
2.2 Results & Discussion	38
2.2.1 Fabrication and characterization of ‘rough’ microparticles	38

2.2.2	Quantifying particle surface roughness by image analysis	49
2.2.3	2D particle tracking – roughened vs. smooth Brownian motion . . .	51
2.3	Experimental	58
2.3.1	Materials	58
2.3.2	Dispersion polymerisation for synthesis of micron-sized poly(styrene) spheres	58
2.3.3	Fabrication of surface-textured poly(styrene) particles	59
2.3.4	Particle characterization	59
2.3.5	2D particle tracking experiments	60

Chapter 3 Improving the Engine Power of a Catalytic Janus-sphere Micro- motor by Roughening its Surface 65

3.1	Introduction	66
3.2	Results & Discussion	68
3.2.1	Fabrication of deformed PS-Pt micromotors	68
3.2.2	Propulsion experiments	70
3.2.3	Microscopic characterization: resolving surface details	79
3.2.4	A note on roughness	84
3.3	Conclusion	85
3.4	Experimental	85
3.4.1	Materials	85
3.4.2	Dispersion polymerisation of micron-sized poly(styrene- <i>co</i> -methacrylic acid) spheres	86
3.4.3	PS-MAA film formation	86
3.4.4	Physical deformation of PS-MAA microspheres	86
3.4.5	Physical vapour deposition of thin films of platinum	86
3.4.6	Particle characterization	87
3.4.7	2D particle tracking experiments	87

Chapter 4 Fabrication and Dynamics of Silica-Based ‘Matchstick’ Colloids 91

4.1	Introduction	91
-----	------------------------	----

4.2	Results & Discussion	95
4.2.1	Synthesis of silica-based ‘matchstick’ colloids	95
4.2.2	Dynamics of manganese oxide containing ‘matchstick’ particles – propul- sion studies	110
4.3	Conclusion	116
4.4	Experimental	117
4.4.1	Synthesis of silica-metal oxide ‘matchstick’ particles	117
4.4.2	Particle characterization	118
4.4.3	Kinetics of silica growth	119
4.4.4	2D particle tracking experiments	119
Chapter 5 Engineering Anisotropic Silica Colloids for Bio-inspired White-		
	ness Optimization	124
5.1	Introduction	125
5.2	Results & Discussion	127
5.2.1	Synthesis – tuning the reaction conditions	127
5.2.2	Selected candidates for photonics studies – ‘rods’ vs. ‘worms’	133
5.2.3	The whiteness – ‘worms’ vs. ‘rods’	140
5.2.4	Optimizing whiteness	142
5.3	Conclusion	145
5.4	Experimental	146
5.4.1	Materials	146
5.4.2	Synthesis of anisotropic ‘rod’ or ‘worm’ silica particles	146
5.4.3	Preparation of colloidal films	147
5.4.4	Material characterization	148
5.4.5	Transport mean free path measurements	149
Chapter 6 Summary & Outlook		153
Appendix A Additional Characterization		157
A.1	XPS of amorphous manganese oxide powder	157

A.2	Image thresholds of colloidal silica films	160
A.3	Quantification of the extrapolation length for colloidal silica films	161
Appendix B Supporting Videos		163
B.1	SV1 – 2D particle tracking of a rough object	163
B.2	SV2 – Translational to angular propulsion of a rough micromotor	163
B.3	SV3 – Bubble propulsion of manganese oxide powder	163
B.4	SV4 – Brownian motion of matchstick shaped colloids	164

List of Tables

2.1	Comparison of diffusion coefficients of smooth vs. rough colloids	57
3.1	Comparison of D and v from parabolic fits for smooth and rough PS-Pt micromotors	74
3.2	Comparison of D , v and τ_R for smooth and rough PS-Pt micromotors . . .	74
5.1	Comparison of different reaction conditions used to synthesize silica rods and their associated dimensions	147
5.2	Amounts of reagents used for the synthesis of anisotropic silica colloids . . .	148
A.1	Peak fitting of the Mn 2p region	159
A.2	Peak fitting of the Mn 3p region	159
A.3	Peak fitting of the Mn 3s region	159

List of Figures

1.1	Schematic of electrophoresis	5
1.2	Scallop theorem and microscopic artificial swimmer design	8
1.3	Bubble propulsion of tubular microengine	9
1.4	Literature examples of auto/self-phoretic colloids	12
1.5	Point spread function of imaging system	16
1.6	Phase contrast image response of a microsphere	18
1.7	Anomalous diffusion	21
1.8	Self-propelling PS-Pt micromotors	23
2.1	SEM images of literature examples of rough colloids	34
2.2	SEM image of polymer microspheres with defined flat regions	36
2.3	Schematic of boundary conditions and wetting behaviour due to roughness .	37
2.4	SEM images of polymer microspheres and selected inorganic colloids for roughening	40
2.5	TEM images of roughened microspheres	41
2.6	Microspheres roughened by cigar-shaped calcium carbonate	42
2.7	Microspheres roughened by rod-shaped calcium carbonate	43
2.8	Microspheres roughened by nano-sized zinc oxide	44
2.9	TEM image of roughened, buckled microsphere	46
2.10	Aggregation number for dispersed vs. dry roughened particles	48
2.11	SEM of mikado-like stacking of precipitated calcium carbonate	49
2.12	Surface profiles of smooth vs. roughened particles	50
2.13	2D particle tracking of a rough object	53
2.14	MSD of smooth vs. rough polymer microspheres	54
2.15	SEM images used for size analysis	56
3.1	SEM of smooth and roughened polymer microspheres	70
3.2	Self-propulsion of smooth vs. rough PS-Pt micromotors	72

3.3	Ensemble average MSDs of self-propelling smooth vs. rough PS-Pt micromotors	73
3.4	Individual MSD analysis of self-propelling microparticles	76
3.5	Extra trajectory analysis and VACF	78
3.6	Translational and angular propulsion of roughened micromotor	79
3.7	HRTEM of smooth and rough PS-Pt micromotors	80
3.8	SEM of roughened PS-Pt micromotors	81
3.9	SEM of roughened poly(styrene) films	83
3.10	Depiction of roughness from an interfacial packing perspective	84
4.1	Literature synthesis routes to anisotropic silica particles	93
4.2	TEM images of metal oxide nano-particulate	96
4.3	Powder XRD of manganese oxide	97
4.4	Kinetic TEM image series of matchstick particle growth	99
4.5	Kinetic SEM image series of matchstick particle growth	100
4.6	Kinetic SEM image series of matchstick particle growth	101
4.7	SEM image of matchstick particle synthesized with lower manganese content	104
4.8	Particle growth in length vs. time	105
4.9	Further electron microscopy of matchstick particles	107
4.10	ADF-STEM and elemental analysis of matchstick particle	108
4.11	TEM images of other metal oxide matchstick particles	110
4.12	Bubble propulsion of manganese oxide powder	111
4.13	MSD of matchstick particles dispersed in hydrogen peroxide	113
4.14	log-log MSD of matchsticks in hydrogen peroxide	115
5.1	The <i>Cyphocilus</i> beetle scale	126
5.2	SEM images of silica rods produced via numerous different reaction conditions	129
5.3	SEM and TEM images of short ‘worm’-like silica colloids	134
5.4	SEM and TEM images of ‘rod’-like silica colloids	135
5.5	Photograph of <i>Cyphocilus</i> beetle and white film of ‘rod’-like colloids	136
5.6	White films of ‘worm’-like colloids	138
5.7	White films of ‘rod’-like colloids	139

5.8	Transmission spectra for silica ‘rods’ and ‘worms’ of varying film thickness .	141
5.9	Fitted transmission spectra for quantification of l_t	142
5.10	White films of high aspect ratio silica ‘rods’	144
5.11	Transmission spectra for high aspect ratio silica ‘rods’ films of different thick- ness	145
A.1	XPS survey of manganese oxide powder	157
A.2	XPS traces with peak fitting for assignment of manganese oxide	158
A.3	Threshold of ‘worm’-like silica SEM image	160
A.4	Threshold of ‘rod’-like silica SEM image	160
A.5	Threshold of high aspect ratio ‘rod’-like silica SEM image	161
A.6	Angular distribution of intensity for silica films	162

Acknowledgments

There are more than a few fantastic people I'd like to thank for their help over the last four years. I'll start with those who have made a direct contribution to the work here. Without them this thesis wouldn't be nearly as complete! Thanks go to Richard Beanland and Steven Hindmarsh for their help with electron microscopy. Your help both in acquiring images and passing on teachings have heavily influenced the quality of my work. I'd like to also thank Luke Rochford who's help with x-ray diffraction has been much appreciated. Gianni Jacucci deserves an honourable mention, I had a great time working with you during my PhD. I'm also very appreciative of the time spent by Jonathan Howse in helping us choose a good imaging system for particle tracking, your advice was invaluable. I'm thankful of the short time I spent working with Wilson Poon's research group in Edinburgh. Wilson's words of wisdom will always sit with me. Those who I've met at conferences, I'm thankful for all the useful conversations we had especially Ryan Murphy. I've had the pleasure of working with some excellent undergraduate and masters students too: Doug, Chris, Birsen and Jacob have all been a joy to work with. I've learnt as much from them as they have from me.

I would like to thank everyone in the Bonlab who's help, guidance and most of all friendship over the years I wouldn't have survived without. Postdocs Yunhua, Cathy and Corinna I learnt a lot from, and PhD students Tom, Holly, Rob Y, Rob B, Ross, Sam, Andrea, Patrik, Matt, Melody and Josh, all have been excellent friends. I have been incredibly fortunate to work in such a close team with such genuine and caring colleagues. Wherever I go next will struggle to compare.

A massive thank you goes to my supervisor and close friend Stefan. Stefan gave me an opportunity few others ever get – the opportunity to carry out the research I wanted to do with complete academic freedom. Stefan's generous financial and emotional support have helped me develop into the scientist I am today. I owe a huge debt to Stefan and only hope that in the years to come I can repay it in friendship.

My parents Julie and Simon have been a huge support to me. You've both been perfect pillars of stability and care through an incredibly anxious time for me. I'm so lucky to have such an incredible pair for parents. I've also got some amazing friends that have kept me level. My two best men Ben and Adam are superb specimens who I never cease to make me laugh and keep my life enjoyable. Andrew, we've had so many years together from school, to undergrad, to PhD, you've been an awesome friend and it wouldn't have been the same without you.

It goes without saying that I wouldn't have made it this far without my wonderful wife Sarah. Not only have you had to put up with me over these mad years, you've also directly helped with all of my coding woes. Sarah, your brilliant intelligence and warmth, care and love have made this journey bearable. I love you endlessly. Thank you for everything.

Declarations

This thesis is submitted to the University of Warwick in support of my application for the degree of Doctor of Philosophy. It has been composed by myself and has not been submitted in any previous application for any degree. The work presented (including data generated and data analysis) was carried out by the author except in the cases outlined below:

1. Powder X-Ray diffraction (Chapter 4, Figure 4.3) was carried out by Dr. Luke Rochford, University of Warwick.
2. Focused ion-beam section (Chapter 4, Figure 4.9 d) was carried out by Steven Hindmarsh, University of Warwick.
3. Annular Dark Field Scanning Transmission Electron Microscopy elemental analysis (Chapter 4, Figure 4.10) was carried out by Dr. Richard Beanland, University of Warwick.
4. Photonic experiments in Chapter 5 were carried out by collaborator Gianni Jacucci at the University of Cambridge.

Parts of this thesis have been published by the author and are detailed in the publications list overleaf.

Publications List

- **Longbottom, B. W.;** Rochford, L. A.; Beanland, R.; Bon, S. A. F. Mechanistic Insight into the Synthesis of Silica-Based “matchstick” Colloids. *Langmuir* 2015, **31**, 9017–9025. — Chapter 4
- **Longbottom, B. W.;** Somuncuoğlu, B.; Punter, J. J.; Longbottom, S.; Bon, S. A. F. Roughening up Polymer Microspheres and Their Diffusion in a Liquid. *Soft Matter* 2017, **13**, 4285–4293. — Chapter 2
- **Longbottom, B. W.;** Bon, S. A. F. Improving the engine power of a catalytic Janus-sphere micro-motor by roughening its surface. *Scientific Reports* 2018, **8**, 4622. — Chapter 3
- Lotierzo, A.; **Longbottom, B. W.;** Lee, W. H.; Bon, S. A. F. Synthesis of Janus and Patchy Particles using Nanogels as Stabilizers in Emulsion Polymerization. *ACS Nano* 2018, DOI:10.1021/acsnano.8b06557.

Abstract

This thesis is based around the theme of how anisotropy in colloidal shape can afford interesting transport phenomena. The term ‘transport phenomena’ is used in a broad sense to represent transport processes over length scales ranging from nanometers up to micrometers.

We begin by looking at the simple case of Brownian motion of polymer microspheres and investigate the effect of roughening their surface. A fabrication protocol is presented for tuning the surface roughness by deforming the polymer microspheres in the presence of select inorganic colloidal particles. The scale of roughness imparted is a function of the deformation time and the dimensions of the inorganic particles. Despite a large scale of roughness in comparison to the ‘smooth’ polymer microspheres, the no-slip boundary condition holds and the Brownian motion is modelled exceptionally by the Stokes-Einstein-Sutherland relation. We then move on to look at the phoretic propulsion of these roughened objects by first post-modifying the particles with a sputtered platinum cap and subsequently tracking particles dispersed in hydrogen peroxide solution. Those with smaller surface deformations were found to propel at $\sim 2\times$ the velocity of ‘smooth’ particles and additionally some displayed interesting rotary, angular propulsion. We also present a different design for a self-propelling colloid in the form of a silica-manganese oxide ‘matchstick’ shaped particle of which the aspect ratio can be carefully tuned by monitoring reaction kinetics. We find that the propulsive velocity of the matchstick particles is limited by a silica coating around the catalytic manganese oxide, and thus particles display only enhanced diffusion when dispersed in hydrogen peroxide fuel. Finally we make our way down to the nanoscale and quantify the transport mean free path of white light for colloidal films of silica ‘rod’ and ‘worm’-like colloids to probe the material whiteness. This study, inspired by one of nature’s whitest known thin materials – the *Cyphocilus* beetle shell – shows that anisotropy of scattering centres can lead to excellent whiteness properties.

Abbreviations

ADF	A nnular D ark F ield
AFM	A tomistic F orce M icroscopy
AIBN	2,2'- a zo-bis- i sobutyrylnitrile
DDM	D ifferential D ynamic M icroscopy
DLS	D ynamic L ight S cattering
EDX	E nergy D ispersive X -ray
FIB	F ocused I on B eam
GLAD	G lancing A ngle D eposition
MSD	M ean S quared D isplacement
PCC	P recipitated C alcium C arbonate
PMMA	poly(m ethyl m ethacrylate)
PRINT	P article R eplication I n N on-wetting T emplates
PS	poly(styrene)
PSF	P oint S pread F unction
PVD	P hysical V apour D eposition
PVP	poly(<i>N</i> -vinylpyrrolidone)
SAED	S electd A rea E lectron D iffraction
SEM	S canning E lectron M icroscopy
STEM	S canning T ransmission E lectron M icroscopy
TEM	T ransmission E lectron M icroscopy

TEOS	T etraethyl o rthosilicate
VACF	V elocity A utocorrelation F unction
XPS	X -ray P hotoelectron S pectroscopy
XRD	X -ray D iffraction

1

Introduction

Think so far outside the box that there
is no box.

Prof. Stefan A. F. Bon

1.1 Colloids: a general introduction

The earliest definition of a colloid came from Thomas Graham in 1861 who described colloids as a class of substances: typically aqueous solutions of glue-like substances that diffuse very slowly and do not dialyse.¹ The word ‘colloid’ thus comes from the Greek word for glue: $\kappa\omicron\lambda\lambda\alpha$ (kolla). The term was redefined half a century later by Ostwald,² Weimarn³ and Freundlich⁴ who suggested instead that any substance in the *dispersed* state is colloidal. Near a century since Ostwald’s book titled “Die welt der vernachlässigten dimensionen”⁵ – “the world of neglected dimensions”, and the field of colloids has progressed enormously. Colloids are now used in food, cosmetics, electronic devices, paints and coatings to name a few. Apart from artificial systems, colloids have also been found to be abundant in nature from the latex of the rubber tree to the hormonal secretion of a mammal (milk). What all colloids have in common under the modern IUPAC definition is that they have a dimension roughly between 1 nm and 1 μ m and are dispersed throughout a different phase in which they are not soluble.⁶ A colloidal system is multi-phasic in principle, in its simplest form binary, consisting of a dispersed phase and a continuous phase. Except for the impossible case of two gases, there are many known classifications e.g. foams (gas in liquid), emulsions (liquid in liquid), aerosols (solid in gas) and gels (solid in liquid). In this thesis the colloids studied are solid particles dispersed in liquids (often referred to as a sol or dispersion).

1.2 Transport of microscopic objects – Brownian motion and beyond

At thermal equilibrium, a system is considered to be at rest and in the macroscopic world this looks entirely static to observers. When dimensions are shrunk down to the micro scale however, the observer now sees particles performing random, erratic, jittering motions. It is perhaps not surprising then that early observations made by Jan Ingen-Housz⁷ in 1784 likened the motion to that of “animalcules”, a term earlier dubbed by Antony van Leewenhoeck⁸ (the father of microbiology) whom observed microorganisms swimming in a water droplet with his magnifying glass in 1677. The jittering of small particles was also noted by Adolphe-Théodore Brongniart⁹ and Robert Brown¹⁰ whom both independently watched the random motion of pollen grains and inorganic particles in water. Despite the works of others, Brown has taken the fame for the discovery of the phenomenon and it is now widely referred to as Brownian motion. In fact it was not until the works of Louis Guoy¹¹ that the random motion was attributed to the collisions of thermally excited solvent molecules with the dispersed particle. This was proved experimentally by showing that overall motion decreased with increasing particle size and solvent viscosity.^{12,13}

Einstein¹⁴ was among the first (1905) to comprehensively quantify the motion of a spherical particle by applying the van’t Hoff law for osmotic pressure of molecules, assuming Stoke’s law and treating the motion as a diffusional process. The result was the so called ‘Stokes-Einstein’ equation (1.1) which relates the diffusion coefficient, D , of a particle to its thermal fluctuations divided by a frictional force:

$$D = \frac{RT}{N_A} \frac{1}{6\pi\eta r}, \quad (1.1)$$

where R is the ideal gas constant, N_A is Avagadro’s number, η is the viscosity and r the radius of the sphere. An identical result was derived by William Sutherland¹⁵ in the same year and thus in this thesis we will refer to equation (1.1) as the Stokes-Einstein-Sutherland equation. It should be noted that Marian Smoluchowski¹⁶ also derived a similar result merely a year later. Three years after Einstein’s ground breaking paper, Paul Langevin¹⁷

used an “infinitely more simple” approach to quantify Brownian motion by application of Newton’s second law.¹⁸ Particles are said to experience a viscous force, according to Stoke’s law, which is complemented by an opposing force represented by Gaussian noise. This elegant, and more correct, solution has been instrumental in inspiring new physics.

The derivation of these results was revolutionary as the existence of molecules and kinetic theory were still widely disregarded. The argument was only finally put to rest by the works of Jean Perrin who used several methods to experimentally determine N_A .¹⁹ Perrin tracked the motion of gamboge resin particles which were laboriously separated to extract a uniform distribution of 1 μm colloidal particles that could then be suspended and viewed through an optical microscope. The translational trajectories were manually recorded over time and the mean squared displacements calculated. Using the following expressions (1.2 and 1.3) and Einstein and Sutherland’s results, N_A was calculated, once and for all linking thermodynamics on the macroscopic scale to atomic theory.

$$\langle \Delta x^2(t) \rangle = 2nDt, \quad (1.2)$$

$$N_A = \frac{t}{\langle \Delta x^2(t) \rangle} \frac{RT}{3\pi\eta r}, \quad (1.3)$$

where R is the ideal gas constant, x is displacement and n is the number dimensions.

Apart from the random fluctuations of Brownian motion, there are other processes that take place on the micron scale that transport small objects. If fluid is moved with a certain velocity, the colloids are subject to advective transport, in that the particles are pulled or pushed along with the fluid. An example of this arises when there is a temperature gradient across a sample generating convective flow to dissipate heat to the surroundings. The convection of the fluid drives *advection* of the colloid. The velocity of convective flow can vary significantly in magnitude depending on the strength of the thermal gradient and how quickly heat is transferred i.e. by evaporation. Typically convection can vary from $\sim 10^0 - 10^3 \mu\text{m s}^{-1}$.²⁰

An experimenter often tries to keep the effects of convection minimal in the interest of examining other motional behaviour that would otherwise be masked. Some examples of other motions driven by the application of external gradient fields are given in the following

section 1.2.1. Note for clarity, the classic example of electro-osmotic flow vs. electrophoresis will later be used to distinguish between particle motion of advective origin or colloid surface origin (section 1.2.1.1).

1.2.1 Motion by external gradient fields

Perhaps a logical starting point is to consider the effect of gravitational field. A dispersed colloidal particle experiences a gravitational force that is balanced by a buoyancy force and viscous drag (Stoke's law) to reach its terminal velocity. When a colloid is not density matched to its dispersed phase, it will sediment down with a velocity, v_{sed} , according to the Svedberg equation:²¹

$$v_{\text{sed}} = \frac{V_p D_t g (\rho_p - \rho_f)}{k_B T}, \quad (1.4)$$

where V_p represents the volume of the particle, D_t is the translational diffusion coefficient at infinite dilution, g is the gravitational acceleration, ρ_p and ρ_f are the density of the particle and fluid respectively. Knowing the volume of a sphere i.e. $\frac{4}{3}\pi r^3$ and D_t from equation (1.1) this can be reduced to the Stokes settling velocity:

$$v_{\text{sed}} = \frac{2 (\rho_p - \rho_f)}{9 \frac{\eta}{gr^2}}. \quad (1.5)$$

For a polymer colloid, say polystyrene ($\rho = 1.04 \text{ g cm}^{-3}$), with a diameter of $d = 1 \text{ }\mu\text{m}$, $v_{\text{sed}} = 0.024 \text{ }\mu\text{m s}^{-1}$. This will become significant for experiments on the time scale of $t \sim 20 \text{ s}$ whereby the particle has moved a distance r due to sedimentation. For colloids of higher material density and size however, sedimentation becomes considerable.

1.2.1.1 Interfacially driven transport

The interface between two phases is a very thin but finite layer and perhaps surprisingly the transport processes occurring in such a minute area can often dictate the fluid dynamics around the object.²² Well known examples of this phenomena are contained within the field of electrokinetics. The charge on any surface, S , submerged in solution is balanced by a diffuse cloud of counterions in accordance with double layer theory.²³ The distance from the surface at which the charge is screened is known as the Debye screening length, κ^{-1} ,

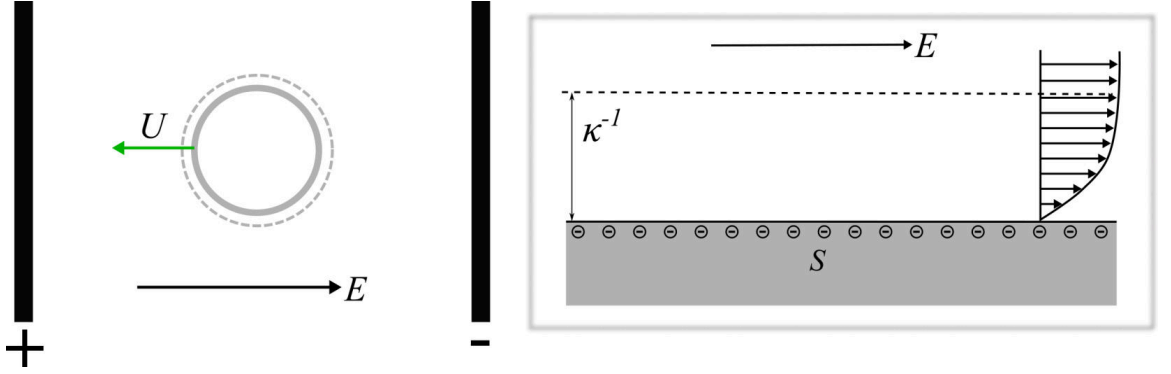


Figure 1.1. Schematic of electrophoresis of a colloidal particle with negative surface charge. An externally applied electric field, E , gives rise to electro-osmotic flow near the surface, S , which results in a particle velocity, U , equal and opposite in direction to the flow.

equation (1.6). When an external electric field, E , is applied, ions in solution are driven into motion and the diffuse cloud moves resulting in fluid flow that slips with velocity, v_s , just outside the screening layer, equation (1.8). This is the basis of electro-osmotic flow which gives rise to two related effects: electro-osmosis and electrophoresis. Electro-osmosis occurs when an electric field is applied along a channel with charged walls giving rise to plug flow. Suspended particles can be dragged along by the flow – one can think of this as an advective effect. Consider now the particle/fluid interface, a similar electro-osmotic flow arises locally giving rise to motion of the particle itself. The latter effect is of colloid surface origin and is termed electrophoresis. The colloid moves with velocity, U , in the opposing direction to this flow (figure 1.1).

The Debye screening length is given by:

$$\kappa^{-1} = \sqrt{\frac{\epsilon_w \epsilon_0 k_B T}{2 I e^2}}, \quad (1.6)$$

where ϵ_w is the relative dielectric permittivity of the solvent (for water ~ 80), ϵ_0 is the permittivity of free space, $I = \frac{1}{2} \sum_{i=1}^n c_i z_i^2$ the ionic strength and e is the charge of an electron. A potential (zeta), ζ , reflecting the electrostatic difference across the diffuse cloud is given by:

$$\zeta = \frac{q}{\epsilon_w \epsilon_0 \kappa}, \quad (1.7)$$

where q represents charge density. Using Poisson's relation to relate the charge density to the double layer electrostatic potential (for full derivation see Hiemenz²⁴) the resultant slip velocity at the outer limit of the double layer is:

$$v_s = -\frac{\epsilon_w \epsilon_0 \zeta}{4\pi\eta} E_{\parallel}. \quad (1.8)$$

where E_{\parallel} is the electric field strength at the outer region of the double layer. The electrophoretic velocity of the colloid is typically $U \approx -v_s$ and using typical values of $\epsilon_w \epsilon_0 = 7 \times 10^{-10} \text{ A}^2 \text{ s}^4 \text{ kg}^{-1} \text{ m}^{-3}$, $\zeta \sim kT/e \sim 0.02 \text{ V}$, $E_{\parallel} \sim 10^2 \text{ V m}^{-1}$, $\eta \sim 10^{-3} \text{ N s m}^{-2}$, U is on the order of micrometres per second.

There are other origins of colloidal transport resulting from the action of different gradients in solution at the interface of the colloid. One closely related phenomenon to electrophoresis is that of diffusiophoresis. Here there is no external electric field and instead a solute gradient generates motion.

A molecular gradient may be made up of charged or neutral species – both can drive diffusiophoresis. The phoretic motion brought about simply by a concentration gradient of uncharged species is driven due to solute molecules interacting with surfaces through excluded volume effects, in addition to van der Waals forces, resulting in a similar fluid flow and slip velocity to electrophoresis, equation (1.9):^{25–27}

$$u = \frac{k_B T}{\eta} \lambda_D K \nabla c, \quad (1.9)$$

where λ_D is a characteristic length for the particle/solute interaction ($10 - 100 \text{ \AA}$), K is the Gibbs adsorption length (amount of solute adsorbed per surface area, divided by the bulk concentration at equilibrium) and c is the solute concentration. Using typical values of $\lambda_D K = 5.8 \times 10^{-16} \text{ cm}^2$ and $c = 0.1 \text{ mol cm}^{-4}$ in the boundary layer Anderson found the velocity, $u \approx -2 \text{ \mu m s}^{-1}$.²² This is on a similar order to electrophoresis.

One other related but less common form of interfacially driven colloid motion is that induced by a temperature gradient about the particle surface. This is not to be confused with convection (an advective form of transport) as we are again now talking about motion driven from interaction at the colloid surface. It has been recently proposed

that thermophoresis, along with *barophoresis* (pressure driven), can be thought of as a form of *pycnophoresis* (density driven) as density gradients arise from both temperature and pressure gradients.²⁸ Nevertheless we are now speaking of single component fluids with a physical, rather than chemical origin, to the gradient field. The first model for thermophoresis was developed by Derjaguin *et al.* and predicts a slip velocity, u_s , resulting from a tangential temperature gradient.²⁹

$$u_s = \mu_T \nabla T, \quad (1.10)$$

where μ_T here is the thermophoretic mobility and ∇T represents the thermal gradient. The magnitude of particle velocity is on the same order as electro- and diffusiophoresis. In fact the essence of phoresis is boiled down to in equation (1.10) whereby a slip velocity arises from a characteristic phoretic mobility, μ , subject to a gradient. These gradient field driven processes are important to consider if one wishes to be able to have some control of the motion of microscopic particles and importantly attempt to overcome Brownian motion. The following section will detail the important factors for achieving propulsion on the micron scale, and will show how experimenters have used principles of interfacially driven transport phenomena generated by the particle itself to allow autonomous propulsion.

1.2.2 Overcoming Brownian motion: propulsion and the requirement of symmetry breaking

Having introduced some of the transport phenomena that can occur on the micron scale we now discuss the difficulties of attempting to achieve autonomous motion of colloidal particles and how we can make use of out-of-equilibrium, active processes to attain this. As a starting frame, the ubiquity of Brownian motion poses a significant challenge in the design of self-propelling micron scale particles. Random thermal fluctuations dictate motion at this scale. Directional propulsion is a highly desirable feature for such small objects as we can foresee microscopic devices that could travel around the human body delivering drugs to target cells. Such specificity is unprecedented and is the revolution in technology that Drexler spoke of in his famous book ‘Engines of creation’.³⁰

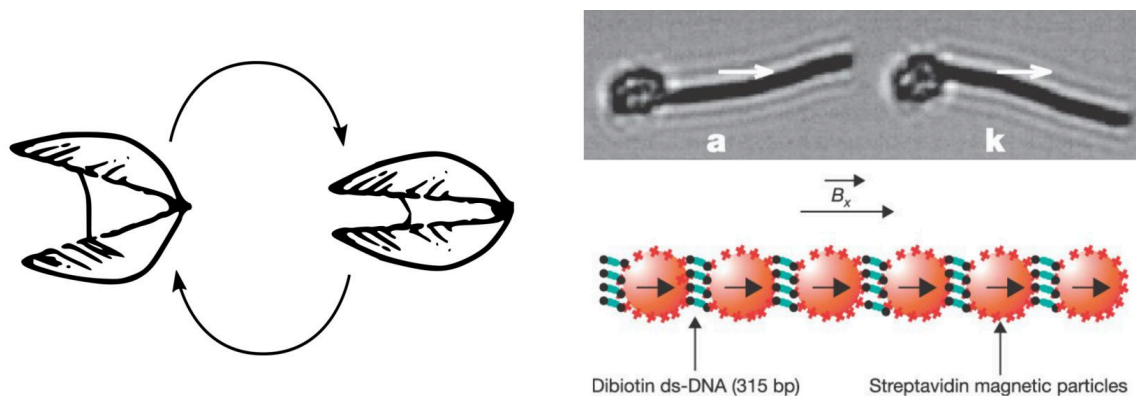


Figure 1.2. Drawing of reciprocal motion from Purcell’s “scallop theorem”³¹ (left) and experimentally realized artificial design of actuating superparamagnetic filaments attached to red blood cells by Dreyfus *et al.*³⁸ (right). Reprinted by permission from Springer Nature: *Nature*, Microscopic artificial swimmers, Dreyfus *et al.*, Copyright Springer Nature, 2005.

Another significant issue to overcome for small self-propelling devices is a result of low Reynolds number i.e. inertial forces are so insignificant that little progress can be made and it is as if particles must swim through a thick, viscous treacle. An apt analogy of low Reynolds number swimming was put forward by Purcell whom suggested what would happen if a scallop was shrunk down to microscopic dimensions.³¹ This “scallop theorem” shows that the opening and closing of the shell (which on the macroscopic scale squirts out fluid in order to propel the scallop) is completely reversible, leaving the poor scallop with no way to make any net progress (figure 1.2). Of course microorganisms exist that are able to overcome these constraints, for example bacteria³² and plankton.³³ These internally convert chemical energy to mechanical work and, importantly, the mechanical deformation breaks symmetry to allow the microorganism to swim. Purcell made design suggestions of microscopic mechanical devices that have a second degree of freedom to the swimmer, for instance his three-link swimmer containing two rotational hinges.^{34–37} Experimental realizations of this essential time-irreversible design criteria have since been accomplished, first by Dreyfus *et al.* who produced elastic superparamagnetic filaments attached to red blood cells.³⁸ Actuating the filaments using an oscillating magnetic field drove propulsion (figure 1.2). Later work by Ghosh and coworkers utilized a nanoscopic magnetic corkscrew design reliant on a similar external oscillating magnetic field to drive motion.³⁹

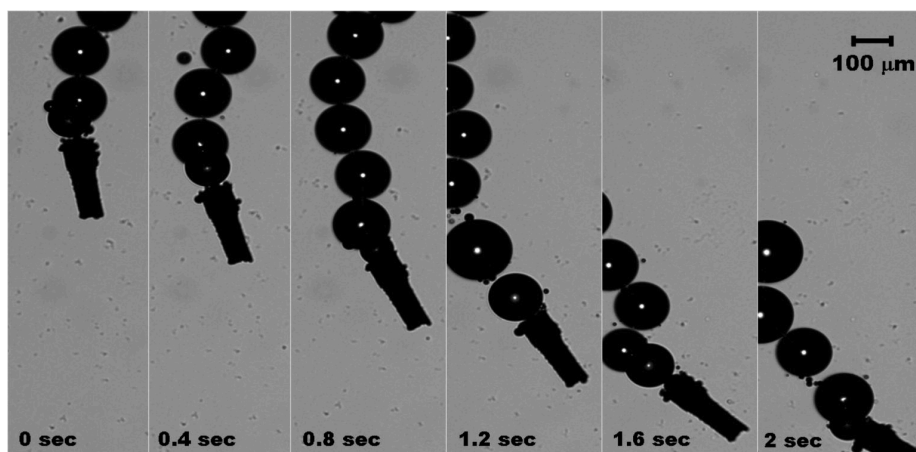


Figure 1.3. Tubular Pt-Au microengine in the presence of 15 vol.% hydrogen peroxide. Oxygen bubbles are ejected from the larger opening driving bubble propulsion.⁴² Reprinted with permission from Manesh *et al.*; Template-Assisted Fabrication of Salt-Independent Catalytic Tubular Microengines, *ACS Nano*, 4, 1799-1804, **2010**. Copyright 2010 American Chemical Society.

Looking to principles of colloidal physics and by exploiting chemistry, researchers have produced small objects that do not self-propel *via* mechanical deformation or an external field and instead make use of chemical reaction. One of the earliest designs utilizing a chemical reaction at the surface of the object itself was implemented by Ismagilov *et al.*⁴⁰ Researchers fabricated small (~ 1 cm) polymer plates with platinum coated rudders on the underside of the object. Floating these objects on a solution containing hydrogen peroxide allowed for rapid propulsion (cm s^{-1}) brought about by decomposition of hydrogen peroxide to oxygen gas at the platinum catalyst. The production of oxygen bubbles on one side of the object and their subsequent ejection displaced the plate causing it to propel. This is the fundamental basis of the bubble propulsion mechanism that has now been widely adopted in the design of autonomous, small self-propelling devices.⁴¹ A microscopic design is presented in figure 1.3 which involves tubular Pt-Au particles that clearly display bubble propulsion.⁴² Note that when bubble propulsion is the swimming mechanism, asymmetry of catalyst location is not necessarily a requirement so long as the bubble detaches from a similar location on the surface each time.

Bubble propulsion results in very high particle motility which has its advantages,

for instance in transporting large cellular objects⁴³ and improving mixing,⁴⁴ however the production of large amounts of gas bubbles can often be destructive to the experimental study. Microscopic observation and study of motion of small particles typically requires sealed observation chambers to avoid distortion effects of a curved droplet interface. Accumulation of gas bubbles inside the chamber not only limits the ultimate observation time, it also introduces convective flow which could be erroneously mistaken for autonomous propulsion. Collective phenomena of active particles is a growing frontier in physics⁴⁵ and bubble propelling particles are not suitable for this kind of study for the above reasons. Instead researchers have looked to other designs involving the auto/self-generation of a gradient field about the particle. Some examples include: self-diffusiophoresis,⁴⁶ self-electrophoresis,⁴⁷ self-thermophoresis⁴⁸ and self-acoustophoresis⁴⁹ to name a few. An important distinction from the transport phenomena discussed in section 1.2.1.1 is that there is no requirement here for an external field and particles can each move independently (autonomous). In these examples of swimmer designs it should be noted that chemical anisotropy, that is an asymmetric inclusion of the gradient inducing metal/catalyst on the particle, is critical in order to achieve propulsion. The following section (1.3) details methods of fabricating anisotropic colloids with this in mind.

1.3 Design & synthesis of self-phoretic anisotropic colloids

In order to break symmetry to give us our desired self-phoretic colloid the particle must exhibit chemical anisotropy, that is it should contain a reactive catalyst (or metal that can be heated) on one area of the surface of the particle. To find synthesis strategies one could look to the field of Janus particles. These were named after the roman God ‘Janus’, whom has two faces looking in opposite directions, by de Gennes in his Nobel prize address.⁵⁰ They have since received considerable attention in their application to self-assembly behaviour.⁵¹ One of the primary challenges in the wet chemical synthesis of anisotropic colloids is the dominance of interfacial tension at this size, forcing a spherical shape. This has limited researchers to take on either post surface modification techniques or crystalline materials in their search for artificial micro-motors.

One of the first and most well-adopted designs of a phoretic Janus micro-motor was fabricated by Howse *et al.*⁴⁶ Poly(styrene) microspheres of low dispersity were deposited onto glass microscope slides and subsequently a layer (~ 5 nm) of platinum catalyst was evaporated onto the upper side of the particle. This directional process allowed for a half coating of catalyst on the particle surface (figure 1.4 a) which could then propel the particle to velocities of up to $\sim 4 \mu\text{m s}^{-1}$ when dispersed in hydrogen peroxide. The advantage of this technique is its simplicity, allowing physicists to readily assume the procedure^{52–54} however being a 2D synthesis (limited to a monolayer of particles on glass slide) it is extremely low yielding. This Janus-sphere micromotor design has been utilized with different materials and/or background electrolyte in order to propel by diffusiophoresis,⁴⁶ electrophoresis⁵⁵ and thermophoresis.⁴⁸ Recently the synthesis of these motors has been modified to increase yield using a Pickering emulsion technique.⁵⁶ The procedure involves adhering spherical microspheres at the interface of emulsified wax droplets hereby protecting one side of the colloid, a technology initially developed by Perro *et al.*⁵⁷ The exposed side of the microsphere is reacted with an amine functional silane (3-aminopropyl triethoxysilane) which can then couple to platinum nanoparticles and a layer of platinum can be deposited around these resulting in the half-coated phoretic micro-motor design.

A different design was presented by Paxton *et al.* whom synthesized striped Au-Pt nanorods (figure 1.4 b) that propelled by self-electrophoresis to maximum velocities of $6.6 \mu\text{m s}^{-1}$.⁴⁷ The synthesis involves sequential electrochemical deposition into a porous alumina membrane in order to form striped bi-metallic rods.⁵⁸ Owing to the specialist electroplating equipment required for this synthesis and perhaps the initial uncertainty in the exact propulsion mechanism, this system has not been as widely adopted as the Janus PS-Pt micromotor. One of the distinct advantages of this design however is its persistence in directionality owing to the fact that Brownian rotation is dampened in the direction normal to propulsion. Efforts were made to improve the power output of the nanorods by adding carbon nanotubes to the Pt end along with the introduction of hydrazine to the aqueous hydrogen peroxide phase.⁵⁹ This veritable rocket fuel mixture lead to staggering propulsion speeds of up to $200 \mu\text{m s}^{-1}$ showing that with highly efficient catalytic turnover, phoretic propulsion can be on the order of 100 body-lengths-per-second.

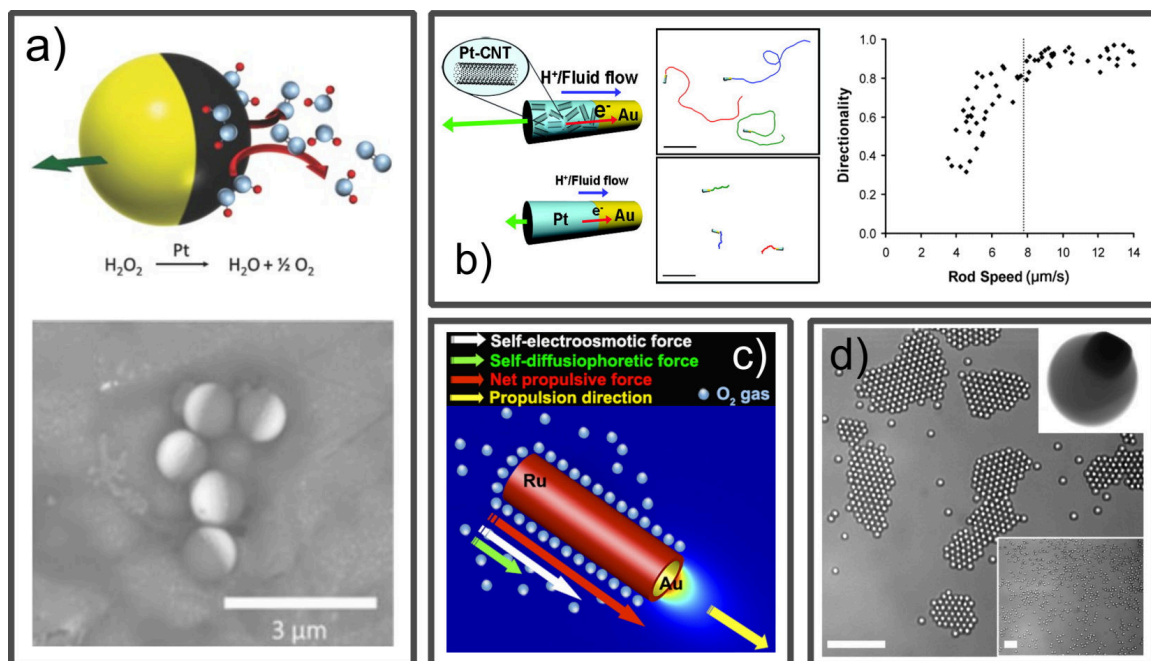


Figure 1.4. Examples of different anisotropic self-phoretic colloid designs. SEM of Janus sphere micro-motors⁵⁶ with half coating of Pt a). Au-Pt nanorods displaying enhanced propulsion with the inclusion of carbon nanotubes⁵⁹ and highly directional motion b). Reprinted with permission from Laocharoensuk *et al.*; Carbon-nanotube-induced acceleration of catalytic nanomotors, *ACS Nano*, 2, 1069-1075, **2008**. Copyright 2008 American Chemical Society. Au-Ru core-shell nanowires⁶⁰ c). Reprinted with permission from Jang *et al.*; Catalytic Locomotion of Core-Shell Nanowire Motors, *ACS Nano*, 10, 9983-9991, **2016**. Copyright 2016 American Chemical Society. Light activated polymer-encapsulated iron oxide motors⁶¹ showing collective swimming crystals d). From Palacci *et al.*; Living crystals of light-activated colloidal surfers., *Science*, 339, 936-940, **2013**. Reprinted with permission from AAAS.

A similar electrochemical deposition technique involving a porous alumina template was used by Jang *et al.* to fabricate self-phoretic nanorods except in this case the design involved a core-shell Au-Ru structure (figure 1.4 c) instead of striped rods.⁶⁰ Interestingly researchers found that increasing the length of the nanorod, increased the propelled velocity (up to $\sim 40 \mu\text{m s}^{-1}$) which lead to the conclusion that nanorods of this design propel by both diffusiophoresis and electro-osmosis simultaneously.

Light activated phoretic colloids were synthesized by Palacci and coworkers. Here the catalyst itself is a colloidal particle (iron oxide or titania) that has been encapsulated

by a silane functional polymer (figure 1.4 d) but has a surface exposed to react in solution.⁶² The encapsulation is relatively straightforward and involves reacting the silane (3-methacryloxypropyl trimethoxysilane) with the metal oxide colloid under basic conditions prior to polymerising with a common azo initiator (2,2'-azo-bis-isobutyronitrile, AIBN). A distinct advantage to this synthesis is it is a bulk wet chemical technique and thus large quantities of phoretic colloids can be produced. When dispersed in hydrogen peroxide solution the particle could be activated by blue light whereby the metal oxide catalyst begins to decompose the peroxide and the particles exhibit phoretic propulsion at velocities up to $\sim 15 \mu\text{m s}^{-1}$. Adding this additional control trigger and allowing larger concentrations of the colloid to be introduced lead to the observation of collective colloidal crystal formation and 'dissolution' upon shining and turning off the light.⁶¹

1.4 Methods to analyse colloid dynamics

Classically the dynamics of colloidal dispersions have been measured using light scattering techniques, for instance dynamic light scattering (DLS). These are ensemble measurements and work based on intensity-intensity fluctuations in a scattered speckle pattern.⁶³ The dynamics of the particles is derived from the autocorrelation of the intensity response:

$$g(q, \tau) = \frac{\langle I(t)I(t + \tau) \rangle}{\langle I(t) \rangle^2}, \quad (1.11)$$

where $I(t)$ is the intensity at time, t , and $I(t + \tau)$ is the intensity at t plus some lag time, τ . As the lag time increases, the correlation decays exponentially and the function of this decay tells us about the motion of the particles in the sample. For spherical Brownian particles, using the Siegert relation,⁶⁴ the decay in the correlation function is related to the diffusion coefficient, D , by

$$g(\tau) = 1 + e^{-2Dq^2\tau}, \quad (1.12)$$

where q is the scattering wave vector which depends on the wavelength, λ and the scattering angle, θ , $q = \frac{4\pi}{\lambda} \sin(\theta/2)$. One can then assume the size of the particle, as DLS is often used, with the Stokes-Einstein-Sutherland relation (equation (1.1)). Of course this only

holds for spherical particles with $1 \text{ nm} < d < 1 \text{ }\mu\text{m}$ (due to a lower detection limit and sedimentation effects for larger particles), under dilute conditions and at thermodynamic equilibrium. Departing from any one of these criteria complicates the matter. Also working in reciprocal space does not allow us to visualize our particles and a more direct real space measurement is required to complement DLS measurements.

Some recent efforts have been made to extend the sampling of colloidal dynamics making use of traditional light microscope based instrumentation. This technique, named Differential Dynamic Microscopy (DDM), uses a light microscope equipped with a high speed camera and standard optics and involves analyzing the temporal fluctuations in number density of particles via image analysis.^{65,66} Essentially the same scattering correlation function, equation (1.11), can be accessed by looking at the difference between images at given τ and operating in Fourier space. This opens up the possibility of studying the dynamics of larger particles ($> 1 \text{ }\mu\text{m}$) which DLS struggles with due to number fluctuations (large fluctuations in scattered intensity due to relatively low number of large particles) and sedimentation. It also allows dynamics to be probed below the minimum $q \sim 4.5 \text{ }\mu\text{m}^{-1}$ ($\theta \sim 20^\circ$) accessible by DLS where motility can be properly characterized.⁶⁷ DDM has been utilized to characterize anisotropic colloidal dynamics⁶⁸ as well as the motility of bacteria⁶⁹ and thus it holds promise as a technique to measure other kinds of colloid transport phenomena. Typically however the technique is carried out in combination with single particle tracking in order to provide a fit to the correlation function. The ease and wide spread availability of open source tracking algorithms have made particle tracking the predominant technique for characterizing the propulsion of active colloids. The following section introduces 2D particle tracking (section 2.3.5). The discussion is limited to two dimensions as tracking in 3D requires more sophisticated equipment which the majority of researchers do not have access to.

1.4.1 2D particle tracking

The ability to directly watch microscopic particles move around in solution in a non-invasive manner makes light microscopy an incredibly attractive technique for deciphering their complex motion. Accurate determination of particle positions by microscopy was essential

in the early quantification of Brownian motion, a result which contributed towards Perrin’s Nobel prize in 1926.¹⁹ The field of biophysics in particular has benefited enormously from the advent of optical microscopy and single particle tracking allowing quantification of dynamic cellular processes.⁷⁰ The principle of 2D particle tracking is presented in this section to give a brief background and overview of the process. Most modern algorithms and thus what will be discussed herein are based on the criteria for 2D particle tracking outlined by Crocker and Grier in their paper titled: ‘Methods of Digital Video Microscopy for Colloidal Studies’.⁷¹

To begin we must consider how the colloidal object is presented in light microscope images. The intensity distribution of a point source is spread out in 3D by diffraction, concentrically decaying from the centre of the point according to the point-spread-function (PSF) (figure 1.5a). In this way, what we measure is actually the convolution of the image point source and the PSF along with any noise. The PSF in 2D or diffraction pattern by a circular aperture can be represented analytically by the Airy function:⁷²

$$I_{xy} = I_0 \left(\frac{2J_1(\rho)}{\rho} \right)^2, \quad (1.13)$$

where J_1 is a first order Bessel function of the first kind and $\rho = 2\pi r NA / \lambda$. The distance from the centre point is r , and NA is the numerical aperture with $NA = n \sin \theta$ where n is the refractive index and θ is the half-angle of a cone of light that can exit the aperture/lens. Lastly λ is the wavelength of the light. The distance from the central maximum to the first minimum is given by the Airy disk:

$$r_{\text{Airy}} = 0.61 \frac{\lambda}{NA}. \quad (1.14)$$

This equation formalizes the diffraction resolution limit – in order to resolve two points, their intensity maxima should be separated by at least r_{Airy} . Aside from this point, a convenient form of the Airy function is that it closely resembles a 2D Gaussian.

So, having some knowledge of how the imaging system responds to colloidal particles, we can now attempt to treat this data in a way that allows us to extract positional information. It is often important to apply some pre-processing to images in order to elim-

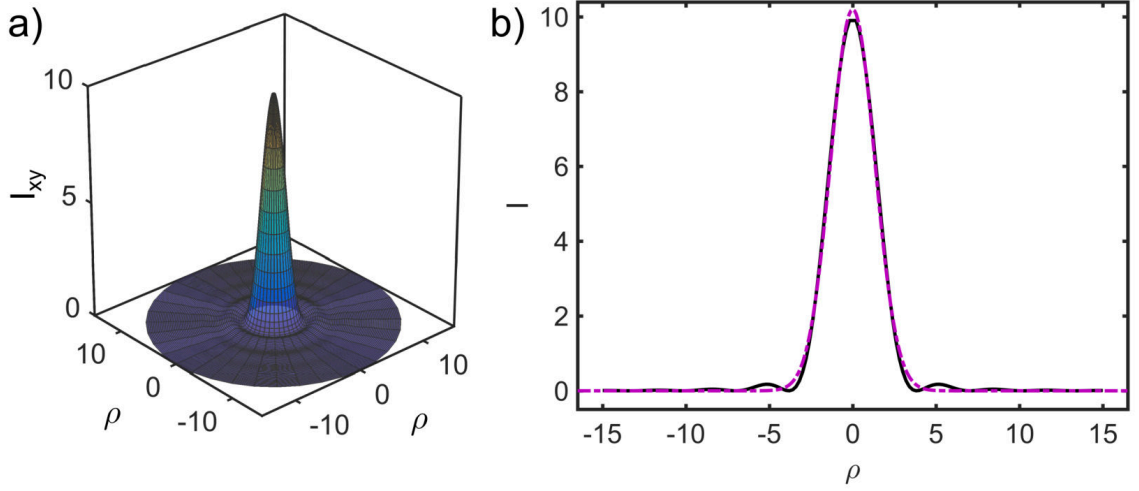


Figure 1.5. The intensity distribution seen by the microscope imaging system as a result of diffraction – the point-spread-function (PSF) a) and its lateral projection b). The purple dashed line is a Gaussian fit.

inate background noise from the images and avoid spurious particle detection. In fact it has been shown for several types of detection algorithm that accuracy and precision drop off rapidly below a signal-to-noise ratio of 4.^{73,74} These considerations should be taken into account by the microscopist during imaging and video acquisition. Essentially one should aim to set up the imaging system so that contrast between the particle and background is maximized without over saturating the detector and introducing noise. A good example of this is presented for confocal imaging systems by Jenkins and Egelhaaf which can be applied as a rule to other imaging systems.⁷⁵ Our aim here is to give our algorithm the best chance to distinguish objects from background.

1.4.1.1 Pre-processing

Scientific imaging equipment tends to be designed to operate with the lowest possible noise, however in practice digitization noise is unavoidable and there is always a certain random noise in each acquired image. On top of this noise there may be other imaging artefacts particularly if phase optics are used to enhance the contrast of the imaging system. In such cases particles are often surrounded by a bright halo due to a lack of spatial filtering

allowing some the light diffracted from the sample to interfere at the second phase annulus.⁷⁶ Recently, a new approach involving installation of an additional interferometry module to the imaging system allowed a significant reduction in these halo artefacts.⁷⁷ Classically however, image processing has been utilized in order to reduce noise and artefacts from images prior to performing detection steps.

Perhaps the simplest method to reduce noise is to apply a median filter to the image which replaces each pixel with the median value from its neighbourhood within a specified search size.⁷⁸ This works very well for eliminating ‘salt & pepper’ noise and is not computationally expensive making it quite attractive as an initial noise filter. Many researchers opt to apply a Gaussian filter which convolves the image with a Gaussian kernel.^{74,75,79,80} This can be done in combination with ‘boxcar’ averaging to even out contrast gradients in the background due to uneven illumination as originally suggested by Crocker and Grier.⁷¹ Other image processing algorithms used involve wavelet based methods,⁸¹ the Laplacian-of-Gaussian⁸² operation and Rolling-ball background subtraction.⁸³ Most of these pre-processing algorithms have similar performance and it is often up to the user to select one based on their use case. An example of the rolling ball algorithm implemented in ImageJ on a phase contrast image of a poly(styrene) microsphere is shown below in figure 1.6. Note that the maxima due to the halo are suppressed by $\sim 10\%$ and some of the noise is smoothed out.

1.4.1.2 Particle Detection

Once an image has been sufficiently processed we can attempt to find the location of particle centres. A variety of different methods can be used to do so. The most widely used method involves local maxima searching which selects a pixel so long as no other pixel within a certain distance is brighter. This distance is commonly defined according to the filter used in the pre-processing step and is chosen as an integer slightly larger than the radius of the particle of interest.⁷¹ Locations can actually be refined to get sub-pixel precision by calculating the offset from the selected pixel to the brightness weighted centroid of the surrounding pixels.⁷¹ In this way particle tracking algorithms can become highly precise quantification tools.

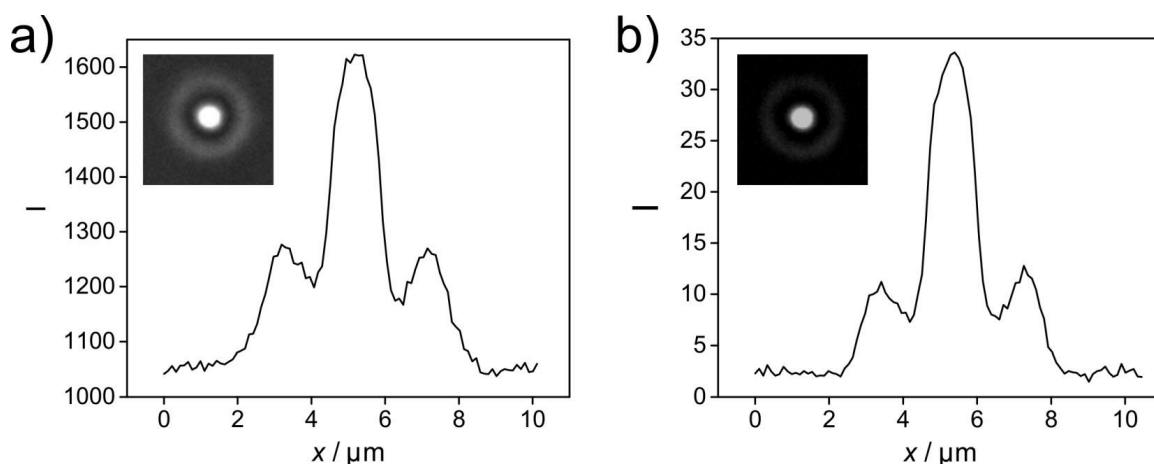


Figure 1.6. Micrograph and intensity response (gray scale) from a poly(styrene) microsphere imaged with phase contrast (Olympus LUCPlan FLN 60 \times Ph objective and Andor Zyla 4.4 Plus camera) before a), and after applying rolling ball filter b).

Other methods of particle detection involve fitting (typically Gaussian^{70,75}) or correlation based methods. Correlation methods require a template image of the particle of interest, are the most computationally expensive and only really necessary in biological systems where the objects are of complex morphology i.e. cells. It has been found overall that most detection methods perform equally so long as there is sufficient signal-to-noise.^{74,84}

1.4.1.3 Linking of Particle Locations – Trajectory generation

Having located the estimated positions of particles in each video frame the computer now has the task of joining up the dots. The simplest approach to do this is by nearest-neighbour searching which, as implied by the name, looks for the shortest distance to a detected particle in the following frame. This algorithm fails when there are gaps in the trajectory caused by missing detections which happens when a particle leaves the focal plane momentarily. As it is important to track particles for as long as possible in order to reduce the error in the subsequent calculation of the mean-squared-displacement (MSD) (a point we will come back to later), researchers often look to other methods to link particle locations. Additionally when volume fractions of particles in the dispersion are higher there may be many crossing trajectories which nearest-neighbour linking may fail to distinguish.

Global linking strategies can be used to overcome some of these issues. In so called

‘multiple hypothesis tracking’⁸⁵ one looks at the entire image data, i.e. every frame, and searches for the optimal path for each particle without violating a simple rule that says that no two paths can share the image of the same particle in any frame. This is by far the most computationally intensive method to approach the problem and thus other more efficient solutions have since been proposed.⁸⁶ A related approach is to consider weighting the probability of belonging to a trajectory and constructing a cost matrix. Subsequent minimization of the global cost function allows for rigorous and efficient tracking with the opportunity to close gaps in the trajectory.^{86,87} For brevity we will not detail alternative methods but notable options include Kalman filtering⁸⁸ and dynamic programming.^{79,89} Note, if care is taken during sample preparation and imaging, most colloidal studies should find nearest neighbour searching adequate with the addition of gap closing to ensure sufficiently long trajectories.

1.4.2 Trajectory analysis

Once particle tracking has been performed we must analyse and quantify the motional behaviour of our little particles. The universal approach to quantifying the average movements of particles is in the computation of the mean squared displacement (MSD) of each particle. This quantity describes the average distance squared, Δx^2 , a particle travels as a function of lag time, t , and it is often expressed as an ensemble average, $\langle \Delta x^2 \rangle$, to represent the behaviour of the system as a whole. The MSD is calculated using all pairs of displacements with their associated lag time. For N particles, with position at a certain lag time $x_n(t)$ and reference position $x_n(0)$:

$$\langle \Delta x^2(t) \rangle = \frac{1}{N} \sum_{n=1}^N [x_n(t) - x_n(0)]^2. \quad (1.15)$$

An implication of calculating the MSD in this way is that larger lag times are sampled far less than shorter lag times. This leads to a scaling of the standard deviation with $\langle x^2 \rangle$ and as such the data at larger lag times should be regarded cautiously. In fact Saxton suggests cutting off the data at 25% of n ⁹⁰ and Ernst and Köhler suggest that any fitting should be applied to the first 4 fitting points.^{91,92} This is dependent on the sampling rate

and the total acquisition time however – for longer time intervals between frames and shorter videos more fitting points may be required.

The dependence of the MSD on time is indicative of the type of motion that the particles are subject to. For a particle moving in a random walk following Brownian motion we have already shown the MSD scales linearly with diffusion coefficient, D , and time, t – equation (1.2). When the motion is transported or hindered however the form of the time dependence and hence scaling of the MSD can change. This has been known by biophysicists for years^{90,93} and has led to the modelling of so-called ‘anomalous’ diffusion by a power law:

$$\langle \Delta x^2(t) \rangle = \Gamma t^\alpha, \quad (1.16)$$

where Γ represents the generalized diffusion coefficient and α is the anomalous exponent. For sub-diffusive, hindered motion $\alpha < 1$ whereas for super-diffusive, transported motion $\alpha > 1$. In the biological world hindered motion is common due to obstacles and traps in the crowded environment that particles inhabit.⁹⁴ Super-diffusive motion occurs for actively transported processes for instance cargo transport by motor proteins.⁹⁵ This analysis is also relevant to artificial colloidal systems where particles may be hindered or trapped due to obstacles and barriers or adhesion to surfaces. There are also numerous transport processes (some of which are outlined in section 1.2.1.1) that can be modelled with a super-diffusive exponent. In some active transport cases this model will struggle to fit the data and so one can attempt to characterize the motion by a ballistic term:

$$\langle \Delta x^2(t) \rangle = 4Dt + v^2 t^2, \quad (1.17)$$

where v is the propulsive velocity. The motion of molecular motors on microtubules is found to fit this type of directed motion⁹⁶ along with other processes such as convection and sedimentation.⁹⁷

An alternative and often complementary quantity of motional analysis is contained within the velocity autocorrelation function (VACF), briefly described in the next section – equation (3.4).

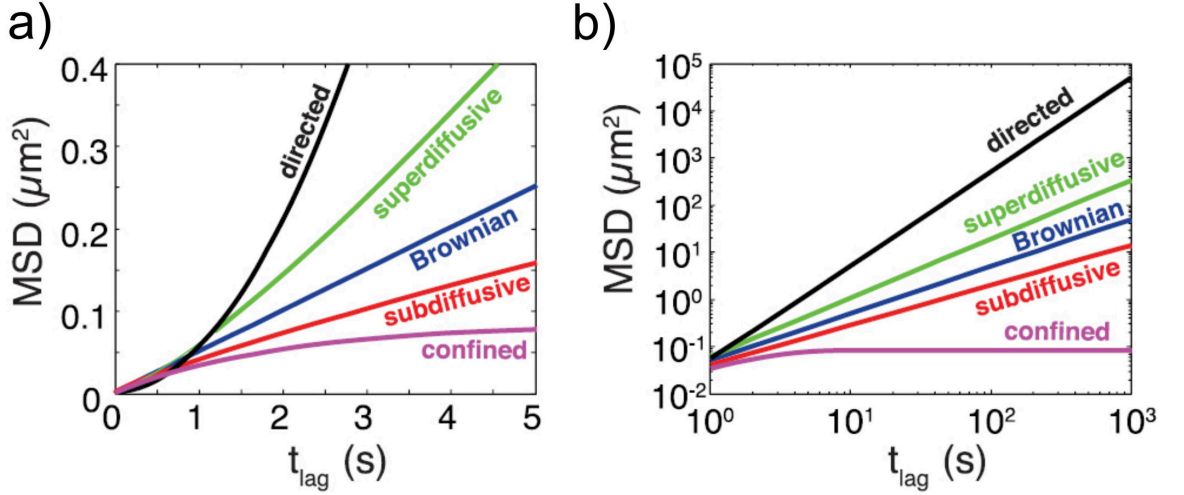


Figure 1.7. Dependence of mean squared displacement with lag time, t_{lag} , for different types of transport processes in 2D. Brownian diffusion is purely linear according to equation (1.2). Anomalous diffusion has power law dependency dependent on whether the motion is super- or sub-diffusive – equation (1.16). Directed or propulsive motion has quadratic scaling according to a propelled velocity – equation (1.17). Confined motion due to trapping shows a plateau in the MSD which is related to the confinement area.⁷⁰ Reprinted with permission from Manzo *et al.*; A review of progress in single particle tracking: from methods to biophysical insights, *Rep. Prog. Phys.*, 78, 124601, **2015**. Copyright IOP Publishing.

1.4.2.1 Auto/Self-phoretic Colloids

In order to effectively determine whether a colloid is in motion due to an auto/self-phoretic mechanism we must first determine the order of magnitude of its propulsive velocity. If this is in accordance with previous data and that expected for a phoretic mechanism (i.e. $\sim 1\text{--}20 \mu\text{m s}^{-1}$) then we can be confident that we are on the right track. The propulsive velocity, v , can be extracted by fitting of the MSD with equation (1.17). A simpler method is to divide the displacement over a certain short time period to give an ‘instantaneous’ velocity, however this only works $v \gg D$. Both of these methods are only valid when motion from other transport mechanisms are negligible which may not be the case as convection, sedimentation and other advective processes are usually present to some degree.⁹⁷

Fortunately there is a characteristic of auto/self-phoretic colloids that allows us to distinguish phoretic propulsion from other types of transported processes. To understand

this we consider the simple case of a spherical colloid with one half of the sphere containing a catalytic surface that drives propulsion. The particle propels in a direction relative to the flow field being established due to the reaction at the catalytic surface. This provides persistent directional force (towards or away from the catalytic cap depending on electrokinetic effects^{52,55}) driving the particle forward. All colloids are also subject to Brownian rotation on top of this however which, over time, randomizes the propelled direction of the particle. The rotational diffusion coefficient, D_r , is related to the radius, r , of the spherical colloid according to:

$$D_r = \frac{k_B T}{8\pi\eta r^3}, \quad (1.18)$$

with units expressed in s^{-1} . A characteristic rotation time, τ_R , for the sphere to perform a full rotation is found from the inverse of equation (1.18). The consequence of these random rotations is that the form of the MSD begins parabolic with v and decays back to a linear form with τ_R ⁴⁶:

$$\langle \Delta x^2(t) \rangle = 4Dt + \frac{v^2 \tau_R^2}{2} \left[\frac{2t}{\tau_R} + e^{-2t/\tau_R} - 1 \right]. \quad (1.19)$$

As such we can distinguish between advective processes, which will not see a decay in the parabola of the MSD back to linear unlike self-propulsive processes. This is presented graphically in figure 1.8 from the works of Howse *et al.*⁴⁶ and is fitted with the two limiting forms of equation (1.19),

$$\langle \Delta x^2(t) \rangle = \begin{cases} 4Dt + v^2 t^2 & \text{when } t \ll \tau_R, \\ 4Dt + v^2 t \tau_R & \text{when } t \gg \tau_R. \end{cases} \quad (1.20)$$

Another useful analytical tool is the velocity autocorrelation function (VACF). This is commonly used in the field of molecular dynamics to interrogate the structural dynamics of a system. The normalized VACF was used by Ke *et al.* to aid in the characterization of the motion of self-propelled Pt-Silica particles.⁹⁸ We can apply it here to clearly distinguish between propulsion and advection (from a uniform flow field). The velocity, v , is compared

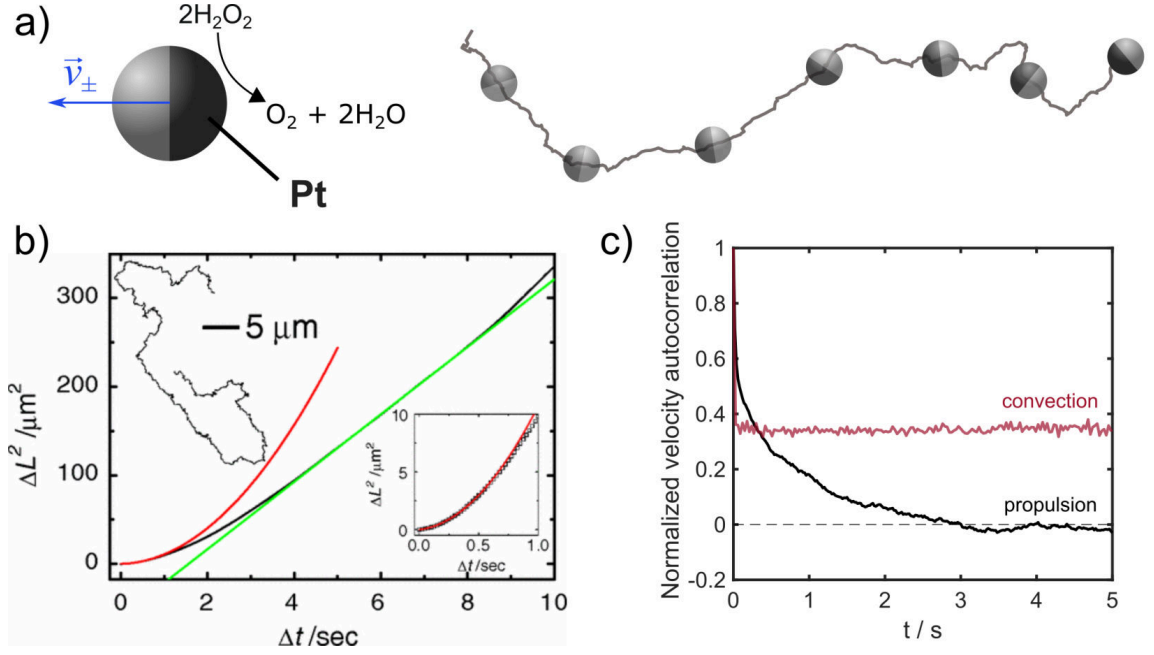


Figure 1.8. Depiction of a catalytic half-coated self-propelling colloid and its trajectory when dispersed in a fuel mixture a). Their characteristic MSD behaviour which is parabolic at short times, $t \ll \tau_R$, and linear at long times, $t \gg \tau_R$ b)⁴⁶ Reprinted with permission from Howse *et al.*, Self-Motile Colloidal Particles: From Directed Propulsion to Random Walk, *Phys. Rev. Lett.*, 99, 048102, **2007**. Copyright 2007 by the American Physical Society. A comparison between the normalized velocity autocorrelation function of self-propelling PS-Pt particles (black) and those experiencing a uniform convection field (red) c).

at each time point with the initial velocity according to:

$$\langle v_i(0) \cdot v_i(t) \rangle = \frac{1}{N} \sum_{i=1}^N [v_i(0) \cdot v_i(t_0 + n\Delta t)]. \quad (1.21)$$

In the presence of a uniform flow field (i.e. convection) where velocity is persistent in one direction we see a non-zero VACF where particles are transported in this flow field. When a particle is exhibiting auto/self-phoresis, the velocity comes from the particle itself and thus its direction can be randomized leading to a decorrelation and zero VACF after time has been allowed for it to fully rotate (figure 1.8c). With these tools the experimenter should be well equipped to study the active motion of colloidal particles.

1.5 Thesis outline

The work in this thesis is based around the theme of how anisotropy in colloidal shape can afford interesting transport phenomena. The term ‘transport phenomena’ is used in a broad sense to represent the dynamic behaviour over length scales ranging from nanometers up to micrometers. The focus for this introduction has been on dynamics at the micron scale which covers the basics for content in Chapters 2–4, however the final chapter of this thesis (Chapter 5) deals with the transport phenomena of light (i.e. nano scale) with static, anisotropic particle films. A separate discussion is given therein to introduce the topic and establish some background theory.

In **Chapter 2** we investigate the effect of roughening the surface of polymer microspheres on their Brownian motion. A new approach to fabricating rough polymer colloids with an important emphasis on preserving volume of the rough particle relative to its ‘smooth’ derivative is presented. The technique is based on the physical deformation of polymer particles above their glass transition temperature in the presence of a select inorganic colloid that is readily removed afterwards. The diffusion of ‘smooth’ and ‘rough’ polymer colloids are directly compared by 2D particle tracking.

Chapter 3 extends the synthesis protocol of Chapter 2 by post modification of the rough micro-particles with platinum sputtering to produce chemically anisotropic particles with rough surfaces capable of self-phoretic propulsion. The effect on the propulsive behaviour due to roughening the surface prior to sputtering is investigated with a particular focus on speed.

The synthesis of ‘matchstick’ shaped silica-manganese oxide particles is presented in **Chapter 4**. These anisotropic particles are produced with a catalytic manganese oxide containing head and silica tail, the length of which can be carefully tuned. The dynamics of these colloids are measured by 2D particle tracking and their potential for an auto/self-phoretic response is tested by introduction of hydrogen peroxide fuel.

Chapter 5 details the synthesis of silica ‘rod’ and ‘worm’-like colloids of which the matchstick synthesis in the previous chapter was derived. An exploration of the synthesis conditions and wide range of produced morphologies is presented with the aim of selecting

prime candidates for the broadband scattering of white light. With the selected candidates, colloidal films were assembled for quantitative comparison studies on the material whiteness. This work was carried out in collaboration with Silvia Vignolini's bio-inspired photonics group at Cambridge University.

References

- [1] T. Graham, *Philos. Trans. R. Soc. London*, 1861, **151**, 183–224.
- [2] W. Ostwald, *Koll.-Zeitschr.*, 1907, **1**, 331.
- [3] P. P. V. Weimarn, *Grundzüge der Dispersoidchemie*, Dresden, 1911, pp. 1–123.
- [4] H. Freundlich, *Kapillare Chemie*, Leipzig, 4th edn., 1930, pp. 388–399.
- [5] W. Ostwald, *Die Welt der Vernachlässigten Dimensionen: Eine Einführung in die Kolloidchemie, mit besonderer Berücksichtigung ihrer Anwendungen.*, Leipzig, 1927, pp. 1–325.
- [6] D. H. Everett, *Pure Appl. Chem.*, 1972, **31**, 577–638.
- [7] J. Ingen-Housz, *Vermischte Schriften physisch-medicinischen Inhalts*, Wappler, 1784, pp. 1–452.
- [8] A. van Leewenhoeck, *Philos. Trans. R. Soc. London*, 1677, **12**, 821–831.
- [9] A. T. Brongniart, *Ann. Sci. Nat.*, 1827, **12**, 44–46.
- [10] R. Brown, *Edinburgh New Philos. J.*, 1828, **6**, 358–371.
- [11] L. Guoy, *J. Phys.*, 1888, **7**, 561.
- [12] L. Guoy, *Acad. Sci., Paris*, 1889, **109**, 102.
- [13] L. Guoy, *Rev. Ge'n. Sci.*, 1895, **6**, 1.
- [14] A. Einstein, *Ann. Phys.*, 1905, **17**, 549–560.
- [15] W. Sutherland, *Phil. Mag.*, 1905, **9**, 781–785.

- [16] M. Smoluchowski, *Ann. Phys. Paris*, 1906, **21**, 757–779.
- [17] P. Langevin, *C. R. Acad. Sci. Paris.*, 1908, **146**, 530–533.
- [18] D. S. Lemons and A. Gythiel, *Am. J. Phys.*, 1997, **65**, 1079–1081.
- [19] J. Perrin, *Atoms*, New York D. Van Nostrand Company, 1916, pp. 1–240.
- [20] D. Rivi re, B. Selva, H. Chraibi, U. Delabre and J. P. Delville, *Phys. Rev. E*, 2016, **93**, 1–11.
- [21] T. Svedberg and K. O. Pedersen, *The Ultracentrifuge.*, Oxford : Clarendon Press, 1940, pp. 1–478.
- [22] J. L. Anderson, *Ann. Rev. Fluid Mech.*, 1989, **21**, 61–99.
- [23] H. Helmholtz, *Ann. der Phys. und Chemie*, 1853, **165**, 211–233.
- [24] P. C. Hiemenz and R. Rajagopalan, *Principles of Colloid and Surface Chemsitry*, Marcel Dekker, 1997, pp. 1–629.
- [25] B. V. Derjaguin, G. P. Sidorenko, E. A. Zubashchenko and E. V. Kiseleva, *Kolloidn. Zh.*, 1947, **9**, 335–348.
- [26] J. L. Anderson, M. E. Lowell A N and D. D. C. Prieve, *J. Fluid Mech*, 1982, **117**, 107–121.
- [27] P. O. Staffeld and J. A. Quinn, *J. Colloid Interface Sci.*, 1989, **130**, 88–100.
- [28] H. Brenner, *Phys. Rev. E*, 2011, **84**, 066317.
- [29] B. V. Derjaguin, *Prog. Colloid Polym. Sci.*, 1987, **74**, 17–30.
- [30] E. Drexler, *Engines of creation*, Doubleday, 1986, pp. 1–216.
- [31] E. M. Purcell, *Am. J. Phys.*, 1977, **45**, 3–11.
- [32] G. Tortora, B. Funke and C. Case, *Microbiology: An Introduction*, Addison-Wesley Longman, Inc., 1995, p. 275.

- [33] J. S. Guasto, R. Rusconi and R. Stocker, *Annu. Rev. Fluid Mech.*, 2012, **44**, 373–400.
- [34] L. E. Becker, S. A. Koehler and H. A. Stone, *J. Fluid Mech.*, 2003, **490**, 15–35.
- [35] D. Tam and A. Hosoi, *Phys. Rev. Lett.*, 2007, **98**, 1–4.
- [36] J. E. Avron and O. Raz, *New J. Phys.*, 2008, **10**, 1–19.
- [37] E. Lauga, *Soft Matter*, 2011, **7**, 3060–3065.
- [38] R. Dreyfus, J. Baudry, M. L. Roper, M. Fermigier, H. a. Stone and J. Bibette, *Nature*, 2005, **437**, 862–865.
- [39] A. Ghosh and P. Fischer, *Nano Lett.*, 2009, **9**, 2243–2245.
- [40] R. F. Ismagilov, A. Schwartz, N. Bowden and G. M. Whitesides, *Angew. Chem. Int. Ed.*, 2002, **114**, 674–676.
- [41] J. G. Gibbs and Y.-P. Zhao, *Appl. Phys. Lett.*, 2009, **94**, 163104.
- [42] K. M. Manesh, M. Cardona, R. Yuan, M. Clark, D. Kagan, S. Balasubramanian and J. Wang, *ACS Nano*, 2010, **4**, 1799–1804.
- [43] S. Balasubramanian, D. Kagan, C.-M. J. Hu, S. Campuzano, M. J. Lobo-Castañon, N. Lim, D. Y. Kang, M. Zimmerman, L. Zhang and J. Wang, *Angew. Chem. Int. Ed.*, 2011, **50**, 4161–4.
- [44] L. Soler, V. Magdanz, V. M. Fomin, S. Sanchez and O. G. Schmidt, *ACS Nano*, 2013, **7**, 9611–9620.
- [45] S. Ramaswamy, *Annu. Rev. Condens. Matter Phys.*, 2010, **1**, 323–345.
- [46] J. Howse, R. Jones, A. Ryan, T. Gough, R. Vafabakhsh and R. Golestanian, *Phys. Rev. Lett.*, 2007, **99**, 048102.
- [47] W. F. Paxton, K. C. Kistler, C. C. Olmeda, A. Sen, S. K. St Angelo, Y. Cao, T. E. Mallouk, P. E. Lammert and V. H. Crespi, *J. Am. Chem. Soc.*, 2004, **126**, 13424–13431.
- [48] H. R. Jiang, N. Yoshinaga and M. Sano, *Phys. Rev. Lett.*, 2010, **105**, 268302.

- [49] A. Lenshof, C. Magnusson and T. Laurell, *Lab Chip*, 2012, **12**, 1210.
- [50] P. G. De Gennes, *Rev Mod Phys*, 1992, **64**, 645–648.
- [51] A. Walther and A. H. E. Müller, *Chem. Rev.*, 2013, **113**, 5194–5261.
- [52] A. Brown and W. Poon, *Soft Matter*, 2014, **10**, 4016–4027.
- [53] A. T. Brown, W. C. K. Poon, C. Holm and J. de Graaf, *Soft Matter*, 2015, **13**, 1200–1222.
- [54] A. T. Brown, I. D. Vladescu, A. Dawson, T. Vissers, J. Schwarz-Linek, J. S. Lintuvuori and W. C. K. Poon, *Soft Matter*, 2016, **12**, 131–140.
- [55] S. Ebbens, D. A. Gregory, G. Dunderdale, J. R. Howse, Y. Ibrahim, T. B. Liverpool and R. Golestanian, *Europhys. Lett.*, 2013, **106**, 58003.
- [56] R. J. Archer, A. J. Parnell, A. I. Campbell, J. R. Howse and S. J. Ebbens, *Adv. Sci.*, 2017, **1700528**, 1700528.
- [57] A. Perro, F. Meunier, V. Schmitt and S. Ravaine, *Physicochem. Eng. Asp.*, 2009, **332**, 57–62.
- [58] B. R. Martin, D. J. Dermody, B. D. Reiss, M. Fang, L. A. Lyon, M. J. Natan and T. E. Mallouk, *Adv. Mater.*, 1999, **11**, 1021–1025.
- [59] R. Laocharoensuk, J. Burdick and J. Wang, *ACS Nano*, 2008, **2**, 1069–1075.
- [60] B. Jang, W. Wang, S. Wiget, A. J. Petruska, X. Chen, C. Hu, A. Hong, D. Folio, A. Ferreira, S. Pané and B. J. Nelson, *ACS Nano*, 2016, **10**, 9983–9991.
- [61] J. Palacci, S. Sacanna, A. P. Steinberg, D. J. Pine and P. M. Chaikin, *Science*, 2013, **339**, 936–940.
- [62] J. Palacci, S. Sacanna, S. Kim, G. Yi, D. J. Pine and P. M. Chaikin, *Philos. Transactions R. Soc. A*, 2014, **372**, 20130372.
- [63] W. I. Goldberg, *Am. J. Phys.*, 1999, **67**, 1152–1160.

- [64] A. J. F. Siegert, *On the fluctuations in signals returned by many independently moving scatterers*, Massachusetts institute of technology technical report, 1943.
- [65] R. Cerbino and V. Trappe, *Phys. Rev. Lett.*, 2008, **100**, 188102.
- [66] V. A. Martinez, R. Besseling, O. A. Croze, J. Tailleur, M. Reufer, J. Schwarz-Linek, L. G. Wilson, M. A. Bees and W. C. K. Poon, *Biophys. J.*, 2012, **103**, 1637–1647.
- [67] J. P. Boon, R. Nossal and A.-H. Chen, *Biophys. J.*, 1974, **14**, 847–864.
- [68] M. Reufer, V. A. Martinez, P. Schurtenberger and W. C. K. Poon, *Langmuir*, 2012, **28**, 4618–4624.
- [69] L. G. Wilson, V. A. Martinez, J. Schwarz-Linek, J. Tailleur, G. Bryant, P. N. Pusey and W. C. K. Poon, *Phys. Rev. Lett.*, 2011, **106**, 7–10.
- [70] C. Manzo and M. F. Garcia-Parajo, *Rep Prog Phys*, 2015, **78**, 124601.
- [71] J. Crocker, J. Crocker and D. Grier, *J. Colloid Interface Sci.*, 1996, **179**, 298–310.
- [72] G. B. Airy, *Trans. Cambridge Philos. Soc.*, 1835, **5**, 1–287.
- [73] M. K. Cheezum, W. F. Walker and W. H. Guilford, *Biophys. J.*, 2001, **81**, 2378–2388.
- [74] B. C. Carter, G. T. Shubeita and S. P. Gross, *Phys. Biol.*, 2005, **2**, 60–72.
- [75] M. C. Jenkins and S. U. Egelhaaf, *Adv. Colloid Interface Sci.*, 2008, **136**, 65–92.
- [76] Z. Yin, T. Kanade and M. Chen, *Med Image Anal*, 2012, **16**, 1047–1062.
- [77] T. H. Nguyen, M. Kandel, H. M. Shakir, C. Best-Popescu, J. Arikath, M. N. Do and G. Popescu, *Sci. Rep.*, 2017, **7**, 1–10.
- [78] R. C. Gonzalez and R. E. Woods, *Digital Image Processing*, Addison-Wesley, 1992, pp. 1–772.
- [79] N. Chenouard, I. Smal, F. de Chaumont, M. Maška, I. F. Sbalzarini, Y. Gong, J. Cardinale, C. Carthel, S. Coraluppi, M. Winter, A. R. Cohen, W. J. Godinez, K. Rohr, Y. Kalaidzidis, L. Liang, J. Duncan, H. Shen, Y. Xu, K. E. G. Magnusson, J. Jaldén,

- H. M. Blau, P. Paul-Gilloteaux, P. Roudot, C. Kervrann, F. Waharte, J.-Y. Tinevez, S. L. Shorte, J. Willemsse, K. Celler, G. P. van Wezel, H.-W. Dan, Y.-S. Tsai, C. Ortiz de Solórzano, J.-C. Olivo-Marin and E. Meijering, *Nat. Methods*, 2014, **11**, 281–9.
- [80] B. Shuang, J. Chen, L. Kisley and C. F. Landes, *Phys. Chem. Chem. Phys.*, 2014, **16**, 624–634.
- [81] J.-C. Olivo-Marin, *Pattern Recognit.*, 2002, **35**, 1989–1996.
- [82] A. Huertas and G. Medioni, *IEEE Trans. Pattern Anal. Mach. Intell.*, 1986, **5**, 651–664.
- [83] S. Sternberg, *Computer (Long. Beach. Calif.)*, 1983, **16**, 22–34.
- [84] I. Smal, M. Loog, W. Niessen and E. Meijering, *IEEE Trans. Med. Imaging*, 2009, **29**, 282–301.
- [85] S. Manley, J. M. Gillette, G. H. Patterson, H. Shroff, H. F. Hess, E. Betzig and J. Lippincott-Schwartz, *Nat. Methods*, 2008, **5**, 155–157.
- [86] K. Jaqaman, D. Loerke, M. Mettlen, H. Kuwata, S. Grinstein, S. L. Schmid and G. Danuser, *Nat. Methods*, 2008, **5**, 695–702.
- [87] I. F. Sbalzarini and P. Koumoutsakos, *J. Struct. Biol.*, 2005, **151**, 182–195.
- [88] R. E. Kalman, *J. Basic Eng.*, 1960, **82**, 35.
- [89] J. Rink, E. Ghigo, Y. Kalaidzidis and M. Zerial, *Cell*, 2005, **122**, 735–749.
- [90] M. J. Saxton, in *Methods Mol. Biol.*, Humana Press Inc., 2007, vol. 400, pp. 295–321.
- [91] D. Ernst and J. Köhler, *Phys. Chem. Chem. Phys.*, 2013, **15**, 3429–32.
- [92] D. Ernst and J. Köhler, *Phys. Chem. Chem. Phys.*, 2013, **15**, 845–9.
- [93] T. J. Feder, I. Brust-Mascher, J. P. Slattey, B. Baird and W. W. Webb, *Biophys. J.*, 1996, **70**, 2767–2773.
- [94] F. Höfling and T. Franosch, *Rep. Prog. Phys.*, 2013, **76**, 046602.

- [95] J. F. Revere, J.-H. Jeon, H. Bao, M. Leippe, R. Metzler and C. Selhuber-Unkel, *Sci. Rep.*, 2015, **5**, 11690.
- [96] M. J. Saxton and K. Jacobson, *Annu. Rev. Biophys. Biomol. Struct.*, 1997, **26**, 373–399.
- [97] G. Dunderdale, S. Ebbens, P. Fairclough and J. Howse, *Langmuir*, 2012, **28**, 10997–11006.
- [98] H. Ke, S. Ye, R. Lloyd Carroll and K. Showalter, *J. Phys. Chem. A*, 2010, **114**, 5462–5467.

2

Roughening up Polymer Microspheres and their Brownian Motion

Be cleverer.

Prof. dr. ir. Stefan A. F. Bon

Abstract

The difference between the diffusive motion of smooth and rough polymer colloids is currently unresolved. Here a simple approach for the roughening of the surface of polymer microparticles via a deformation technique in the presence of an inorganic matrix is presented. The process consists of straightforward steps: 1. Preparation of a bicomposite colloidal sol (polymer + inorganic particles), 2. Drying of the mixture onto a suitable hard substrate, 3. Heating the dried film above the glass transition temperature of the polymer, and 4. Re-dispersion and chemical etching of the inorganic medium. The primary driver is capillary imbibition of the polymer melt into the inorganic colloidal template. In addition, 2D particle tracking experiments were performed and despite large scale roughness (up to 10 % asperity size with respect to particle diameter), Stokes law is obeyed and the particles motion can be modelled simply with the Stokes-Einstein-Sutherland relation obeying no-slip boundary conditions.

Parts of this chapter are published elsewhere, see: Longbottom, B. W.; Somuncuoğlu, B.; Punter, J. J.; Longbottom, S.; Bon, S. A. F. *Soft Matter* 2017, **13**, 4285–4293.

2.1 Introduction

Spherical microscopic particles with a rough surface topography demonstrate intriguing behaviour when dispersed in liquids. Concentrated dispersions of rough particles show interesting rheological features. For instance they display an earlier onset of the jamming transition of colloidal suspensions under flow¹ and as such are considered a useful model for studying friction in suspensions.² Additionally, rough particles show a distinct wetting behaviour when compared to smooth microspheres when adhered to a soft deformable interface (for example an emulsion droplet), a phenomenon known as Pickering stabilization.^{3–5} Apart from interest in the physical sciences rough particles have shown promise in other disciplines, for instance biomedical research, where there is an emerging trend to study and understand particle-cell interactions upon variation of particles shape.⁶ It has been recognized that the shape of the particle plays an important role in the mechanism of cell uptake and exocytosis.⁷ Thompson and co-workers proposed, with simulation work, that nanoscale surface roughness can significantly enhance interactions at the nanoparticle-biological interface and therefore promote colloidal adhesion and cell uptake.⁸

An approximate definition for surface roughness can be approached by looking at the size and number of so-called asperities or ‘bumps’ on the outer periphery of the particle. The driver for this chapter was to develop a process to maximize asperities and therefore roughness on microspheres. A common, and well-studied, class of microspheres are made up of amorphous non-cross-linked polymers. To introduce large asperities (10 % particle diameter) to the surface of polymer colloids is challenging, due to the dominance of surface tension and hence Laplace pressure. Fabrication strategies are relatively limited. An established potential synthetic chemical method involves swelling of a lightly cross-linked particle with monomer and subsequent elevation of temperature and polymerisation leading to the formation of one or more protrusions.^{9–11} This technique involves a critical phase separation event that drives the formation of secondary lobes on the surface of a smooth polymer particle. The number of protrusions is limited by the drive to minimize surface tension and thus the attributed surface roughness is limited. Another synthetic route, developed previously by Bon *et al.*, is through Pickering heterogeneous polymerisation.^{12–19}

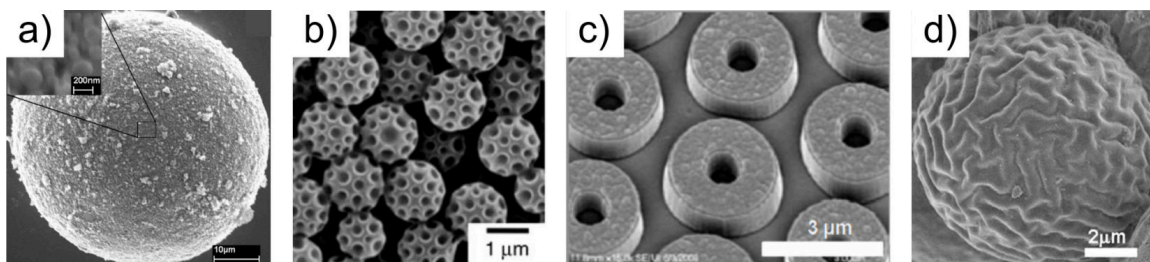
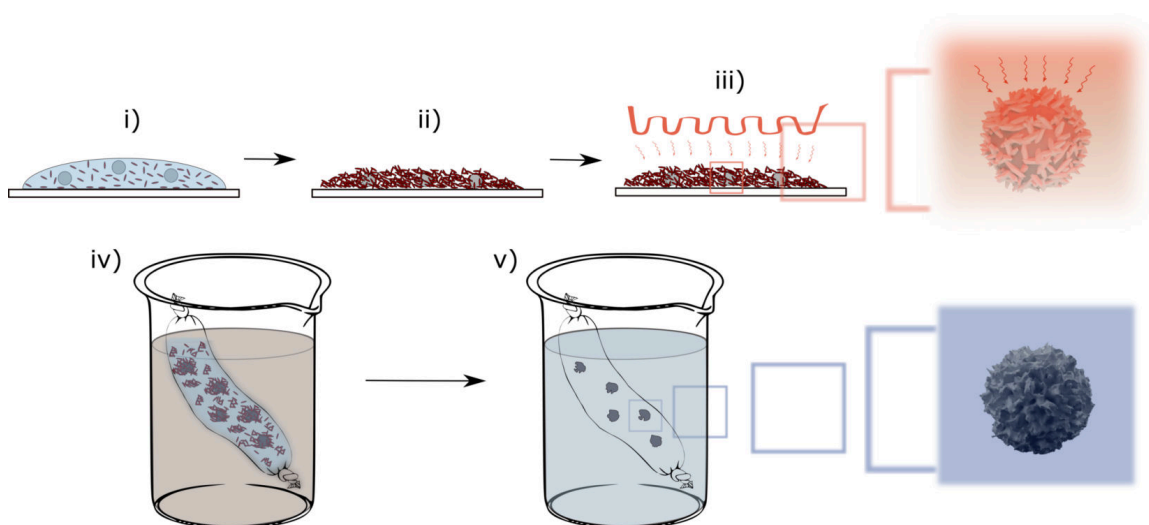


Figure 2.1. Scanning Electron Microscopy (SEM) images of examples of rough polymer colloids produced *via* different synthetic procedures: Pickering heterogeneous polymerisation¹⁴ a), multistage emulsion/dispersion polymerisation²⁰ b), PRINT²³ c) and post surface oxidation²¹ d).

Here, colloidal polymer particles are synthesized with small, typically inorganic colloids *in situ* that act as solid stabilizers for the growing polymer colloids. The packing of these small particles on the surface of the polymer spheres imparts roughness. The resultant roughness in this case is then limited by the dimensions of the small patterning particles and thus these dictate the asperities (See figure 2.1 a). Some further examples of routes involving synthetic polymer chemistry are multistage emulsion/dispersion polymerisation with phase separation events in the surface regions of the particles²⁰ (figure 2.1 b) and buckling of microspheres through post crosslinking (figure 2.1 d).²¹ Examples of other potential strategies are photolithographic methods,²² and Particle Replication In Non-wetting Templates (PRINT) (figure 2.1 c),²³ both are applied in a 2D fashion limiting roughness to one section of the particle.

The aforementioned processes are good examples for fabricating rough colloids however they require skill and experience of chemical synthesis. Fabrication methods that do not rely on synthesis are less known, one example being hetero-coagulation in a binary system of small colloids onto oppositely charged larger spheres.^{24–28} The experimenters have the propensity to tune the ultimate roughness scale by selecting the size and morphology of the colloids involved in hetero-coagulation. In this case simplicity leads to extensibility without getting tied down to complex synthetic procedures. The philosophy of such an approach is implemented here in our methodology with an aim to improve on the ultimate roughness reached.

The methodology is simple in principal. It does not rely on chemical synthesis for the



Scheme 2.1. Illustration of the fabrication procedure for rough poly(styrene) (PS) micro particles. A dispersion consisting of 0.1 wt.% PS and 10 wt.% inorganic colloid in water were drop-casted to glass slides i), time was allowed to dry at ambient temperature ii), slides were transferred to an oven at 110 °C for controlled periods of $t = 10, 30, 60$ and 120 mins and subsequently allowed to cool to ambient temperature iii) and finally particles were removed from the glass surface and re-dispersed in water and dialysed against 2 M (*aq.*) acetic acid to dissolve the inorganic particles iv), after dissolution of the inorganic colloid the isolated roughened PS dispersion was purified further by dialysis against de-ionised water v).

production of rough colloidal species and instead starts from a spherical, smooth particle to which a simple physical modification process is applied. A two component colloidal mixture of polymer microparticles and inorganic nano/microparticles was prepared and subsequently heated above the glass transition temperature (T_g) of the polymer to induce deformation and hence impart roughness. The protocol is represented in Scheme 2.1 and relies on capillary imbibition of a polymer melt into the interstitial spaces of a colloidal inorganic matrix. This idea was inspired by the works of Nagy and Keller,²⁹ and Velegol and coworkers.³⁰ The first of these teams fabricated ellipsoidal polymer particles via deformation of embedded polymer particles in a soft stretched elastomeric matrix above their glass transition temperature. Notable advances have been made here, firstly that of Ottewill *et al.*³¹ by amplifying the original process and more recently Champion and coworkers³² by fabricating a wide range of particle shapes. However the conception of this idea was more directly inspired by Velegol *et al.* whom substituted elastic deformation forces with wetting forces to form

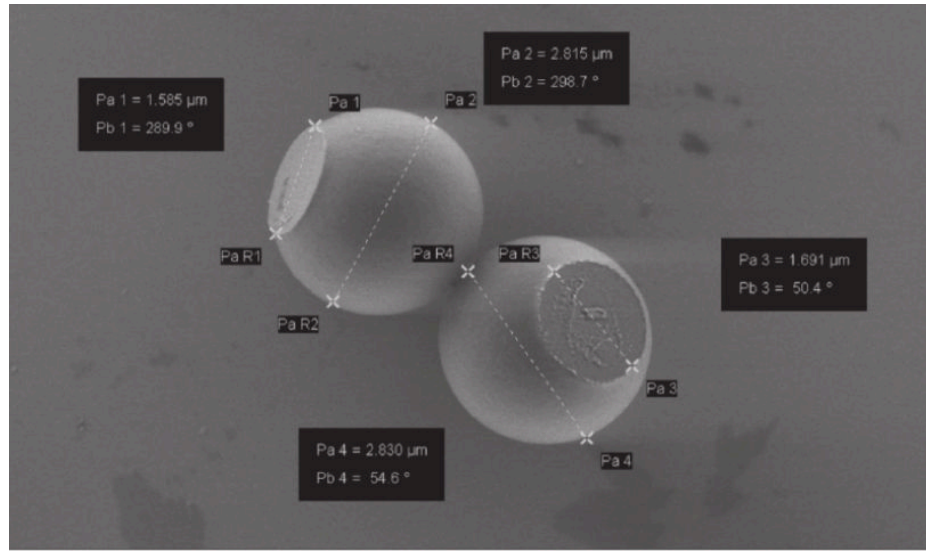


Figure 2.2. Scanning Electron Microscopy (SEM) image of flattened polymer microspheres deformed by wetting forces whilst above the polymer glass transition temperature.³⁰

flattened patches on PS spheres by heating them whilst deposited onto a hard underlying flat substrate (figure 2.2).

In addition to presenting a fabrication method that transforms ‘smooth’ polymer particles into their ‘rough’ analogues, the diffusional behaviour of one set of rough microparticles when dispersed in water was studied and compared their motion to that of the original smooth microspheres. The voyage of these roughened microscopic objects through the bulk and on their approach to a macroscopic and flat solid interface was thought to be interesting. In soft matter physics the study of diffusive motion of a large solute particle dispersed into a fluid of much smaller solvent particles is of key interest, especially when the morphology of the solute particle departs from the well-understood spherical norm.³³ The translational diffusion coefficient of colloidal hard smooth spheres can be described by the relation between their thermal energy, $k_B T$, and friction coefficient, ξ , in the Stokes-Einstein-Sutherland relation (equation (1.1)).^{34–36} For no-slip boundary conditions $\xi = 6\pi\mu r$. The friction coefficient is modified to $\xi = 4\pi\mu r$ for slip boundary conditions.³³ Experimental evidence from light scattering almost exclusively show that, for mesoscopic polymer colloids, the no-slip boundary conditions are satisfied.^{37,38} The hydrodynamics becomes more complex as we depart from a perfect spherical shape and therefore a solution

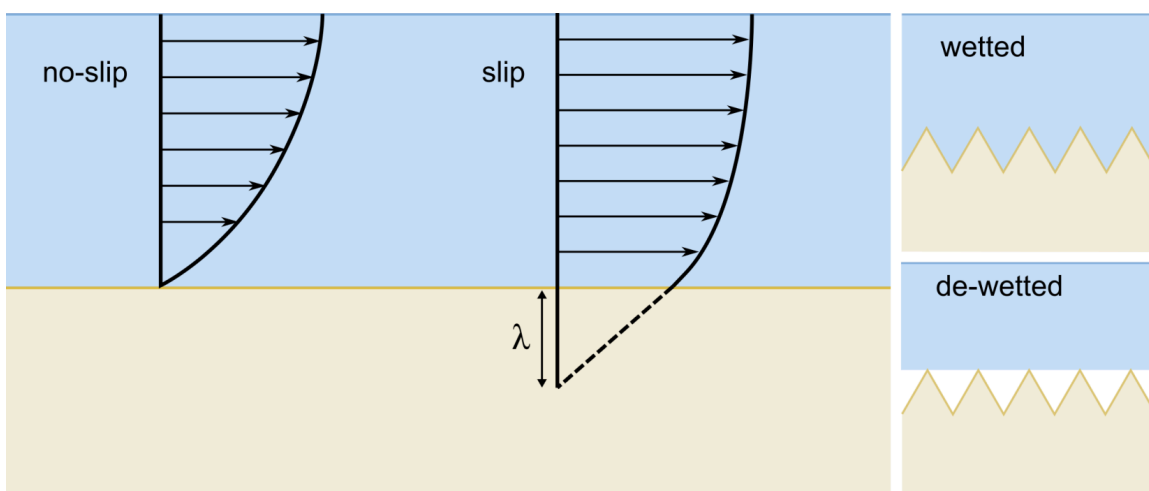


Figure 2.3. Schematic of the no-slip and slip boundary conditions represented by fluid velocity profiles passed a boundary. The fluid velocity is zero at the surface for the no-slip boundary condition whereas it is non-zero for the slip boundary condition with an associated slip length, λ (left). The Wenzel (completely wetted) and Cassie-Baxter (superhydrophobic) regimes on rough surfaces (right).

for the friction coefficient is harder to reach.

There are two main material parameters to consider when thinking of friction: adhesion and roughness. Adhesive forces are related to the chemistry of the solid surface and its interaction with the dispersion medium – friction is higher for fluids that wet surfaces well. Logically one would assume that with increasing surface roughness in a wetted system there is an increased resistance to flow at the surface and therefore reduced motion. However contradictory experimental findings exist in the literature that would suggest both an increase^{39,40} and decrease⁴¹ in friction coefficient with increasing surface roughness. The latter work by Bonaccorso *et al.* concludes that with large scale surface roughness in completely wetted (Wenzel) systems, slip (see figure 2.3 for boundary conditions) occurs at the boundary and is amplified by roughness leading to lower friction. These findings have since been attributed to an ambiguity in the exact location (at the peaks or valleys of surface asperities) of the surface, hereby the suggestion of an intermediate location results in reviving our original logic.⁴²

Yet it is now well documented that roughness can promote de-wetting and a so-called super-hydrophobic state (Cassie-Baxter regime)⁴³ which exhibits accelerated flow at

the surface due to slip.^{44–46} The reasoning here is that nanobubbles are trapped in these surface asperities and the result of this evolved gas-liquid interface is a reduced resistance at the surface.⁴⁷ It would seem then that roughness exaggerates the effects of the underlying surface i.e. for completely wetted systems increasing roughness increases friction and for de-wetted systems the opposite is true. Evidently the difference between the motion of smooth and rough polymer colloids is not immediately obvious and careful attention of the wetting characteristics should be made.

With this system, the behaviour of ‘rough’ and ‘smooth’ microspheres could be directly compared in bulk, and when approaching a solid and flat macroscopic surface. The works of this chapter aim to shed light on the differences (if any) between the diffusive motion of ‘rough’ vs. ‘smooth’ polymer colloids. The chapter involves an experimental study verifying that the no-slip boundary condition holds despite large scale surface roughness after first detailing a novel fabrication technique for roughened polymer microspheres.

2.2 Results & Discussion

2.2.1 Fabrication and characterization of ‘rough’ microparticles

To fabricate rough microparticles, initially, a sample of smooth microspheres was synthesized by dispersion polymerisation of styrene (see Experimental section 2.3.2). This synthesis technique begins with a miscible mixture of monomer, initiator, solvent and polymeric stabilizer (here poly(*N*-vinylpyrrolidone)). The technique utilizes a solvent that is good for the monomer but bad for its related polymer. As such, when polymerizing, the propagating chains reach a certain critical chain length at which they are no longer soluble in the solvent and so collapse into small unstable nuclei. These continue to coagulatively assemble until a stable number of colloidal particles is formed, hereby absorbing polymeric stabilizer in the process.^{48,49} Note that polymeric stabilizer may be grafted during the polymerisation.⁵⁰ Polymer particles can continue to grow to micron-sized dimensions with very low particle size dispersity if the conditions are favourable. These two parameters were crucial for the ensuing microscopic observation and comparative study.

The methodology used to convert smooth, spherical polymer particles to rough ob-

jects (Schematic 2.1) is detailed as follows: PS particles were cleaned by multiple centrifugation steps, hereby removing excess poly(*N*-vinylpyrrolidone), and other remaining impurities such as initiator and monomer (see Experimental section 2.3.2). The particles (diameter = $1.217 \pm 0.026 \mu\text{m}$) can then be dried and stored as a powder. The PS particles were re-suspended in water by mild sonication, in presence of a large excess, typically a hundred-fold by mass, of various inorganic colloids with distinctive shape. The dispersion mixtures were applied as a liquid film onto a solid glass substrate, and water was subsequently evaporated at room temperature. The dried films were then exposed to temperatures ($283 - 303 \text{ K}$) above the glass transition temperature (T_g) of the polymer particles (that is approximately 373 K for atactic polystyrene) for select time periods.

The inorganic particles selected (figure 2.4 b-d) could be easily dissolved in water upon acidification (etching), and included ‘cigar’-shaped (figure 2.4 b) and rod-shaped (figure 2.4 c) calcium carbonate, along with nano-sized zinc oxide (figure 2.4 d). These inorganic colloidal particles form a matrix with characteristic interstitial spacing and acts like a template, allowing for the capillary imbibition of the polymer melt. This changes the morphology of the microspheres into colloidal objects with a roughened surface topography. A large excess of inorganic colloids was used to minimize the probability that polymer particles would be nearest neighbours or on any outside boundary of the dried film. The now ‘rough’ polymer particles were isolated readily by scraping off the dried films, re-dispersing and breaking up the fragments into acidic water, placing all into a dialysis membrane, and subsequently dissolving the inorganic phase by dialysing it against acidic water.

An overview of the results of these experiments can be determined by examining the collected TEM images (figure 2.5). As can be seen from figure 2.5 the particles gradually become more deformed and thus rough, the longer that the PS is above its T_g , with a maximum to its deformation dependent on reaching an equilibrium status in wettability. This equilibrium is observed as only a small difference in asperity size between figure 2.5 c at 1 hr of heating and figure 2.5 d at 2 hrs. After only 10 mins of heating has been applied to the sample (figure 2.5 a,e,i) the deformation of the particles is fairly limited. Evidently the scale of roughness that can be reached with this procedure is large (i.e. asperity size) and goes beyond the aforementioned synthesis techniques. The school of thought here is

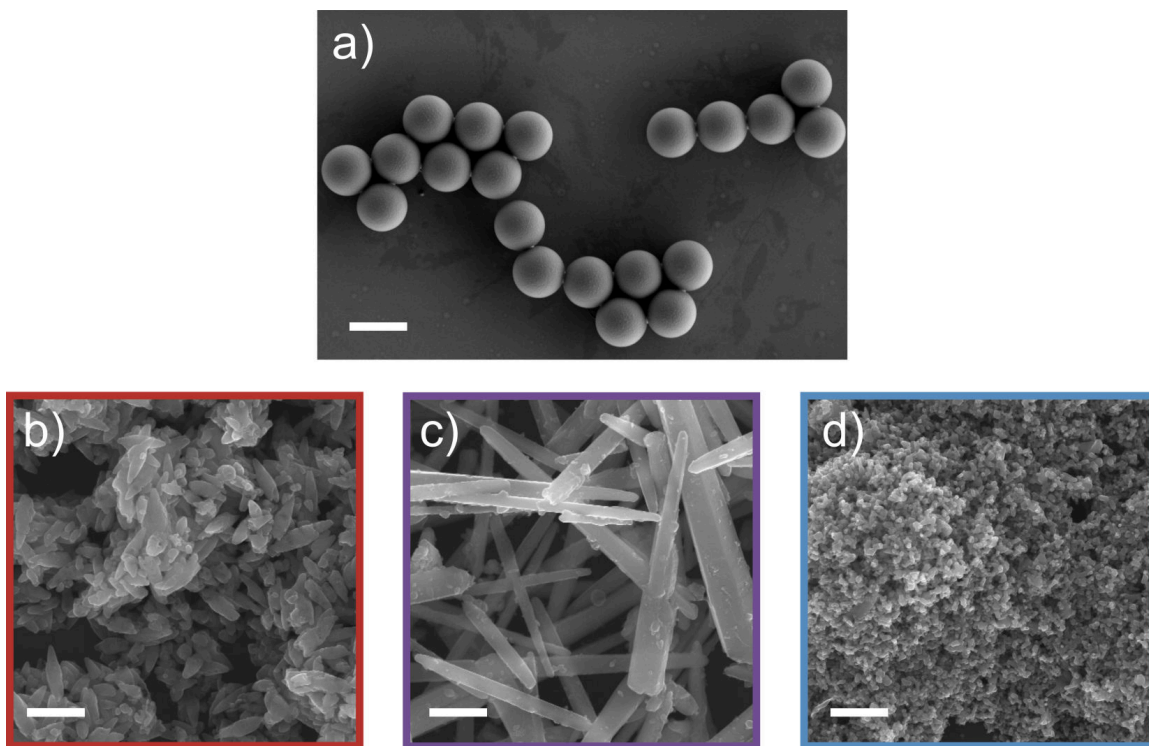


Figure 2.4. Scanning Electron Microscopy (SEM) images of poly(styrene) microspheres synthesized by dispersion polymerisation a), cigar-shaped calcium carbonate b), and rod-shaped calcium carbonate c) nano-sized zinc oxide particles d). Scale bar = 1.5 μm .

that rather than *adding* particles to the surface to endow roughness, instead the inorganic particles are used like a negative mask essentially taking away from the smooth surface. This is not an entirely accurate description however as in fact nothing is being taken away – there must be volume preservation (no chemical reaction occurs between the inorganics and polymer) – but the idea is that a higher degree of roughness (sharper features) can be reached by ‘imprinting’ onto the particle surface.

The different bi-composite colloidal systems are discussed separately in the subsequent sections (cigar-shaped CaCO_3 2.2.1.1, rod-shaped CaCO_3 2.2.1.2, nano-sized ZnO 2.2.1.3).

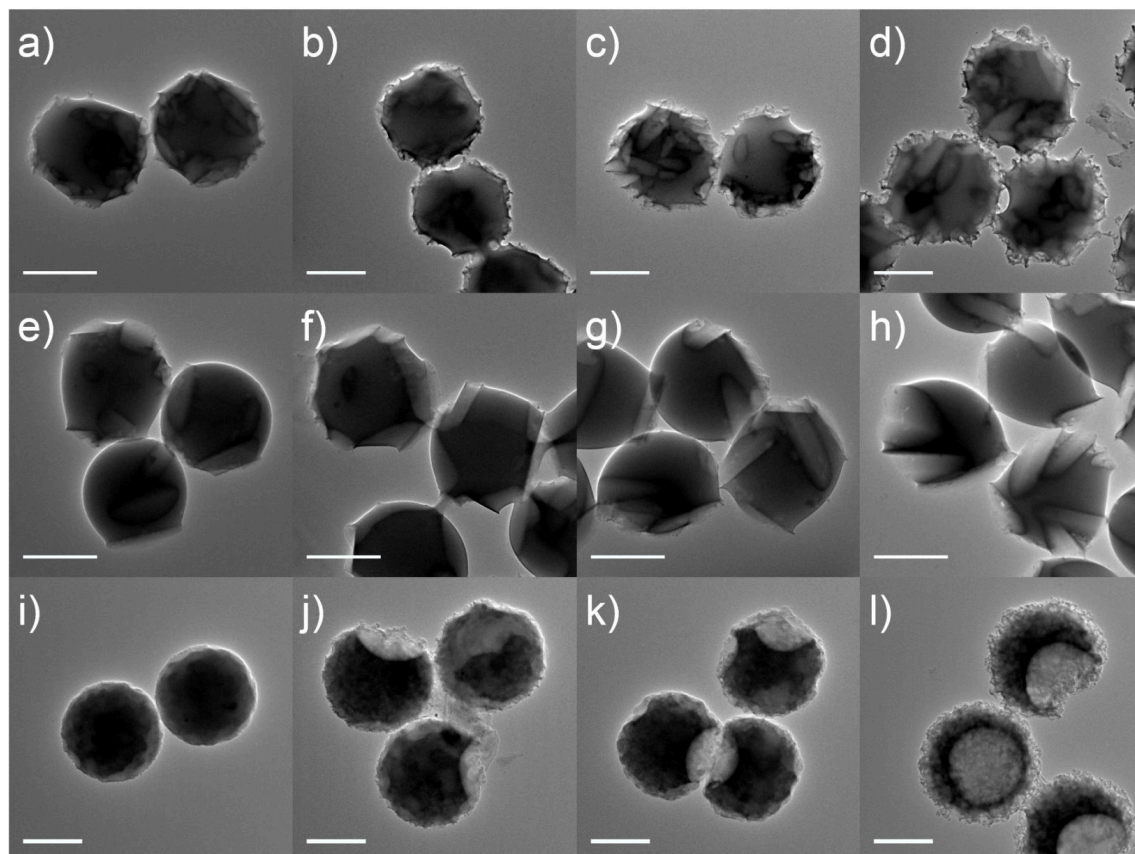


Figure 2.5. Transmission Electron Microscopy (TEM) images of poly(styrene) microspheres deformed at 110°C within a dried colloidal inorganic matrix for approximate time periods of 10, 30, 60 and 120 mins (a-d),(e-h),(i-l). The inorganic particles utilized were cigar-shaped calcium carbonate (a-d), large, rod-shaped calcium carbonate (e-h) and small, spherical/oblong-shaped zinc oxide (i-l). Scale bars = 1.0 μm .

2.2.1.1 Roughening via ‘cigar’-shaped calcium carbonate

In the first system investigated, commercially sourced cigar-shaped CaCO_3 , known as SOCAL P3 was utilised as the type of inorganic particle for the fabrication of the surface-textured ‘rough’ PS microspheres. SOCAL P3 has a calcite scalenohedral type crystal structure and an approximate average diameter of 210 nm with a length of 0.5 to 1.0 μm and an approximate density in the range of 2.70–2.95 g cm^{-3} . The difference in geometry and dimensional scale between the PS microspheres and the SOCAL P3 particles is clearly observed from the SEM images presented in figure 2.4 a and b). Numerous sharp asperities were formed once the sample was heated for more than one hour forming a very rough new surface (figure 2.5 a–d & figure 2.6) .

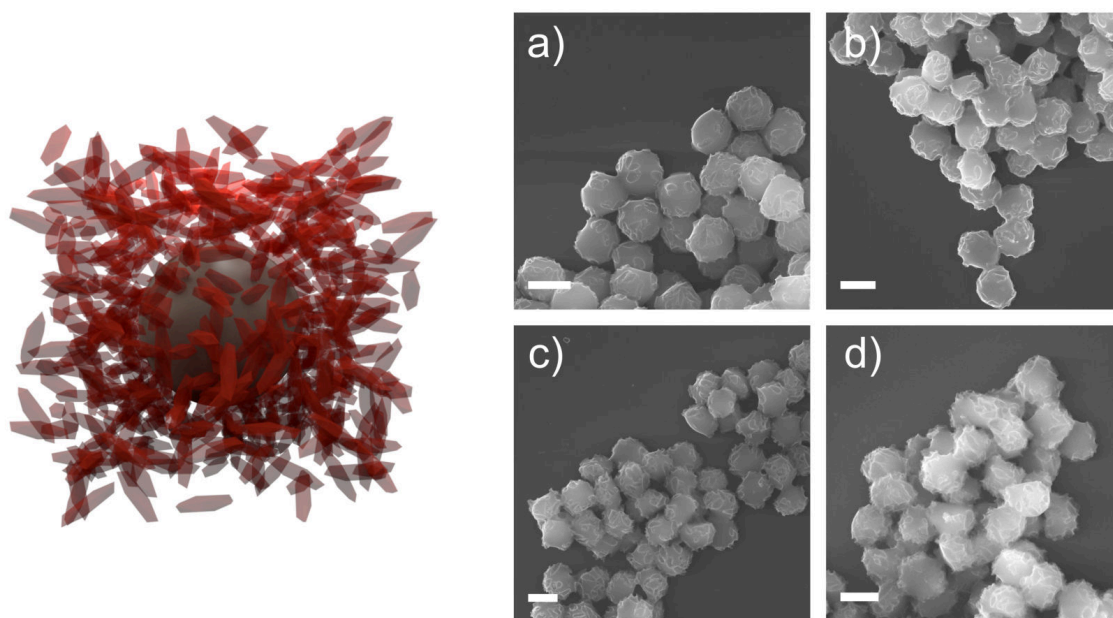


Figure 2.6. Depiction of the colloidal mixture of PS microspheres (grey) amongst cigar-shaped calcium carbonate (red) and representative Scanning Electron Microscopy (SEM) micrographs of rough PS particles deformed in the presence of cigar-shaped calcium carbonate. The PS particles were exposed to heat for (a): 10 mins, (b): 30 mins, (c): 1 hr, (d): 2 hrs. Scale bars = 1.5 μm .

2.2.1.2 Roughening via high aspect ratio rod-shaped calcium carbonate

The procedure was applied to a second system consisting of calcium carbonate with a different morphology - PCC rods $d = 0.5$ and $L = 3\text{--}15\text{ }\mu\text{m}$ (figure 2.4 c). In this case the size of the inorganic constituent is considerably larger than the PS particle size and thus we expect the number of asperities, i.e. physical ‘bumps’, to be far less. figure 2.5 e-h) and figure 2.7 display the TEM and SEM images acquired after deforming the PS particles in a supposed matrix of PCC calcium carbonate rods with increasing time periods (a-d) as in the previous case. A similar trend is observed in which the particles are deformed to a greater extent over time. We assume there is some time taken to uniformly heat the sample material to 110°C and as such after only 10 mins have elapsed, the degree of deformation is small. The rate of capillary imbibition is correlated with viscosity and the relatively high viscosity of the high molecular weight PS limits this. We find here then that the particle takes time to fully deform and again that there is not a great difference between 60 and 120 mins as an equilibrium is approached.

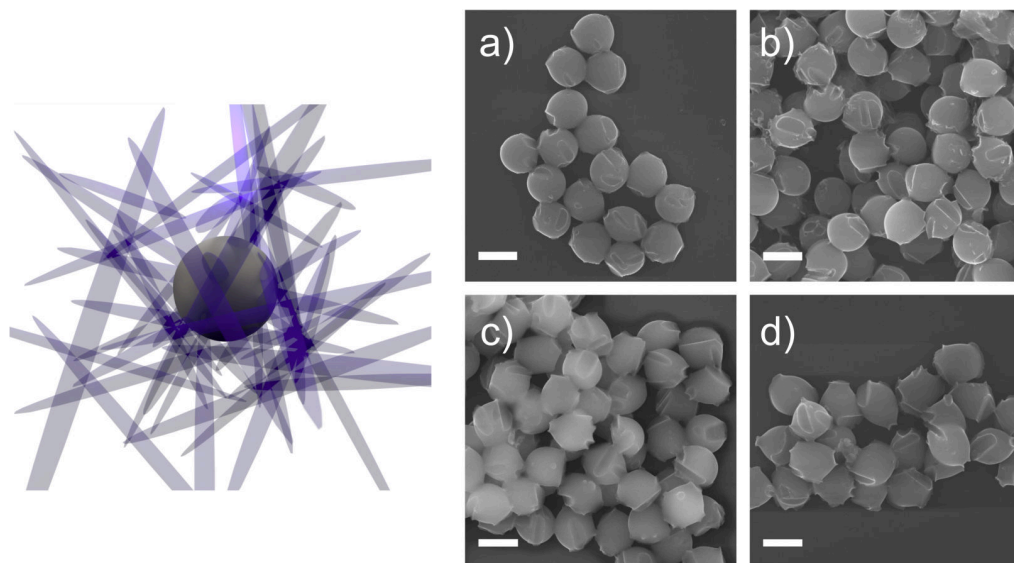


Figure 2.7. Depiction of the colloidal mixture of PS microspheres (grey) amongst rod-shaped calcium carbonate (purple) and representative Scanning Electron Microscopy (SEM) micrographs of rough PS particles deformed in the presence of rod-shaped calcium carbonate. The PS particles were exposed to heat for (A): 10 min, (B): 30 min, (C): 1 hr, (D): 2 hr. Scale bars = $1.5\text{ }\mu\text{m}$.

2.2.1.3 Roughening via nano-sized zinc oxide

A third and final system incorporating small zinc oxide (ZnO) nanoparticles as the inorganic ‘template’ was constructed and examined. Here the dimensions of the ZnO particles were an order of magnitude smaller (~ 100 nm diameter spheres/oblongs, figure 2.4 d) than the PS microspheres and thus they should impart a different scale of roughness. As with the other two cases, the degree of particle deformation increased with exposure time to temperatures above the T_g of poly(styrene) as observed by electron microscopy, TEM and SEM (figure 2.5 i-l and figure 2.8). After 10 mins (figure 2.5 i) the surface of the particles showed only a minor roughness ($< 5\%$ particle diameter) owing to the small size of the inorganic template. However, after prolonged time periods of 30 mins, 1 hr and 2 hrs, unexpected dimpled morphologies evolved, the structures now resembling concave polymer microbuckets⁵¹ with a roughened outer surface. Intriguingly the size of the cavity and roughness of the outer surface became more pronounced upon longer heat exposure.

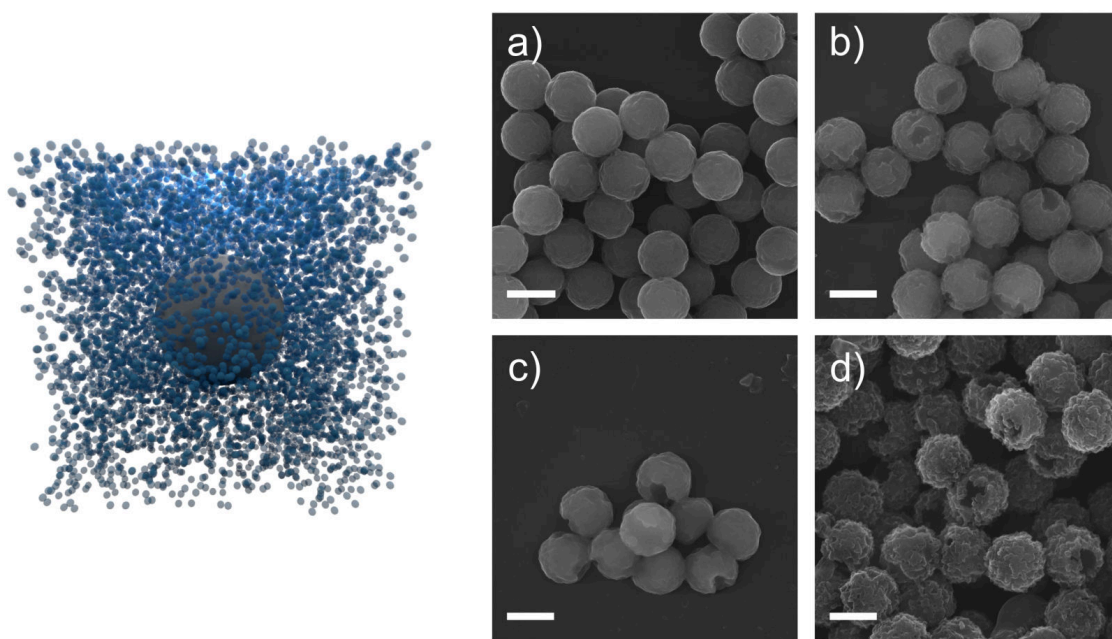


Figure 2.8. Depiction of the colloidal mixture of PS microspheres (grey) amongst ZnO (blue) and representative Scanning Electron Microscopy (SEM) micrographs of rough PS particles deformed in the presence of nano-sized ZnO. The PS particles were exposed to heat for (A): 10 min, (B): 30 min, (C): 1 hr, (D): 2 hr. Scale bars = $1.5\ \mu\text{m}$.

The buckled structures are difficult to rationalize. In an attempt to explain, let us picture the physical state of a single particle throughout the heating and cooling process. As the particle is heated, thermal volume expansion of the polymer occurs and the opposing volume contraction upon cooling. For an un-crosslinked polymer particle this happens uniformly and the particle returns to the original shape. Consider the scenario in which, once the expansion has occurred, simultaneously a cross-linking reaction occurs to form a rigid surface. Now, upon subsequent cooling, the outer surface will not contract with the rest of the soft material and so must buckle to conserve volume. This scenario is presented as a possible explanation for the observed microstructure here.

The origin of the possible cross-linking reaction taking place at the surface of the PS particle could be inorganic and potentially involving PVP. Zinc oxide is routinely surface modified by industry to ensure colloidal stability in the final product. It may be the presence of non-disclosed surface groups that can participate in cross-linking at elevated temperatures that leads to the effect that we observe. We assume a thin shell of cross-linked material, a maximum thickness approximately the diameter of the ZnO particles (100 nm max.), is formed along with an increase in specific volume of the polymer sphere at elevated temperatures. We can assess the plausibility of our suggested buckling mechanism by measuring the dimple size assuming no loss in mass of the poly(styrene) spheres (no decomposition). According to Quilliet⁵² the volume variation relative to a non-deformed sphere, ΔV , due to the inversion of a spherical cap is given by:

$$\frac{\Delta V}{V_{sphere}} = \frac{(1 - \cos \alpha)^2(2 + \cos \alpha)}{2}, \quad (2.1)$$

where α is a half-angle measure for the aperture of the depression. Looking to figure 2.9 as an example from figure 2.5 j), the particle has a fairly obvious inverted cap with $\alpha = 38.5^\circ$ which equates to $\Delta V \sim 6.3\%$. Consulting the literature, the volume expansion, ΔV , for bulk high molecular weight ($M_w \sim 1.5 \times 10^5$) poly(styrene) over the temperature range of 303 – 408 K has been measured as $\Delta V = 3\%$.⁵³ The volume expansion difference is too small to fully explain the observed bucket morphology, especially when one would account for increased Laplace pressure. The discrepancy may originate in the accuracy of the half-

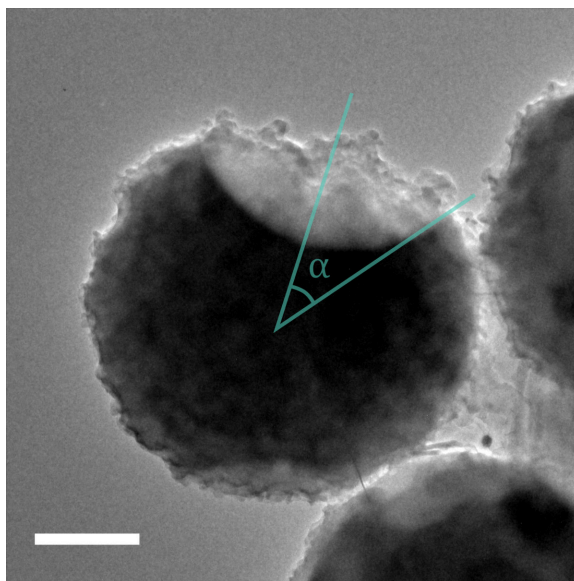


Figure 2.9. Region of interest of TEM image from figure 2.5 j) containing a PS particle with small deformations roughened in the presence of ZnO. The particle has a distinct inverted cap-shaped buckle. Scale bar = 300 nm.

angle measurement. It relies on working from a 2D projection of a particle so we have some orientation dependency here and also requires a knowledge of the centre of mass of the particle in study. However, we do not believe this explanation is the reason. The only other plausible explanation would be that polystyrene is decomposed catalytically (perhaps by the close vicinity of ZnO) at elevated temperatures, accounting for a larger volume reduction. We currently have not unravelled whether if this is the case, and if so how it mechanistically works.

2.2.1.4 Overview & discussion of the roughening process

To explain the deformation process in these systems, we imagine the scenario in which a polymer sphere entrapped in a porous, inorganic matrix is given enough thermal energy to convert to a liquid state and migrate into the interstitial spaces present. For the polystyrene particles to deform from spherical in the dried matrix of inorganic particles, there has to be wetting to allow for capillary imbibition. The capillary forces are the primary driver for physical deformation through flow and thus alteration of the particle shape. Spontaneous imbibition can only occur if there is a capillary under pressure and hence there has to be

a contact angle of the polymer, air and calcium carbonate of less than 90° . Our synthetic polystyrene particles have a surface layer of PVP which provide steric stabilization to the microspheres and is known to be amphiphilic. It has a favourable interaction with both polystyrene and the inorganics and can therefore also promote wetting and hence reduce the contact angle.

One of the key design rules in the fabrication procedure was to have the large excess of inorganic material (1:100 wt.% of PS:inorganic particles) to maximize the probability that the polymer spheres are individually dispersed throughout the dried bicomposite colloidal film. This is important as if polymer particles were to be nearest neighbours in the packed film, they would fuse into clusters upon heating. One should also consider the effect of depletion in the colloidal wet state which is known to occur for mixtures of particles with different geometries.⁵⁴ And finally, boundary effects should be considered throughout the film formation process whereby any spheres located near the glass surface or air interface will experience different deformation. With the above in mind, we ensured the statistical distribution of PS particles to inorganic particles was significant and thus these effects should be of minor concern. Nonetheless, a low fraction of fused aggregates ($<20\%$) was observed in our experiments. This can be seen for instance in the TEM (transmission electron microscopy) images of the deformed particles (figure 2.5 b and f) where thin sections of polymer have bridged between two neighbouring particles (also observable in scanning electron microscopy (SEM) images, figure 2.6 and figure 2.7). It appears from the SEM images (figure 2.6 and figure 2.7) that, predominantly, large clusters (20–50) of particles are present.

We believe, however, that the formation of the observed clusters are not wholly ascribed to the reasons mentioned above, but also due to capillary attraction of rough particles at the interface between the water droplet and air when samples were dried for imaging. This phenomenon is known, for example in the suppression of the coffee ring effect by anisotropic colloids⁵⁵ driven by the generation of capillary quadrupoles as a consequence of an undulated contact line.⁵⁶ We tested this for our system by imaging rough particles – those depicted in figure 2.5 d - both dispersed in water, and in the dry state (figure 2.10). The vast majority ($\sim 80\%$) of rough particles remain well dispersed, i.e. $N_{Ag} = 1$, as single

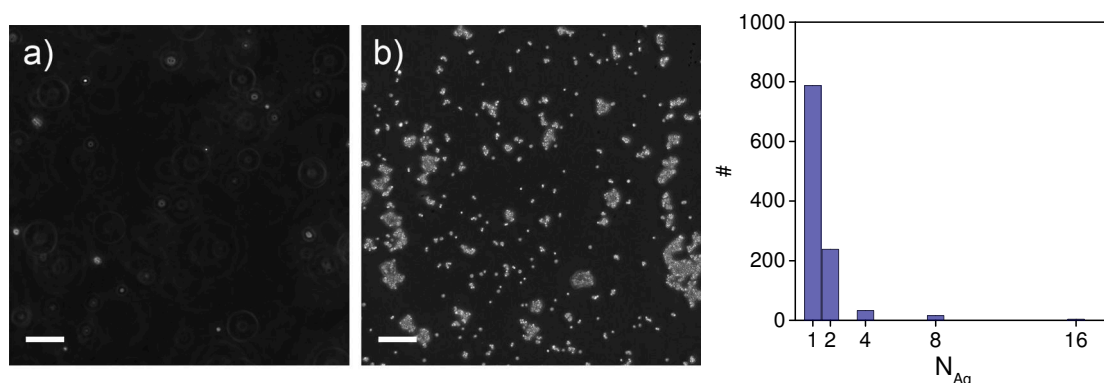


Figure 2.10. Sample phase contrast light microscope images of rough particles dispersed in water (a), and after drying onto glass cover slips (b). Scale bar = 25 μm . Distribution of rough particles in aggregation states according to the number of particles, N_{Ag} (right) measured from light microscopy images of dispersed particles. The projected particle areas were measured and normalized against the average particle diameter for a single rough particle (determined from SEM images see figure 2.15), giving N_{Ag} .

particles (See figure 2.10 for a histogram of Particle Aggregation Number, N_{Ag} .) Once dry, much higher order aggregates are present.

One can ask the question if stratification upon film formation may off-set a random distribution in height of the polymer particles into the inorganic colloidal matrix. The calcium carbonate particles are more likely to aggregate and next sediment as result of a higher Hamaker constant,⁵⁷ potentially positioning the polymer particles nearer to the upper regions of the drying film. In this case however we would expect to see obvious spherical cap (or non-deformed) sections on the vast majority of the deformed particles which are not present in figure 2.5 and figure 2.6. On first glance it appears this could have happened in our second system where the large calcium carbonate rods were deployed (figure 2.5 e-h). The non-deformed sections however do not appear to be exclusive to one side of these particles and we propose that these are present as the high aspect ratio calcium carbonate rods stack in a criss-cross manner like Mikado (observable in figure 2.4 c and low Mag SEM in figure 2.11). This inefficient stacking leads the polymer particles to be trapped in the empty space between rods where they may not have contact with calcium carbonate on all sides.

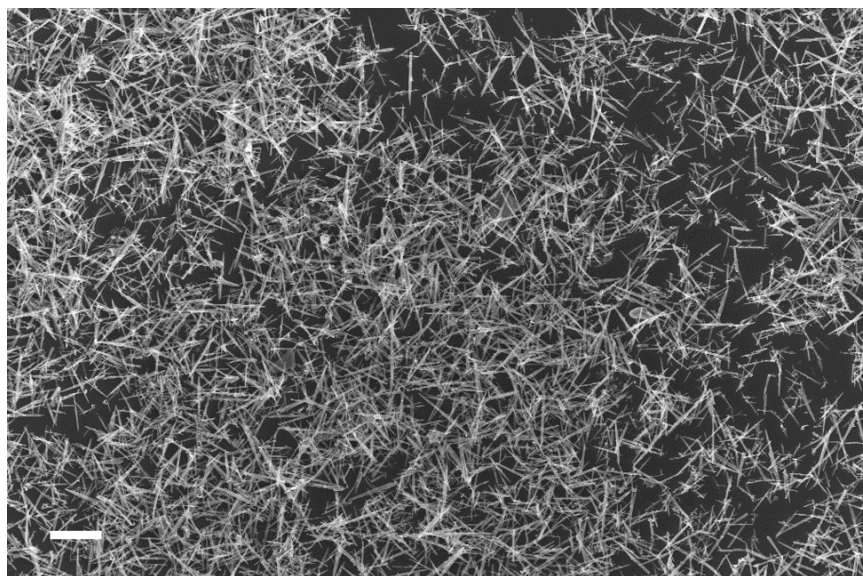


Figure 2.11. Low Magnification Scanning Electron Microscopy (SEM) micrograph of rod-shaped PCC calcium carbonate particles with ‘crisscross’ stacking. Scale bar = 20 μm .

2.2.2 Quantifying particle surface roughness by image analysis

The task of quantifying the roughness of the microspheres in this study was certainly a challenge, not least due to the magnitude and randomness of roughness making atomic force microscopy (AFM) difficult because of potential tip crashing. Recently, Hsu *et al.* utilized a specialized AFM technique to probe particle roughness and friction whereby a rough particle was adhered to a cantilever and was essentially used as a probe in place of the AFM tip.⁵⁸ In our case there is a large variability in roughness between microparticles due to the fact that the inorganic colloids used to deform the surface of the poly(styrene) spheres have an inherent dispersity. Therefore, to collect sufficient statistics, we would need to measure tens to hundreds of particles making specialized AFM techniques such as this laborious and infeasible.

As an alternative solution, roughness was measured from the 2D projections of the rough colloids from SEM images. Similar image analysis has in fact been shown as a useful technique for the classification of breast tumours in medical imaging.^{59,60} The routine was semi-automated and involved the following steps: 1. pre-processing and segmentation of images to obtain thresholded binary images of an isolated particle, 2. centroid localization

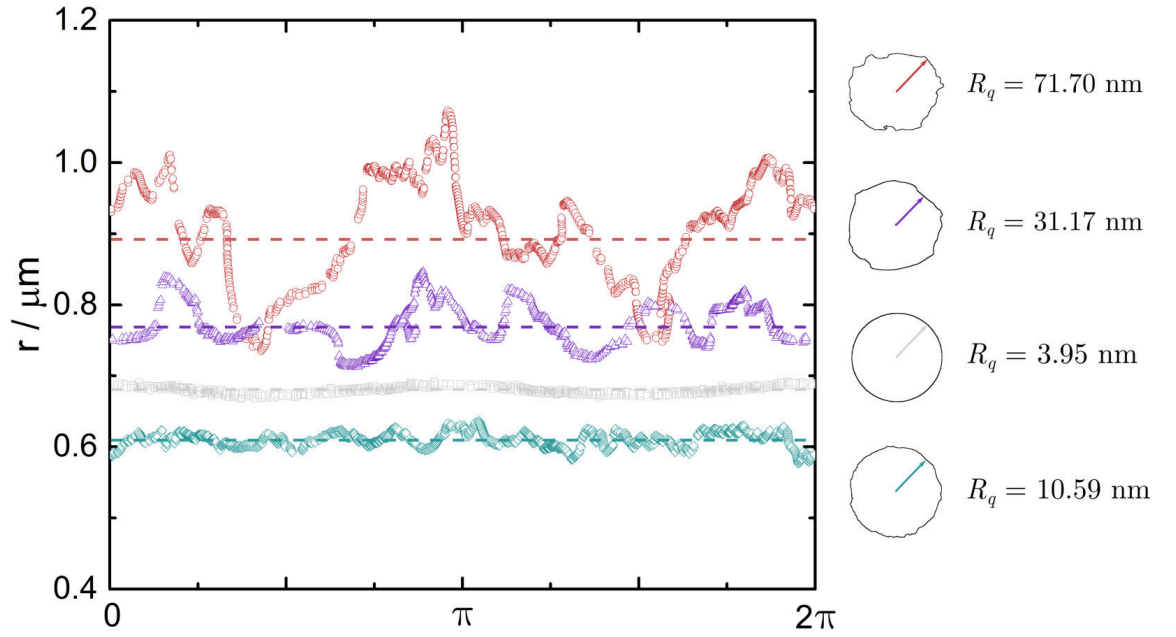


Figure 2.12. Radial surface profiles from image analysis of Scanning Electron Microscopy (SEM) images of roughened and ‘smooth’ microspheres. A particle roughened in the presence of cigar-shaped calcium carbonate is displayed in red, long rod-shaped calcium carbonate in purple, nano-sized ZnO in cyan and a ‘smooth’ standard in grey. Dashed lines indicate the mean radial distance. The associated perimeter outlines are displayed to the right of the plot.

and 3. radial distance calculation using the centroid as the origin and polar coordinates of each perimeter pixel. By measuring the distance between the particle centroid and its boundary pixels in this way, a radial surface plot could be extracted as a function of θ , or here shown as π (figure 2.12). Performing this for several particles in each roughness case, statistical roughness parameters can be found. The most commonly reported roughness parameter is the root-mean-squared-roughness, $R_q = \sqrt{\frac{1}{n} \sum_{i=1}^n y_i^2}$ where y_i is the vertical distance from the mean line. Taking an average of at least 10 particles we obtain roughness parameters of $R_q = 3.95, 10.59, 31.17$ and 71.70 nm for ‘smooth’ (grey), ZnO (cyan), rod-shaped (purple) and cigar-shaped (red) calcium carbonate roughened particles respectively. With these values we observe a trend of increasing magnitude of roughness using ZnO < rod-shaped calcium carbonate < cigar-shaped calcium carbonate.

2.2.3 2D particle tracking – roughened vs. smooth Brownian motion

One key advantage of our fabrication methods is that the rough product particles have identical mass to their smooth counterparts. This allows us to perform a near-direct comparison between the behaviour of the two types of colloidal object, that is ‘rough’ vs. ‘smooth’.

At this stage, we ask: how can these rough objects be modelled when dispersed in a liquid? Can their diffusional motion still be approximated by treatment as a sphere? The motivation here was to experimentally examine whether an object can be roughened/deformed to a state where its behaviour deviates from a Brownian sphere according to the Stokes-Einstein-Sutherland (S-E-S) relation – equation (1.1).

A series of videos were taken at a constant 25°C and image processing and particle tracking was carried out in ImageJ using the TrackMate algorithm⁶¹ and exported to Matlab for analysis (see Experimental section 2.3.5) for details). The particles depicted in figure 2.5d were selected as our rough candidates as they have very interesting large-scale, anisotropic surface roughness. As well as this, we were confident that complete etching of the inorganic material had taken place and therefore the density of the rough objects should be identical to their smooth analogues making a direct comparison valid.

The TrackMate algorithm for 2D particle tracking follows the essential criteria originally outlined by Crocker & Grier,⁶² that is: 1. an initial particle detection step, 2. refining of locations and 3. linking of locations into trajectories. TrackMate implements Laplacian-of-Gaussian segmentation for intermediately sized objects (5 – 20 pix diameter) in order to determine particle locations. The images are first smoothed by Gaussian convolution with standard deviation, σ , suited to a user input for the estimated particle size. Then the Laplacian (2 dimensional second derivative) is computed to accentuate maxima in image intensity which are then located by local maxima searching with a discriminatory distance set by σ . This is a sensitive detection technique and therefore the algorithm relies on a fastidious linking step – the linear assignment protocol. The protocol links particle locations by computing cost matrices based on the square distance between particles in concurrent frames and is derived from the framework set out by Jaqaman *et al.*⁶³ A snapshot from the processed time series with an overlay of the result from the Laplacian-of-Gaussian detection and linear assignment protocol for linking displaying a typical Brownian trajectory is shown

in figure 2.13. This algorithm, originally primarily designed for analysing fluorescence microscopy time series, is well suited to our processed phase contrast microscopy images with decent location of the particle centres despite the anisotropic shape of the Gaussian blob projected from a rough particle (see Supplementary Video SV1 in Appendix B.1).

Polystyrene microspheres were density matched in a 50:50 volume fraction mixture of $\text{H}_2\text{O}:\text{D}_2\text{O}$, $\rho \sim 1.05 \text{ g cm}^{-3}$, the viscosity of which we can calculate using a simple linear expression, $\eta_{\text{mix}} = \chi_{\text{H}_2\text{O}}\eta_{\text{H}_2\text{O}} + \chi_{\text{D}_2\text{O}}\eta_{\text{D}_2\text{O}} = 9.93 \times 10^{-4} \text{ kg m}^{-1} \text{ s}^{-1}$, according to Kestin *et al.*⁶⁴ Particles were tracked both in the bulk solution, far from any boundaries, and near to the underlying glass surface. In this way we can overrule any boundary effects, known to influence colloidal diffusion,⁶⁵ and perhaps examine any differences between the rough and smooth colloids. A representative trajectory of a rough particle displaying random walk behaviour is presented in figure 2.13 b) along with the normalized velocity autocorrelation function, $\langle v_i(0) \cdot v_i(t) \rangle$, for all accrued tracks in the rough particle sample (figure 2.13 c). The velocity autocorrelation function compares velocity values at specified lag times, t , with those previous. Positive values indicate correlation which here would suggest persistent directed motion. For random – Brownian – motion, velocity should be constantly averaged out by the changes in direction to give $\langle v_i(0) \cdot v_i(t) \rangle = 0$. Indeed velocity is uncorrelated over the course of the tracks again indicating random, Brownian behaviour and the absence of drift.

The corresponding mean-squared displacements (MSDs) and calculated 2D diffusion coefficients, D , for the smooth and rough particles in both scenarios are presented in figure 2.14 and table 2.1 ($D_{\text{s,b}}$ represents the 2D diffusion coefficient for smooth particles in the bulk, $_{\text{r}}$ denotes rough particles and $_{\text{s}}$ denotes particles tracked near to the underlying glass surface). The MSDs were first plotted over all time intervals investigated (0.02 – 50 s) displayed in the log – log plot (figure 2.14 c). The slope, α , of these data gives an indication of how Brownian or purely diffusive the motion is. Where the slope approaches unity the motion is purely diffusive. For anything lower ($\alpha < 1$) the motion may be hindered and for anything higher ($\alpha > 1$) the motion may be propulsive.⁶⁶ For this description the MSD curve is modelled by a power law: $\langle \Delta x_i^2 \rangle = \Gamma \times t^\alpha$ and therefore in logarithmic form: $\log \langle \Delta x_i^2 \rangle = \alpha \times \log(t) + \log(\Gamma)$ can be easily fitted by linear relationships (see previous

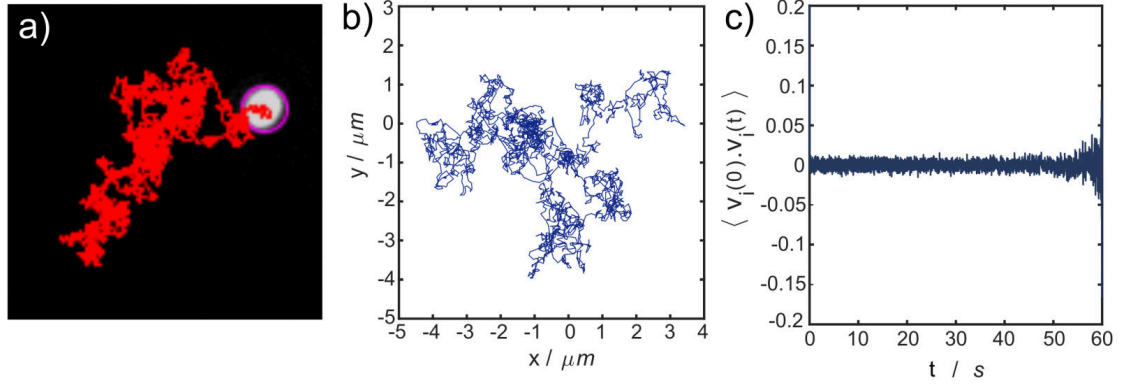


Figure 2.13. A snapshot from the processed time series of a rough PS particle diffusing in bulk $\text{H}_2\text{O}/\text{D}_2\text{O}$ with an overlay of the result from the Laplace-of-Gaussian detection (purple circle) and linear assignment protocol for linking displaying a typical Brownian trajectory a). Displacement of a typical Brownian rough poly(styrene) particle tracked in the bulk for 50 s at a time interval of 0.02 s b) and the Normalized velocity autocorrelation function for all 25 rough particle tracks c).

discussion in introduction section 1.4.2). For our data we extract all α close to 1 further indicating predominantly Brownian behaviour. It is noted however that as the particles approach the underlying surface (dashed lines) there is a slight reduction in α (0.9397 for smooth and 0.9136 for rough colloids). This is discussed further after the diffusion coefficients are extracted.

To find the diffusion coefficients, D , for each scenario linear unweighted fits were applied to the linear MSD plots (figure 2.14 d) for $n = 5$ data points excluding the first datum which is known to deviate due to localisation error. This analysis was selected because the error increases with number of fitting points and the variations in mean diffusion coefficient diminish passed this amount of fitting points as pointed out by Ernst and Köhler.⁶⁷ The fits for each particles MSD were averaged together to obtain the reported D and the standard deviation of D over the fits was computed. It is also possible to infer the localisation uncertainty from the intercept of the fit so long as certain vital conditions of the analysis are met.⁶⁸ However in this study we chose to omit this as the primary contribution to the deviation in the MSD data comes from the particle size distribution ($\sim 10 \times 10^{-2} \mu\text{m}^2 \text{s}^{-1}$ for size distribution vs. $\sim 10 \times 10^{-4} \mu\text{m}^2 \text{s}^{-1}$ for localization uncertainty).

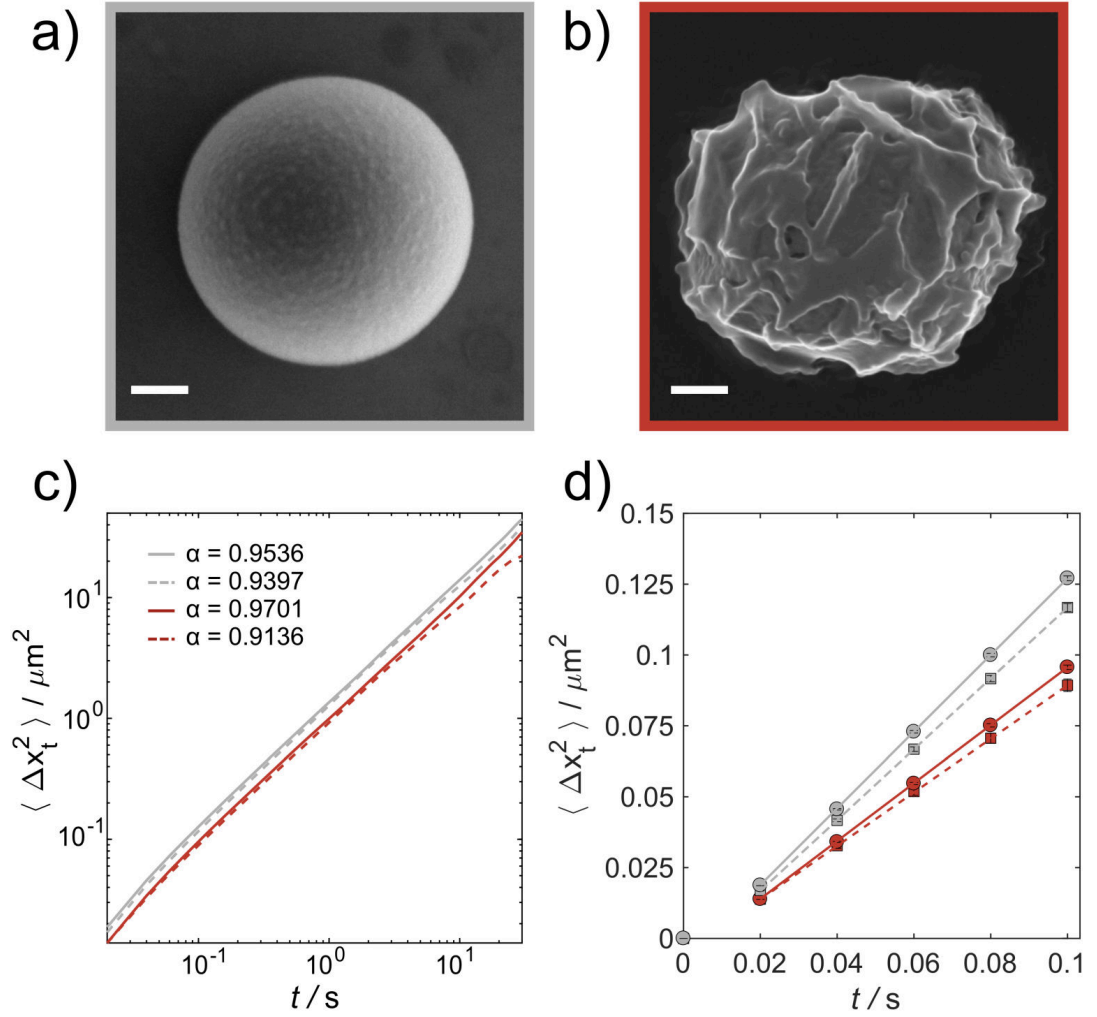


Figure 2.14. Representative SEM close-ups of both the smooth a) and rough b) poly(styrene) microspheres, scale bar = 250 nm. Mean-Squared Displacement (MSD), $\langle \Delta x_i^2 \rangle$, at given lag times, t , c) and d) of smooth (grey) and rough (red) poly(styrene) microspheres displaying Brownian motion. The legend in c) details the linear fits of the log-log MSD plot. A sample of 25 objects were tracked for a total of 50 s at 50 fps in two scenarios: in the bulk (circles, solid line) and close to the surface of the glass slide (squares, dashed line). Fitting was applied from data points $n = 2$ to $n = 6$ of the MSD plots to extract the diffusion coefficients – MSDs were re-plotted to show this region with associated error bars (standard deviation) d).

The 2D diffusion coefficients decrease appreciably when the particles come close to the glass surface which has been demonstrated for hard spheres diffusing near rigid boundaries.⁶⁵ The decrease in diffusion coefficient is equivalent for both the smooth and rough particles upon approaching the underlying surface, $D_{s,s}/D_{s,b} = 0.91$ and $D_{r,s}/D_{r,b} = 0.93$ where these are the ratios of the diffusion coefficients near the surface over the diffusion coefficients in the bulk. This gives us confidence that our tracking in the bulk case is far from any boundaries and the volume fractions are low enough that particles do not influence each other's motion. The difference between the smooth and rough spheres is significant and already interesting considering the equivalent mass and volume of the objects. However, to underpin whether the difference is due to a deviation from Stokes-Einstein-Sutherland behaviour, we must first determine the effective radius of the objects.

In the case of the smooth, spherical particles it was fairly straightforward to determine the particle size from image analysis of Scanning Electron Microscopy (SEM) images, hence 2D projections of the particles. This analysis was performed in ImageJ over three hundred particles utilizing a plugin that performs Hough space operations to detect circular objects. It is more difficult to approach a reasonably accurate solution for the particle diameter of a rough sphere and especially in our case where the roughness is not uniform between different particles. We can treat the projected area of the object as though it belonged to something spherical and, in this case, have a sort of 'averaged out' estimate to the diameter (projected circle area diameter). This analysis has a similar apparent accuracy in determining particle perimeters as the Hough space operation for the smooth spheres (figure 2.15).

Another definition we look to is the Feret diameter which essentially is a measure for the maximum diameter of the object. This of course is orientation dependent and so to retrieve a reasonable estimate of the average diameter, several thousands of particles should be analysed from their 2D projections. For the purpose of this work, as this property is not vital to our analysis, the measurement was performed on a more reasonable number of particles ($N \sim 500$).

The calculated radii can be plugged into the S-E-S equation with $k_B = 1.38 \times 10^{-23} \text{ m}^2 \text{ kg}^{-2} \text{ K}^{-1}$, $T = 298 \text{ K}$ and $\eta = 9.93 \times 10^{-4} \text{ kg m}^{-1} \text{ s}^{-1}$ to obtain the theoretical diffusion

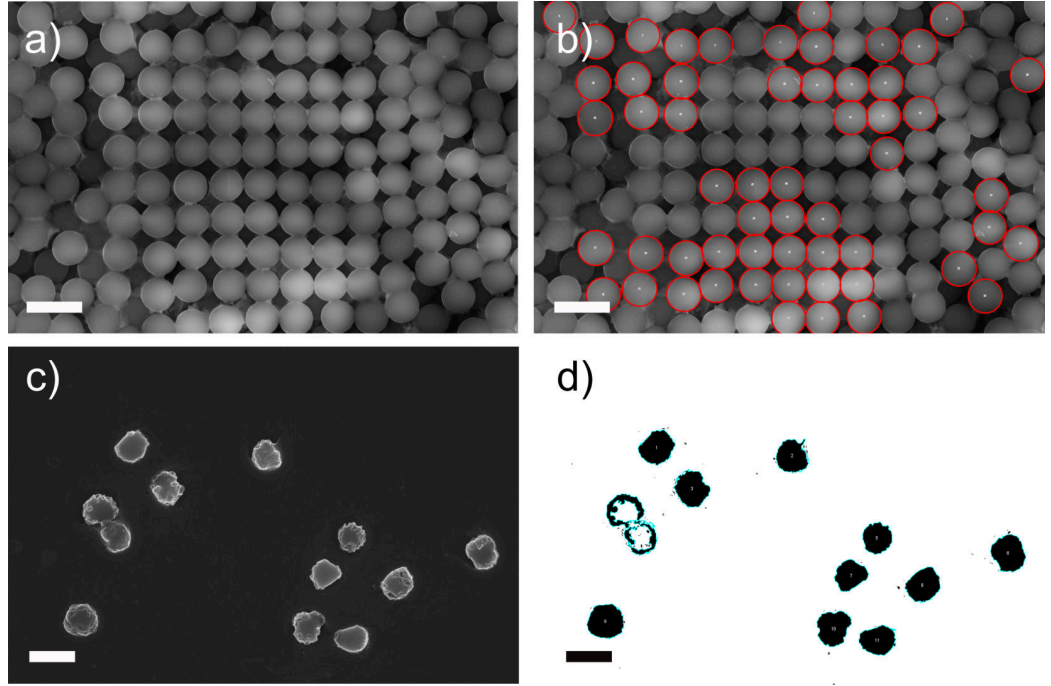


Figure 2.15. Typical SEM images of smooth and rough particles utilized for size analysis a) and c) respectively. The result of the detect circles/Hough circles algorithm applied in ImageJ b) and the result of particle size analysis on the SEM image of the rough particles utilizing a thresholding technique d).

coefficient, D_{Theo} assuming no-slip boundary conditions. (See table 2.1). Our experimental findings are in reasonable agreement to these values: $D_{\text{s,b}}$ 6.5%; $D_{\text{r,b}}$ 4.3% for projected area and 17.5% for Feret (percentage difference of the experimental diffusion coefficients in the bulk for the rough, $D_{\text{r,b}}$, and smooth objects, $D_{\text{s,b}}$, against the calculated theoretical diffusion coefficient D_{Theo}). These are within our confidence bounds especially considering the dispersity in particle size of the samples. We conclude that these results are in fact a testament to the robustness of S-E-S equation, displaying that even particles with a large-scale anisotropic surface roughness relative to their size obey Stokes Law with no-slip boundary conditions.

The diffusion coefficient, D , for the rough objects appears larger in experiment than theory, whereas it is smaller in experiment for the smooth spheres. This observation is initially peculiar as we would expect that both should be smaller in experiment as we have measured the radius of the objects in a dry state and so underestimate the actual

Particle	$d / \mu\text{m}$	$D_{\text{Theo}} / \mu\text{m}^2 \text{s}^{-1}$	$D_{\text{Exp.,b}} / \mu\text{m}^2 \text{s}^{-1}$	$D_{\text{Exp.,s}} / \mu\text{m}^2 \text{s}^{-1}$
Smooth	1.217 ± 0.026	0.361 ± 0.021	0.339 ± 0.023	0.311 ± 0.024
Rough	$1.789 \pm 0.062^\alpha$	$0.246^\alpha \pm 0.035$	0.257 ± 0.030	0.240 ± 0.041
	$2.074 \pm 0.138^\beta$	$0.212^\beta \pm 0.067$		

Table 2.1. Comparison table of the theoretical values, D_{Theo} , for diffusion coefficient from the S-E-S equation vs. the experimental data, $D_{\text{Exp.,}}$, from the MSD fits in figure 2.14 for smooth and rough particles in the bulk, $D_{\text{Exp.,b}}$, and near the underlying surface, $D_{\text{Exp.,s}}$. The measured diameters and associated D_{Theo} for the rough particles: $^\alpha$ projected circle area diameter, d_{pa} , and $^\beta$ Feret diameter, d_{f} , are included. Uncertainties are reported from the standard deviation of data where appropriate.

size in solution (hydrodynamic radius). The deviation, however, is small, that is less than 10%. Small experimental errors introduced during acquisition or analysis such as drift, vibration or tracking errors are plausible reasons. We would expect that vibration would be appreciably small in both cases and that drift was minimized by sealing the imaging chamber with grease. In practice, it is difficult to eliminate drift as any small air bubbles, evaporation or convection can contribute to fluid flow. Considering that there is no apparent correlation in the velocity autocorrelation function (figure 2.13 c) we can conclude that drift is negligible and so should not be a contributor to the raised D . As well as this, it is tricky to determine the particle centres of objects that are not perfectly spherical and so we likely have some tracking error introduced here. A common challenge associated with particle tracking of phase contrast image sequences of microparticles is caused by the presence of halos brought about by low-spatial-frequency diffracted light from the specimen passing through the phase ring. These can lead to erroneous particle detection, mistaking the bright halo for a particle centre. It is therefore an important consideration to take when processing images prior to tracking, which in our case was ensured by a rolling ball background subtraction, taking away features smaller than the particle radius. Without tracking in 3D and sampling over a much longer time period or utilizing an ensemble technique such as Differential Dynamic Microscopy⁶⁹ (DDM) it is difficult to achieve a more accurate, representative result.

2.3 Experimental

2.3.1 Materials

Styrene ($\geq 99\%$) and poly(vinyl-pyrrolidone) (PVP K-30: Average molecular weight = $40.000 \text{ g mol}^{-1}$), azobisisobutyronitrile (AIBN) (98%) and dialysis tubing cellulose membrane (typical molecular weight cut-off = $14,000 \text{ g mol}^{-1}$) were obtained from Sigma Aldrich. AIBN was recrystallized in methanol to remove impurities prior to use. Acetic acid glacial (99%) and Ethanol p.a. were obtained from Fischer Scientific. Calcium carbonate, Socal P3 powder (diameter = $250\text{--}350 \text{ nm}$) (length = $500\text{--}1000 \text{ nm}$) was received as a donation from Akzo-Nobel. Calcium carbonate, PCC rods powder (diameter $\sim 500 \text{ nm}$) (length = $3\text{--}15 \text{ }\mu\text{m}$) was received as a donation from Unilever. The Z-COTE zinc oxide (diameter $\sim 120 \text{ nm}$) was received as a donation from BASF.

2.3.2 Dispersion polymerisation for synthesis of micron-sized poly(styrene) spheres

AIBN (0.1215 g), PVP K-30 (0.85 g), ethanol (86.25 g) and styrene (12.15 g) were charged to a 250 ml round bottom flask and purged with nitrogen for 40 minutes. Next, the flask was submerged into an oil bath heated to 70°C (IKA RCT Basic) and left to react for 24 hours whilst agitating with a magnetic stirrer at 500 rpm and kept under a slight nitrogen gas overpressure. The obtained particle dispersions were centrifuged using an Eppendorf 5430 and re-dispersed in ethanol three times to remove excess PVP and unreacted organics. The particles were then dried out in a vacuum oven at $T = 60^\circ\text{C}$ and stored as dry powder for further use.

The average particle diameter was measured to be $1.217 \pm 0.026 \text{ }\mu\text{m}$ by image analysis of over 300 individual particles from SEM micrographs using detect circles (Hough space transform) in ImageJ. Expressing dispersity as standard deviation in diameter over the average diameter, $\sigma/\langle d \rangle = 0.021$.

2.3.3 Fabrication of surface-textured poly(styrene) particles

The PS particles (dried powder: 0.01 g), inorganic colloid - Socal P3, PCC rods or Z-COTE ZnO (1.0 g) and water (10.0 g) were mixed together under vigorous magnetic stirring and subsequently sonicated in an ultrasound bath for 5 min to ensure an even dispersion. This dispersion was then cast on to 10 separate glass microscope slides (Fischer) by dropping 500 μ L on each with a micropipette (Fischer). They were left at room temperature to dry overnight and then they were placed into a lab oven thermostated at 110 °C for 10 min, 30 min, 1 h and 2 h. Note that the choice of substrate can be readily exchanged for any larger, clean and hard substrate that is inert at 110 °C. Particles were removed from the surface by friction with a stainless steel spatula and were re-dispersed in a small amount of deionized acidified water, 1 M aqueous acetic acid (10 ml). This crude dispersion was then inserted into dialysis tubing and was dialysed against 2 M aqueous acetic acid to remove the calcium carbonate and/or zinc oxide. The acidic solution was replaced 3 times at 4 hour intervals. The dispersion was then dialysed against deionized water twice for 24 hr each time to remove excess ions.

2.3.4 Particle characterization

Samples for SEM were prepared by diluting the particle solutions to around 0.5 mg mL⁻¹ in water and allowing them to dry onto silicon wafers supported on aluminium stubs with adhesive and electrically connected with silver Electrodeag paste. The samples were then coated with a conductive film of evaporated carbon. Four or five cycles were elapsed to ensure a reasonable coating thickness. SEM imaging was performed on a Zeiss Supra 55VP at 15 kV or Zeiss Gemini SEM 500 at 0.5 kV without a carbon coating. For TEM analysis samples were prepared by dropping a relatively dilute dispersion (0.01 wt.%) of particles in water on to lacey carbon grids and allowing the samples to dry. Particles were imaged using a JEOL 2000FX TEM or JEOL 2100.

2.3.5 2D particle tracking experiments

Videos were recorded using an Andor Zyla 4.4 Plus camera attached to an Olympus IX73 inverted light microscope. Samples were prepared by diluting particles to approximately 2 mg mL^{-1} in deionized water. Two parallel lines of grease were drawn out to the approximate size of the cover slips being used ($20 \text{ mm} \times 20 \text{ mm}$) onto a Linkam Warm Stage. The coverslip was placed lightly over the lines of grease and a micropipette was used to inject the sample solution underneath the assembled cell. Capillary action ensures the solution fills the well efficiently and it is subsequently sealed at the other edges with grease. Videos, $512 \times 512 \text{ px.}$ at 50 fps for 50 s, were then recorded after time was allowed for the Linkam warm stage to heat up to 25°C . A magnification of $60\times$ (Olympus LUCPlanFLN $60\times$ Ph) was used with phase to enhance the contrast of particles and give a uniform background.

Image processing was performed in ImageJ and consisted of subtracting the median image and applying a rolling ball filter to all frames. A tracking algorithm, Trackmate,⁶¹ distributed with ImageJ(Fiji) was then utilized to perform the 2D particle tracking. Our analysis was then performed using msdalyzer, a Matlab class created for analysing tracking data.⁷⁰

References

- [1] D. Lootens, H. Van Damme, Y. Hémar and P. Hébraud, *Phys. Rev. Lett.*, 2005, **95**, 1–4.
- [2] S. Gallier, E. Lemaire, F. Peters and L. Lobry, *J. Fluid Mech.*, 2014, **757**, 514–549.
- [3] N. Ballard and S. A. F. Bon, *Polym. Chem.*, 2011, **2**, 823–827.
- [4] A. R. Morgan, N. Ballard, L. A. Rochford, G. Nurumbetov, T. F. Skelhon and S. A. F. Bon, *Soft Matter*, 2013, **9**, 487–491.
- [5] A. San-Miguel and S. H. Behrens, *Langmuir*, 2012, **28**, 12038–12043.
- [6] L. Florez, C. Herrmann, J. M. Cramer, C. P. Hauser, K. Koynov, K. Landfester, D. Crespy and V. Mailänder, *Small*, 2012, **8**, 2222–2230.

- [7] B. Parakhonskiy, M. V. Zyuzin, A. Yashchenok, S. Carregal-Romero, J. Rejman, H. Möhwald, W. J. Parak and A. G. Skirtach, *J. Nanobiotechnology*, 2015, **13**, 53.
- [8] A. E. Nel, L. Mädler, D. Velegol, T. Xia, E. M. V. Hoek, P. Somasundaran, F. Klaessig, V. Castranova and M. Thompson, *Nat. Mater.*, 2009, **8**, 543–557.
- [9] H. R. Sheu, M. S. El-Aasser and J. W. Vanderhoff, *J. Polym. Sci. Part A Polym. Chem.*, 1990, **28**, 629–651.
- [10] J. W. Kim, D. Lee, H. C. Shum and D. A. Weitz, *Adv. Mater.*, 2008, **20**, 3239–3243.
- [11] S. A. F. Bon, H. Van Beek, P. Piet and A. L. German, *J. Appl. Polym. Sci.*, 1995, **58**, 19–29.
- [12] O. Rohm and E. Trommsdorff, *Process for the polymerization of methyl methacrylate*, US2171765 A, 1939.
- [13] v. E. Trommsdorff, *Die Makromol. Chemie*, 1954, **13**, 76–89.
- [14] T. Chen, P. J. Colver and S. A. F. Bon, *Adv. Mater.*, 2007, 2286–2289.
- [15] S. A. F. Bon, S. Cauvin and P. J. Colver, *Soft Matter*, 2007, **3**, 194–199.
- [16] S. Fortuna, C. A. L. Colard, A. Troisi and S. A. F. Bon, *Langmuir*, 2009, **25**, 12399–12403.
- [17] C. A. L. Colard, R. F. A. Teixeira and S. A. F. Bon, *Langmuir*, 2010, **26**, 7915–21.
- [18] S. A. F. Bon, in *Part. Emuls. Colloids Form. Appl.*, RSC, 2014, pp. 65–92.
- [19] A. Lotierzo and S. A. F. Bon, *Polym. Chem.*, 2017, **8**, 5100–5111.
- [20] N. Konishi, T. Fujibayashi, T. Tanaka, H. Minami and M. Okubo, *Polym. J.*, 2010, **42**, 66–71.
- [21] J. Yin, X. Han, Y. Cao and C. Lu, *Sci. Rep.*, 2014, **4**, 1–8.
- [22] S. Badaire, C. Cottin-Bizonne and A. D. Stroock, *Langmuir*, 2008, **24**, 11451–11463.

- [23] T. J. Merkel, K. P. Herlihy, J. Nunes, R. M. Orgel, J. P. Rolland and J. M. DeSimone, *Langmuir*, 2010, **26**, 13086–13096.
- [24] A. Bleier and E. Matijevic, *J. Colloid Interface Sci.*, 1976, **55**, 510–524.
- [25] B. Vincent, C. Young and T. Tadros, *Faraday Discuss*, 1978, **65**, 296–305.
- [26] B. Vincent, C. A. Young and T. F. Tadros, *J. Chem. Soc. Faraday Trans. 1 Phys. Chem. Condens. Phases*, 1980, **76**, 674–682.
- [27] P. F. Luckham, B. Vincent and T. F. Tadros, *Colloids and Surfaces*, 1983, **6**, 119–133.
- [28] R. F. A. Teixeira and S. A. F. Bon, *Adv. Polym. Sci.*, 2012, **233**, 19–52.
- [29] M. Nagy and A. Keller, *Polym. Comm.*, 1989, **30**, 130–132.
- [30] L. M. Ramírez, S. T. Milner, C. E. Snyder, R. H. Colby and D. Velegol, *Langmuir*, 2010, **26**, 7644–7649.
- [31] C. C. Ho, A. Keller, J. A. Odell and R. H. Ottewill, *Colloid Polym. Sci.*, 1993, **271**, 469–479.
- [32] J. A. Champion, Y. K. Katare and S. Mitragotri, *Proc. Natl. Acad. Sci. U. S. A.*, 2007, **104**, 11901–11904.
- [33] J. R. Schmidt and J. L. Skinner, *J. Chem. Phys.*, 2003, **119**, 8062–8068.
- [34] A. Einstein, *Ann. Phys.*, 1905, **17**, 549–560.
- [35] A. Einstein, *Ann. Phys.*, 1906, **324**, 289–306.
- [36] W. Sutherland, *Phil. Mag.*, 1905, **9**, 781–785.
- [37] G. L. Paul and P. N. Pusey, *J. Phys. A. Math. Gen.*, 1981, **14**, 3301–3327.
- [38] M. H. Kao, A. G. Yodh and D. J. Pine, *Phys. Rev. Lett.*, 1993, **70**, 242–245.
- [39] R. Pit, H. Hervet and L. Léger, *Phys. Rev. Lett.*, 2000, **85**, 980–983.
- [40] Y. Zhu and S. Granick, *Phys. Rev. Lett.*, 2002, **88**, 106102.

- [41] E. Bonaccorso, H. J. Butt and V. S. Craig, *Phys. Rev. Lett.*, 2003, **90**, 144501.
- [42] O. I. Vinogradova and G. E. Yakubov, *Phys. Rev. E - Stat. Nonlinear, Soft Matter Phys.*, 2006, **73**, 1–4.
- [43] D. Quéré, *Annu. Rev. Mater. Res.*, 2008, **38**, 71–99.
- [44] C. Cottin-Bizonne, J. L. Barrat, L. Bocquet and E. Charlaix, *Nat. Mater.*, 2003, **2**, 237–240.
- [45] T. H. Fan and O. I. Vinogradova, *Phys. Rev. E - Stat. Nonlinear, Soft Matter Phys.*, 2005, **72**, 066306.
- [46] M. P. Brenner and D. Lohse, *Phys. Rev. Lett.*, 2008, **101**, 214505.
- [47] E. Lauga, M. P. Brenner and H. A. Stone, in *Handb. Exp. Fluid Dyn.*, Springer, New York, 2007, pp. 1219–1240.
- [48] C. M. Tseng, Y. Y. Lu, M. S. El-Aasser and J. W. Vanderhoff, *J. Polym. Sci. Part A Polym. Chem.*, 1986, **24**, 2995–3007.
- [49] S. Shen, E. D. Sudol and M. S. El-Aasser, *J. Polym. Sci. Part A Polym. Chem.*, 1994, **32**, 1087–1100.
- [50] A. J. Paine, W. Luymes and J. McNulty, *Macromolecules*, 1990, **23**, 3104–3109.
- [51] S. Ma, J. Thiele, X. Liu, Y. Bai, C. Abell and W. T. S. Huck, *Small*, 2012, **8**, 2356–2360.
- [52] C. Quilliet, *Phys. Rev. E - Stat. Nonlinear, Soft Matter Phys.*, 2006, **74**, 1–6.
- [53] D. Walsh and P. Zoller, *Standard Pressure Volume Temperature Data for Polymers*, Technomic Publishing Company, Inc., 1995, p. 10.
- [54] M. Adams, Z. Dogic, S. L. Keller and S. Fraden, *Nature*, 1998, **393**, 349–352.
- [55] P. J. Yunker, T. Still, M. A. Lohr and A. G. Yodh, *Nature*, 2011, **476**, 308–311.
- [56] P. A. Kralchevsky, N. D. Denkov and K. D. Danov, *Langmuir*, 2001, **17**, 7694–7705.
- [57] D. B. Hough and L. R. White, *Adv. Colloid Interface Sci.*, 1980, **14**, 3–41.

- [58] C.-P. Hsu, S. N. Ramakrishna, M. Zanini, N. D. Spencer and L. Isa, *PNAS*, 2018, **115**, 5117–5122.
- [59] J. Kilday, F. Palmieri and M. D. Fox, *IEEE Trans. Med. Imaging*, 1993, **12**, 664–669.
- [60] S. Pohlman, K. A. Powell, N. A. Obuchowski, W. A. Chilcote and S. Grundfest-Broniatowski, *Med. Phys.*, 1996, **23**, 1337–1345.
- [61] J.-Y. Tinevez, N. Perry, J. Schindelin, G. M. Hoopes, G. D. Reynolds, E. Laplantine, S. Y. Bednarek, S. L. Shorte and K. W. Eliceiri, *Methods*, 2016, **115**, 80–90.
- [62] J. Crocker, J. Crocker and D. Grier, *J. Colloid Interface Sci.*, 1996, **179**, 298–310.
- [63] K. Jaqaman, D. Loerke, M. Mettlen, H. Kuwata, S. Grinstein, S. L. Schmid and G. Danuser, *Nat. Methods*, 2008, **5**, 695–702.
- [64] J. Kestin, N. Imaishi, S. Nott, J. Nieuwoudt and J. Sengers, *Phys. A Stat. Mech. its Appl.*, 1985, **134**, 38–58.
- [65] M. D. Carbajal-Tinoco, R. Lopez-Fernandez and J. L. Arauz-Lara, *Phys. Rev. Lett.*, 2007, **99**, 138303.
- [66] M. J. Saxton, in *Methods Mol. Biol.*, Humana Press Inc., 2007, vol. 400, pp. 295–321.
- [67] D. Ernst and J. Köhler, *Phys. Chem. Chem. Phys.*, 2013, **15**, 3429–32.
- [68] X. Michalet, *Phys. Rev. E - Stat. Nonlinear, Soft Matter Phys.*, 2010, **82**, 1–13.
- [69] M. Reufer, V. A. Martinez, P. Schurtenberger and W. C. K. Poon, *Langmuir*, 2012, **28**, 4618–4624.
- [70] N. Tarantino, J. Y. Tinevez, E. F. Crowell, B. Boisson, R. Henriques, M. Mhlana, F. Agou, A. Israël and E. Laplantine, *J. Cell Biol.*, 2014, **204**, 231–245.

3

Improving the Engine Power of a Catalytic Janus-sphere Micromotor by Roughening its Surface

Don't think so much.

Prof. dr. ir. Stefan A. F. Bon

Abstract

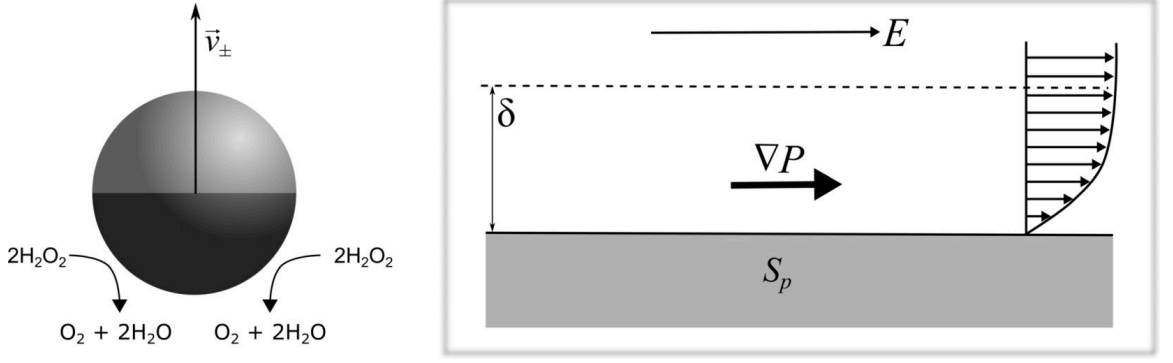
Microspheres with catalytic caps have become a popular model system for studying self-propelled colloids. Existing experimental studies involve predominantly ‘smooth’ particle surfaces. In this study we determine the effect of irregular surface deformations on the propulsive mechanism with a particular focus on speed. The particle surfaces of polymer microspheres were deformed prior to depositing a layer of platinum which resulted in the formation of nanoscopic pillars of catalyst. Self-propulsion was induced upon exposure of the micromotors to hydrogen peroxide, whilst they were dispersed in water. The topological surface features were shown to boost speed ($\sim 2\times$) when the underlying deformations are small (nanoscale), whilst large deformations afforded little difference despite a substantial apparent catalytic surface area. Colloids with deformed surfaces were more likely to display a mixture of rotational and translational propulsion than their ‘smooth’ counterparts.

Parts of this chapter are published elsewhere, see: Longbottom, B. W.; Bon, S. A. F. *Scientific Reports* 2018, 8, 4622

3.1 Introduction

Small particles dispersed in a fluid that undergo continuous energy consumption to induce motion are an interesting form of active matter.¹ Within this branch of colloid science a particular focus on self-propelling particles has emerged.^{2–8} These ‘micromotors’ are under the microscope (quite literally) for their potential in a variety of scientific pursuits, examples include drug delivery,⁹ medical applications,¹⁰ environmental remediation¹¹ and the popular studies of dissipative assembly (swarming).¹² This chapter re-iterates and builds upon some of the topics highlighted in the introduction (section 1.4.2.1) to give a clear picture of how the behaviour of auto/self-phoretic colloids can be measured.

A prominent model system in self-propulsion studies are poly(styrene) (PS) spheres with a catalytic platinum (Pt) surface coating on half of the sphere (so-called Janus PS-Pt ‘swimmers’) dispersed in hydrogen peroxide (H_2O_2) fuel.⁷ Propulsion is facilitated by the decomposition of H_2O_2 to oxygen (O_2) and water (H_2O) at the Pt surface. The self-propelling design was initially realised from theoretical predictions that colloids with a catalytic patch should move via a self-generated phoretic mechanism when placed in a homogeneous medium containing fuel.¹³ Phoretic transport is classically described as the colloidal motion induced by the interaction of external fields with the interfacial boundary region of the particle.¹⁴ The external field can consist of a solute concentration gradient which here can be established by asymmetric catalytic reaction across the particle surface itself. In this way the particles are said to be autonomous and ‘self-phoretic’. For PS-Pt Janus particles it was originally thought to occur purely by self-diffusiophoresis, whereby a concentration gradient is established, dynamically, in the direct environment of the microsphere through the catalytic reaction at its surface. The precise mechanism has been the subject of debate due to observations of ionic effects, including influence of propulsion direction, indicating electrophoretic contributions to the motion.^{15–17} Self-electrophoresis involves the transport of ions and the generation of an electric field which serves as the external field acting on the particle surface. Nevertheless, in both cases the propulsion originates from a local pressure imbalance resulting in the generation of an effective slip velocity along a thin interfacial layer driving fluid flow (Scheme 3.1). In the current study we focus



Scheme 3.1. Schematic of self-generated phoresis. Decomposition of hydrogen peroxide occurs asymmetrically at the Pt cap (dark patch) of the PS-Pt microsphere leading to propulsion with velocity, \vec{v}_{\pm} , the direction of which depends on the chemical environment. The interaction of an external field, E , with the surface of the particle, S_p , (in the interfacial region, δ) generates a tangential pressure gradient, ∇P , which in turn drives fluid flow.

primarily on the magnitude of propulsive velocity and omit discussions of direction.

Self-generated phoretic motion of PS-Pt Janus microspheres leads to speeds on the order of $2\text{--}17\ \mu\text{m s}^{-1}$.^{15–18} To put this into perspective the Brownian velocity of a micron-sized sphere we know from the previous chapter (chapter 2) is $\sim 0.4\ \mu\text{m}^2\text{s}^{-1}$ and its sedimentation velocity is $\sim 0.024\ \mu\text{m s}^{-1}$, around $50\text{--}400\times$ slower than phoretic propulsion. One could ask: which parameters influence the propelled velocity? In order to answer this question we require knowledge of the origin of speed. Two fundamental properties of the material, proposed in the original theoretical framework for phoretic propulsion¹⁹ and recently highlighted by Michelin and Lauga,²⁰ govern speed: 1. Surface chemical activity which involves the generation of the local gradient by chemical reaction and 2. Surface phoretic mobility, which concerns the generation of fluid flow from a local gradient. In other words we must consider how fast a concentration gradient can be established and how effectively the surface interacts with this gradient to generate flow. In consideration of the first property for our system the surface coverage of Pt catalyst, its topography (roughness), and thickness will determine the overall catalytic activity and hence influence the magnitude and shape of the induced chemical gradient. Considering property 2: our geometry on the micron-scale is fixed. However, nanoscale roughness of our catalytic patch may influence the interaction at the slip boundary. It is known that induced slip at the

surface leads to an amplification in interfacial transport phenomena.²¹ We would like to also note that particle morphology should play an important role and in fact symmetry breaking in particle shape alone has been theorised to facilitate propulsion despite homogeneous catalyst distribution.²²

To date there are a few studies that examine the effect of surface topography on the self-propulsion of micromotors.^{23–26} Choudhury *et al.* reported a speed increase of up to four times for SiO₂-Pt Janus microspheres with a rough Pt surface compared to their smooth counterparts²⁵ attributed to the increase in catalytic surface area. Nanoscale surface roughness was imparted by first depositing an 80 nm SiO₂ under layer and a subsequent thin (8 nm) Ti layer for adhesion of Pt at different substrate angles using a glancing angle deposition (GLAD) method. A GLAD method was also utilized by Archer and co-workers to synthesize PS-Pt micromotors with defined rotational velocity.²⁷ On top of this Archer *et al.* have recently produced a new higher yield route to synthesizing active Janus colloids using chemical deposition in solution rather than relying on physical vapour deposition (PVD).²⁸ In this report they compare the resultant active SiO₂-Pt colloids and find an increased roughness for those produced *via* chemical deposition with higher propulsive velocities per nm thickness of Pt catalyst.

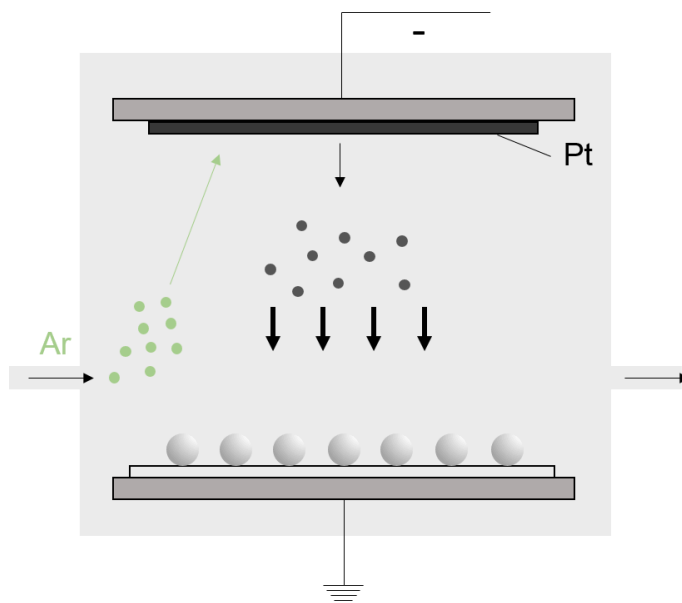
Here, we introduce a methodology to access PS-Pt micromotors with irregular surface morphologies and demonstrate their propulsive behaviour. The self-propelling colloids are made from spherical PS precursors which are roughened using a recently established physical route (chapter 2),²⁹ prior to Pt deposition by sputtering. With this strategy the underlying surface chemistry should be practically identical in each case and we can make reasonable conclusions about the propulsive mechanism and magnitude.

3.2 Results & Discussion

3.2.1 Fabrication of deformed PS-Pt micromotors

In order to fabricate Janus PS-Pt microspheres with varying surface deformations, PS microspheres synthesized by dispersion polymerization were first roughened using a previously established procedure (see chapter 2, Scheme 2.1).²⁹ Subsequently physical vapour depo-

sition (PVD), specifically sputtering, of Pt onto deposited PS particles resulted in a half-coated Janus PS-Pt morphology due to the underside of the particle being masked (Scheme 3.2, figure 3.2 a–c). The PS microspheres had a monomodal particles size distribution with an average diameter of $1.19 \pm 0.02 \mu\text{m}$ (see figure 3.1 a for a representative SEM image).



Scheme 3.2. Schematic of the sputtering process used to half coat the polymer microspheres in Pt. The underside of the particles are masked from the incident plasma and therefore receive no Pt coating.

Three distinct candidate samples were selected based on the scale of the particle surface deformations. The first sample, a control standard, had no deformations applied and thus exhibited a smooth surface (figure 3.1 a). The second sample was deformed well above, 130°C , the glass transition temperature (T_g) of PS, in the presence of cigar-shaped calcium carbonate with $d \sim 0.2 \mu\text{m}$, $l \sim 0.75 \mu\text{m}$ (figure 3.1 b). The PS particle shows ‘large deformations’ characterized by deep irregular craters across the entire surface of the particle with an overall slight departure from a spherical shape. A third and final candidate selected was deformed in the presence of small ($d \sim 0.1 \mu\text{m}$) oblong-shaped zinc oxide (ZnO) nanoparticles at 110°C (figure 3.1 c). Nanoscale roughness, and hence ‘small deformations’, with similar dimensions to the ZnO was imparted to the PS microsphere. As a side note, in our previous study it was found that PS microspheres deformed in the presence of ZnO

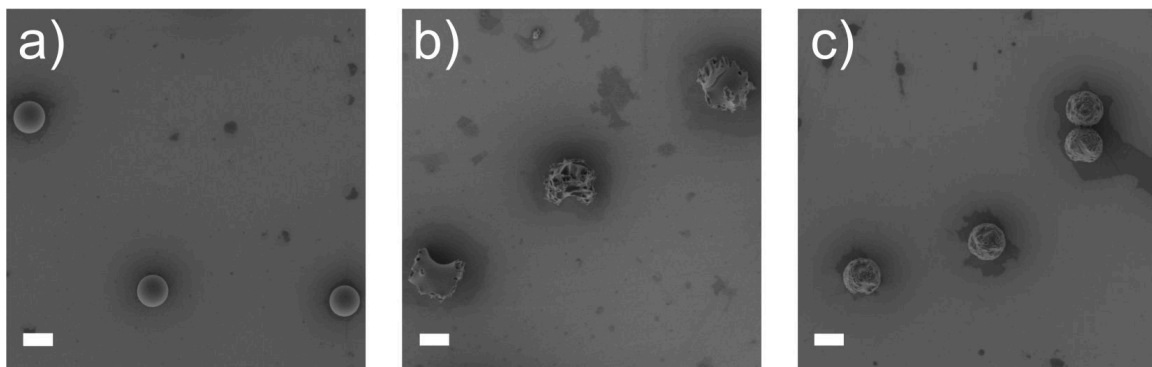


Figure 3.1. Scanning Electron Microscopy (SEM) images of poly(styrene-*co*-methacrylic acid) microspheres synthesized by dispersion polymerisation (a), after deformation at 130 °C in the presence of cigar-shaped calcium carbonate to impart ‘large deformations (*ld*)’(b) and at 110 °C with spherical zinc oxide to yield ‘small deformations (*sd*)’(c).

had buckled structures which was not found in the current work. We suggest this could be down to the change in surface chemistry due to the presence of methacrylic acid groups introduced *via* our functional co-monomer.

Particle dispersions (volume fraction, $\phi \sim 0.01$ in iso-propyl alcohol) for each candidate were prepared to deposit sub-monolayers of particles onto glass slides. Subsequent sputtering of Pt (~ 15 nm) onto deposited PS particles resulted in the desired half-coated Janus PS-Pt morphology (figure 3.2 a–c). Note that we found it essential to incorporate a small amount of carboxylic acid-functional co-monomer, methacrylic acid, in the dispersion polymerisation in order to facilitate adhesion of Pt onto the particle surface. Without the co-monomer present, the Pt film flaked off upon attempted re-dispersion of the microspheres. To help prevent re-dispersion of Pt flakes and nanoparticles, wet lens tissue was gently wiped over the glass slide to lift off only the PS-Pt Janus micro particles.

3.2.2 Propulsion experiments

To begin, the translational Brownian diffusion of each candidate sample was determined by 2D particle tracking under aqueous conditions at 25 °C and without fuel present. Particles were tracked near the underlying glass surface as they tend to sediment here due to a density mismatch between the poly(styrene) microspheres and water, added to by the presence of the heavy Pt cap.³⁰ For 2D translational Brownian motion any boundary effects from the

underlying glass surface are small^{29,31} and the significant mass anisotropy of the Pt cap does not have a large effect.³⁰ Applying linear fits to the mean-squared-displacement (MSD), $\langle \Delta x_t^2 \rangle$, (figure 3.3 b) yields the 2D diffusion coefficient, D , according to equation (3.1).

$$\langle \Delta x_t^2 \rangle = 4Dt \quad (3.1)$$

Each particles MSD was fitted from $n = 2$ (0.02 s) to $n = 7$ (0.12 s) data points and subsequently averaged to yield: smooth $D_s = 0.348 \pm 0.022$, large deformations $D_{ld} = 0.263 \pm 0.016$ and small deformations $D_{sd} = 0.289 \pm 0.0156 \mu\text{m}^2\text{s}^{-1}$. All are comparable to the theoretical values ($D = 0.27$ to $0.41 \mu\text{m}^2\text{s}^{-1}$) from the Stokes-Einstein-Sutherland (S-E-S) relation, $D = k_B T / 6\pi\eta r$, for colloids of this size range ($r = 0.6$ to $0.9 \mu\text{m}$). The differences between these D values is down to a change in the effective hydrodynamic radii of the deformed particles, in that the more deformed the particle is the larger its effective diameter (measured from the two furthest peripheral points) and therefore the lower D is, as shown previously.²⁹

At 10 vol.% hydrogen peroxide particles are propelled with a translational velocity, v , that relates to the MSD according to equation (3.2).⁷ Note that this is the reduced form of equation (3.3) in the limit that $t \ll$ the rotational diffusion time of the colloid, τ_R .

$$\langle \Delta x_t^2 \rangle = 4Dt + v^2 t^2 \quad (3.2)$$

The theoretical rotational diffusion can be calculated from $\tau_R = 8\pi\eta r^3 / k_B T$ which gives a minimum $\tau_R \sim 1.5$ s for our colloids. Thus from a quadratic fit of the MSD data at a suitable t below τ_R i.e. 10% of $\tau_R = 0.15$ s, $n = 7$ data points, v can be extracted. Two fits were carried out on the data, one being unconstrained (parameters D and v were both allowed to vary in computing the fit), the other constrained to the experimentally determined values of D from the Brownian results at 0% H_2O_2 (table 3.1), corrected for a viscosity change caused by the introduction of 10 vol.% hydrogen peroxide to the water (a minor effect). These constraints are valid as D and v are decoupled and D has little to no dependence on hydrogen peroxide concentration.

PS-Pt micromotors with large surface deformations exhibited similar velocities to

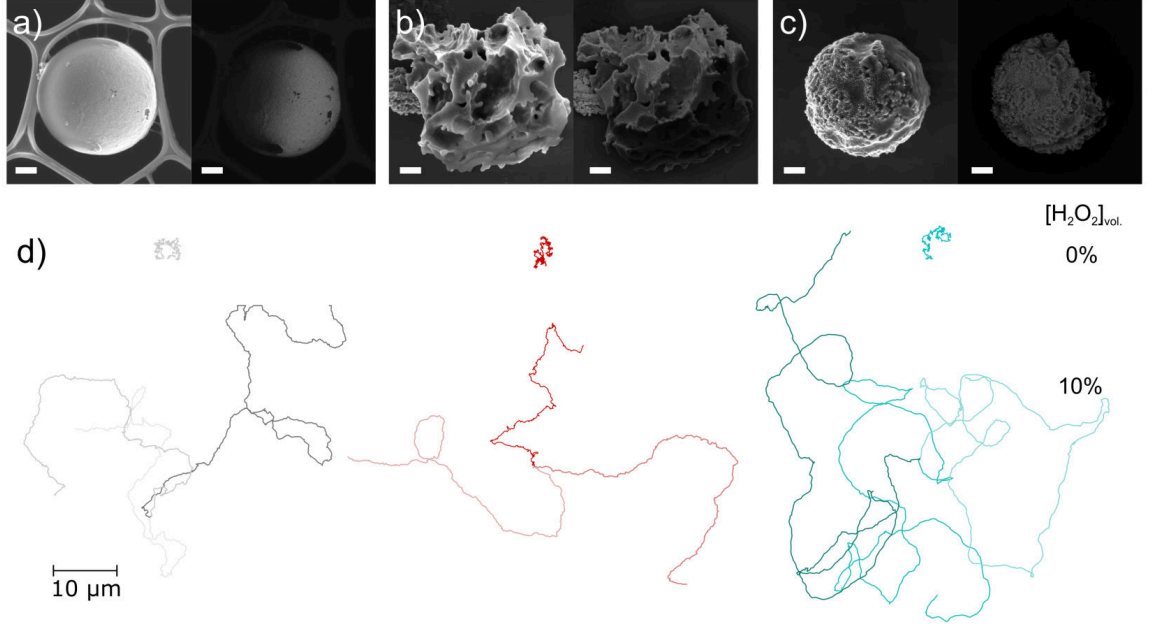


Figure 3.2. Scanning Electron Microscopy (SEM) images of poly(styrene-*co*-methacrylic acid) microspheres half-coated with platinum (a–c) with large surface deformations (b) and small surface deformations (c). Scale bars = 200 nm. The left images are from the detection of secondary electrons, right are primarily from back-scattered electrons. Representative particle trajectories (10 s) with no fuel present and at 10 vol.% H₂O₂ (d).

their ‘smooth’ counterparts whereas those with small scale deformations saw an effective doubling of speed. In order to rule out additional effects of convective transport, which can erroneously raise v , the full expression for the MSD at all delay times⁷ was fitted to the data up to $t = 1$ s (equation (3.3)).

$$\langle \Delta x_t^2 \rangle = 4Dt + \frac{v^2 \tau_R^2}{2} \left[\frac{2t}{\tau_R} + e^{-2t/\tau_R} - 1 \right] \quad (3.3)$$

As the delay time, t , approaches τ_R the MSD begins to decay from a parabola back to a linear form as the direction of propulsion has been allowed time to fully randomise. The data shows good agreement with this expected behaviour when a constrained (using D) fit was applied (3.3 d). Further extraction of both v and τ_R for each particle is possible with this fit (table 3.2).

The velocities are comparable to those extracted from the parabolic fit (equation (3.2)),

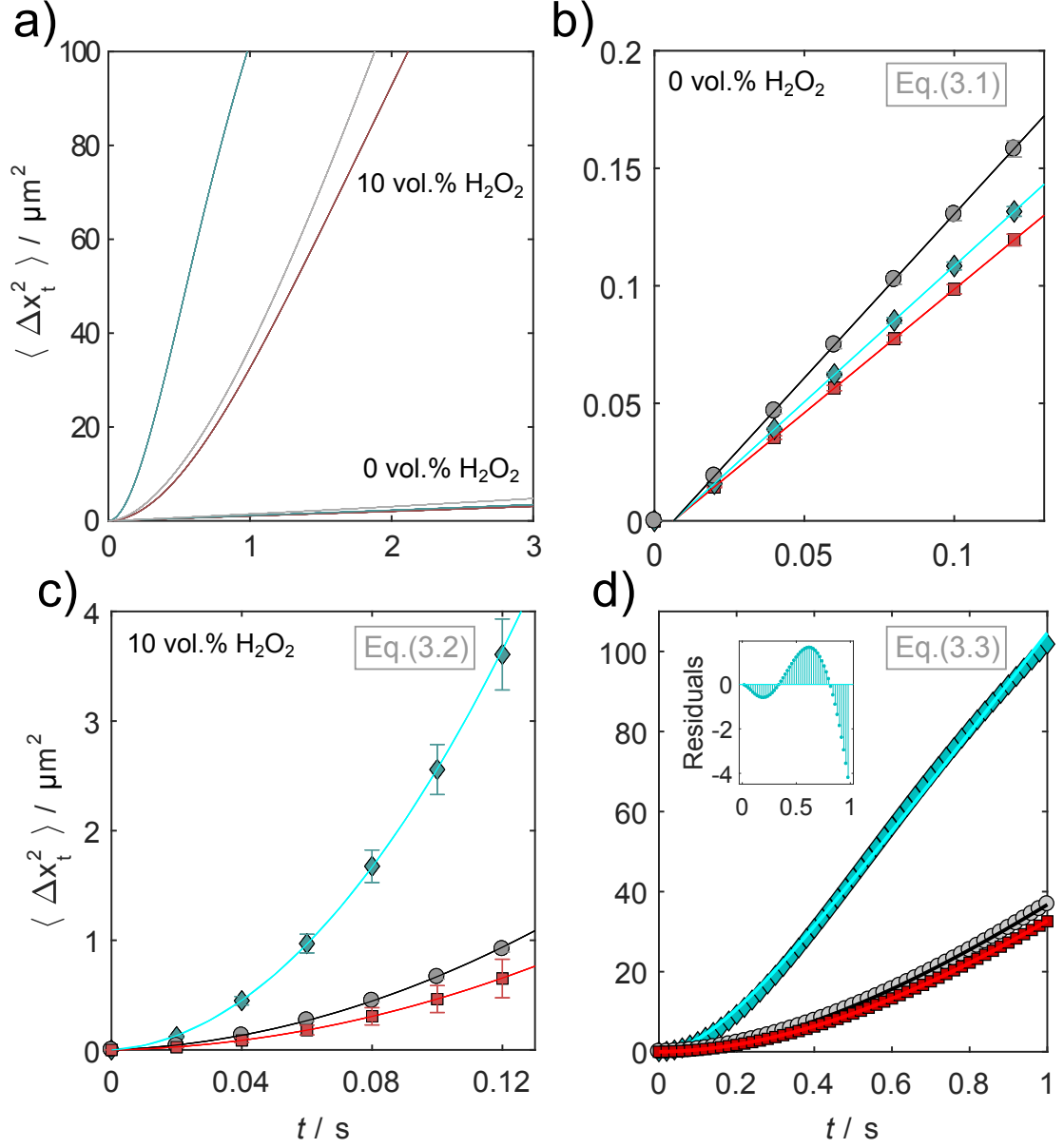


Figure 3.3. Average mean-squared-displacement, $\langle \Delta x_t^2 \rangle$, graphs at given delay time, t a-d) for smooth PS-Pt micromotors (grey), with large surface deformations (red) and small surface deformations (cyan) with no fuel present and at 10 vol.% H_2O_2 . Fitting regions are displayed for each case with associated error bars (standard error). The equations used to fit the MSDs are labelled as insets on each graph and are detailed in the main text.

		$D / \mu\text{m}^2 \text{s}^{-1}$	$v / \mu\text{m s}^{-1}$
Smooth (<i>s</i>)	U	0.27	7.48
	C	0.35	7.24
Rough (<i>ld</i>)	U	0.14	6.41
	C	0.26	5.99
Rough (<i>sd</i>)	U	0.44	15.5
	C	0.29	15.59

Table 3.1. Comparison of the determined diffusion coefficients, D , and velocities, v , extracted from the parabolic fits, equation (3.2), of mean-squared-displacements of PS-Pt micromotors (Fig4). U - unconstrained fits, C - fits were constrained to experimentally determined values of D at 0 vol.% Fuel.

		$D / \mu\text{m}^2 \text{s}^{-1}$	$v / \mu\text{m s}^{-1}$	$\tau_{\text{R}} / \text{s}$
Smooth (<i>s</i>)	U	0.59	7.03	1.68
	C	0.35	7.36	1.41
	w	0.35	7.26	1.55
Rough (<i>ld</i>)	U	4.8×10^{-10}	6.75	1.83
	C	0.26	6.46	2.24
	w	0.26	6.24	3.01
Rough (<i>sd</i>)	U	3.6×10^{-8}	19.62	.032
	C	0.29	19.40	0.33
	w	0.29	16.84	0.52

Table 3.2. Comparison of the diffusion coefficient, D , velocities, v , and rotational times, τ_{R} , determined by fitting equation (3.3) to the mean-squared-displacements of PS-Pt micromotors up to $t = 1 \text{ s}$ (Fig 4). U - unconstrained fits, C - fits were constrained to experimentally determined values of D at 0 vol.% Fuel, w – weighted ($1/\sigma^2$), constrained fits.

table 3.1) with a noticeable difference ($\sim 20\%$) only in the case of particles with small deformations (see table 3.2). Rotation times, τ_{R} , are also comparable with theory for the PS-Pt micromotors with ‘smooth’ and large deformations but significantly lower than expected for those with small deformations assuming a translational propulsion mechanism. Note that an inherent issue with unconstrained multiple parameter fits is that they can force unphysical parameter values to materialize, such as the exceedingly low values extracted here for D of the deformed PS-Pt micromotors. Also the error in MSD data scales with the square and thus fitting to long delay times introduces significant error to the analysis. An experimental route to minimize the error in MSD data involves tracking the particles for a

longer overall time period (at least an order of magnitude of the fitting region). However in practice this is difficult as the rapidly moving micromotors can leave the field of view during imaging. Reducing the objective magnification, allowing for a larger field of view, to combat this lowers the resolution and thus increases particle localization error. Therefore the preferred method is by fitting equation (3.2) to the early MSD data (table 3.1) providing that the propulsion mechanism has first been distinguished from convection or other transport mechanisms.³²

Weighting the fits with weights equal to the reciprocal of the standard deviation squared, $w = 1/\sigma^2$, provides a more rigorous fit. Even in doing so we still extract a low value for τ_R for micromotors with small deformations suggesting more complex propulsion behaviour in this case. Recent findings from Archer and co-workers saw a negative correlation between v and τ_R ²⁸ with comparable $\tau_R \sim 0.45$ s at $v \sim 14 \mu\text{m s}^{-1}$ to our data and thus we support the conclusion that imbalances in the local flow field brought about by non-uniform reactivity across the catalyst surface may drive down τ_R .

Upon close examination of the MSD for PS-Pt micromotors with small deformations a departure from the expected behaviour was noticed (figure 3.3 d) with a tailing off of the parabola between $0.4 < t < 1.0$ s, this is exemplified by a plot of the residuals (inset figure 3.3 d). The change in MSD suggests a different propulsive mechanism may be present. A superimposed angular component to the velocity could potentially yield an MSD shape akin to this, as has been previously shown for PS-Pt micromotors with defined Pt cap size.²⁷ Using the expression proposed in this work appears to over fit our data if unconstrained, yielding an excessively high value for D , and reduces to a parabola with $v = 9.66 \mu\text{m s}^{-1}$ if constrained to more reasonable values of D and D_r . Hence we can conclude that the effect is too subtle to probe with this analysis. If we instead look at the MSDs of the individual particle trajectories (figure 3.4) we begin to unravel the rich behaviour of particles with small deformations (cyan, c). There is a distinct oscillation to many of the trajectories suggesting some particles exhibit a persistent angular propulsion mechanism.

Plotting the normalized velocity autocorrelation (VACF) (equation (3.4)), reveals additional clues to the type of motion (figure 3.5). For a typical PS-Pt micromotor exhibiting translational propulsion this should decay to 0 after the rotational diffusion time, i.e.

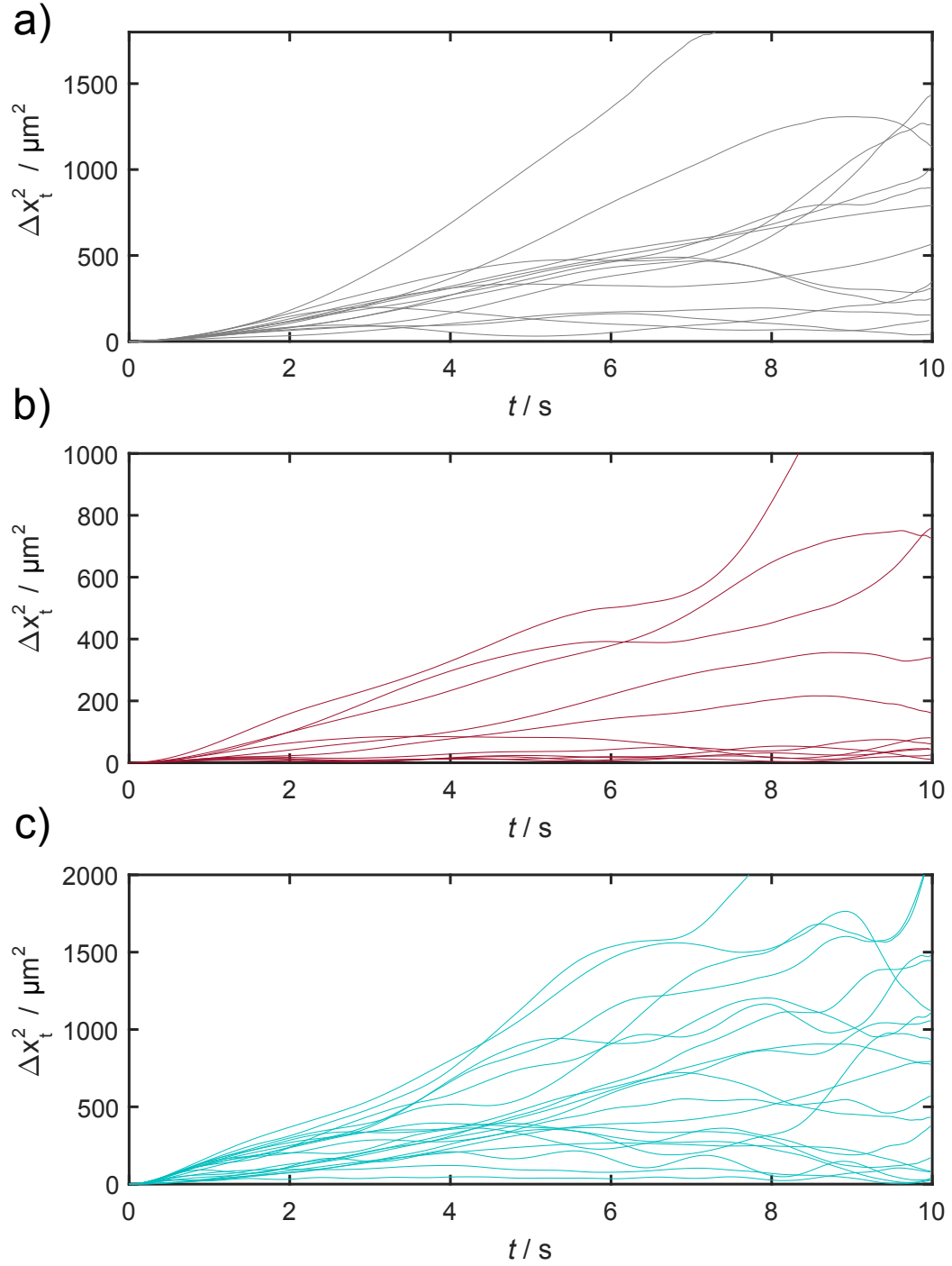


Figure 3.4. Mean-squared-displacements, Δx_t^2 , for individual particle trajectories of PS-Pt Janus particles in 10 vol.% H_2O_2 with ‘smooth’ surfaces a), rough surfaces with large deformation (*ld*) b) and small deformations (*sd*) c).

once the propulsive direction of the motor has been randomized. This is the case for our smooth PS-Pt micromotors, however for those with surface deformations there appears to be a small persistent oscillation (larger than the magnitude of noise) after the initial decay period. Again this is further evidence of some angular velocity, although the effect is fairly weak. Additional inspection of all particle trajectories in the sample revealed that some of the deformed micromotors followed a spiralling path for at least part of their trajectory (figure 3.5 a).

$$\langle v_i(0).v_i(t) \rangle = \frac{1}{N} \sum_{i=1}^N (v_i(0).v_i(t_0 + n\delta t)) \quad (3.4)$$

The origin of angular velocity in the deformed PS-Pt micromotors is most likely caused by the irregularity of surface roughness. This can give rise to uneven catalytic activity across the surface of the particle, mass anisotropy and potentially enhanced interaction between the particle and glass surfaces. In a few cases we observed that PS-Pt micromotors with large surface deformations displayed predominantly translational propulsion when away from (or parallel to) the glass surface and began propelling rotationally suddenly (figure 3.6, Supplementary Video SV2 Appendix B.2). We hypothesize that this may be caused by an (unidentified) object or surface in close proximity. This behaviour was exclusive to this particle system and not observed for the ‘smooth’ PS-Pt micromotors or those with small deformations. Note particles were only located in x and y. Precise z (height) locations would give more information about when this switch over in propulsion mechanism occurs. A combination of gravitational and hydrodynamic forces are likely to promote this phenomenon, as predicted and experimentally observed for self-phoretic micromotors near boundaries.^{33–36}

It was initially intriguing to us that micromotors with large surface deformations had a similar propulsion velocity to their non-deformed cousins as we expected a larger catalytic surface area to promote faster motion. Large surface deformations lead to an effective diameter increase of $\sim 40\%$ as found in the previous study in chapter 2.²⁹ If we consider no change in the phoretic mechanism and ignore effects of the altered particle shape, according to Ebbens *et al.* an equivalent reduction in propulsion velocity should be observed, $v \propto 1/r$.¹⁸ Only a 17% reduction was measured, suggesting size alone cannot

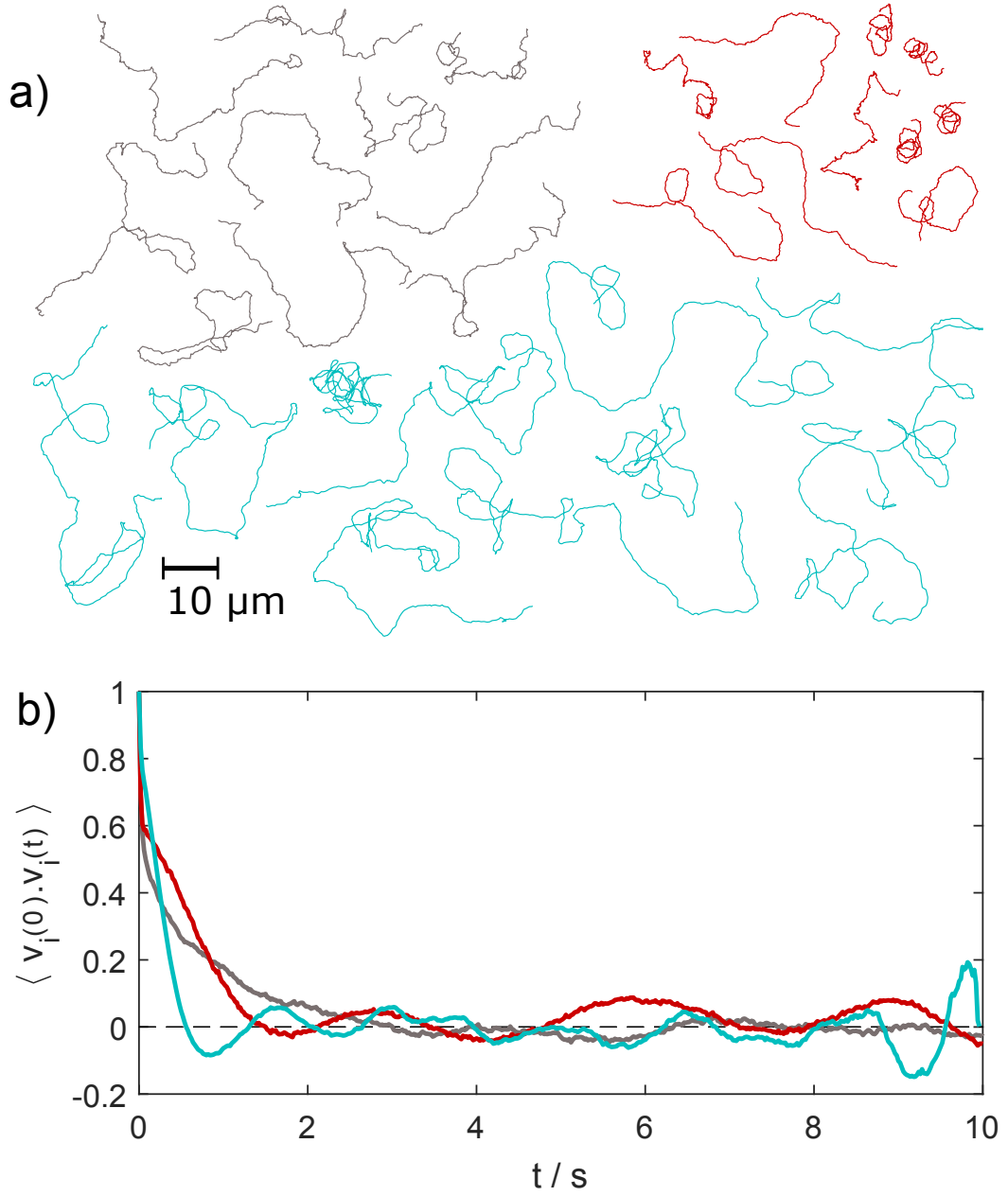


Figure 3.5. Propelled PS-Pt particle trajectories (10 vol.% H₂O₂) (a). Normalized velocity autocorrelation over 10 s (b) for ‘smooth’ PS-Pt micromotors in 10 vol. % H₂O₂ (grey) and those with large deformations (*ld*) (red) and small deformations (*sd*) (cyan).

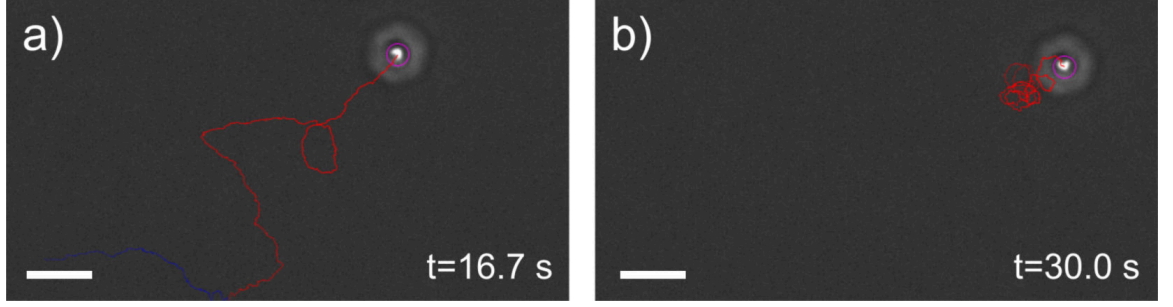


Figure 3.6. Snapshots of a video with trailing particle tracks (1000 frames) displaying a rough particle with large deformations self-propelling in the presence of H_2O_2 and transitioning from a translational a) to angular b) propulsion mechanism. Scale bar = $5\text{ }\mu\text{m}$.

explain the result. We propose that the significant irregularity in the particle shape and presence of larger craters may lead to a hindrance in establishing an even concentration gradient and flow profile about the particle.

3.2.3 Microscopic characterization: resolving surface details

Before drawing conclusions from the motion analysis of deformed PS-Pt micromotors, it was imperative that the surface details of the PS-Pt micromotors were properly resolved. Transmission Electron Microscopy (TEM) images (figure 3.7) revealed the morphology of the supposed thin-film of Pt produced from the sputtering procedure. The un-deformed PS-Pt particle appeared to have a largely smooth surface with features on the order of 1–2 nm, in contrast to the deformed particles upon which pillars of Pt ($\sim 10\text{ nm}$) were found. The presence of these features is intriguing considering the underlying surface chemistry and sputtering procedure was unchanged. Upon close examination it appears that areas of high curvature, i.e. sharp edges, could promote their formation (SEM, figure 3.8). This may be due to low adatom (atoms at the surface of the crystal) diffusion and effective ‘pinning’ of Pt nuclei on these surface asperities. Columnar features with high porosity are proposed to be formed at low deposition temperatures³⁷ when surface diffusion is limited. High resolution TEM and selected area electron diffraction (SAED) (figure 3.7 g) of the Pt features on the surface of particles with small deformations reveals a polycrystalline structure with a predominant lattice spacing of $2.20\text{ }\text{\AA}$ indicative of Pt (111).³⁸ It would be interesting to properly resolve the exposed faces of the Pt pillars and thus the active sites of

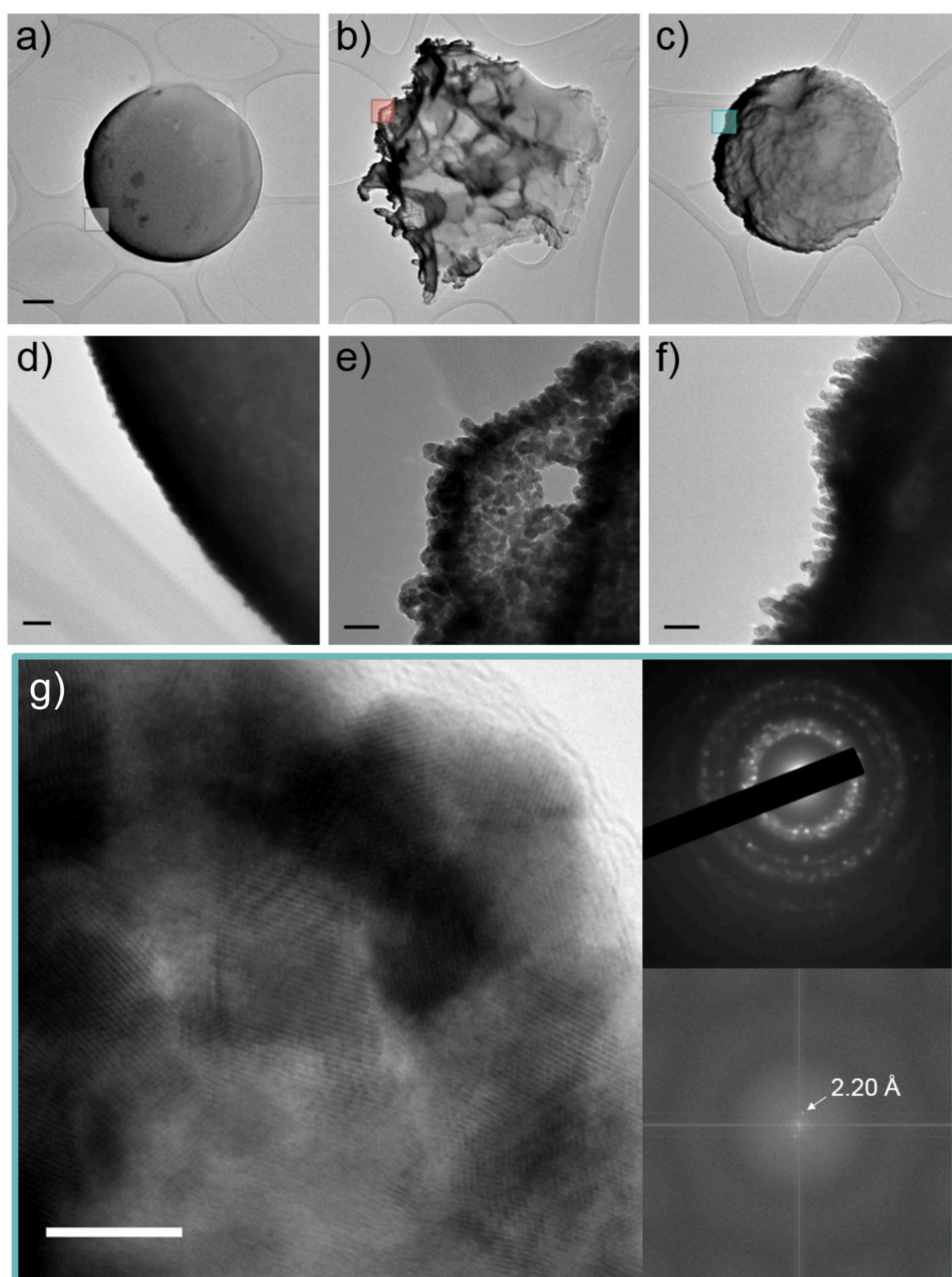


Figure 3.7. Transmission Electron Microscopy (TEM) images of poly(styrene-*co*-methacrylic acid) microspheres half-coated with platinum (a–f). Low (a–c) and high (d–f) magnification images of PS-Pt Janus micromotors without roughening applied (a,d), with large surface deformations (b,e) and small surface deformations (c,f). Scale bars (a–c) = 200 nm, (d–f) = 20 nm. Boxes highlight region of interest for high magnification images.

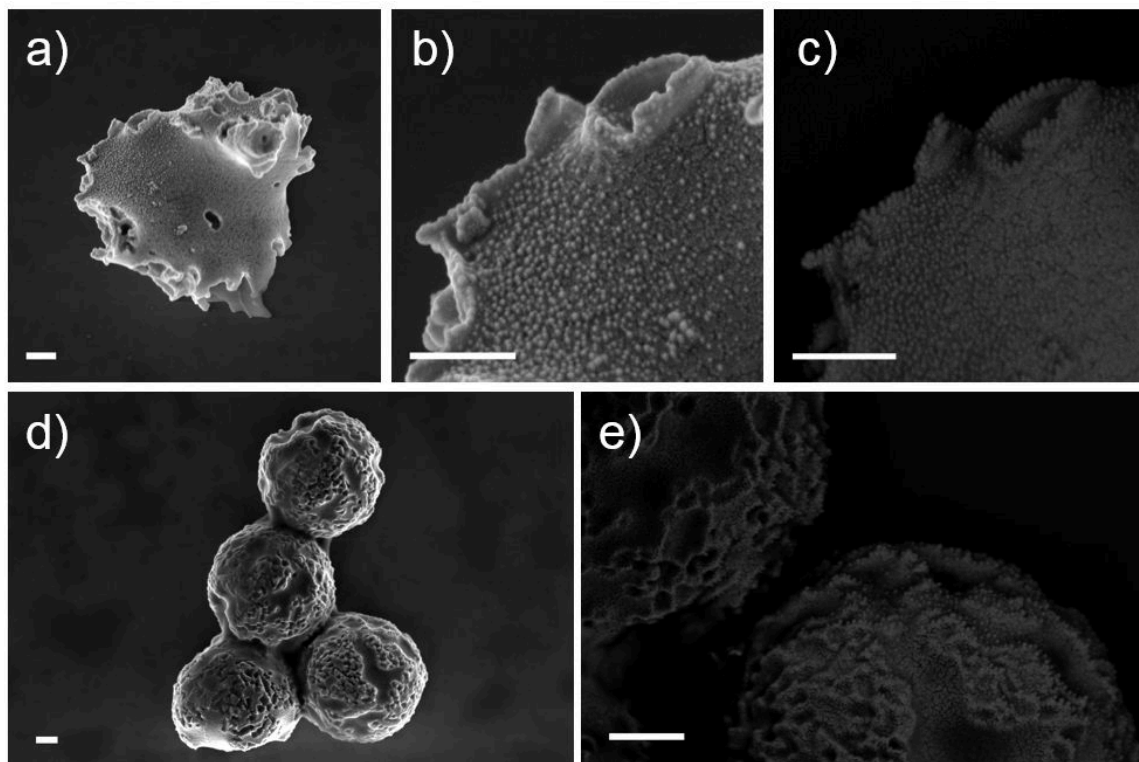


Figure 3.8. Scanning Electron Microscopy (SEM) images of deformed PS microparticles after sputtering with Pt (a–e). Back-scattered electron images (c,e) enhance compositional contrast and highlight locations of Pt pillars. Scale bars = 200 nm.

the catalyst,³⁹ however the large underlying insulating polymer material of the microsphere makes this a significant challenge. Nevertheless we can conclude that these features lead to a vastly increased catalytic surface area which in turn affects the overall reaction rate at the surface.

As a side-by-side comparison of the scale of roughness and to further examine the potential formation of Pt nano structures, PS films were produced with varying roughness following identical procedures to the previous samples with the exception of an additional step to encourage prior film formation (see 3.4.3). These films were examined by SEM (figure 3.9) after sputtering with Pt via the same procedure used for the Janus PS-Pt spheres. The difference in the scale of the imprinted surface roughness is immediately evident at low and high magnification (figure 3.9 d and e for ‘*ld*’ and figure 3.9 g and h for ‘*sd*’). In addition we observe bright features indicative of nanoscopic Pt domains

accumulated at the sharper, roughened areas of the sample. This is further exaggerated in the red areas of the false coloured images (figure 3.9 f-i). Note that care was taken so that each sample was imaged with near identical conditions i.e. 0.5 kV, 2.6 mm working distance and without alteration to brightness/contrast settings. It is worth also pointing out that bright features can be a factor of charging or edge effects whereby secondary electrons are preferentially ejected out of sharp edges. Here imaging was performed at such a low accelerating voltage (500 V) in an to attempt to avoid this. With this in mind and due to the apparent fine structure of these bright features we are confident that the primary contrast mechanism is back scattering i.e. compositional contrast from Pt.

Sputtered metallic thin films on an underlying surface universally exhibit a certain roughness.⁴⁰ The ‘smooth’ polymer films interestingly show a degree of roughness (domains of average diameter, $d = 12.01 \pm 4.32$ nm) after sputtering Pt (figure 3.9 a-c). It is logical that this roughness is a function of the amount of material deposited and that also the wetting/adhesion characteristics of the underlying substrate play a role.⁴¹ Indeed Choudhury *et al.* varied surface roughness on spherical silica micromotors by depositing a significant (80 nm) underlayer of silica before sputtering 20 nm of Pt.²⁵ In this current study we have shown that relatively small changes in the polymer particle surface roughness can promote the formation of nanoscopic Pt pillars. These columnar features further increase the fractal dimension of surface roughness and hence there is a larger than expected catalytic surface area. As a direct result, there will be a shift in velocity magnitude and an increased probability of non-uniformity across the particle surface for the composed micromotor. Therefore we suggest that a keen eye (and high resolution electron microscope) are crucial for experimental studies of micromotors fabricated in this manner.

For most Pt micromotor studies, homogeneous catalytic activity is assumed across the catalyst surface. In reality, varying thickness of the catalyst layer¹⁶ and crystallographic orientation affect the number distribution of exposed active sites. The magnitude of velocity is therefore further dependent on these properties.

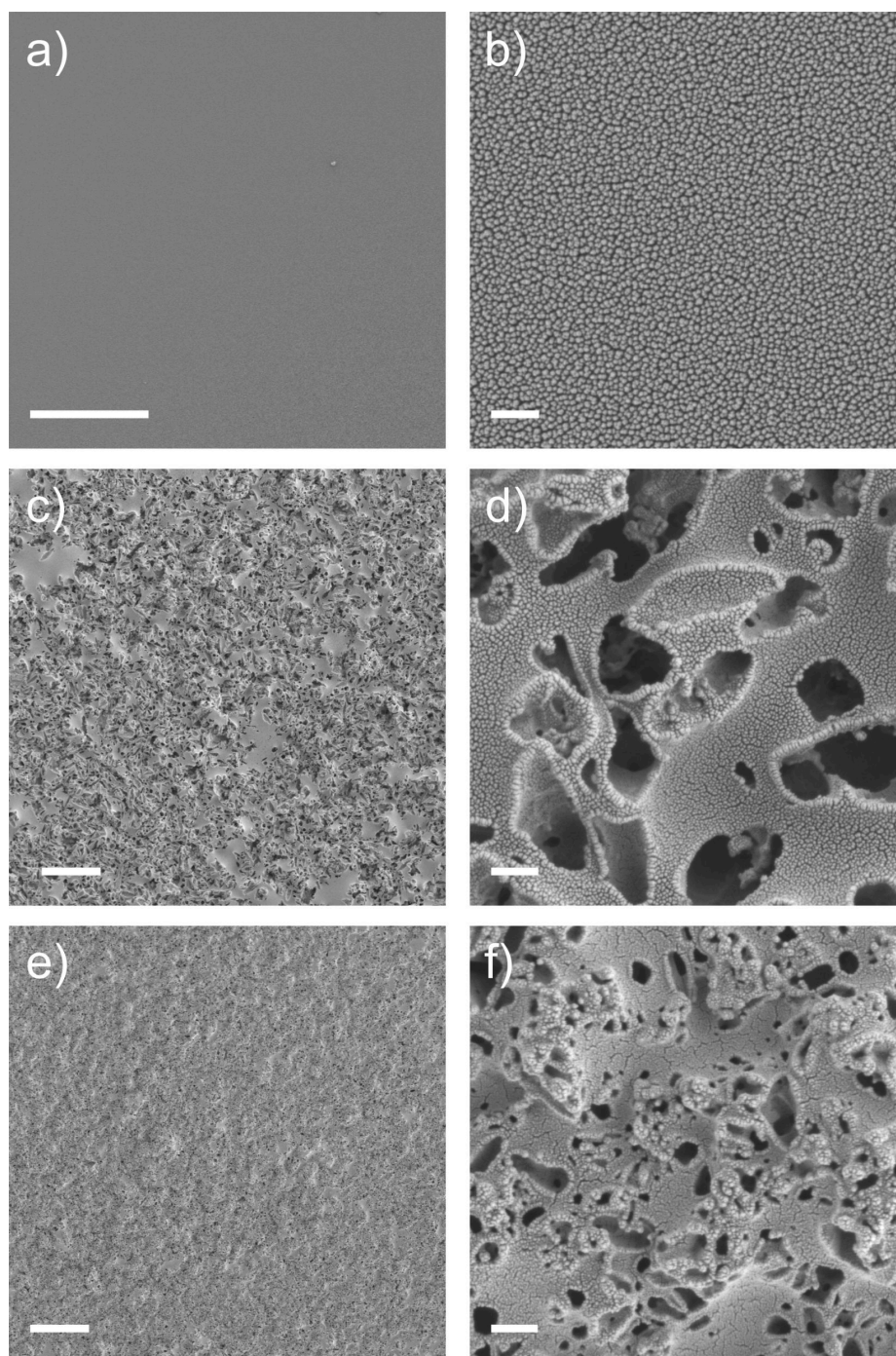


Figure 3.9. Scanning Electron Microscopy (SEM) images of PS-MAA films sputtered with Pt with smooth surface features (a,b), large (c,d) and small deformations (e,f). Scale bars (a,c,e) = 5 μm , (b,d,f) = 200 nm.

3.2.4 A note on roughness

As a back-of-the-envelope thought experiment, if we consider a surface roughness to be the product of depositing small hemi-spheres on a large sphere (figure 3.10), the maximum increase in surface area is less than two times the original sphere's surface area.

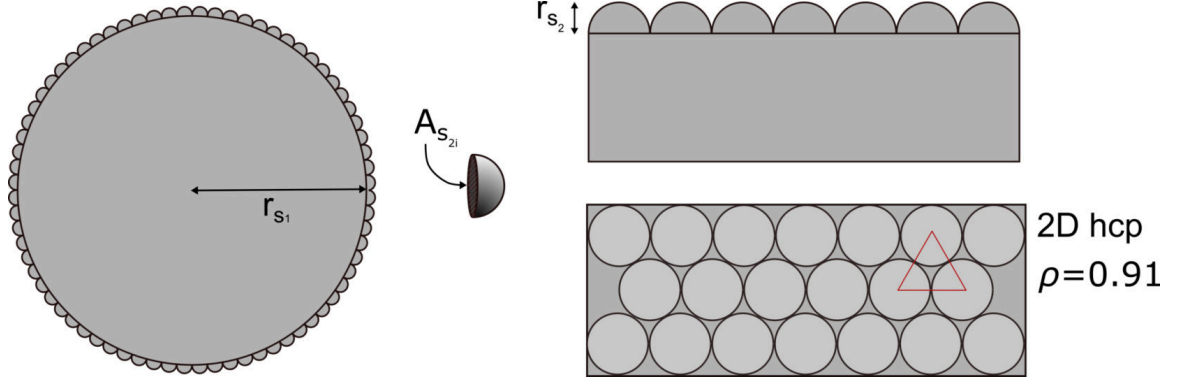


Figure 3.10. Packing of small hard hemi-spheres, s_2 , onto a larger sphere, s_1 , as a model for roughness.

Assuming 2D hexagonal close-packing (face-centered-cubic, fcc) of s_2 on s_1 to give a packing efficiency, $\rho = 0.91$. The new surface area of the rough sphere A_{rs} can be approximated by dividing the area covered by hemispheres, ρA_{s1} , by the intersecting face of each hemisphere, A_{s2i} , to yield the number hemispheres covering the surface. The product of this and the area of each exposed hemisphere, A_{s2} , plus the uncovered surface gives the new, rough surface:

$$A_{rs} = \left(\frac{\rho A_{s1}}{A_{s2i}} \right) A_{s2} + (1 - \rho) A_{s1} \quad (3.5)$$

The relative increase in surface area is $A_{rs}/A_{s1} = 1.91$ which in fact holds for any $r_{s2} < r_{s1}$ in this model. Note that as r_{s2} increases relative to r_{s1} , the curvature of the large sphere becomes more important and thus the intersection area increases. Also perfect fcc packing is not possible on a curved surface as the sum of the interior angles of the triangular lattice must exceed π , introducing strain and therefore defects.⁴² These effects are omitted here for simplicity.

Real surface roughness is much more complex, however it stands without saying that in order to increase it, higher aspect ratio features or increased fractal dimension are

necessary. Surface roughness may promote faster motion by both increased catalytic activity and a modification to the slip velocity - known to have a dependence on roughness.⁴³ In fact in a recent study by Archer *et al.* the authors also suggest that there is more to consider (i.e. surface mobility parameters) than just an increase in catalytic turnover as this did not correlate directly with their observed velocity increase.²⁸

3.3 Conclusion

In summary, we have demonstrated that the surface roughness of micromotors influence their propulsion behaviour significantly. Surface deformations in our catalytic micromotors lead to considerable enhancement of the nanoscale surface roughness of the platinum catalytic layer, hereby increasing propulsion velocities and thus ‘engine power’. Moreover, rotary oscillations in the displacement of the micromotors was observed, with a questionable correlation between frequency of surface roughness and frequency of the angular oscillations. Non-uniformity in the reaction at the catalyst surface and modifications to the surface mobility are proposed to be the primary causes of this departure from a purely translational propulsion mechanism.

3.4 Experimental

3.4.1 Materials

Styrene ($\geq 99\%$) and poly(*N*-vinyl-pyrrolidone) (PVP K-30: Average molecular weight = $40,000 \text{ g mol}^{-1}$), methacrylic acid (99%), azobisisobutyronitrile (AIBN) (98%) and dialysis tubing cellulose membrane (typical molecular weight cut-off = $14,000 \text{ g mol}^{-1}$) were obtained from Sigma Aldrich. AIBN was recrystallized in methanol to remove impurities prior to use. Acetic acid glacial ($>99\%$) and Ethanol p.a. were obtained from Fischer Scientific. Hydrogen peroxide (30 wt.%, *aq.*) was obtained from Honeywell. Calcium carbonate, Socal P3 powder (diameter = 250–350 nm) (length = 500–1000 nm) was received as a donation from Akzo-Nobel. Calcium carbonate, PCC rods powder (diameter ~ 500 nm) (length = 3–15 μm) was received as a donation from Unilever. The Z-COTE zinc oxide

(diameter ~ 120 nm) was received as a donation from BASF.

3.4.2 Dispersion polymerisation of micron-sized poly(styrene-*co*-methacrylic acid) spheres

AIBN (0.1215 g), PVP K-30 (0.85 g), ethanol (86.25 g), styrene (12.15 g) and methacrylic acid (MAA, 0.1215 g) were charged to a 250 ml round bottom flask and purged with nitrogen for 40 minutes. Next, the flask was submerged into an oil bath heated to 70 °C (IKA RCT Basic) and left to react for 24 hours whilst agitating with a magnetic stirrer at 500 rpm and kept under a slight nitrogen gas overpressure. The obtained particle dispersions were centrifuged and re-dispersed in de-ionized water and ethanol three times each.

The average particle diameter and associated standard deviation and dispersity (in parenthesis) were: 1.19 ± 0.02 (0.017) μm .

3.4.3 PS-MAA film formation

Polymer films were produced by first depositing a concentrated suspension ($\xi \sim 0.2$) of PS-MAA microspheres synthesized previously (See 3.4.2) onto silicon wafers. After drying, the samples were heated in an oven at 130 °C for 24 hr to allow for full inter-diffusion of polymer chains and the production of a smooth polymer film.

3.4.4 Physical deformation of PS-MAA microspheres

Physical roughening was performed by heating samples above the glass transition temperature of poly(styrene) in the presence of a hard colloidal matrix for *ca.* 2 hr, as described previously.²⁹ In this study the oven temperature was 110 °C for those deformed with small ZnO particles and 130 °C for those deformed with CaCO₃.

3.4.5 Physical vapour deposition of thin films of platinum

Low volume fraction ($\xi = 0.01$) suspensions of PS-MAA particles in isopropyl alcohol were deposited onto glass microscope slides. Sputtering was performed using a platinum source

in a DC Magnetron sputter coater (Quorum Technologies SC7640) at 2.5 kV, ~ 20 mA for two consecutive 60 s cycles, ~ 15 nm film thickness according the manufacturer.

3.4.6 Particle characterization

Samples for SEM were prepared by dropping suspensions and allowing them to dry onto silicon wafers supported on aluminium stubs with a conductive copper adhesive. SEM imaging was performed on a Zeiss Gemini SEM 500 at 2 kV. Back scattered electron images were captured using the InLens detector with a bias of 450 V. For TEM analysis samples were prepared by dropping a relatively dilute dispersion (~ 0.01 wt.%) of particles in water on to lacey carbon grids and allowing the samples to dry. Particles were imaged using a JEOL 2100.

3.4.7 2D particle tracking experiments

Suspensions of PS-Pt particles were prepared by removing them from the glass slides by careful wiping with 1×1 cm² wetted lens tissue. The lens tissue was then inserted into small Eppendorf tubes containing approximately 0.5 ml de-ionized water. Tubes were then vortexed to remove the PS-Pt particles from the lens tissue and suspend them in solution. For experiments when fuel was present, 10 μ L of PS-Pt particle suspension was pipetted into 990 μ L of 10 vol.% H₂O₂.

Two parallel lines of grease were drawn out to the approximate size of the cover slips being used (20 mm \times 20 mm) onto a Linkam Warm Stage. The coverslip was placed lightly over the lines of grease and a micropipette was used to inject the sample solution underneath the assembled cell. Capillary action ensures the solution fills the well and it is subsequently sealed at the other edges with grease. Videos (20–30) of 5–10 particles in motion near to the underlying glass, 1024 \times 1024 px. at 50 fps for 10 s, were recorded using an Andor Zyla 4.4 Plus camera attached to an Olympus IX73 inverted light microscope. Time was allowed for the Linkam warm stage to heat up to 25 °C. A magnification of 60 \times (Olympus LUCPlanFLN 60 \times Ph) was used with phase to enhance the contrast of particles.

A tracking algorithm, Trackmate,⁴⁴ distributed with ImageJ(Fiji) was then utilized to perform the 2D particle tracking. Our analysis was then performed using msdalyzer,

a Matlab class created for analysing tracking data.⁴⁵ Fits were performed using the Matlab curve fitting toolbox.

References

- [1] S. Ramaswamy, *Annu. Rev. Condens. Matter Phys.*, 2010, **1**, 323–345.
- [2] H. R. Jiang, N. Yoshinaga and M. Sano, *Phys. Rev. Lett.*, 2010, **105**, 268302.
- [3] I. Buttinoni, J. Bialké, F. Kümmel, H. Löwen, C. Bechinger and T. Speck, *Phys. Rev. Lett.*, 2013, **110**, 238301.
- [4] W. Wang, W. Duan, S. Ahmed, A. Sen and T. E. Mallouk, *Acc. Chem. Res.*, 2015, **7**, 1938–1946.
- [5] J. Palacci, S. Sacanna, A. P. Steinberg, D. J. Pine and P. M. Chaikin, *Science*, 2013, **339**, 936–940.
- [6] W. Wang, W. Duan, S. Ahmed, T. E. Mallouk and A. Sen, *Nano Today*, 2013, **8**, 531–554.
- [7] J. Howse, R. Jones, A. Ryan, T. Gough, R. Vafabakhsh and R. Golestanian, *Phys. Rev. Lett.*, 2007, **99**, 048102.
- [8] A. R. Morgan, A. B. Dawson, H. S. McKenzie, T. S. Skelton, R. Beanland, H. P. W. Franks and S. A. F. Bon, *Mater. Horizons*, 2014, **1**, 65–68.
- [9] F. Peng, Y. Tu, J. C. M. van Hest and D. A. Wilson, *Angew. Chem. Int. Ed.*, 2015, **127**, 11828–11831.
- [10] W. Gao, R. Dong, S. Thamphiwatana, J. Li, W. Gao, L. Zhang and J. Wang, *ACS Nano*, 2014, **9**, 117–123.
- [11] H. Wang, B. Khezri and M. Pumera, *Chem*, 2016, **1**, 473–481.
- [12] A. A. Solovev, S. Sanchez and O. G. Schmidt, *Nanoscale*, 2013, **5**, 1284–1293.
- [13] R. Golestanian, T. Liverpool and A. Ajdari, *Phys. Rev. Lett.*, 2005, **94**, 220801.

- [14] J. L. Anderson, *Ann. Rev. Fluid Mech.*, 1989, **21**, 61–99.
- [15] A. Brown and W. Poon, *Soft Matter*, 2014, **10**, 4016–4027.
- [16] S. Ebbens, D. A. Gregory, G. Dunderdale, J. R. Howse, Y. Ibrahim, T. B. Liverpool and R. Golestanian, *Europhys. Lett.*, 2013, **106**, 58003.
- [17] A. T. Brown, W. C. K. Poon, C. Holm and J. de Graaf, *Soft Matter*, 2015, **13**, 1200–1222.
- [18] S. J. Ebbens, G. a. Buxton, A. Alexeev, A. Sadeghi and J. R. Howse, *Soft Matter*, 2012, **8**, 3077.
- [19] R. Golestanian, T. B. Liverpool and A. Ajdari, *New J. Phys.*, 2007, **9**, 126–126.
- [20] S. Michelin and E. Lauga, *Sci. Rep.*, 2017, **7**, 42264.
- [21] L. Bocquet and J.-L. Barrat, *Soft Matter*, 2007, **3**, 685–693.
- [22] S. Michelin and E. Lauga, *Eur. Phys. J. E*, 2015, **38**, 1–16.
- [23] N. S. Zacharia, Z. S. Sadeq and G. A. Ozin, *Chem. Comm.*, 2009, **0**, 5856–5858.
- [24] S. Wang and N. Wu, *Langmuir*, 2014, **30**, 3477–3486.
- [25] U. Choudhury, L. Soler, J. G. Gibbs, S. Sanchez and P. Fischer, *ChemComm*, 2015, **51**, 8660–8663.
- [26] R. Laocharoensuk, J. Burdick and J. Wang, *ACS Nano*, 2008, **2**, 1069–1075.
- [27] R. J. Archer, A. I. Campbell and S. Ebbens, *Soft Matter*, 2015, **11**, 6872–6880.
- [28] R. J. Archer, A. J. Parnell, A. I. Campbell, J. R. Howse and S. J. Ebbens, *Adv. Sci.*, 2017, **1700528**, 1700528.
- [29] B. W. Longbottom, B. Somuncuoğlu, J. J. Punter, S. Longbottom and S. A. F. Bon, *Soft Matter*, 2017, **13**, 4285–4293.
- [30] A. I. Campbell and S. J. Ebbens, *Langmuir*, 2013, **29**, 14066–14073.

- [31] M. D. Carbajal-Tinoco, R. Lopez-Fernandez and J. L. Arauz-Lara, *Phys. Rev. Lett.*, 2007, **99**, 138303.
- [32] G. Dunderdale, S. Ebbens, P. Fairclough and J. Howse, *Langmuir*, 2012, **28**, 10997–11006.
- [33] G. Volpe, I. Buttinoni, D. Vogt, H.-J. Kümmerer and C. Bechinger, *Soft Matter*, 2011, **7**, 8810–8815.
- [34] S. E. Spagnolie and E. Lauga, *J. Fluid Mech.*, 2012, **700**, 105–147.
- [35] W. E. Uspal, M. N. Popescu, S. Dietrich and M. Tasinkevych, *Soft Matter*, 2015, **11**, 434–438.
- [36] A. I. Campbell, R. Wittkowski, B. Ten Hagen, H. Löwen and S. J. Ebbens, *J. Chem. Phys.*, 2017, **147**, 084905.
- [37] J. A. Thornton, *Proc. SPIE*, 1988, **821**, 95–105.
- [38] W. P. Davey, *Phys. Rev.*, 1925, **25**, 753–761.
- [39] L. Y. Chang, A. S. Barnard, L. C. Gontard and R. E. Dunin-Borkowski, *Nano Lett.*, 2010, **10**, 3073–3076.
- [40] D. Marton and J. Fine, *Thin Solid Films*, 1990, **185**, 79–90.
- [41] D. L. Bellac, G. A. Niklasson and C. G. Granqvist, *Europhys. Lett.*, 1995, **32**, 155–159.
- [42] V. N. Manoharan, *Science*, 2015, **349**, 1253751.
- [43] Y. W. Kim and R. R. Netz, *Europhys. Lett.*, 2007, **72**, 837–843.
- [44] J.-Y. Tinevez, N. Perry, J. Schindelin, G. M. Hoopes, G. D. Reynolds, E. Laplantine, S. Y. Bednarek, S. L. Shorte and K. W. Eliceiri, *Methods*, 2016, **115**, 80–90.
- [45] N. Tarantino, J. Y. Tinevez, E. F. Crowell, B. Boisson, R. Henriques, M. Mhlanga, F. Agou, A. Israël and E. Laplantine, *J. Cell Biol.*, 2014, **204**, 231–245.

4

Fabrication and Dynamics of Silica-Based ‘Matchstick’ Colloids

Think like a five year old.

Prof. dr. ir. Stefan A. F. Bon

Abstract

In this chapter an insight into the synthesis of silica-based ‘matchstick’-shaped colloidal particles is reported. The generation of aqueous emulsion droplets dispersed in an n-pentanol-rich continuous phase and their use as reaction centres allows for the fabrication of siliceous microparticles that exhibit anisotropy in both particle morphology, that is a ‘matchstick’ shape, and chemistry, that is a transition metal oxide enriched head. We provide series of kinetic studies to gain a mechanistic understanding and unravel the particle formation and growth processes. Additionally we demonstrate the ability to select the aspect ratio of the ‘matchstick’ particle in a straightforward manner and study their enhanced Brownian motion in the presence of hydrogen peroxide.

4.1 Introduction

Rod-like colloidal objects can show interesting behaviour in motility and collective interactions when dispersed in liquid media.^{1–3} As such they are of interest for a range of

Parts of this chapter are published elsewhere, see: Longbottom, B. W.; Rochford, L. A.; Beanland, R.; Bon, S. A. F. *Langmuir* 2015, **31**, 9017–9025

applications, including sensing and imaging,⁴ electronics⁵ and even biologically inspired 2D membranes.⁶ Beside anisotropy in shape, complexity can be added by imposing chemical anisotropy as a platform to further extend behavioural functions of the colloids. Examples include the fabrication of Janus rods as efficient swimmers,^{7,8} and particles that exhibit distinctive self-assembly behaviour.^{9,10}

In the search for suitable candidates for the studies of the physical behaviour mentioned above, silica has emerged as a promising material. A dispersion of silica microrods has been shown to generate unique crystal phase behaviour when exposed to external electric fields.¹¹ One of the advantages of silica is the ease at which chemical modification of the particle surface can be achieved due to the reactivity of the terminal Si-OH bonds. A vast range of different functionalities can be attained through post-modification including, but certainly not limited to, fluorescent moieties.^{12,13} It is however not straightforward to achieve chemical anisotropy through a post modification technique, requiring stringent conditions and often producing a low product yield, for instance by sputtering onto a particle monolayer.¹⁴ Though quite theoretically challenging, innovative wet chemical techniques can provide a relatively inexpensive and experimentally simple route to chemically anisotropic colloids. Generically, perhaps the most well explored route is through a two-step phase separation method to produce particles with two chemically distinct lobes.^{15,16}

The well-known hydrolysis-condensation reactions of alkoxy-silanes are a classical route to the synthesis of colloidal silica spheres, a method first developed by Stöber.¹⁷ Kinetic studies have managed to elucidate that spherical silica particles nucleate via an aggregation of siloxane clusters and then grow via a surface-limited reaction.^{18,19} In comparison relatively little is known from a mechanistic standpoint with regards to how rod-shaped silica particles are synthesized.

Nakamura demonstrated in 1995 that rod-shaped silica particles with micron-sized dimensions in length could be synthesized via a sol-gel type process in the presence of tartaric or citric acid.^{20,21} It was suggested that rod-shaped ammonium citrate or tartrate crystals form prior to silica nucleation and subsequently act as templates for silica growth (Figure 4.1 A). This was also proposed by Mann *et al.*²² Zhang *et al.* performed syntheses of silica nanotubes in the presence of PVP and citric acid-stabilized gold nanoparticles.²³

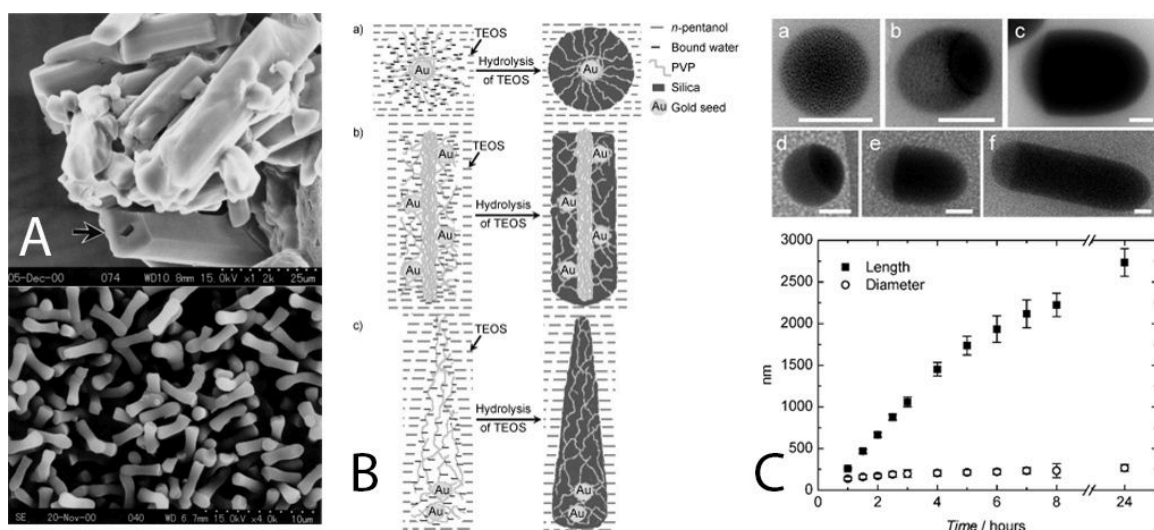
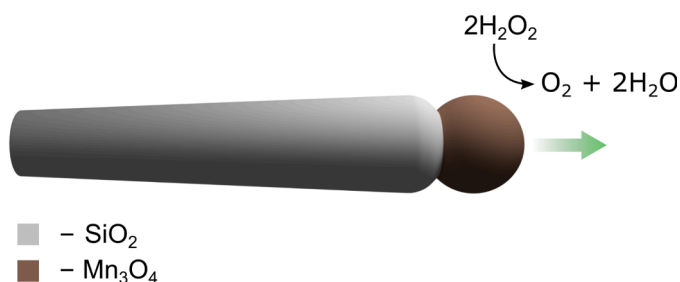


Figure 4.1. Three proposed synthetic routes to silica rods via hydrolysis-condensation reactions of alkoxy silanes in the presence of citric acid: templating of ammonium citrate crystals (top) and subsequent growth of silica around said crystals (bottom) (A),²² gold-induced soft PVP-water templates for shaped controlled growth of silica (B)²³ and silica rod growth through anisotropic nucleation and subsequent deposition within water droplets (C).¹²

It was proposed that in a water/PVP/*n*-pentanol system with a high concentration of PVP, the water molecules are bound in aggregates with the polymer. The presence of gold nanoparticles was said to induce distinctive aggregates containing bound water in a shape-selective manner such that soft templates are formed where silica growth can occur (Figure 4.1 B). A similar theory involving PVP templating was presented by Mao and co-workers whereby fibrous silica networks were formed by supposed precipitation onto self-assembled PVP fibres.²⁴

An alternative model for the growth mechanism of silica rods in a similar PVP-water system, minus the presence of gold nanoparticles, was presented by van Blaaderen and co-workers.¹² Instead of growth occurring from soft rod-like templates, it was suggested that growth proceeds by silica nucleation at the interface of the water droplet, followed by a phase separation inside the droplet and subsequent protrusion of the silica rod by precipitating onto the existing nucleus. This was evidenced following the reaction by imaging with TEM and cryo-TEM (Figure 4.1 C).



Scheme 4.1. Schematic of anisotropic silica-manganese oxide ‘matchstick’ particles. Hydrogen peroxide decomposition occurs over manganese oxide catalyst in the head of the ‘matchstick’ particle to generate propulsion. Note that propulsion magnitude and direction is unknown.

Recently attempts at kinetic control over silica particle morphology was made in a group of similar systems by Chen *et al.*²⁵ A solution-solution-solid mechanism analogous to the vapour-liquid-solid mechanism²⁶ was proposed, not dissimilar to the suggestion of van Blaaderen and co-workers. This work adds to the discussion by describing the effects of varying the ammonia and sodium citrate concentrations as well as the introduction of additional metal salts. Prior to this work Bon *et al.* showed that ‘matchstick’ shaped silica rods, which have the ability to undergo self-propulsion, could be prepared when manganese sulfate was included as part of the reaction mixture. It was demonstrated that manganese oxide nanoparticles were formed *in situ* and were located predominantly in the head of the ‘matchstick’ colloids. The asymmetric inclusion of manganese oxide is a crucial feature in achieving colloidal self-propulsion. It acts as an efficient engine owing to its high catalytic activity in the decomposition of hydrogen peroxide (Scheme 4.1).^{27–29} When the ‘matchstick’ particles were exposed to a gradient field of hydrogen peroxide (low concentrations to avoid bubble propulsion) they underwent chemotaxis.³⁰

We seek to unravel the synthesis from a mechanistic standpoint to develop our understanding of how these ‘matchstick’ colloids are formed. In doing so we may be able to kinetically isolate colloids with the most effective structure for propulsion and swimming i.e. optimum aspect ratio and catalyst loading / accessibility at colloid surface. It is clear from the above discussion that there are potentially different explanations on how such colloids can be formed. By means of series of kinetic experiments we intend to build up

an understanding and unravel the reasons behind their non-trivial anisotropic shape and chemical composition.

4.2 Results & Discussion

4.2.1 Synthesis of silica-based ‘matchstick’ colloids

For clarity we split the synthesis of the ‘matchstick’-shaped particles into two parts. Firstly, we discuss the formation of the metal oxide particulate in the head of the particle (Stage 1) and then we go on to discuss the silica condensation to form the rest of the ‘matchstick’ (Stage 2).

4.2.1.1 Stage 1 - Metal Oxide Precipitation

In a typical reaction* 24.42 g of *n*-pentanol (2.6×10^{-1} mol), 2.37 g of ethanol (5.0×10^{-2} mol), 3.00 g of PVP (MW *ca.* 40 kDa), 0.009 g of trisodium citrate dihydrate (3.6×10^{-5} mol), 1.32 g of water (7.3×10^{-2} mol), 0.441 g of ammonium hydroxide (35 wt.%) (0.9×10^{-3} mol ammonia), and 0.014 g of manganese sulfate monohydrate (8.4×10^{-5} mol) were used. Manganese sulfate was also substituted for other metal salts in equivalent molarity to test the versatility of the reaction procedure. These specific amounts of pentanol, water, and ethanol are fully miscible.³¹ Note that ethanol is plausibly used to facilitate partitioning of (partially) hydrolysed tetraethyl orthosilicate (TEOS) later in the reaction. Presence of the PVP as polymeric stabilizer alone does not lead to phase separation. Phase separation is induced upon the introduction of ionic species (ammonium and manganese as cations, and citrate, sulfate, and hydroxide as anions) which are introduced in the form of ammonia (*aq.*), manganese sulphate (*aq.*), and sodium citrate (*aq.*). This leads to the formation of an inverse emulsion, in which aqueous droplets are dispersed in a pentanol rich continuous phase. The diffusion of ammonia into the droplets containing manganese (II) ions initiates the subsequent oxidation and precipitation to manganese (III/IV) oxide. Raising the pH lowers the equilibrium to oxidation which can take place in the presence of atmospheric or

*Mass calculated using densities at 20 °C, $\rho_{\text{pentanol}} = 0.814 \text{ g cm}^{-3}$, $\rho_{\text{ethanol}} = 0.789 \text{ g cm}^{-3}$, $\rho_{\text{water}} = 1.000 \text{ g cm}^{-3}$, $\rho_{\text{ammonia}} = 0.881 \text{ g cm}^{-3}$.

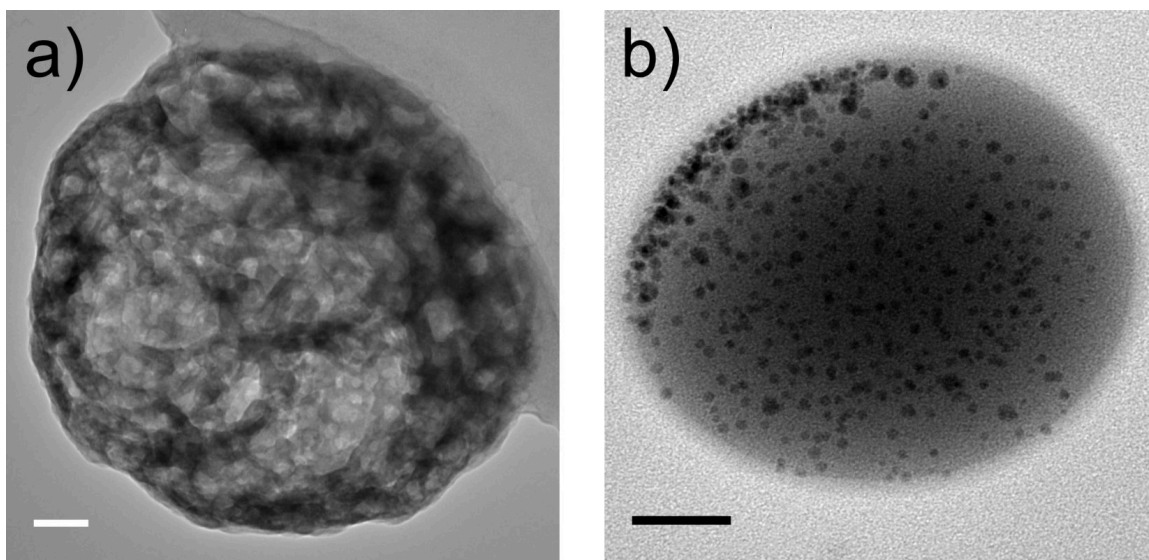


Figure 4.2. Transmission Electron Microscopy (TEM) images of metal oxide - poly(vinyl pyrrolidone) nano particulate formed from an emulsion droplet; manganese oxide (a), iron oxide (b) scale bars = 25 nm.

dissolved oxygen.³²

The TEM image in Figure 4.2 a shows the structure of manganese oxide particulate formed from the emulsion droplet constituting the ‘matchstick’ head of the particle. The result appears to be a spherical mesh of manganese oxide nanoparticles intertwined with PVP, arguably with some enrichment on the surface as a result of a combination of Pickering stabilization and nanoparticle exclusion from the polymer matrix to gain entropy (later on confirmed by FIB section image figure 4.9 d). The object appears rough and buckled at the interface and this is likely due to deformation upon drying of the nanocomposite droplet in combination with exposure to the high energy electron beam. A similar particulate was evidenced when manganese sulfate was substituted for iron chloride (Figure 4.2 b). In this case imaging was performed promptly, avoiding exposure, leaving the majority of the droplet intact and containing spherical iron oxide particles of approximately 2–5 nm in diameter.

Further analysis was performed on the manganese oxide – the catalyst of focus for the majority of this work. Following three rounds of centrifugation (4200 g) with re-dispersion in ethanol, once re-dispersing in water and then again in ethanol the manganese oxide can be

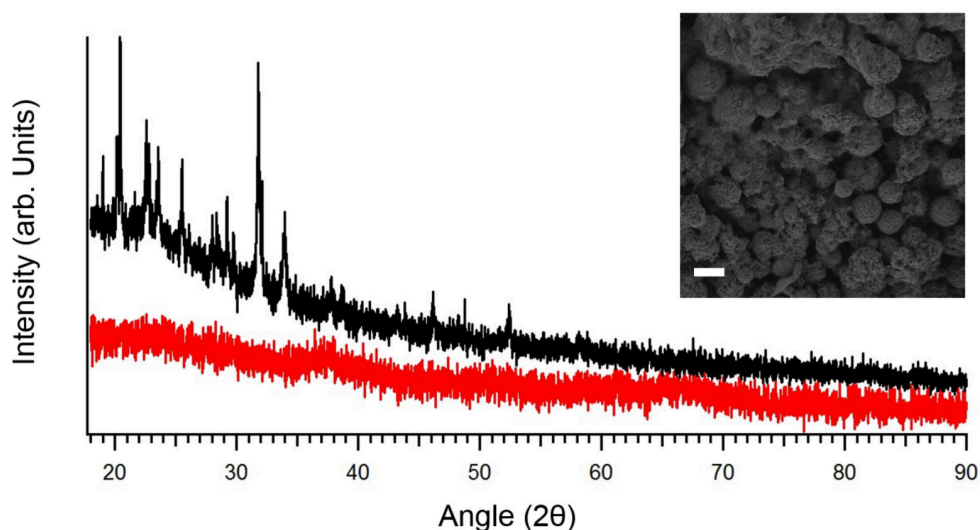


Figure 4.3. Powder x-ray diffraction (XRD) pattern of manganese oxide particulate cleaned only with ethanol (black) and washed once with water (red). Inset right is Scanning Electron Microscopy (SEM) image of manganese oxide nanoparticulate obtained after washing. Scale bar = 500 nm.

seen to exist as small, rough spherical and ellipsoidal particles with an approximate diameter of 15 nm (Figure 4.3 a). The particulate was further characterized by x-ray diffraction (Figure 4.3 b) and x-ray photoemission spectroscopy (figure A.1). The sharp peaks in intensity in the first (black) XRD pattern indicate crystalline material in the sample and are likely due to ammonium citrate or sulfate which are water soluble. The second (colour) trace shows the diffraction pattern of a sample after washing with deionized water. The absence of sharp peaks in intensity indicates amorphous material (or crystallites too small to be detected by the instrument). As it is difficult to match up this broad spectrum to a literature reference, x-ray photoemission spectroscopy (XPS) was performed which revealed mixed oxidation state manganese with the best fit to the molecular formula of Mn_3O_4 from a ratio of 0.66 Mn^{III} to 0.33 Mn^{II} (See Appendix A, figure A.2) across the Mn 2p, 3p and 3s regions.^{33,34}

4.2.1.2 Stage 2 - silica growth

The second stage of the particle synthesis resulted from the addition of 0.282 g tetraethyl orthosilicate (TEOS, 1.34×10^{-3} mol) to form the body (or stick) of the ‘matchstick’ particle. The structural growth of the particles was monitored by imaging with both TEM (Figure 4.4) and SEM (Figure 4.5). Figure 4.4 shows individual transmission electron microscopy snapshots of particles during growth i.e. with the droplet still attached to the growing particle (in the images indicated with an arrow) at $t = 30$ (A), $t = 60$ (B), $t = 90$ (C), $t = 120$ (D), $t = 180$ (E), $t = 240$ (F), $t = 360$ (G) and $t = 480$ mins (H). Figure 4.5 shows both low and high magnification scanning electron microscopy images of particles grown for specified time, t , and terminated by detaching the droplet via centrifugation and with associated lengths of $t = 30$ mins, $L = 0$ μm (A); $t = 60$ mins, $L = 0.40 \pm 0.08$ μm (B); $t = 90$ mins, $L = 0.51 \pm 0.08$ μm (C); $t = 120$ mins, $L = 0.53 \pm 0.09$ μm (D); $t = 150$ mins, $L = 0.62 \pm 0.11$ μm (E); $t = 180$ mins, $L = 0.64 \pm 0.11$ μm (F); $t = 210$ mins, $L = 0.71 \pm 0.10$ μm (G); $t = 240$ mins, $L = 0.80 \pm 0.08$ μm (H); $t = 300$ mins, $L = 0.87 \pm 0.10$ μm (I); $t = 360$ mins, $L = 0.96 \pm 0.12$ μm (J); $t = 420$ mins, $L = 1.08 \pm 0.11$ μm (K); and $t = 480$ mins, $L = 1.17 \pm 0.12$ μm (L). Both techniques were deployed as SEM allowed for significant statistics on the particle growth to be gathered whilst TEM allowed for imaging to be performed without washing cycles as the excess PVP that forms a layer over the sample upon drying has relatively low opacity to the transmitted electron beam (a strategy previously shown by van Blaaderen *et al.*)¹²

Similar to these previous works we found that a secondary lobe structure appeared to have survived the high vacuum environment and beam power of the TEM. It is likely that this structure consists mainly of PVP, ionic salts and a small amount of water. We suggest the presence of this secondary lobe formed after thirty minutes of reaction time is down to phase separation of the water and PVP from the solid silica-manganese oxide sphere (see Figure 4.4 A). The formation of silica inside the original droplet will lead to the expulsion of the water phase, which logically follows the preservation of volume. The reason why this now excess water phase appears as a distinct droplet is a direct result of dewetting (a hypothetical thin film of water as a shell on the outside of the manganese oxide – silica colloid with the pentanol phase on the other side, is unstable). In addition it

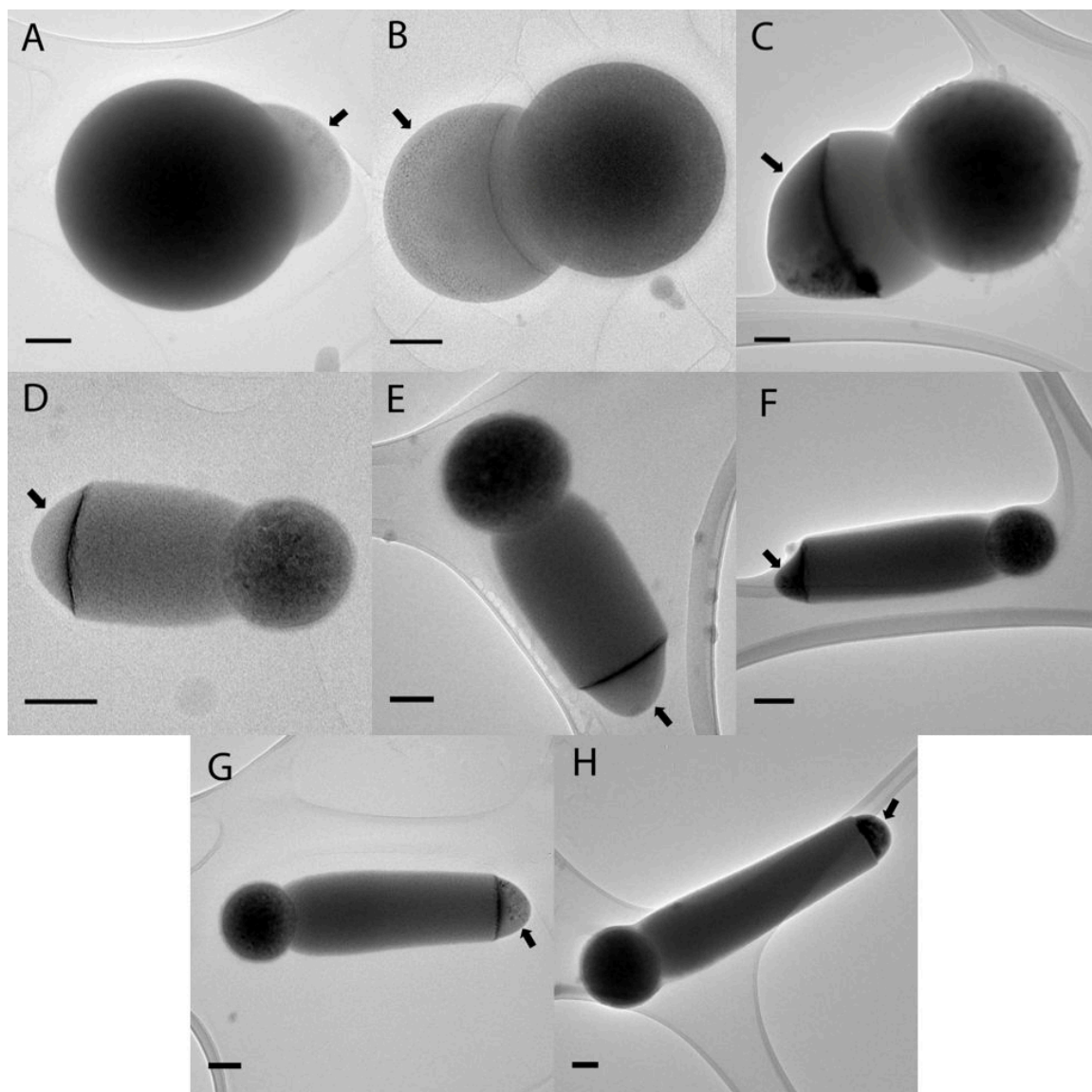


Figure 4.4. A series of Transmission Electron Microscope (TEM) images taken at 30 (A), 60 (B), 90 (C), 120 (D), 180 (E), 240 (F), 360 (G) and 480 mins (H) during the synthesis of silica-manganese oxide ‘matchstick’ particles . A manganese oxide enriched head is produced first (which gives a darker appearance), after which expulsion of the aqueous phase (indicated on the TEM image by arrows) induced by silica formation and continuous influx of reactants leads to the formation and growth of the silica tail. All scale bars = 100 nm.

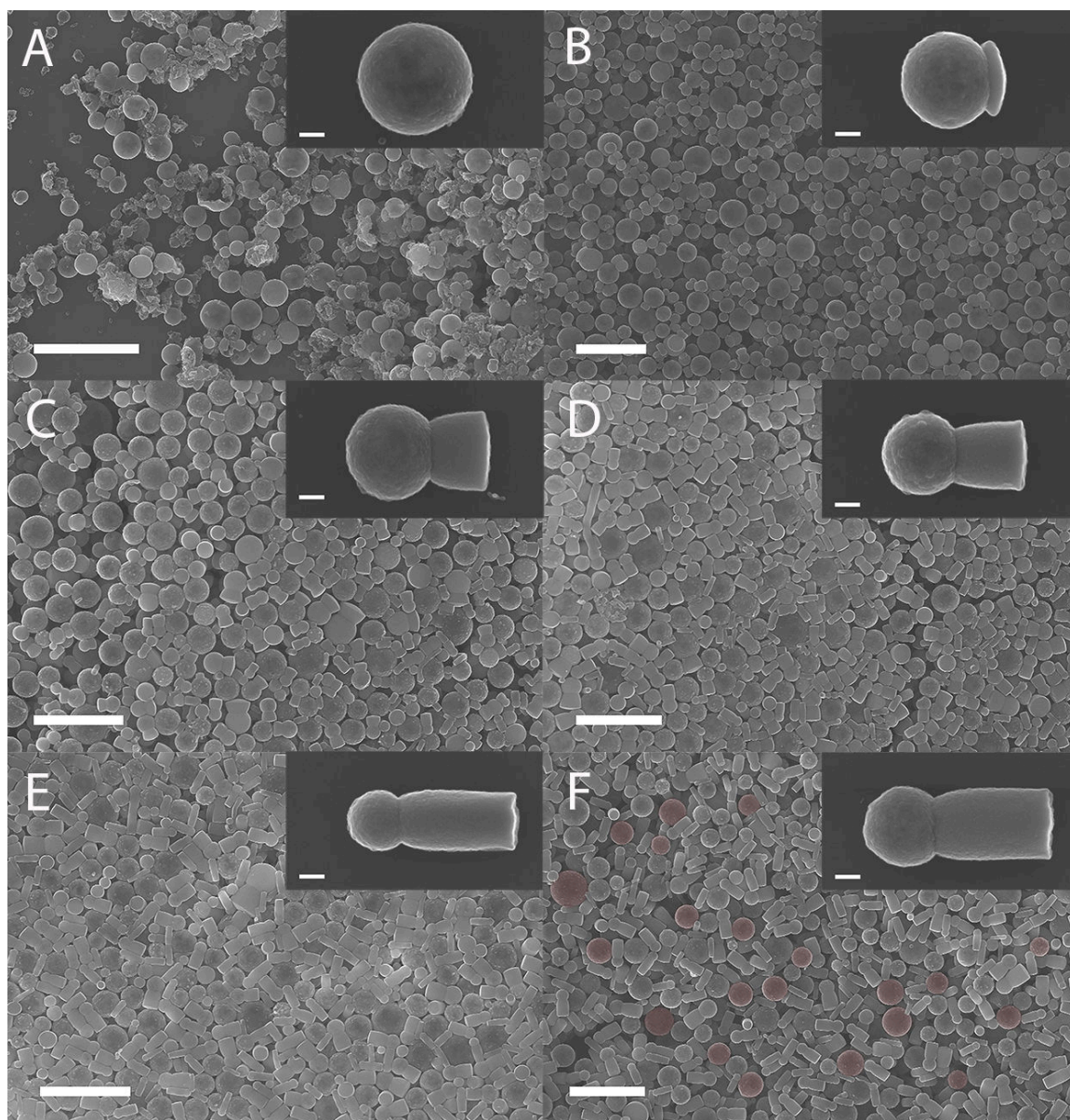


Figure 4.5. Scanning Electron Microscope (SEM) images of silica-manganese oxide ‘matchstick’ particles following growth after 30 (A), 60 (B), 90 (C), 120 (D), 150 (E), 180 min (F) (scale bars = $2\text{ }\mu\text{m}$) with insets of High Resolution SEM images of single particles (scale bars = 100 nm). Rough spherical particles are also produced, a portion of which are highlighted by false-coloring (red) in F. Figure continued overleaf.

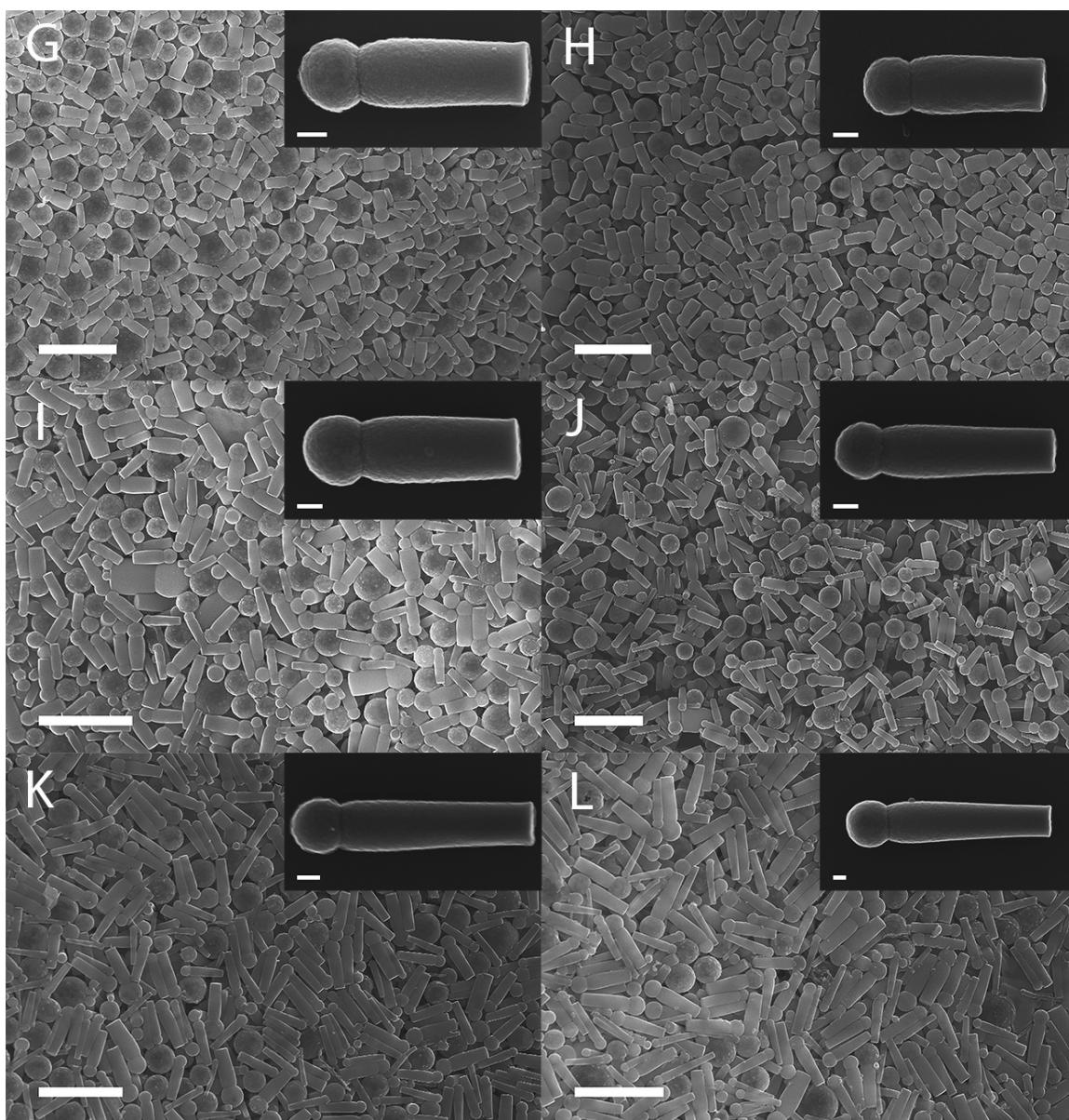


Figure 4.6. Scanning Electron Microscope (SEM) images of silica-manganese oxide ‘matchstick’ particles following growth after 210 (G), 240 (H), 300 (I), 360 (J), 420 (K), 480 min (L) (scale bars = 2 μm) with insets of High Resolution SEM images of single particles (scale bars = 100 nm).

is plausible that entry of hydrolysed TEOS into the porous sphere leads to an increase in local osmotic pressure initiating an influx of additional water, balancing the total volume of the water phase. The influx must occur as water is consumed in the production of silica. There is a substantial ‘reservoir’ of water in the pentanol phase³¹ that is tapped into during the reaction.

After 60 mins, the initial formation of the silica tail is evident (see Figure 2.3 B). The dark rim observed at the tail edge of the particle is most likely due to the precipitation of the remaining manganese species (salts or oxide nanoparticulate) upon partial drying of the sample on the carbon support film. The fact that the small particulate must be mobile in this secondary lobe and can migrate to the solid interface of the particle is in itself evidence for a liquid-like structure. Following this phase separation step the barrier to successful entry of (hydrolysed) TEOS is reduced as there now exists a secondary ‘soft’ lobe, which simply contains a larger concentration of water. We suggest that the majority of (hydrolysed) TEOS molecules are formed and enter the colloidal object here (the water drop attached to the ‘matchstick’), and subsequently condense and precipitate onto the existing silica surface. One question we can ask in support of the above is: how far would particle growth proceed using only the water present in an attached spherical droplet (Figure 4.4 B, time = 60 min)? If we assume that exactly two molecules of water are consumed to every unit of silica produced, the droplet has a diameter of 350 nm (Figure 4.4 B) and for simplicity is purely water (therefore an over estimation) then we can do a rough geometrical calculation for the resultant additional silica rod length. We can equate the length of the silica rod formed to the volume of water in the droplet over the area of silica produced:

$$L = \frac{\frac{\pi}{6}d^3\rho_w M_{rs}}{2M_{rw}\rho_s \frac{\pi}{4}d^2} \quad (4.1)$$

Where d is the particle diameter, ρ is the density and M_r is the molecular weight which are denoted by w for water and s for silica (we used values of $\rho_w = 1.00 \text{ g cm}^{-3}$ and $\rho_w = 2.20 \text{ g cm}^{-3}$). This can be simplified to:

$$L = \frac{d\rho_w M_{rs}}{3\rho_s M_{rw}} \quad (4.2)$$

This gives a total length of 116.67 nm which we can clearly see is far exceeded, as tails of the matchsticks can easily be made up to a few microns in length. It should be noted however that the silica structure is not densely packed and more likely a porous network, a factor not taken into account in this calculation. Nevertheless, a correction for the resulting lower density would still not account for the total amount of water required to produce the ‘matchstick’ colloids of the observed length. The porosity of these silica rods in a similar system was evidenced by Kuijk et al.¹² where they associated the cause with PVP. We suggest that porosity can also be attributed to by the presence of sodium citrate, known to induce porous silica and titanate particle formation.^{35,36} In these two studies it was suggested that the porosity was induced either by the prior formation of nano-sized ammonium citrate crystals or by the H-bonding interactions of an amorphous network of citric acid with the surrounding polymeric silica. The presence of sodium citrate in our reactions, is vital in producing rod-like structures. Reactions carried out in absence of sodium citrate produce spheres and not ‘matchstick’ rods. The generation of porous silica allows for continuous diffusion of reactants into the spherical head of the ‘matchstick’ particle, formed early on in the reaction, and subsequent volume displacement of internal liquid to drive the lobe formation.

A series of snapshots representative of a majority of growing particles in the system were collected using SEM (Figure 4.5). Sample preparation here involved cleaning by centrifugation and re-dispersion in ethanol to remove the large quantities of pentanol and PVP. Removal of PVP is necessary as it otherwise forms a thick film over the particles upon drying, making imaging difficult. We would like to first address that from Figure 4.5 it is apparent that there are also spherical particles present throughout the reaction, often larger in diameter than the ‘matchstick’-shaped particles (a portion are indicated in red in figure 4.5). We suggest these are formed from larger droplets which, having a larger volume relative to thier surface area, have a higher potential for the interface to be occuppied by particles that migrate there from within the droplet. Since the manganese oxide particulate partly sits at the interface of the droplet and can act as nucleation sites for silica to condense onto, a higher oxide content can lead to a denser, impenetrable shell that makes it more difficult for water and other species to enter. To test this hypothesis we synthesized a batch

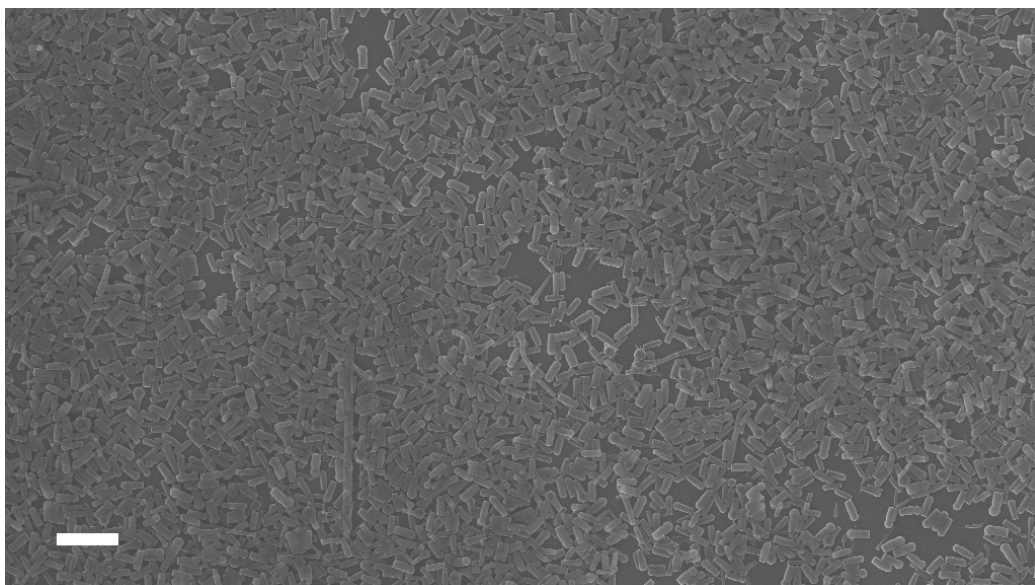


Figure 4.7. Scanning Electron Microscopy (SEM) image of ‘matchstick’ particles synthesized using a 0.05 M solution of manganese (ii) sulfate. Scale bar = 2 μm .

of particles using a lower initial concentration of manganese (II) sulfate (See Figure 4.7). Here the probability of forming a manganese oxide particulate shell is lower and a product of this is that we have fewer spherical particles present. A narrower particle dispersity is evident likely because the electric double layer of droplets is less suppressed at lower ionic strength and thus stability to coalescence is higher. The disadvantage of using a lower manganese content is that we have a lower theoretical yield of manganese oxide catalyst in the head of the particle, undesirable for its propensity to self-propel. The concentration of manganese (ii) sulfate utilized in our ‘matchstick’ synthesis was maximized whilst still considering reasonable particle dispersity.

It is apparent from Figure 4.5 that there is a fairly wide dispersity in particle diameter throughout the reaction. If desired, the ‘matchstick’ colloids can be fractionated through centrifugation, but this lay outside the scope of this work. The purpose of this study was to collect all particle sizes in order to get a total representation of the system.

The evolution of particle length with time is clear from Figure 4.5 and occurs in apparent linear fashion (Figure 4.8) over the time scale studied. Towards the latter images it can be seen that there is a slight taper to the particle. One might assume that this

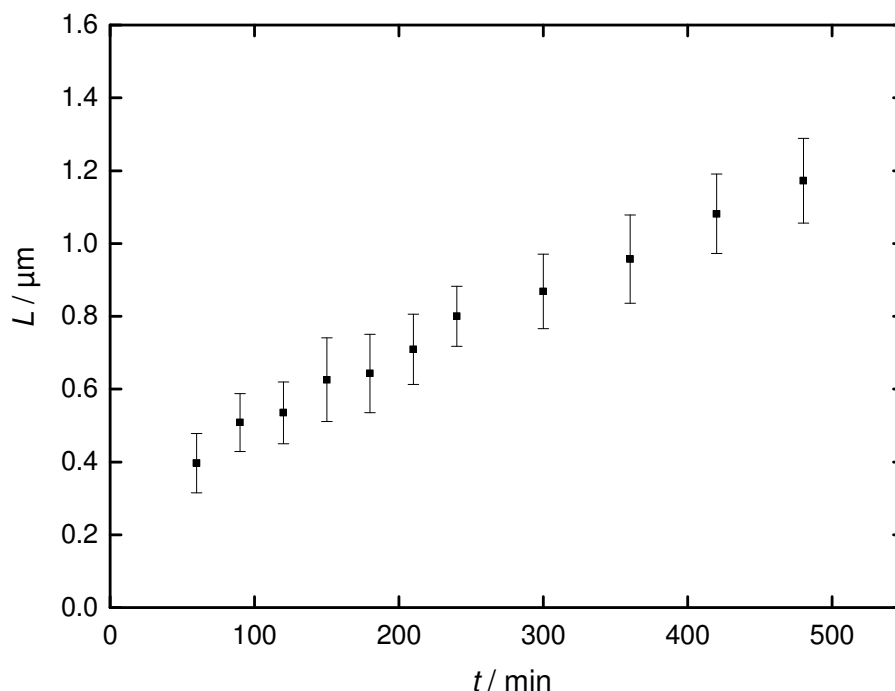


Figure 4.8. Particle growth in length over time measured by image analysis of multiple Scanning Electron Microscope (SEM) images. Error bars represent the standard deviation, σ .

is due to the loss of water in the droplet through evaporation or consumption during the reaction. Notably a recent study showed that this effect could in fact be exploited by timed addition of ethanol to modify the particle morphology.³⁷ In our case however we consider that growth is not unidirectional and also occurs in diameter, though at a much reduced rate. This can explain the tapering as, by the end of reaction, the particle will have grown more in diameter closer to the nucleus than at its extremity. It would be interesting to determine whether this growth also has a linear dependence on time and TEOS conversion. Unfortunately though it becomes difficult to study the system as a whole due to the issue of dispersity and little significance can be taken from the result.

4.2.1.3 Further compositional characterization of ‘matchstick’ particles

After 24 hours of reaction time we can see a significant taper to the particle (Figure 4.9 a,b), note though that these particles were produced in a separate reaction and the extent

of tapering is dependent on the ratio between the growth rates in the two directions. Using TEM, if we magnify the head of the particle (Figure 4.9 c), we can see a thin layer (~ 10 nm) of silica material surrounding a denser core bringing further justification to the idea of multidirectional growth. The internal structure of the particle was also examined by slicing a thin section of a single particle using FIB-SEM and mounting this on a grid for analysis with TEM (Figure 4.9 d). Here again we observed a thin silica layer around the head of the particle. It is advised however that there is also a white coating around the entire particle due to a deposited layer of carbon which reduced surface damage to the particle by the focused ion beam.

These findings evoke consideration of previous studies that claimed chemical anisotropy could be introduced via a seeding method.^{10,38} These studies are based on the same rod-like synthesis with an additional step involving a mono-substituted silane agent to form amphiphilic structures that self-assemble in varying solvent conditions. We suggest that on the surface these particles are not truly chemically anisotropic and take advantage of the long-range van der Waals and hydrophobic interactions to drive self-assembly i.e. there is a certain penetration depth to the interaction.

A total element map of several isolated particles was constructed using ADF-STEM (Figure 4.10) and an EDX detector to determine the location of manganese oxide. The element maps show that there is indeed a significant enrichment of manganese in the head of the ‘matchstick’ particle along with carbon. The carbon signal is thought to be from PVP and citrate wrapped around the manganese oxide and incorporated into the head. The apparent enrichment along the left hand side of the particle (shadow artefact) can be attributed to absorption of low energy X-rays by the particle itself. In this experiment the detector was positioned on the left relative to the particle so signals for lower atomic number elements, e.g. carbon, are affected as such. The total elemental composition in wt.% of the sum spectra in the map was as follows: carbon = 12, oxygen = 49, silicon = 38, manganese = 1. It should be noted that these are not fully quantitative results and are relative only to what is contained in the sample. More detail of the manganese oxide structure can be seen from element maps of a close-up of only the head of the particle (figure 4.10 b).

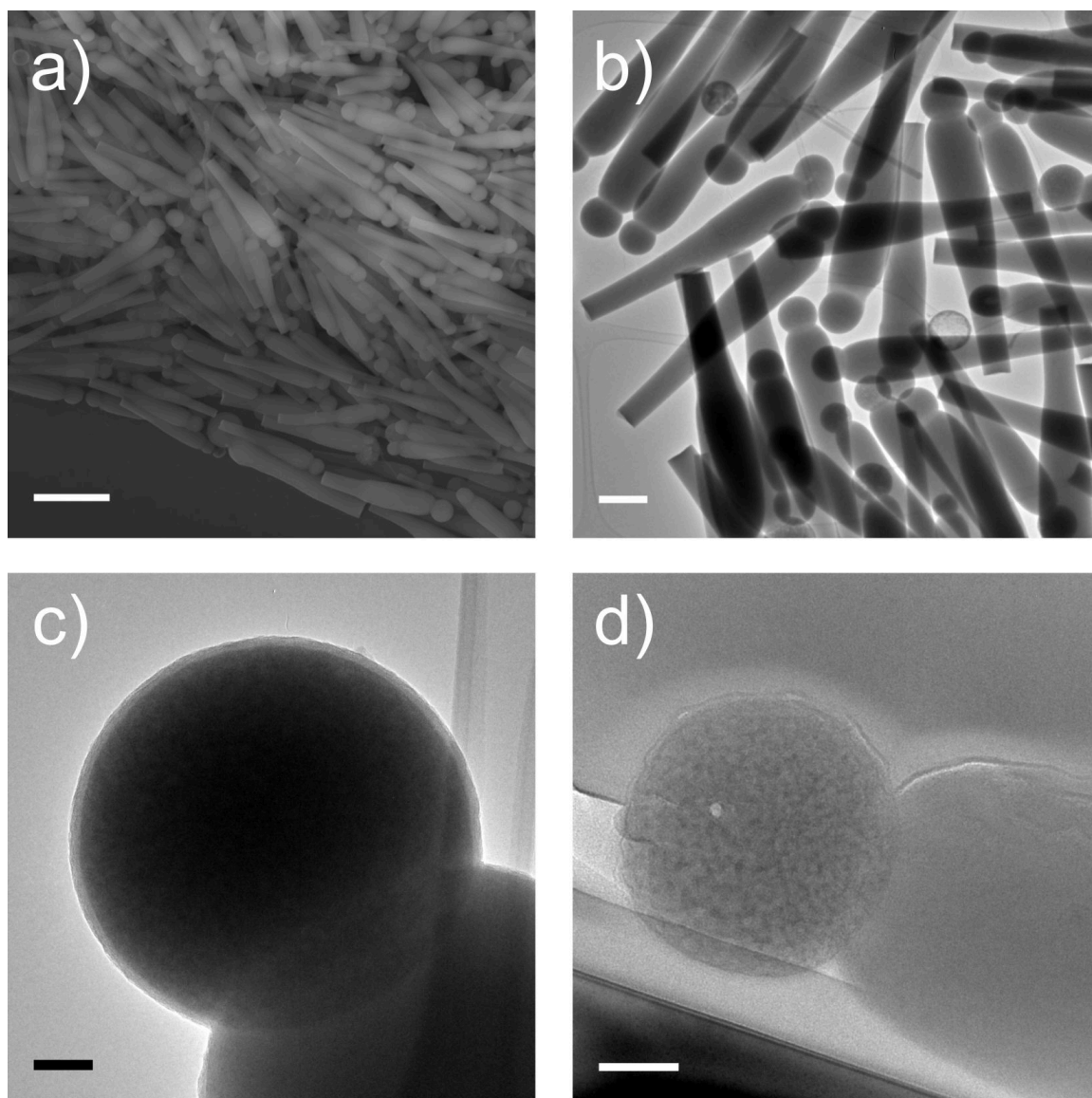


Figure 4.9. Scanning Electron Microscopy (SEM) (a) and Transmission Electron Microscopy (TEM) (b) images of particles formed after reacting for 24 hrs. High magnification Transmission Electron Microscopy (TEM) image of ‘matchstick’ particle head of particle formed after reacting for 24 hrs (c) and of a focused ion beam (FIB) section of the particle (d). Scale bars = 2000 nm, 500 nm, 50 nm and 100 nm for a), b), c) and d) respectively.

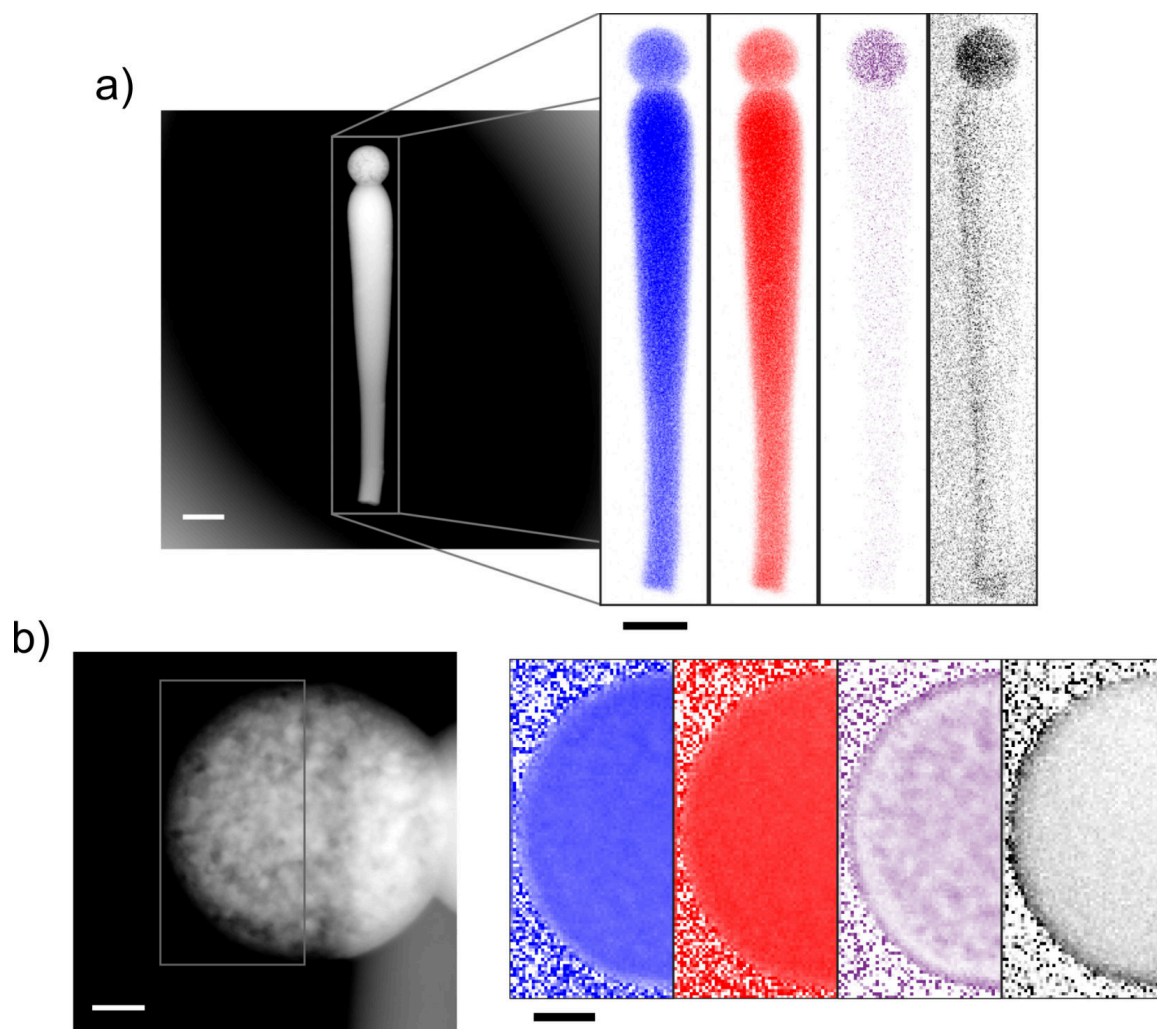


Figure 4.10. Annular Dark Field-Scanning Transmission Electron Microscopy (ADF STEM) image of a single particle (a, left) and a ‘matchstick’ head (b, left). Element maps of selected regions (right) for silicon (blue), oxygen (red), manganese (purple) and carbon (black). Scale bars (a) = 500 nm, (b) = 100 nm.

4.2.1.4 Synthesis with different metal oxides

Finally we show that we can apply the concept of particle formation, utilizing different metal oxides and result in similar morphologies (Figure 4.11). Again we can see a defined head region of different density to the rest of the particle. Interestingly, with iron oxide and specifically larger particle heads, there are cases with multiple rod growths from the same nucleus. This is perhaps due to a difference in surface charge³⁹ and composition and therefore a different droplet wetting than with manganese oxide. We postulate that the slightly lower surface charge of iron oxide promotes dewetting and can therefore encourage the formation of multiple lobes upon volume displacement from the spherical core. Another possible explanation was discerned upon examination of the iron oxide formed prior to TEOS addition (see Figure 4.2) we can see the particulate is larger and less uniform than in the case of manganese oxide. This will mean that packing at the surface of the droplet will be less efficient and may provide several ‘holes’ for volumetric outburst of internal liquid during the early stages of the reaction. There are only 2, 3 or 4 protrusions evident and we might then expect there to be more rods growing from the central nucleus but the droplets forced out can diffuse around the surface of the spherical particle and fuse to minimize interfacial energy. This also gives an explanation to why these protrusion are often on opposing sides of the nucleus i.e. droplets have a limited distance of which they can diffuse over the surface and those on opposite sides never meet. We can also further rationalise the presence of spheres as a by-product in the case of manganese oxide, as previously discussed. The manganese oxide particulate is relatively uniform in shape and size, thus surface coverage of the droplet is uniform hindering the transport of fluids. Interestingly the multiple rod protrusions on particles proceed to the same final length which gives further evidence for an asymmetric delivery of reaction species.

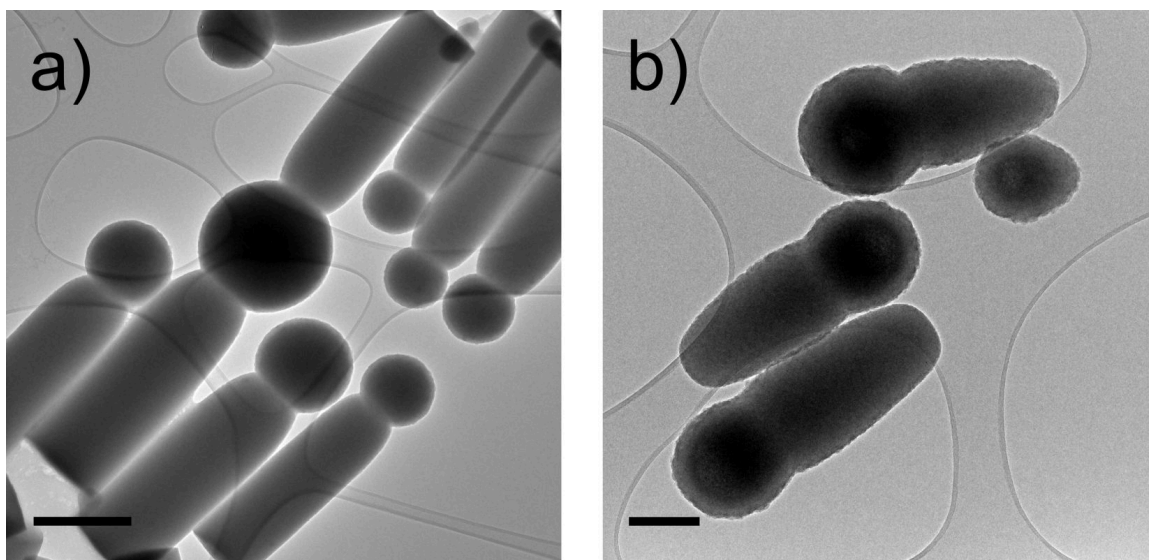


Figure 4.11. Transmission Electron Microscopy (TEM) images of iron (a) and zinc (b) oxide ‘matchstick’ particles. Scale bars = $0.5\ \mu\text{m}$ (a) and $0.2\ \mu\text{m}$ (b) respectively.

4.2.2 Dynamics of manganese oxide containing ‘matchstick’ particles – propulsion studies

Initially we elected to test the manganese oxide nanoparticles produced from stage 1 of the ‘matchstick’ particle synthesis (Section 4.2.1.1) for their catalytic activity. Manganese oxide powder was isolated by washing several times in ethanol and water and was subsequently dried for further use. A small amount ($< 1\ \text{mg}$) of manganese oxide powder was dispersed in 10 vol.% H_2O_2 and instantaneous bubble production was observed. An aliquot was taken for microscopic observation to reveal agglomerates of manganese oxide particles propelling rapidly ($v = 30\text{--}170\ \mu\text{m s}^{-1}$) in solution via bubble propulsion (figure 4.12, Supporting Video SV3 Appendix B.3). This initial study gave us confidence that the manganese oxide produced from our synthesis is sufficiently active to act as the catalytic engine for a micro motor.

Subsequently the next avenue to investigate was the motion of silica-manganese oxide ‘matchstick’ particles both without any fuel present (see Supporting Video SV4 Appendix B.4) and in the presence of hydrogen peroxide. To begin, the Brownian motion of ‘matchstick’ colloids (i.e. no fuel present) was studied utilizing a similar 2D particle track-

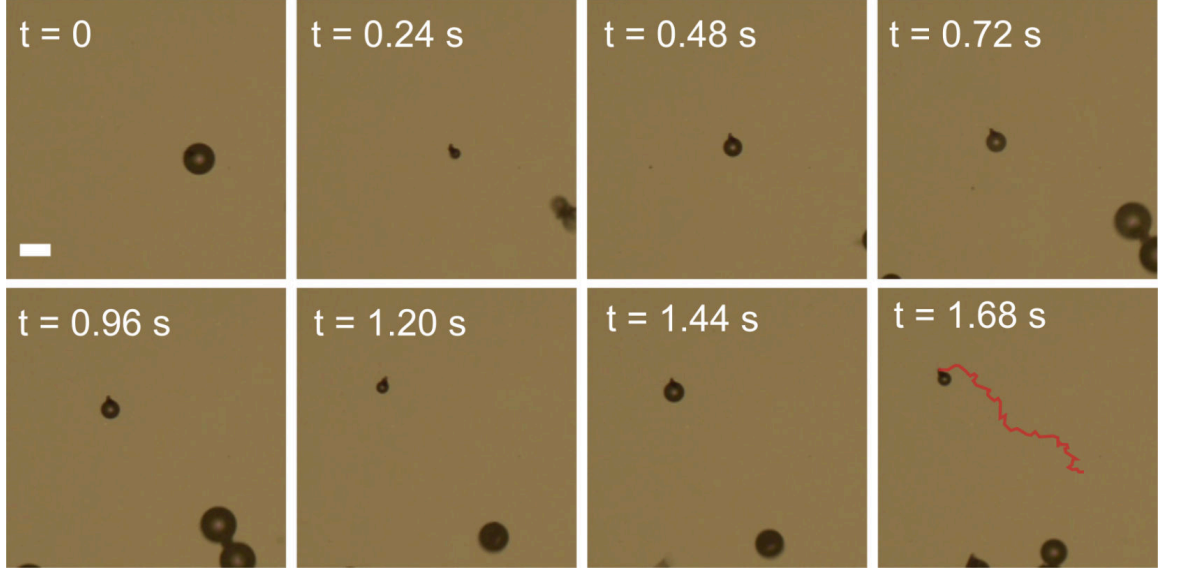


Figure 4.12. Time frames from a video recorded at 25 fps of a manganese oxide nanoparticle cluster upon exposure to 10 vol.% H_2O_2 exhibiting bubble propulsion. Scale bar = 15 μm .

ing protocol to previous work (chapter 3). Here the microscopic projection of ‘matchsticks’ were treated as gaussian blobs and a large diameter equivalent to the length (largest particle dimension) was selected for particle localization (See Experimental 4.4.4).

The matchstick geometry is relatively complex and so far as the author is aware there no known theoretical solutions for the diffusion coefficient of such an object. Considering the matchstick geometry is axisymmetric and approximately comparable to a rod, a theoretical description can be approached using an analytical solution for hard cylinders⁴⁰ – used previously to compare to experimental particle tracking of rod-shaped silica colloids,⁴¹

$$D_t = \frac{2}{3}D_{\perp} + \frac{1}{3}D_{\parallel} \quad (4.3)$$

$$D_{\perp} = \frac{k_B T}{4\pi\eta l} (\log l/d + \delta_{\perp}) \quad (4.4)$$

$$D_{\parallel} = \frac{k_B T}{2\pi\eta l} (\log l/d + \delta_{\parallel}) \quad (4.5)$$

$$D_R = \frac{3k_B T}{\pi\eta l^3} (\log l/d + \delta_R) \quad (4.6)$$

where l represents length, d is the diameter and thus l/d is the aspect ratio of the particle. δ is an ‘end-effect’ correction term for the finite aspect ratio of cylinders given as⁴²:

$$\delta_{\perp} = 0.839 + 0.185/(l/d) + 0.233/(l/d)^2, \quad (4.7)$$

$$\delta_{\parallel} = -0.207 + 0.980/(l/d) - 0.133/(l/d)^2. \quad (4.8)$$

$$\delta_{\text{R}} = -0.662 + 0.917/(l/d) - 0.050/(l/d)^2. \quad (4.9)$$

The ‘matchstick’ particles under study here were measured to have average dimensions of $l = 4.11 \mu\text{m}$, $d = 0.62 \mu\text{m}$ ($l/d = 6.63$) for the high aspect ratio sample and $l = 1.19 \mu\text{m}$, $d = 1.72 \mu\text{m}$ ($l/d = 1.72$) for low aspect ratio particles. Using these dimensions and the above equations (equation (4.3)) theoretical diffusion coefficients for each aspect ratio were obtained: $D_t = 0.274 \mu\text{m}^2 \text{s}^{-1}$ for high aspect ratio and $D_t = 0.462 \mu\text{m}^2 \text{s}^{-1}$ for low aspect ratio.

Initially the propulsion behaviour of different aspect ratio ‘matchsticks’ was the focus of this chapter spurred by previous research in the group.³⁰ Of course first it was imperative that the motion of these ‘matchstick’ colloids were examined when no fuel was present, both as a control experiment and also for interest in their Brownian motion. The diffusion coefficients for the two different aspect ratio ‘matchsticks’ were determined by performing 2D particle tracking experiments and calculating the ensemble averaged mean-squared-displacements (figure 4.13) with subsequent linear fitting, as performed previously (chapter 2). The high aspect ratio ‘matchsticks’ had a measured diffusion coefficient, $D = 0.236 \pm 0.075 \mu\text{m}^2 \text{s}^{-1}$, 86% of the theoretical diffusion coefficient calculated above for an equivalent hard cylinder. The difference here is not significant but one should not hasten to draw conclusions by direct comparison to this model. Reasons for the apparent lower D are threefold: 1. geometry difference to a simple cylinder, 2. non-density matched system and 3. particles are tracked near a glass boundary once sedimentation has occurred (known to reduce D ⁴³, chapter 2). Similarly for the short ‘matchsticks’ a diffusion coefficient of $D = 0.377 \pm 0.09 \mu\text{m}^2 \text{s}^{-1}$ was extracted, 82% of the theoretical value. It is interesting that these matchsticks can be modelled relatively well with hard cylinders and this further gives us

confidence in the accuracy of our results. Both colloids exhibit purely Brownian behaviour which is further highlighted by a rapid decorrelation (0.04 s) in the velocity autocorrelation (figure 4.13 right).

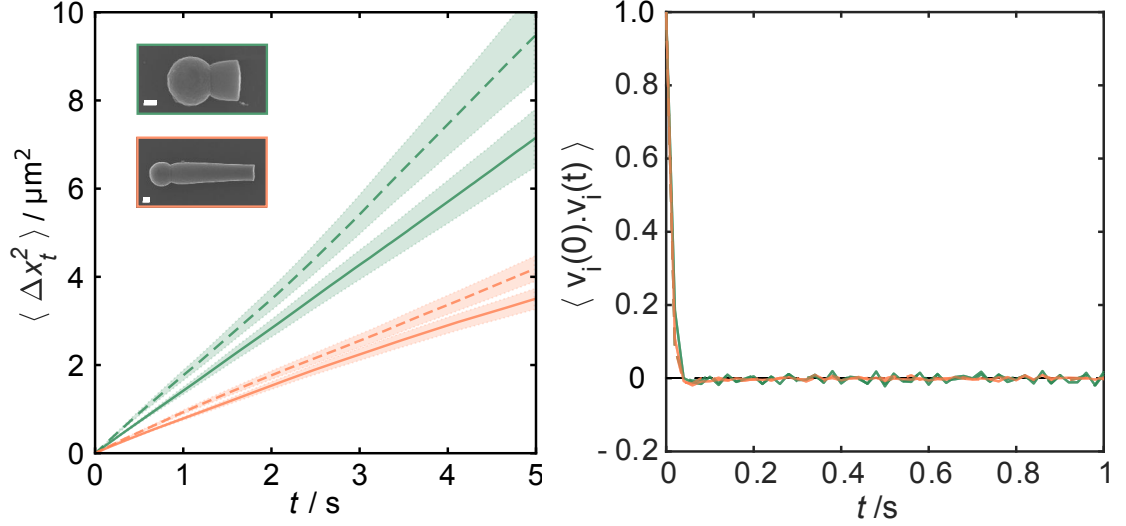


Figure 4.13. Average mean-squared-displacement, $\langle \Delta x_t^2 \rangle$, graphs (left) at given delay time, t for short [$l = 1.19 \mu\text{m}$, $d = 0.81 \mu\text{m}$] (green) and long [$l = 4.11 \mu\text{m}$, $d = 0.62 \mu\text{m}$] (orange) matchsticks at no fuel (solid lines) and with 5 vol.% H_2O_2 present (dashed). Inset Scanning Electron Microscopy (SEM) images display the typical ‘matchstick’ aspect ratios investigated. Scale bars = 100 nm. Shaded colour regions show the standard error for each ensemble average, σ/\sqrt{N} . Normalized velocity autocorrelation for the same data series is displayed on the right.

Previously, the findings by Morgan *et al.* indicated that these manganese-oxide containing silica ‘matchsticks’ exhibited enhanced motion in the presence of hydrogen peroxide and was attributed to a self-diffusiophoretic propulsion mechanism. A propulsive velocity was not recorded in this work however the authors disclosed an enhanced diffusion coefficient that increased linearly with hydrogen peroxide concentration, the magnitude of which varied from $2.74 - 4.52 \mu\text{m}^2 \text{s}^{-1}$ with an addition of 0.8 vol.% H_2O_2 .

The experimental 2D particle tracking data (figure 4.13) in this chapter reveals only a small increase in the diffusional behaviour with the introduction of a large quantity (5 vol.%) H_2O_2 (dashed lines). Clearly there is no propulsive (parabolic) component to the MSD when fuel is added which should be the case for an asymmetric diffusiophoretic mechanism.⁴⁴

Caveats to this rule have been observed before where small colloids with asymmetric surface activity that are said to exhibit self-phoresis of some sort propel with a velocity that is masked by the rapid rotational diffusion of the particle.^{45–47} By this it is meant that the particle rotates on a time scale that is shorter than its propulsive velocity and thus direction is randomized and only a linear response in the MSD is observed. Indeed we do find linearity in our MSD data with an increased slope, $D = 0.279 \pm 0.09 \mu\text{m}^2 \text{s}^{-1}$ for high aspect ratio and $D = 0.487 \pm 0.15 \mu\text{m}^2 \text{s}^{-1}$ for low, suggestive of this type of ‘enhanced’ Brownian motion. For this to be the case for our high aspect ratio ($l/d = 6.63$) matchsticks a predicted rotational diffusion coefficient, $D_{\text{R}} = 0.089 \text{ s}^{-1}$ (from equation (4.6)) thus characteristic inverse rotational time, $\tau_{\text{R}} = 11.24 \text{ s}$ suggests a very sluggish propulsive velocity. In fact this could be the case as looking closely at the previous TEM characterization (figure 4.9 c) there is an apparent thin, $\sim 10 \text{ nm}$, layer of silica (as discussed earlier in Section 4.2.1.3). Notably during imaging there was no accumulation of oxygen bubbles in the imaging chamber which has typically been found for PS-Pt micromotors. With these considerations and knowing that free, uncoated manganese oxide produced in this synthesis exhibits bubble propulsion in H_2O_2 , it can be concluded that the silica layer almost completely inhibits catalytic activity.

The lower aspect ratio ($l/d = 1.72$) ‘matchsticks’ have a much faster predicted rotational diffusion, $D_{\text{R}} = 0.848 \text{ s}^{-1}$ and $\tau_{\text{R}} = 1.18 \text{ s}$ making non-Brownian behaviour more difficult. However these particles are selected by terminating the synthesis early on and so the silica layer may not have had enough time to grow around the head of the matchstick. We consider this assuming our suggestion of multiple direction of growth holds which has been recently independently verified by post etching experiments revealing the mid-section of the particle etches more rapidly than the head.⁴⁸ When H_2O_2 was introduced to the low aspect ratio ‘matchsticks’ the increase in diffusion was more than for their high aspect ratio brethren (29% vs. 18%). This suggest that the catalyst may well be more accessible for the shorter ‘matchsticks’. All in all though the engine power is not enough for the particle to out swim its Brownian rotation and thus we have a compromise between increasing the accessibility of the catalyst and the rotation time of the colloid.

Linear fitting of the log-log MSD over the full time period ($t = 30 \text{ s}$) for each scenario

(as performed in chapter 2) again yields all α close to 1 showing purely diffusive motion throughout. In the cases where hydrogen peroxide was absent (solid lines) a slightly lower $\alpha \sim 0.87$ was found suggesting a slightly hindered motion. This is a result of the close proximity of ‘matchstick’ particles to the underlying glass substrate restricting the full (3-D) degrees of freedom. The increase in α upon introduction of H_2O_2 provides evidence of some kind of driven system though for typical anomalous (superdiffusive) diffusion this is usually on the order of $\alpha = 1.5$ ⁴⁹ and $\alpha = 2$ for propulsion which we did not find across the measured time period in our experiments (figure 4.14). Considering we have an asymmetric catalytic reaction the logical explanation for this is simply that the reaction is not fast enough to continuously establish the concentration gradient necessary to induce propulsion on a time scale less than the rotation of the colloid.

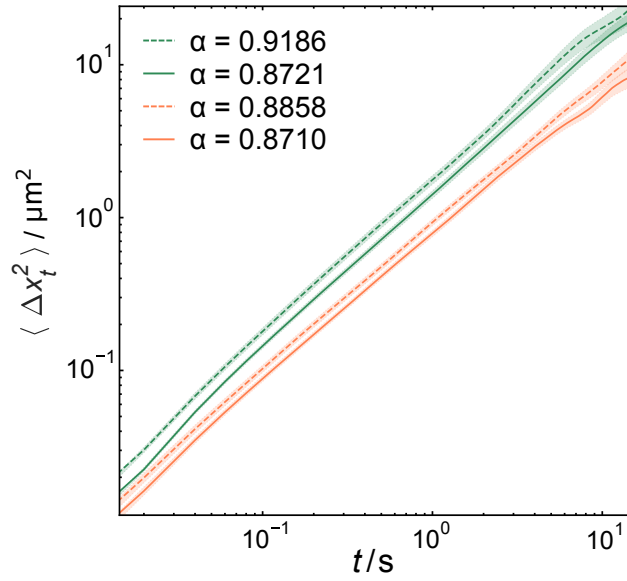


Figure 4.14. log-log average mean-squared-displacement, $\langle \Delta x_t^2 \rangle$, plots at given delay time, t for short [$l = 1.19 \mu\text{m}$, $d = 0.81 \mu\text{m}$] (green) and long [$l = 4.11 \mu\text{m}$, $d = 0.62 \mu\text{m}$] (orange) ‘matchsticks’ at no fuel (solid lines) and with 5 vol.% H_2O_2 present (dashed). Shaded colour regions show the standard error for each ensemble average, σ/\sqrt{N} .

Results here put to question the previous findings of Morgan *et al.* especially considering the measured diffusion coefficient was an order of magnitude higher than those mea-

sured here. The ‘matchsticks’ in the previous study had dimensions significantly smaller ($L = 1.7\text{ }\mu\text{m}$, $d = 0.2\text{ }\mu\text{m}$) than here and so one would expect higher diffusion coefficients, however the measured values are still significantly larger even in the Brownian case than we would expect if we consider the solution to Equation 4.3 $= 0.69\text{ }\mu\text{m}^2\text{ s}^{-1}$. Therefore we suggest that particles may have been erroneously tracked perhaps due to mistaking them for smaller spherical by-products of the synthesis or a higher than recorded temperature in the imaging chamber. Both are plausible considering the use of the Nanosight imaging system where direct imaging of particles is not possible and the laser causes the sample chamber to heat up.

4.3 Conclusion

An effective strategy for the fabrication of chemically anisotropic metal-oxide / silica ‘matchstick’ particles was presented in this chapter. The incorporation of iron oxide is particularly interesting as it may allow for motional manipulation of the particles in both a chemical and magnetic field. The ability to select the aspect ratio of the ‘matchstick’ particle by appropriate reaction termination opens up the possibility of studying the affect of aspect ratio of the motion of active colloids. Unfortunately the engine power of the incorporated manganese oxide is not significant enough to propel the colloid faster than its Brownian rotation. Considering that the difference between two fairly extreme cases of aspect ratio presented here is only minor we can expect that with the in-between cases we would not see statistical significance ($> 10\%$).

In order to extend the current work and carry out the aspect ratio vs. swimming efficiency study the issue of catalyst accessibility must be resolved. A recent study has shown that similar ‘matchstick’ shaped colloids with catalytic iron oxide heads can self-propel if the particles are first etched with sodium hydroxide to remove the silica layer around the head of the particle.⁵⁰ In our case attempting a similar protocol did not yield ‘matchsticks’ that could self-propel in the presence of hydrogen peroxide. The difference here is that manganese oxide nanoparticles were generated *in-situ* during synthesis and it is likely that each particle becomes fully encapsulated by silica during ‘matchstick’ growth. It

is therefore difficult to fully expose the catalytic surface by post etching without dissolving most of the ‘matchstick’ body.

In conclusion the silica-based ‘matchstick’ particles presented in this chapter are certainly an interesting anisotropic colloid that can be modelled relatively well by hard cylinders and show some enhanced diffusion in the presence of hydrogen peroxide. For short time scale collective behaviour experiments, whereby out of equilibrium physics is observed within seconds, these colloids are not suitable due to their sluggish propulsion speeds. However at longer time scales (min – hrs) some interesting behaviour may yet be investigated.

4.4 Experimental

4.4.1 Synthesis of silica-metal oxide ‘matchstick’ particles

The procedure deployed was a modified version of that outlined by Morgan *et al.*³⁰ Initially stock solutions of PVP-K30 (100 g L⁻¹) in 1-pentanol, aqueous sodium citrate (0.18 M) and aqueous metal salts (0.10 M) were made up. PVP-K30 was dissolved in 1-pentanol by brief sonication 30 minutes and further stirring overnight. Following this sodium citrate (0.20 ml, *aq.*), metal salt (0.84 ml, *aq.*), ethanol (3.00 ml) and PVP-K30 in pentanol (30.00 ml) were added by syringe to a 50 ml Eppendorf centrifuge tube. This mixture was shaken vigorously by hand for approximately 30 seconds to generate an emulsion with an opaque, white appearance. After this, ammonia (0.5 ml) was added resulting in a colour change characteristic of each metal oxide formed (dark brown, orange and white for Mn, Fe and Zn respectively). The emulsion was then left overnight to ensure the full precipitation of metal oxide particles and to allow for Ostwald ripening in an attempt to narrow dispersity. Such a length of time was necessary to ripen the inverse emulsion due to the retardation effect of ionic species. The reaction could be stopped here to isolate the metal oxide nanoparticles for analysis. Where this was required, the subsequent addition of silica precursor was omitted and instead we skipped to the purification step by centrifugation. To form the ‘matchstick’, TEOS (0.3 ml) was added to initiate rod growth. The reaction was then left for 24 hours to go to completion.

To clean the particles, a round of centrifugation for 30 minutes at 4200g was performed and the supernatant was removed. Thereafter 3 more rounds of centrifugation were performed for a period of 5 minutes at 4200g re-dispersing the particles in ethanol each time. For the particles formed after reacting for 24 hours, in order to reduce the dispersity of the solution, selective centrifugation was then performed on the clean particles. This involved three rounds of centrifugation for 15 minutes at 30g (keeping supernatant) to remove larger particles.

4.4.2 Particle characterization

Samples for SEM were prepared by diluting the particle solutions to around 0.5 mg ml⁻¹ in ethanol and allowing them to dry onto silicon wafers supported on aluminium stubs. The samples were then coated with a conductive film of evaporated carbon. Four or five cycles were elapsed to ensure a reasonable coating thickness. SEM imaging was performed on a Zeiss Supra 55VP at 15 kV.

For TEM analysis samples were prepared by dropping a relatively concentrated solution (~ 0.01 wt.%) of particles in ethanol on to lacey carbon grids and allowing the samples to dry. Particles were imaged using a JEOL 2000FX TEM.

Elemental mapping was performed using a scanning transmission electron microscopy (STEM) technique with a high-angle detector to spatially resolve the elemental composition of the particles. This was performed on a JEOL ARM 200F TEM equipped with an Oxford Instruments X-Max^N 100TLE detector.

Powder X-ray diffraction experiments were performed on dry powders of manganese oxide particulate produced in the above synthesis without the addition of TEOS using a Panalytical X-Pert Pro MPD diffractometer using Cu $K_{\alpha 1}$ radiation. The sample was supported on vacuum grease (which contributes a small amorphous scatter shoulder to the pattern) on an off-cut silicon crystal.

To obtain a thin section of an individual ‘matchstick’ particle a focused-ion beam/scanning electron microscopy (FIB/SEM) technique was deployed using a JEOL 4500 FIB/SEM. This involved preparing a dilute sample of particles on a silicon wafer as before and depositing a layer of carbon thick enough to protect the surface of an individual particle from the damaging focused ion beam. Following this, a series of gradual slices were taken until the sample was thin enough for imaging with TEM (~ 100 nm for electron transparency). The particle and surrounding material was then lifted out onto a copper grid using a micromanipulator and was imaged on a JEOL 2100 TEM.

X-ray photoemission spectra were recorded on the dried powder of manganese oxide (as isolated for XRD) using a Kratos Axis Ultra DLD spectrometer. The charge neutralizer system was used and measurements were carried out within ~ 2 hr to avoid x-ray induced reduction of manganese in the powder during acquisition.

4.4.3 Kinetics of silica growth

In order to determine the growth progression in terms of particle length and diameter, a series of reactions were performed which were each terminated at an appropriate time by immediate centrifugation and re-dispersion in ethanol. Particles were then cleaned as before and were prepared for SEM analysis. At this stage however no selective centrifugation was performed so that the samples were representative of the total system. Image analysis was performed using ImageJ software and by manually measuring particle dimensions of at least 300 particles. Note that for TEM analysis there was no need for particle cleaning and so a drop of the reaction mixture was pipetted on to a grid and was immediately blotted with filter paper and allowed to dry.

4.4.4 2D particle tracking experiments

Suspensions of ‘matchstick’ particles were prepared by dispersing dried particles in de-ionised water (~ 1 mg ml $^{-1}$) with the aid of sonication if required. An aliquot (500 μ l) was mixed with 500 μ l fuel solution containing varying quantities of hydrogen peroxide (0 and 10 vol.% for 0 fuel and 5 vol.% respectively).

Two parallel lines of grease were drawn out to the approximate size of the cover slips being used ($20\text{ mm} \times 20\text{ mm}$) onto a Linkam Warm Stage. The coverslip was placed lightly over the lines of grease and a micropipette was used to inject the sample solution underneath the assembled cell. Capillary action ensures the solution fills the well and it is subsequently sealed at the other edges with grease. Videos (15) of 30 particles in motion near to the underlying glass, 1024×1024 px. at 50 fps for 30 s, were recorded using an Andor Zyla 4.4 Plus camera attached to an Olympus IX73 inverted light microscope. Two minutes were allowed for the Linkam warm stage to heat up to 25°C . A magnification of $100\times$ (Olympus UPlanFLN $100\times$ Ph) was used with phase to enhance the contrast of particles.

A tracking algorithm, Trackmate,⁵¹ distributed with ImageJ(Fiji) was then utilized to perform the 2D particle tracking. Our analysis was then performed using msdanalyzer, a Matlab class created for analysing tracking data.⁵² Fits were performed using the Matlab curve fitting toolbox.

References

- [1] F. Perrin, *J. Phys. Radium*, 1934, **5**, 497–511.
- [2] F. Perrin, *J. Phys. Radium*, 1936, **7**, 1–11.
- [3] M. P. B. V. Bruggen, F. M. V. D. Kooij and H. N. W. Lekkerkerker, *J. Phys. Condens. Matter*, 1999, **8**, 9451–9456.
- [4] C. J. Murphy, T. K. Sau, A. M. Gole, C. J. Orendorff, J. Gao, L. Gou, S. E. Hunyadi and T. Li, *J. Phys. Chem. B*, 2005, **109**, 13857–13870.
- [5] Y. Huang, X. F. Duan, Q. Q. Wei and C. M. Lieber, *Science*, 2001, **291**, 630–633.
- [6] Y. Yang, E. Barry, Z. Dogic and M. F. Hagan, *Soft Matter*, 2011, **8**, 707–714.
- [7] F. Lugli, E. Brini and F. Zerbetto, *J. Phys. Chem. C*, 2012, **116**, 592–598.
- [8] W. F. Paxton, K. C. Kistler, C. C. Olmeda, A. Sen, S. K. St Angelo, Y. Cao, T. E. Mallouk, P. E. Lammert and V. H. Crespi, *J. Am. Chem. Soc.*, 2004, **126**, 13424–13431.

- [9] S. Park, J.-H. Lim, S.-W. Chung and C. A. Mirkin, *Science*, 2004, **303**, 348–351.
- [10] J. He, B. Yu, M. J. Hourwitz, Y. Liu, M. T. Perez, J. Yang and Z. Nie, *Angew. Chem. Int. Ed.*, 2012, **51**, 3628–3633.
- [11] B. Liu, T. H. Besseling, M. Hermes, A. F. Demirörs, A. Imhof and A. van Blaaderen, *Nat. Commun.*, 2014, **5**, 1–8.
- [12] A. Kuijk, A. Imhof, M. H. W. Verkuijlen, T. H. Besseling, E. R. H. van Eck and A. van Blaaderen, *Part. Part. Syst. Charact.*, 2014, **31**, 706–713.
- [13] A. van Blaaderen and A. Vrij, *Langmuir*, 1992, **81**, 2921–2931.
- [14] A. Perro, S. Reculosa, S. Ravaine, E. Bourgeat-Lami and E. Duguet, *J. Mater. Chem.*, 2005, **15**, 3745.
- [15] J. W. Kim, R. J. Larsen and D. a. Weitz, *J. Am. Chem. Soc.*, 2006, **128**, 14374–14377.
- [16] J. Parvole, I. Chaduc, K. Ako, O. Spalla, A. Thill, S. Ravaine, E. Duguet, M. Lansalot and E. Bourgeat-Lami, *Macromolecules*, 2012, **45**, 7009–7018.
- [17] W. Stöber, *J. Colloid Interface Sci.*, 1968, **69**, 62–69.
- [18] J. Bailey and M. Mecartney, *Colloids and Surfaces*, 1992, **63**, 151–161.
- [19] A. van Blaaderen, J. van Geest and A. Vrij, *J. Colloid Interface Sci.*, 1992, **154**, 481–501.
- [20] H. Nakamura and Y. Matsui, *J. Am. Chem. Soc.*, 1995, **117**, 2651–2652.
- [21] K. Hidenori Nakamura, Y. Yasushi Matsui and I. Takao Goto, *Fine Silica Tube and Process for Making Same*, 1996.
- [22] F. Miyaji, S. a. Davis, J. P. H. Charmant and S. Mann, *Chem. Mater.*, 1999, **11**, 3021–3024.
- [23] J. Zhang, H. Liu, Z. Wang and N. Ming, *Chem. Eur. J.*, 2008, **14**, 4374–4380.
- [24] P. Qiu and C. Mao, *ACS Nano*, 2010, **4**, 1573–1579.

- [25] A.-Q. Zhang, H.-J. Li, D.-J. Qian and M. Chen, *Nanotechnology*, 2014, **25**, 135608.
- [26] K. a. Dick, *Prog. Cryst. Growth Charact. Mater.*, 2008, **54**, 138–173.
- [27] S. B. Kanungo, K. M. Parida and B. R. Sant, *Electrochim. Acta*, 1981, **26**, 1157–1167.
- [28] V. Russo, L. Protasova, R. Turco, M. H. J. M. De Croon, V. Hessel and E. Santacesaria, *Ind. Eng. Chem. Res.*, 2013, **52**, 7668–7676.
- [29] M. a. Hasan, M. I. Zaki, L. Pasupulety and K. Kumari, *Appl. Catal. A Gen.*, 1999, **181**, 171–179.
- [30] A. R. Morgan, A. B. Dawson, H. S. Mckenzie, T. S. Skelhon, R. Beanland, H. P. W. Franks and S. A. F. Bon, *Mater. Horizons*, 2014, **1**, 65–68.
- [31] M. Resa, M. Goenaga, M. Iglesias, R. Gonzalez-olmos and D. Pozuelo, *J. Chem. Eng. Data*, 2006, **51**, 1300–1305.
- [32] R. M. McKenzie, *Mineral. Mag.*, 1971, **38**, 493–502.
- [33] M. C. Biesinger, B. P. Payne, A. P. Grosvenor, L. W. Lau, A. R. Gerson and R. S. C. Smart, *Appl. Surf. Sci.*, 2011, **257**, 2717–2730.
- [34] E. S. Ilton, J. E. Post, P. J. Heaney, F. T. Ling and S. N. Kerisit, *Appl. Surf. Sci.*, 2016, **366**, 475–485.
- [35] Y. Zhang, G. Li, Y. Wu, Y. Luo and L. Zhang, *J. Phys. Chem. B*, 2005, **109**, 5478–5481.
- [36] R. Takahashi, S. Sato, T. Sodesawa, M. Kawakita and K. Ogura, *J. Phys. Chem. B*, 2000, **104**, 12184–12191.
- [37] P. Datskos and J. Sharma, *Angew. Chem. Int. Ed.*, 2014, **53**, 451–454.
- [38] J. He, M. J. Hourwitz, Y. Liu, M. T. Perez and Z. Nie, *ChemComm*, 2011, **47**, 12450–12452.
- [39] G. A. Parks, *Chem. Rev.*, 1964, **65**, 177–195.

- [40] M. M. Tirado, C. López Martínez, J. García De La Torre, C. López Martínez and J. García de la Torre, *J. Chem. Phys.*, 1984, **81**, 2047–2052.
- [41] T. H. Besseling, M. Hermes, a. Kuijk, B. de Nijs, T. S. Deng, M. Dijkstra, a. Imhof and a. van Blaaderen, *J. Phys. Condens. Matter*, 2014, **194109**, 1–12.
- [42] M. M. Tirado and J. G. de la Torre, *J. Chem. Phys.*, 1979, **71**, 2581.
- [43] M. D. Carbajal-Tinoco, R. Lopez-Fernandez and J. L. Arauz-Lara, *Phys. Rev. Lett.*, 2007, **99**, 138303.
- [44] J. Howse, R. Jones, A. Ryan, T. Gough, R. Vafabakhsh and R. Golestanian, *Phys. Rev. Lett.*, 2007, **99**, 048102.
- [45] T. C. Lee, M. Alarcón-Correa, C. Miksch, K. Hahn, J. G. Gibbs and P. Fischer, *Nano Lett.*, 2014, **14**, 2407–2412.
- [46] X. Ma, K. Hahn and S. Sanchez, *J. Am. Chem. Soc.*, 2015, **137**, 4976–4979.
- [47] X. Ma, S. Jang, M. N. Popescu, W. E. Uspal, A. Miguel-López, K. Hahn, D. P. Kim and S. Sánchez, *ACS Nano*, 2016, **10**, 8751–8759.
- [48] F. Hagemans, E. B. Van der Wee, A. Van Blaaderen and A. Imhof, *Langmuir*, 2016, **32**, 3970–3976.
- [49] R. Golestanian, *Phys. Rev. Lett.*, 2009, **102**, 1–4.
- [50] J. Kim, H. J. Hwang, J. S. Oh, S. Sacanna and G.-r. Yi, *J. Am. Chem. Soc.*, 2018, **140**, 9230–9235.
- [51] J.-Y. Tinevez, N. Perry, J. Schindelin, G. M. Hoopes, G. D. Reynolds, E. Laplantine, S. Y. Bednarek, S. L. Shorte and K. W. Eliceiri, *Methods*, 2016, **115**, 80–90.
- [52] N. Tarantino, J. Y. Tinevez, E. F. Crowell, B. Boisson, R. Henriques, M. Mhlanga, F. Agou, A. Israël and E. Laplantine, *J. Cell Biol.*, 2014, **204**, 231–245.

5

Engineering Anisotropic Silica Colloids for Bio-inspired Whiteness Optimization

Imagine you're a particle.

Prof. dr. ir. Stefan A. F. Bon

Abstract

This chapter details results for a bio-mimetic approach to designing colloids for thin white films. Inspiration was taken from the brilliant whiteness of the *Cyphocilus* beetle. The beetle scales have an internal fibrillar structure that is anisotropic allowing for a disordered arrangement – essential for broadband reflection. Suitable artificial candidates were found by systemically screening reaction conditions to yield ‘rod’ and ‘worm’-like silica colloids of comparable dimensions to the *Cyphocilus* fibrils. These colloids were then assembled into thin films by simple drop casting. The structure and whiteness (mean free path, l_t) have been compared for the ‘rod’ and ‘worm’-shaped colloidal films and were found to have similar performance ($l_t \sim 1.8$) which was slightly worse than the *Cyphocilus* beetle ($l_t \sim 1.4$) but significantly better than standard white paper ($l_t \sim 13$). Reasoning that optical crowding limited the whiteness, films with lower volume fraction were produced by utilizing silica rods with higher aspect ratio. Initial results show films with improved performance that now rivals the *Cyphocilus* beetle. Further work is required to elucidate how the different particle morphologies and dimensions determine the observed optical response.

5.1 Introduction

In the natural world, through the passage of time, evolution has produced highly optimized functional bio-materials. Universally these remarkable materials provide a desired adapted function whilst also being lightweight, mechanically stable and constituent of biological matter. To have these properties arise from minimal amounts of material, nature often relies on assembled nanostructures, a prime example being the bright whiteness of the *Cyphocilus* beetle scales due to its microscopic chitinous network.¹ It is thought that the whiteness helps to camouflage the beetle amongst fungi in the shaded environments it inhabits.^{1,2} The whiteness of the beetle is particularly interesting as the starting material, chitin, has a low refractive index (at wavelength, $\lambda = 560$ nm), $n = 1.56$,²⁻⁴ and the scales in the shell are only $\sim 5\mu\text{m}$ thick (figure 5.1).

When thickness is very small, to obtain intense broadband reflection, thus whiteness/opacity, the scattering centres must be arranged randomly in avoidance of resonance that could otherwise result in a photonic band gap producing colour.⁵ There is also an optimum size for the scattering centre with diameters in the range of 200 – 300 nm according to Mie theory.⁴ Producing anisotropic arrangements of scattering particles (of these dimensions) in thin layers whilst still maintaining the considerable volume/packing/filling fraction ($>40\%$) required for efficient scattering^{1,4} is extremely challenging. This is near impossible when the scattering particles are spherical as they preferentially arrange into ordered, isotropic arrays upon film assembly. In addition to this, when volume fractions are too high, the issue of optical crowding appears whereby at a high number density of scattering centres the interaction of radiated electric fields from neighbouring centres reduces the total optical scatter.⁶ Most of the current synthetic materials rely simply on high refractive index, e.g. titanium dioxide with $n = 2.33 - 2.87$,^{7,8} for application as opacifying agents in paints and coatings.

Other synthetic designs have involved making use of refractive index contrast (difference) by for instance purposefully engineering air voids or pores in the nanostructure. Some examples include formulations for coating paper involving calcium carbonate or kaolin clay¹⁰ and hollow polymer capsules as opacifiers.¹¹ The prior makes use of a high volume

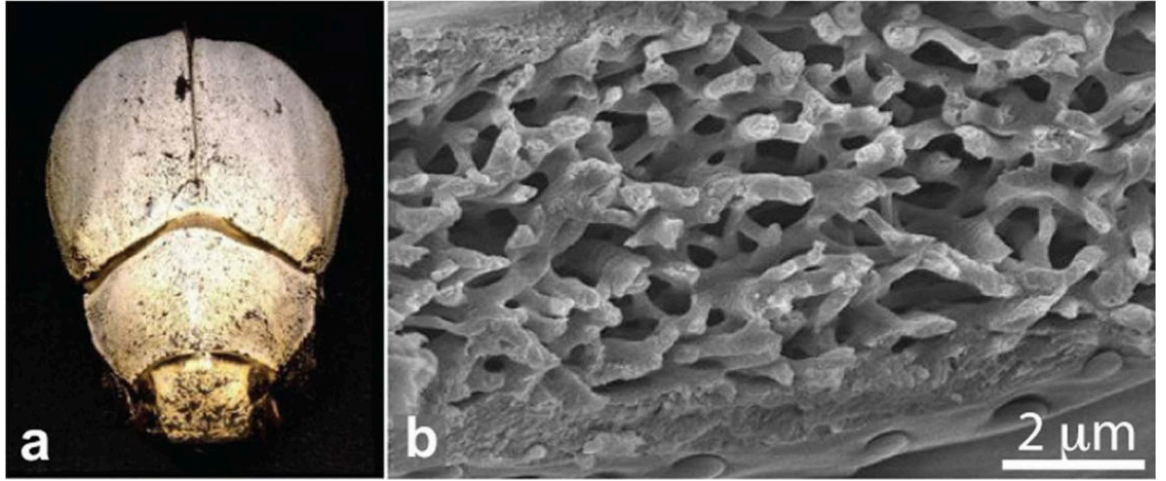


Figure 5.1. Photograph of a *Cyphocilus* beetle a), and a scanning electron microscope (SEM) image of the cross-section of the beetle scale b).⁹ Average fibril diameter, $d \sim 250 \text{ nm}$ ²

fraction of scattering particles in a water-borne formulation (containing soft latex binder and carboxy methyl cellulose thickener) whereby jamming upon drying leads to a network of air-filled pores surrounded by pigment particles.¹² The latter is produced by first synthesizing core-shell polymer latex where the core contains acid groups. Osmotic swelling at high pH above the glass transition temperature of the shell polymer causes internal void formation which can be preserved upon evaporation of water - if the shell properties are optimum. Both of these examples fall far short of the scattering efficiency of the *Cyphocilus* beetle scale. A recent example by Syurik *et al.* has shown paralleled performance utilizing phase separated poly(methyl methacrylate) (PMMA) which when dried formed a highly scattering porous structure.¹³ To our knowledge this is the first example of a low refractive index (PMMA $n \sim 1.49$ ¹⁴) material that matches the bright whiteness of the *Cyphocilus* beetle shell.

The exceptional optical performance of the *Cyphocilus* scales has been reported to be a product of efficient multiple scattering⁹ allowing it to outperform almost all other known low-refractive index materials. The key parameters to its success are the anisotropic shape, dimensions and highly optimized filling fraction of the chitinous fibrils.^{1,15} Efforts have been made to optimize the dimensions and filling fraction (number density and spac-

ing) of scatterers in the aforementioned paper coating formulations.¹⁰ Findings indicated a compromise between size, number density and separation of scatterers. Essentially the larger the scattering centre, the lower the number density and larger the spacing between centres. This led to the authors conceiving the idea of using anisotropic scattering centres to overcome the filling fraction limits.

Inspired by the highly optimized geometry of the *Cyphocilus* beetle scale we sought out a synthetic system whereby the direct dimensional tuning of anisotropic building blocks could afford bright whiteness in assembled thin films. Our chosen system employs silica ($n = 1.46$ at $\lambda = 590$ nm)¹⁶ rod-shaped colloids as anisotropic scatterers, recently shown to improve light trapping in thin film solar cells.^{17,18} Importantly the length, L , and diameter, d , thus aspect ratio (L/d) can be readily tuned over the dimensions of interest by altering reaction conditions or successive coating steps.^{16,19} These colloids have already demonstrated their suitability as a model system for studying liquid crystalline phase behaviour^{20,21} and serve as an ideal system to investigate the optimization of anisotropic scattering particle dimensions for bright white thin films.

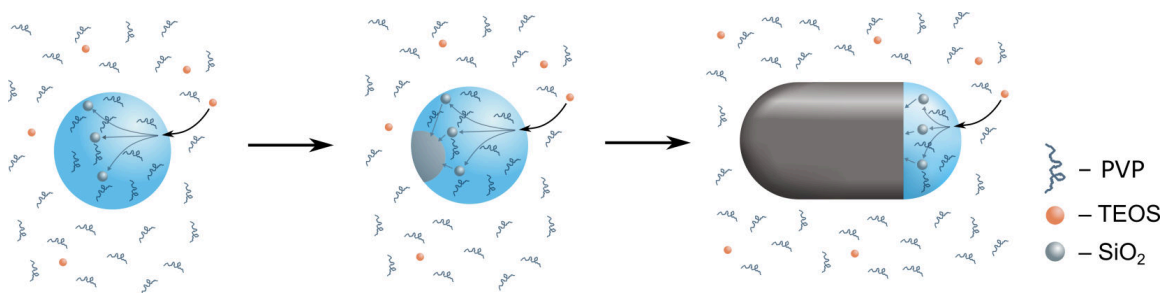
5.2 Results & Discussion

In this study a bottom-up approach was deployed making use of chemistry to control the production of our nanoscale building blocks (i.e. silica particles) that are then assembled into thin white films. Careful control of reaction conditions allows direct tuning of the dimensions of the anisotropic building blocks.

5.2.1 Synthesis – tuning the reaction conditions

In order to fabricate anisotropic silica colloids with dimensions comparable to the fibrillar chitin network of the *Cyphocilus* beetle, we made use of an inverse emulsion technique whereby the morphology and size of silica particles can be controlled by the initial emulsion conditions i.e. droplet size, concentration of base etc.¹⁹ Briefly, water, trisodium citrate dihydrate (0.18 mol dm^{-3}) and ethanol were added to a solution of poly(*N*-vinylpyrrolidone), PVP, in 1-pentanol (100 g l^{-1}) to which ammonia was then added and the mixture shaken

by hand to generate an emulsion. A silica precursor, tetraethyl orthosilicate (TEOS) was subsequently added and diffused through the pentanol phase to collide with water droplets where it reacted via hydrolysis/condensation to form silica. Under the current understanding of the mechanism, oligomers of silica condense together to form nuclei which migrate to the interface of the water droplet and condense together. Phase separation with further silica growth promotes the formation of a cap of silica with an attached water droplet that wets the growing interface only (Scheme 5.1). The final shape of the particle is predominantly dictated by interfacial tension of the adhered water droplet and the degree of silica condensation. It is pertinent to say that this is simply the synthesis from which the ‘matchsticks’ fabricated in chapter 4 were derived, hence one can think of these silica rods as just matchsticks without the catalytic head.



Scheme 5.1. Illustration of the proposed silica rod growth mechanism. Tetraethyl orthosilicate (TEOS) added to the continuous (pentanol) phase migrates to water droplets whereby it enters and reacts to form silica. Subsequent phase separation of a solid silica cap and continuous asymmetric delivery of TEOS via the adhered droplet leads to the formation of rod-shaped colloids.

Systematically varying the reaction conditions: [NH₃], [H₂O], [citrate], [EtOH] allowed for the production of a range particle diameters and aspect ratios (figure 5.2 and table 5.1) with diameters of suitable size for Mie scattering. Note that it has been shown that control of temperature, sonication and the amount of PVP can also influence the final dimensions of the silica particle.^{22,23} For clarity, the effect of each reagent will be detailed in the following subsections: 5.2.1.1, 5.2.1.2, 5.2.1.3 and 5.2.1.4. After exploring these conditions, candidates for photonic studies were selected based on their dimensions (section 5.2.2).

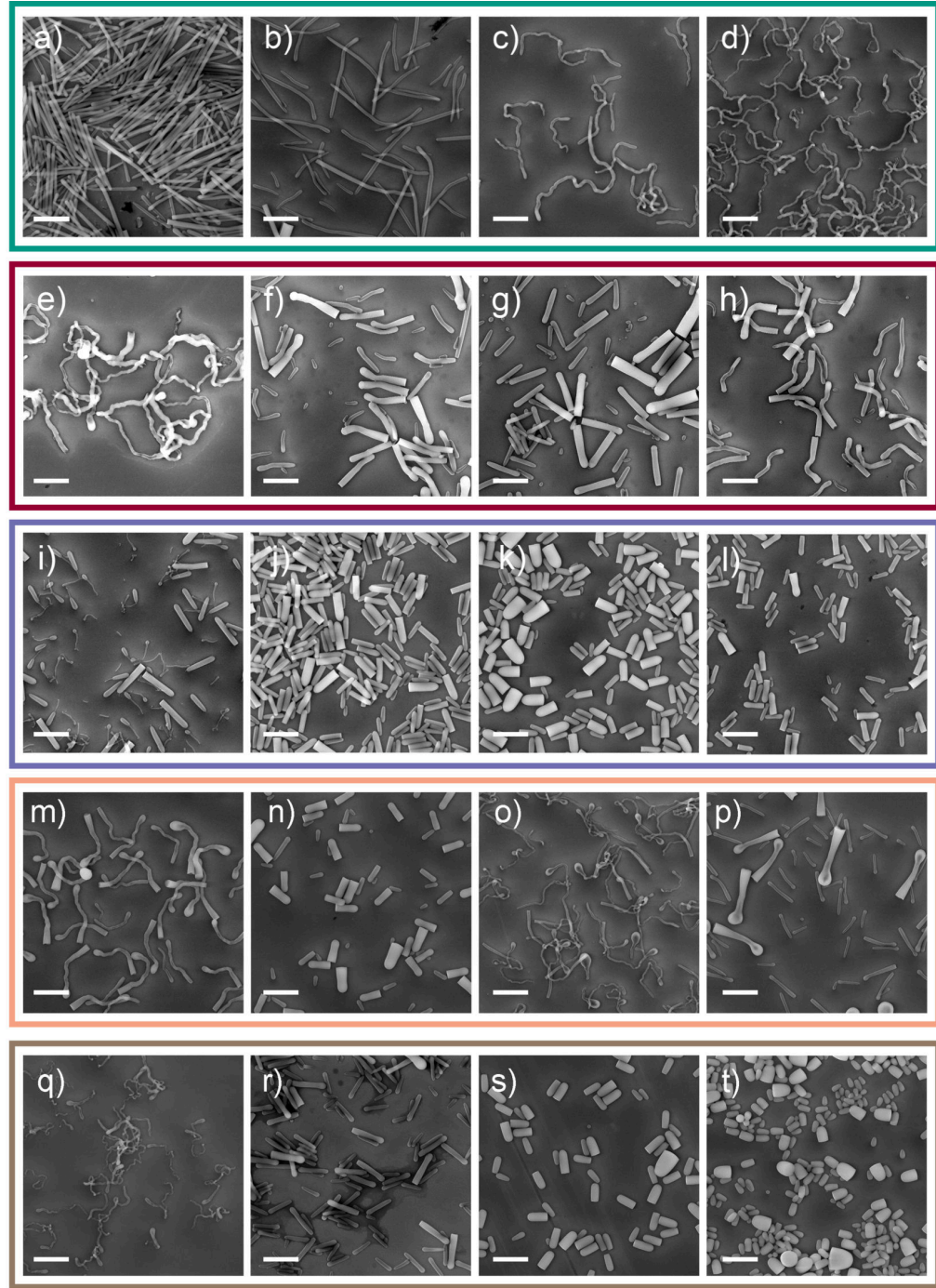


Figure 5.2. Scanning Electron Microscopy (SEM) images of anisotropic silica particles produced by varying $[\text{NH}_3]$: $\chi_{\text{NH}_3} = 12, 8, 4$ and 2 for (a–d cyan), $[\text{citrate}]$: $\chi_{\text{citrate}} = 4.4, 4, 3.6$ and 3.2×10^{-2} for (e–h red), $[\text{H}_2\text{O}]$: $\chi_{\text{H}_2\text{O}} = 55, 50, 45, 42$ for (i–l blue), $[\text{citrate}]$ and $[\text{H}_2\text{O}]$ simultaneously (m–p orange) and $[\text{EtOH}]$: $\text{vol} = 2, 1.5, 1.25$ and 1 ml for (q–t brown). Reagent concentrations decrease reading left to right with amounts detailed in table 5.1. Scale bar = $2 \mu\text{m}$.

5.2.1.1 Ammonia concentration $[\text{NH}_3]$

Considering the hydrolysis and condensation reactions for the synthesis of silica are base catalysed, the content of ammonia in the reaction should have a direct correlation to kinetics and therefore one might also expect variation in the particle morphology. This is indeed what was observed, transitioning from straight ‘rod-shaped’ particles ($L/d = 15.87$) to long, very high aspect ratio ‘worm-like’ curved rods ($L/d = 51.59$) with a decrease in ammonia concentration (figure 5.2 a–d). Notably this effect has been observed by other researchers in the search for hollow nanomaterials as drug carriers.²⁴

Ammonia was introduced to the reaction in its aqueous form (30 wt.% in water) and so with a reduction in the amount of ammonia there also comes a reduction in the amount of water. This was offset by introducing additional distilled water (table 5.1). Whilst water is consumed in the hydrolysis of TEOS, it is present in a large excess in this reaction, and so the reaction kinetics are not greatly impacted by its reduction. The amount of water was also varied later to verify its effect (Section 5.2.1.3).

The large reduction in the observed silica particle diameter evident from figure 5.2 a–d) (see also table 5.1) would originally suggest smaller droplet sizes according to the current understanding of the reaction mechanism. Knowing that the total amount of aqueous phase is similar in each of these reactions, and thus droplet size and number should be consistent, leads to some confusion on the cause of reduction in size. The answer may be explained by considering the kinetics. At low ammonia concentration the rates of hydrolysis and condensation are significantly lower. This leads to a growth mechanism that is dictated by hydrolysis. Partially hydrolysed siliceous oligomers can persist and are allowed time to diffuse to the droplet interface where they can help to stabilize this interface. This promotes both smaller droplet size and the ability to form hollow structures as condensation and subsequent growth will preferentially occur at this interface. In contrast when ammonia concentration is high, hydrolysis and condensation are fast, thus more primary particles are nucleated and there is a more continuous growth front throughout the particle.

The erratic, winding structure of the anisotropic ‘worm-like’ colloids is thought to be caused by the fact that the terminal aqueous droplet (where particle growth occurs) is small and therefore exhibits faster Brownian motion. The particle and droplet therefore

move much more rapidly during particle growth and, considering that the hydrolysis of TEOS and thus growth are slow in comparison, a more random structure is obtained. In fact to some extent the morphology of these particles resemble Brownian particle trajectories and they can perhaps be thought of as fossils of the events that formed them.

5.2.1.2 Citrate concentration [citrate]

The results from the variations in citrate concentration are initially difficult to explain. The highest content of citrate resulted in very long erratic structures (figure 5.2 e), again with narrow diameter in some sections of the particles and an apparent hollow nature. It has been suggested that during the reaction there may be points in which the super saturation concentration for ionic citrate species is exceeded and citrate crystals spontaneously form inside the growing particle.²³ This may be a consequence of local consumption of water (good solvent for citrate) and production of ethanol (poor solvent for citrate). Subsequently silica precipitates around this crystal and continuous dissolution and re-precipitation leads to hollow structures. This may be the case here, and is a different mechanism altogether than for the production of hollow structures when ammonia concentration is low (subsection 5.2.1.1). Alternatively citrate may buffer the local pH inside the water droplet, effectively lowering it and counteracting the effect of ammonia, leading to a reduction in the rate of silica production. This would indeed explain the similar morphologies seen separately for high citrate concentration and low ammonia concentration.

Citrate is also thought to provide ionic stabilization to the water droplets and promote their initial formation due to solvation and a reluctance to go to the more hydrophobic pentanol phase.¹⁹ As such with increasing citrate concentration comes a decrease in droplet size, observed here (figure 5.2 e) and by others.²³

5.2.1.3 Water concentration [H_2O]

When only the amount of added de-ionized water was changed the particles were expected to be consistent in morphology and exhibit only the ‘bullet’/‘rod’ shape. This was largely the case as can be seen in figure 5.2 i-l). There are couple of noteworthy exceptions here: 1. the presence of small tapering species in (i) and 2. the curving midsection of particles in

(l). The small species in figure 5.2 i) may be the consequence of a secondary distribution of droplets formed due to the larger amount of water present. The reasoning for curving midesctions in figure 5.2 l) is less obvious. Perhaps with a lower amount of water present in the reaction mixture a narrowing occurs after the initial ‘head’ of the particle is formed as less water is immediately available from the pentanol phase after this initial phase separation occurs.

It was expected that the reduction of water content would accompany a reduction in particle diameter here. Instead no such trend was found and in fact the diameter increased from i–k and aspect ratio also reduced. Note though that the dispersity in diameter here is very high (>0.3) so little sense can be taken from this comparison. Clearly there is a fine balance in the thermodynamic stability of the emulsions in these reactions and selecting the right reagent conditions is an art in itself.

5.2.1.4 Water and citrate variations

With this series the intent was to keep the ratio between water and sodium citrate constant ($\sim 1000:1$ molar ratio) but vary their quantity versus other reagents. This could then reveal the extent at which hollow structures are formed and whether the salting out of sodium citrate crystals during the synthesis is the primary cause of this. As can be seen from figure 5.2 m–p) a wide range of morphologies were extracted when water and sodium citrate were decreased versus other components. High aspect ratio hollow structures were obtained for high and intermediate citrate/water concentrations (figure 5.2 m&o). The reason for this is not fully understood as one would expect similar morphologies throughout this series. Again it was expected that the droplet size should decrease with less aqueous species which here was largely the case (table 5.1 m–p). The final case (p) saw a bimodal distribution of large ‘drumstick’ shaped particles amongst many smaller ($d > 200$ nm) particles which lead to measuring a very high dispersity in diameter (0.64) and thus the trend is less apparent from the measured average diameter.

5.2.1.5 Ethanol concentration [EtOH]

The ethanol series is perhaps the easiest to understand as ethanol is present in excess with respect to TEOS (at least 10 fold) and thus does not directly affect the reaction kinetics and yet can dramatically change the emulsion characteristics i.e. droplet size. With decreasing ethanol content the droplet size increases and resultant particle diameters increase (figure 5.2 q–t) as also observed previously.²² Notably a large amount of ethanol can be used to drastically reduce the droplet size such that narrow, hollow ‘worm-like’ structures are formed (figure 5.2 q). These structures are similar to those formed with low ammonia content (figure 5.2 d) and high citrate content (figure 5.2 e) which suggests the primary driver for their formation is small initial droplets. Again the hollow nature of the particles here may suggest that citrate crystals form during particle growth and silica precipitates around the crystal. Considering the high ethanol content (poor solvent for citrate) this is plausible.

5.2.2 Selected candidates for photonics studies – ‘rods’ vs. ‘worms’

After having screened several reaction conditions, procedures could be selected to produce rod-like colloids of the proposed optimum diameter (200 - 300 nm) for scattering studies. Initially we were very intrigued by the erratic ‘worm’-like structures that could be formed when base concentration was low (figure 5.2 d). These highly random structures could potentially exhibit different packing and therefore larger spacing between scattering centres in the dried film that would be impossible with straight rods. These ‘worm’-like particles appeared by eye to be more akin to the chitin fibrils in the *Cyphocilus* beetle scale. In the reaction conditions that were probed above however the average diameter of these erratic particles was below (170 nm) the desired optimum value of 250 nm. Therefore some minor modifications were made (see experimental section 5.4.2) in order to increase the diameter. Optimized ‘worm’-like particles with $L = 2.145 \mu\text{m}$ (0.14), $d = 0.235 \mu\text{m}$ (0.25) thus $L/d \sim 9$ are displayed in figure 5.3.

Interestingly these ‘worm’-like particles have a partially hollow structure typically towards the tail end of the particles as evidenced from the high resolution SEM image in

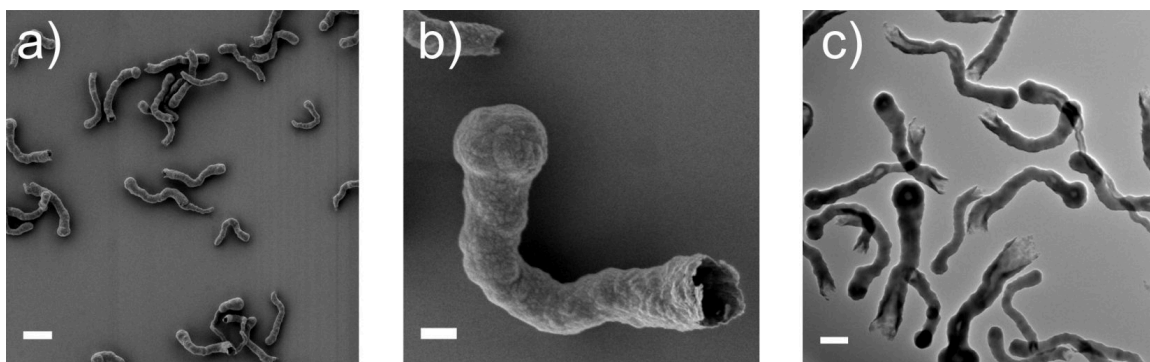


Figure 5.3. Scanning Electron Microscope (SEM) (a,b) and Transmission Electron Microscope (TEM) (c) images of ‘worm’-like silica particles. Low accelerating voltage of 0.3 kV was used to SEM image the particles in order to resolve any surface details. The partially hollow structure of the particles can be seen towards their tail end. Scale bars a) = 1 μm , b) = 200 nm and c) = 250 nm.

figure 5.3 b) and TEM image c). This may arise due to the previously discussed spontaneous crystallization of sodium citrate crystals and subsequent templating of silica around said crystals as postulated by Murphy *et al.*²³ The surface of the particles is also irregular and rough perhaps due to the persistence of high molecular weight siliceous oligomers and pre-particles brought about by the low hydrolysis rate of the reaction. The dimensions of these highly anisotropic particles are ideal for our application and the hollow structure may lead to further interesting behaviour.

In order to determine whether the highly erratic structure of these ‘worm’-like particles can contribute to more efficient multiple scattering, an appropriate standard was needed for comparison. Straight silica rods were thus synthesized with similar length but increased diameter: $L = 2.139 \mu\text{m}$ (0.09), $d = 0.374 \mu\text{m}$ (0.33) thus $L/d \sim 5.7$ see figure 5.4. Note that these rods have an apparently much smoother and regular surface. The absolute densities of ‘rod’ and ‘worm’-like samples was measured by helium pycnometry verifying comparable densities of $\rho = 2.16 \text{ g cm}^{-3}$ and 2.20 g cm^{-3} for ‘rods’ and ‘worms’ respectively.

White films were produced by simple drop casting of solutions containing dispersed particles of known volume fractions onto glass slides (see Experimental 5.4.3 and figure 5.5 for an example). The assembly process during the formation of colloidal films is typically dictated by the evaporation rate, height of the film and diffusion rate of the colloidal

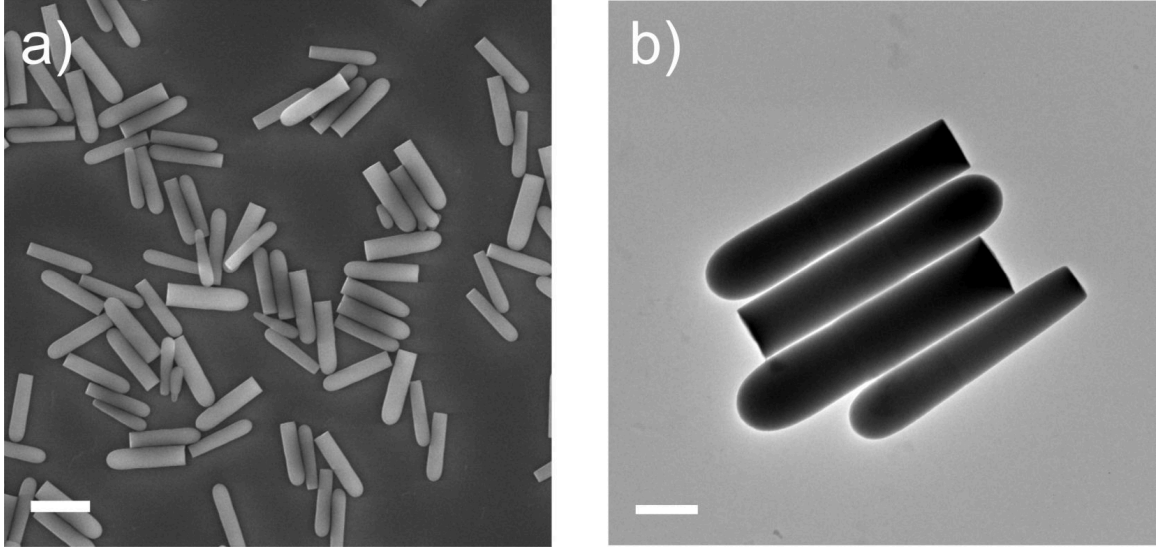


Figure 5.4. Scanning Electron Microscope (SEM) (a) and Transmission Electron Microscope (TEM) (b) images of rod-like silica particles. Scale bars a) = 2 μm and b) = 500 nm.

particles. This is captured by the dimensionless Péclet number:

$$Pe = \frac{H\dot{E}}{D_p}, \quad (5.1)$$

where H is the film height, \dot{E} is the evaporation rate and D_p is the diffusion rate of the particles. When the Péclet number is high, i.e. $Pe \gg 1$ and thus $\dot{E} \gg D_p$, a vertical gradient in volume fraction can occur during drying leading to an enrichment of particles at the surface of the film.²⁵ In the case where Péclet number is low, i.e. $Pe \ll 1$ and thus $\dot{E} \ll D_p$, the fast diffusion of particles continuously rebalances the volume fraction therefore the film remains uniform at all times during drying. In addition it is worth noting that an autostratification effect is found with two component mixtures of different sized particles whereby the final fate of smaller particles is always to the top of the film.²⁶ For our system, using estimations for the film height, evaporation rate and diffusion coefficient (see previous chapter 4, equation (4.3) for equation to estimate the diffusion coefficient for hard cylinders) of 350 μm , 0.002 $\mu\text{m s}^{-1}$ and 0.5 $\mu\text{m s}^{-2}$ respectively we find a Péclet number of $Pe = 1.4$. The estimations are based on the volume of drop cast solution and

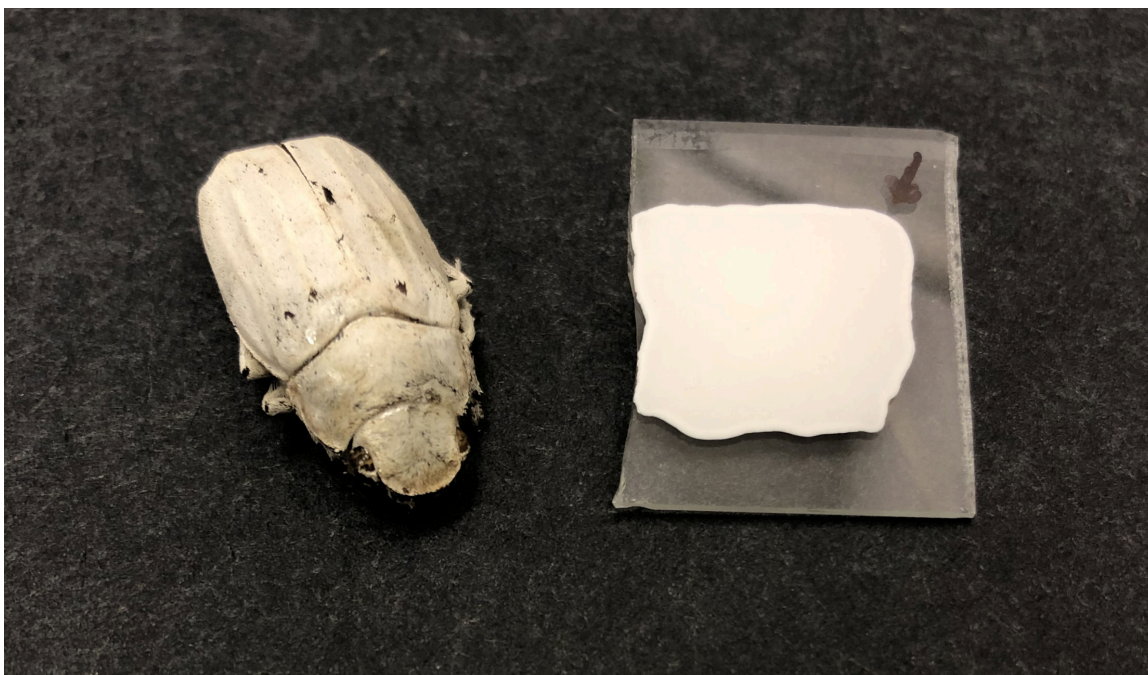


Figure 5.5. Photograph of a typical white film of ‘rod’-like colloids produced by drop casting (thickness = 40 µm) shown next to the *Cyphocilus* beetle (left) for comparison.

its subsequent spread area for the height, and an experimentally determined evaporation rate from a similar reduced air flow setup.²⁷ With Péclet numbers close to unity and the relatively low initial volume fractions of particles employed in the current work we can expect that there will be some stratification of smaller particles towards the top of the film²⁶ and thus it is important to consider this when looking at the final properties of the film.

Particle films were imaged by SEM to examine their top structure and cross-sections (figure 5.6 & figure 5.7). Cross-sections were produced by fracturing the films with a scalpel blade as it was found that attempts to use focused-ion-beam (FIB) milling resulted in large fragments being dislodged and smearing in sections due to charging effects and re-deposition of material during milling. Undoubtedly the scale of the milling required here presents a real challenge and thus simpler fracturing techniques were deployed at the expense of clean and precise cuts. Nevertheless information about the internal structure of the films can be extracted from the SEM images in figure 5.6 a) and figure 5.7 a). Both ‘worm’ and ‘rod’ particles appear to pack down into dense random close-packing. It is difficult to accurately

quantify the volume fraction of these films from SEM images due to noise issues and the nature of extrapolating what is a 2D projection into a 3D quantity. If we assume then that particles are isotropically distributed and the top views are good representations of the film structure then we can approach estimations for the volume fraction of $\phi = 0.67$ for worms and $\phi = 0.76$ for rods from thresholded images (see Appendix A figure A.3 and figure A.4). These are of course poor assumptions but we can at least have a rough estimation for the filling fraction of the films.

From the top views of the films (figure 5.6 & figure 5.7 b) the particles appear to have a low dispersity in average diameter (~ 0.15) but this is merely a product of the aforementioned autostratification process resulting in the sorting of smaller particles to the top of the film. At this point one could suppose that there may be some ordering of particles into a different crystalline phase in these upper layers, however this was not something that was observed anywhere in the films. Therefore we can say with confidence that particles are isotropically distributed in both systems with no ordering that may otherwise give rise to resonance effects i.e. produce structural colour.

The thickness of the films was measured by interferometry – an optical profiling technique that relies upon the interference of white light and can achieve vertical resolution of ~ 10 nm for rough surfaces. The primary advantage of this technique is the speed of acquisition allowing large areas to be measured and stitched together resulting in fast identification of areas of uniform thickness for our subsequent whiteness analysis. The glass microscope slides that films were assembled on acted as a useful baseline reference and the displayed surface images (figure 5.6 & figure 5.7 c) show the uniformity of the selected acquisition areas (highlighted by dashed boxes). The average height in these areas was subtracted from a reference area (glass slide, black regions) after three point levelling was applied in Gwyddion to give the thickness values utilized later in section 5.2.3.

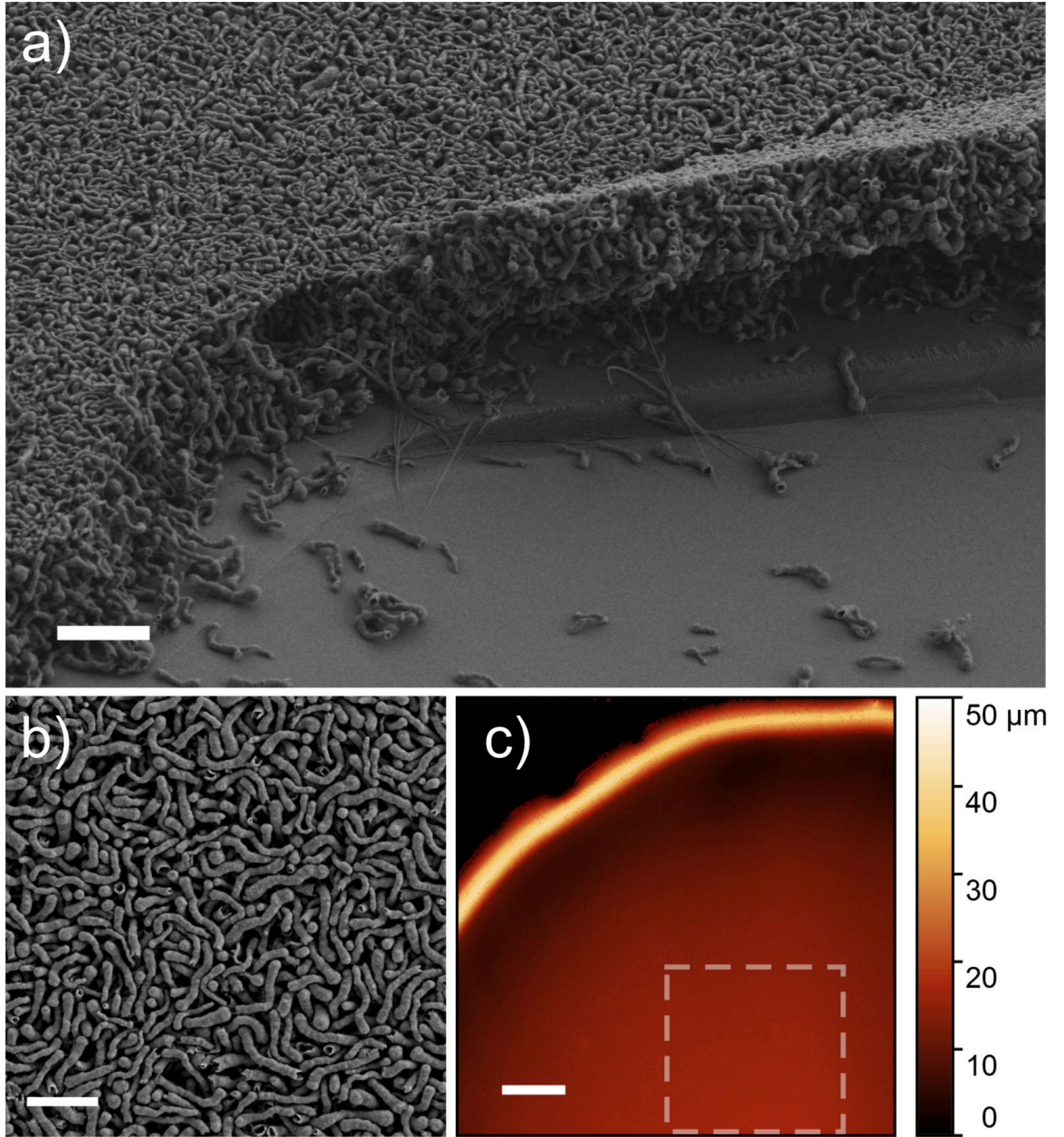


Figure 5.6. Typical assembled film of ‘worm’-like particles. Scanning electron microscope (SEM) image of a cross-section of a film taken at a tilt angle of $\theta \sim 40^\circ$ a) and a high resolution image of the top of the film b). Interferometry surface image of a 7.6×7.6 mm area of the film, transmission measurement area highlighted by dashed box with average film height of $15.48 \pm 1.98 \mu\text{m}$. Scale bars: a) = $5 \mu\text{m}$, b) = $2 \mu\text{m}$ and c) = 1 mm .

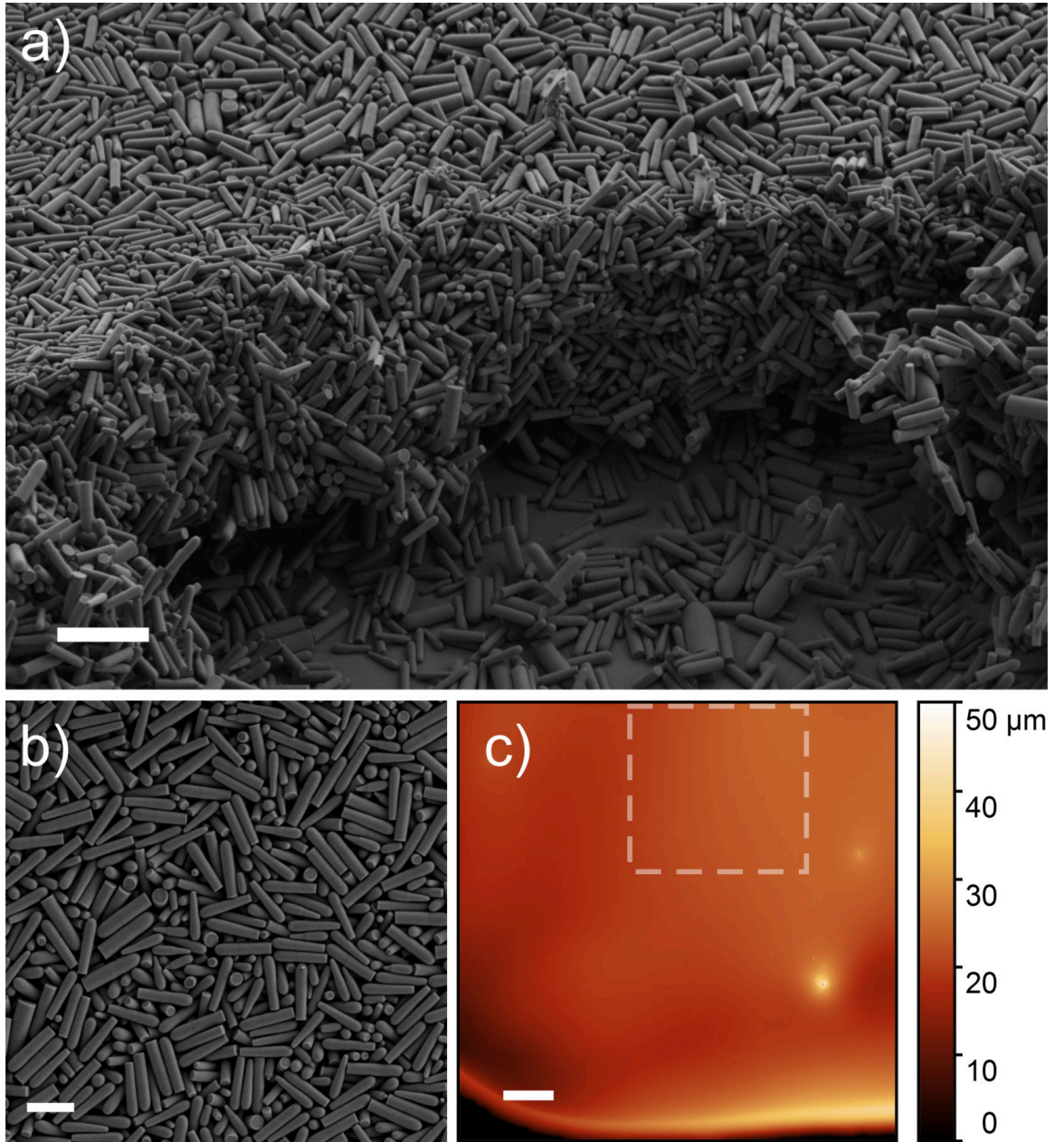


Figure 5.7. Typical assembled films of ‘rod’-like particles. Scanning electron microscope (SEM) image of a cross-section of a film taken at a tilt angle of $\theta \sim 40^\circ$ a) and a high resolution image of the top of the film b). Interferometry surface image of a 10×10 mm area of the film, transmission measurement area highlighted by dashed box with average film height of $19.31 \pm 0.38 \mu\text{m}$. Scale bars: a) = $5 \mu\text{m}$, b) = $2 \mu\text{m}$ and c) = 1 mm .

5.2.3 The whiteness – ‘worms’ vs. ‘rods’

The whiteness of a material can be defined in physical terms as how effectively light is scattered across the full visible spectrum. A description for light propagation through random networks is provided by diffusion theory.²⁸ A key parameter that can be extracted in the diffusion approximation is the transport mean free path, l_t , which describes the average distance light travels before losing memory of its propagation direction. The smaller this value is, effectively the more scattering a material is. In order to quantify l_t in the laboratory, the total transmission, T , of a series of different film thickness, L , was measured and an analytic expression relating these quantities from the diffusion of light through a slab geometry²⁹ was utilized:

$$T = \frac{1}{L_a} \frac{\sinh\left(\frac{2z_e}{L_a}\right) \sinh\left(\frac{z_e}{L_a}\right)}{\sinh\left(\frac{L+2z_e}{L_a}\right)}, \quad (5.2)$$

where z_e is the extrapolation length (dependent on l_t) and L_a is the absorption length. The extrapolation length treats the problem with an extrapolated boundary condition that takes into account internal reflections at the boundary and thus describes the distance outside the turbid medium where average diffuse intensity diminishes.³⁰ This quantity was found to be $z_e = (1.55 \pm 0.21) l_t$ and was determined from independent measurements of the angular distribution of transmitted light (see Appendix section A.3). The absorption length, L_a , is considered to be negligible for silica. Knowing this we can simplify equation (5.2) to:

$$T \approx \frac{2z_e}{L + 2z_e}. \quad (5.3)$$

The total transmission across the visible spectrum (400 – 800 nm) was measured for different film thickness (figure 5.8). The spectra both show an upward slope towards higher wavelengths, λ , indicating a slight bluish tint to the reflected light. The materials therefore are not perfectly white however the slight blue colour can be advantageous for use as opacifying agents as this gives the material good ‘hiding’ power – helps to suppress stains which are often yellowish.

With increasing film thickness (colours getting lighter in figure 5.8) there is clearly

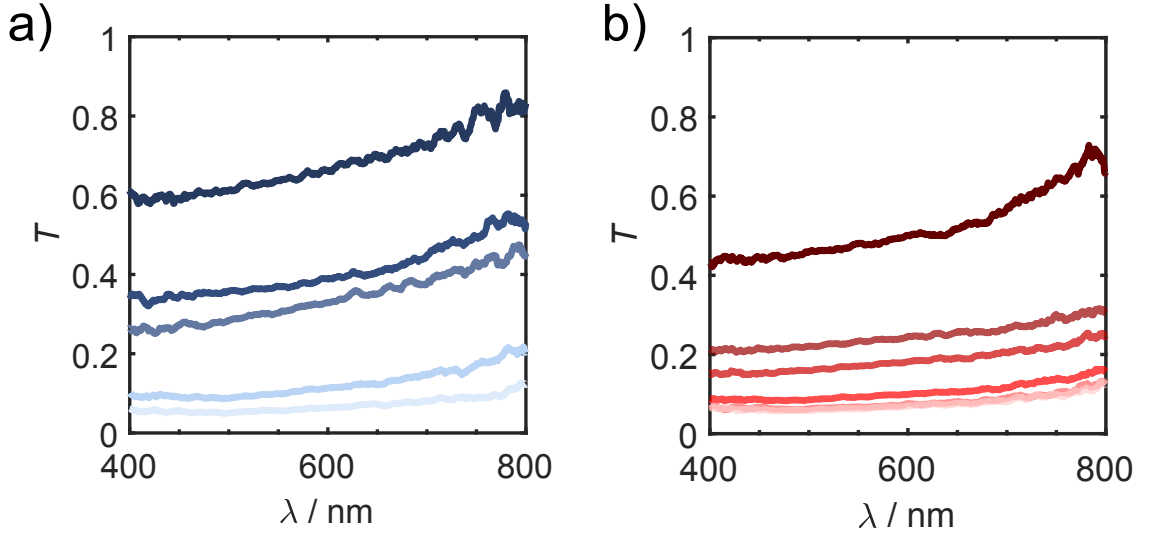


Figure 5.8. Total transmission, T , spectra across the visible spectrum for deposited colloidal ‘worm’ (a) or ‘rod’ (b) films of different thicknesses ranging from $\sim 2 \mu\text{m}$ to $90 \mu\text{m}$. Colour saturation represents thickness i.e. lighter colours = larger thickness.

a reduction in the total transmitted light as logically expected. The magnitude of this reduction appears larger for the ‘rod’-like samples over a comparable thickness range. Using the above equation (5.3) to fit the transmission as a function of thickness, l_t is obtained from its coupling to z_e . An example of the fit for the ‘worm’-like sample at a wavelength of $\lambda = 600 \text{ nm}$ is displayed in figure 5.9 which gives $l_t = 1.68 \pm 0.19$ as opposed to $l_t = 1.98 \pm 0.08 \mu\text{m}$ for rods indicating slightly higher performance for the ‘worm’-like films.

Whilst the exact role of anisotropy is still not entirely clear and there remains a challenge in the photonics community to approach suitable models, we can explain differences in our results based upon different apparent packing fractions. In our comparison unfortunately the diameters of the ‘rod’ and ‘worm’-like colloids are not identical and so we approach the comparison with some caution. That being said, based on diameter of scattering centres alone, we would expect the larger average diameter of the ‘rod’-like colloids to act as more efficient Mie scatterers. Our results show that this is not the case and thus packing must be important. To rationalise this result then it is expected that optical crowding is playing a role in reducing the total optical scatter for the ‘rod’-like films which certainly pack down to higher volume fractions than those consistent of ‘worm’-like

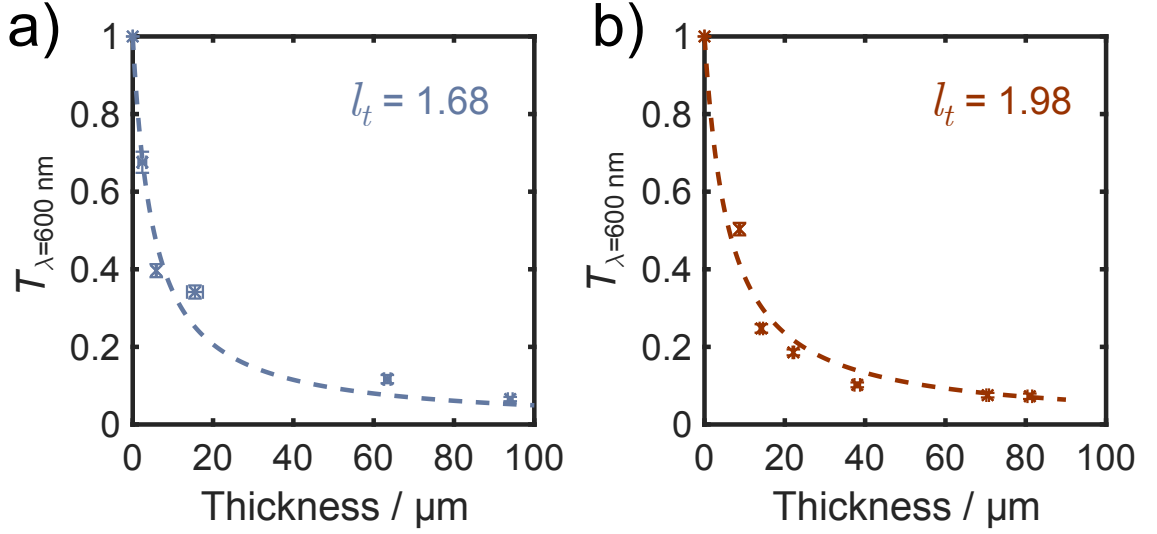


Figure 5.9. Total transmission, T , at $\lambda = 600 \text{ nm}$ as a function of thickness for both ‘worm’-like colloidal films a) and ‘rod’-like colloidal films b). The dotted lines represents the fit to determine l_t from equation (5.3).

particles.

Our colloidal silica films slightly under perform the *Cyphocilus* beetle shell which has a transport mean free path, $l_t = 1.47 \mu\text{m}$.⁹ However they do significantly better than commercial white paper ($l_t = 13 \mu\text{m}$)^{9,31} and photonic glasses ($l_t \sim 2.9 \mu\text{m}$)^{9,32} but are still some way off the high scattering performance of titanium dioxide ($l_t = 0.8 \mu\text{m}$).³³ It is still surprising that our silica materials can exhibit such decent performance despite the low refractive index of silica ($n = 1.46$ as opposed to $n = 2.49$ for titania) and as such they are promising candidates for use in white coatings.

5.2.4 Optimizing whiteness

Further optimizations are likely to come from reducing the volume/filling fraction of the colloidal films. We believe that the current films are limited by optical crowding as has been shown to be a critical feature in the evolutionary optimization of the *Cyphocilus* beetle shell.¹ As such we have set out to fabricate anisotropic silica particles that pack down to lower densities upon drying. Larger, higher aspect ratio particles have the potential to exhibit interesting liquid crystalline phase behaviour²⁰ or become trapped in transient

states due to their increased sedimentation rate. These transient states could potentially involve the jamming of long ‘rod’-like particles akin to what was seen for PCC calcium carbonate in chapter 2 figure 2.11. The resultant colloidal films will have lower volume fraction with more voids between particles.

To test this hypothesis we synthesized silica rods with higher aspect ratio ($l = 4.92 \mu\text{m}$ (0.16), $d = 0.27 \mu\text{m}$ (0.31), $l/d = 18$), approximately double that of the previous ‘worm’-like sample. Indeed these high aspect ratio particles do apparently pack down to lower volume fractions particularly towards the top of the film (figure 5.10 b). We can approximate the volume fraction from the 2D projection of the SEM image (figure A.5) at the top of the film, as done with the previous samples, to give $\phi = 0.51$ which is approaching the optimum value determined for the *Cyphocilus* beetle scale ~ 0.45 with similar fibril diameter to the rod diameters here.¹ Interestingly the film appears to have two distinct layers where particles have aligned near the bottom of the film to pack down densely, and towards the top of the film they are more isotropically distributed. A potential cause of this is likely convection whereby fluid flows towards the droplet edge driven by evaporation. The dense particles sediment near the bottom and get aligned with this flow. Some are swirled up and re-suspended and, as the film height slowly reduces from evaporation, the volume fraction increases and particles eventually jam into the less dense isotropic phase that is seen in the upper layers of the film. It is not known whether this stratification of phases is beneficial for broadband light scattering.

Preliminary experiments have been undertaken to quantify the whiteness (l_t) of these new films. At the time of writing this thesis the analysis is still in progress, however we have measured the transmission for different film thickness (figure 5.11) and see a distinct reduction in transmitted light through the films in comparison to the previous lower aspect ratio colloidal films. These films clearly exhibit much higher broadband scattering with only a weak wavelength dependence across all films. The film with the lowest thickness in this series, $6.85 \pm 0.81 \mu\text{m}$, reflects around 80% of light hitting the sample despite being so thin. Such reflectance is on par with the *Cyphocilus* beetle scale. Quantifying the mean free path at $\lambda = 600 \text{ nm}$, using the same procedure as for the previous samples, we find $l_t = 0.84 \pm 0.04 \mu\text{m}$. Apart from the recent works of Syurik *et al.*,¹³ there are no known

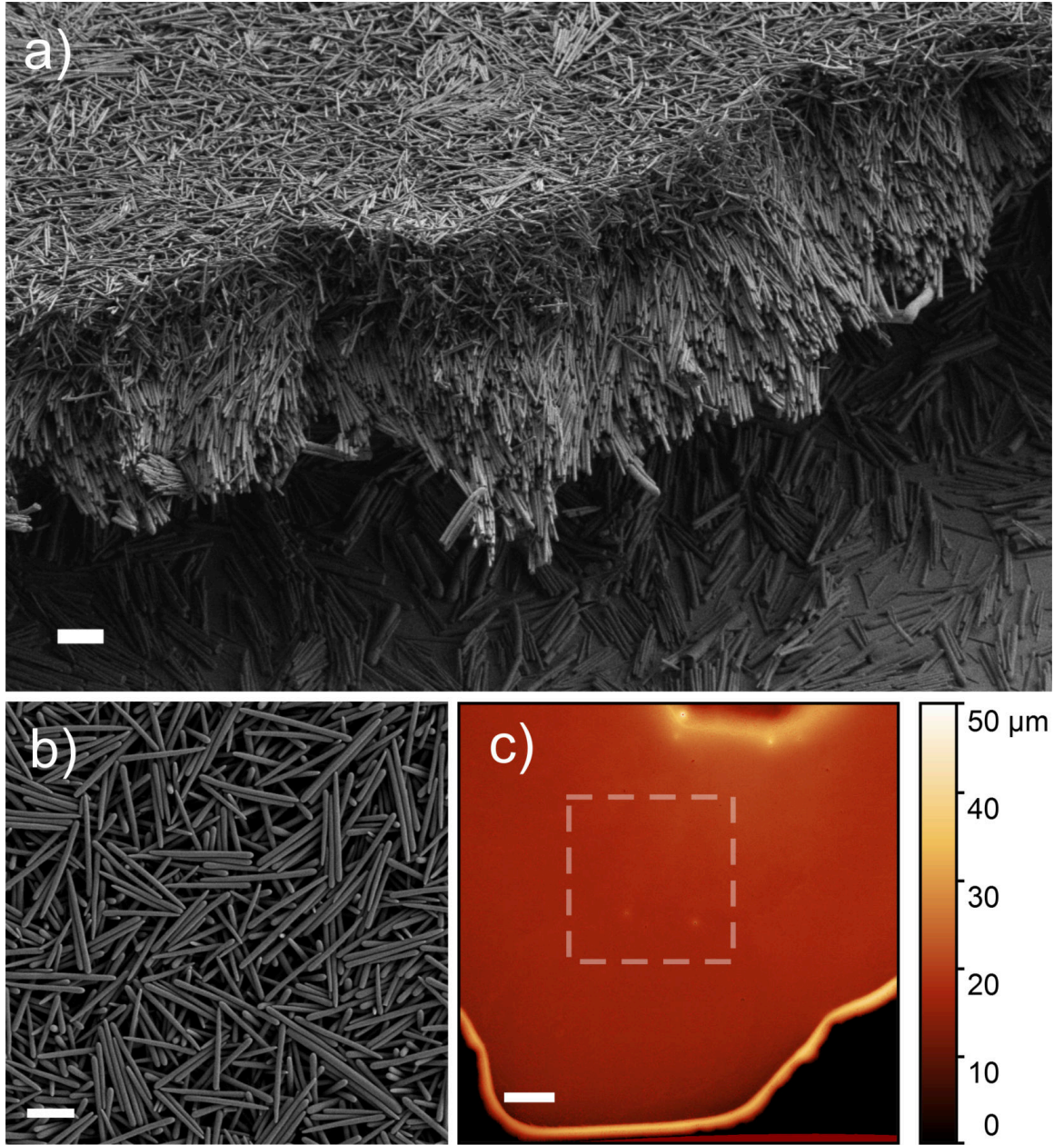


Figure 5.10. Typical assembled films of high aspect ratio ($l/d = 18$) ‘rod’-like particles. Scanning electron microscope (SEM) image of a cross-section of a film taken at a tilt angle of $\theta \sim 40^\circ$ a) and a high resolution image of the top of the film b). Interferometry surface image of a 10×10 mm area of the film, transmission measurement area highlighted by dashed box with average film height of $17.31 \pm 0.68 \mu\text{m}$. Scale bars: a) = $5 \mu\text{m}$, b) = $2 \mu\text{m}$ and c) = 1 mm .

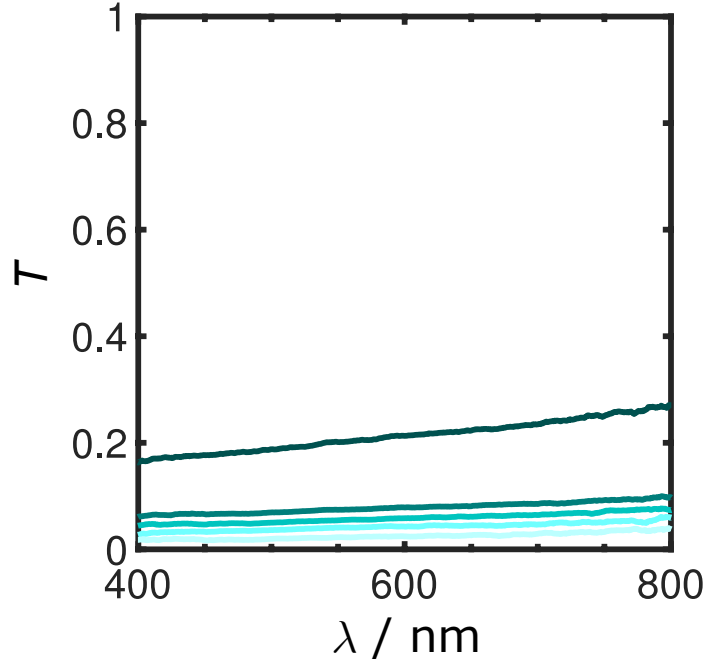


Figure 5.11. Total transmission, T , spectra across the visible spectrum for deposited high aspect ratio colloidal ‘rods’ films of different thicknesses ranging from $\sim 6 \mu\text{m}$ to $90 \mu\text{m}$. Colour saturation represents thickness i.e. lighter colours = larger thickness.

materials with such low refractive index that perform this well in a whiteness application.

5.3 Conclusion

In this chapter we detailed an ongoing investigation into the use of anisotropic silica particles as scattering centres in assembled thin colloidal films. It is apparent from our preliminary results that the broadband reflection and thus whiteness is possible even in extremely thin films of low refractive index silica colloids. In fact by optimizing the geometry of the silica particles constituting the building blocks of the film, the performance rivals that of the *Cyphocilus* beetle – nature’s evolutionary optimized example. This an unprecedented result and shows promise for further investigation into the precise role of anisotropy in affording whiteness in colloidal films. From our findings we would suggest that anisotropy in the building blocks of the film is an essential parameter as it allows for intermediate volume fractions ($\phi \sim 0.5$) to be accessed whilst preserving disorder in the film necessary

for diffuse scattering. We also suggest that optical crowding plays a role in the reduction of total optical scatter from most colloidal films and that a reduced packing fraction of particles can be achieved by using dense, higher aspect ratio particles.

5.4 Experimental

5.4.1 Materials

1-Pentanol ($\geq 99\%$), poly(vinyl-pyrrolidone) (PVP K-30: Average molecular weight = 40,000 g mol⁻¹), tetraethyl orthosilicate TEOS (98%) and sodium citrate tribasic dihydrate (99%) were obtained from Sigma Aldrich. Ammonia (30%) and ethanol were obtained from Fischer Scientific.

5.4.2 Synthesis of anisotropic ‘rod’ or ‘worm’ silica particles

In a typical synthesis, initially stock solutions of PVP-K30 (100 g L⁻¹) in 1-pentanol and aqueous sodium citrate (0.18 M) were made up. PVP-K30 was dissolved in 1-pentanol by vigorous stirring ~ 5 min and further sonication ~ 30 min. Following this sodium citrate (2.00 ml), de-ionised water (10.20 ml for rods) (8.40 ml for worms), ethanol (30.00 ml) and PVP-K30 in pentanol (300.00 ml) were added by syringe to a 500 ml laboratory bottle. This mixture was shaken vigorously by hand for approximately 30 seconds to generate a slightly turbid emulsion. After this, ammonia (5.00 ml for rods) (1.00 ml for worms) was added by syringe and the bottle was again shaken for 30 s to encourage transport of ammonia into water droplets. TEOS (3.0 ml) was subsequently added to initiate growth. The reaction was then left for 24 hours and a subsequent aliquot of TEOS (3.0 ml) was added for the rod sample to promote further growth. For each of the series investigated, reactions were performed on a small scale (1/40th) with variable quantities of ammonia, water, citrate and ethanol as detailed in table 5.2.

To clean the particles, a round of centrifugation for 25 minutes at 4200g was performed and the supernatant was removed. Thereafter 3 more rounds of centrifugation were performed for a period of 5 minutes at 4200g re-dispersing the particles in ethanol each time. When required, in order to reduce the dispersity of the colloids, selective centrifuga-

Series	Label	$\chi_{\text{TEOS}} : \chi_{\text{NH}_3} : \chi_{\text{H}_2\text{O}} : \chi_{\text{citrate}}$	$d / \mu\text{m}$	$L / \mu\text{m}$	L/d
NH_3	a	1 : 12.11 : 47.21 : 0.027	0.218 (0.18)	3.46 (0.25)	15.87
	b	1 : 8.08 : 47.12 : 0.027	0.208 (0.20)	3.82 (0.36)	18.37
	c	1 : 4.04 : 47.03 : 0.027	0.203 (0.21)	6.17 (0.43)	30.39
	d	1 : 2.02 : 47.00 : 0.027	0.170 (0.31)	8.77 (0.29)	51.59
Citrate	e	1 : 6.66 : 41.67 : 0.044	0.200 (0.37)	7.86 (0.16)	39.30
	f	1 : 6.66 : 41.67 : 0.040	0.306 (0.36)	2.25 (0.22)	7.35
	g	1 : 6.66 : 43.48 : 0.036	0.294 (0.38)	2.07 (0.25)	7.04
	h	1 : 6.66 : 45.45 : 0.032	0.252 (0.31)	2.58 (0.19)	10.24
H_2O	i	1 : 7.14 : 55.55 : 0.032	0.225 (0.49)	1.39 (0.32)	6.18
	j	1 : 7.14 : 50.00 : 0.036	0.271 (0.32)	1.29 (0.1)	4.76
	k	1 : 7.14 : 45.45 : 0.040	0.280 (0.38)	1.06 (0.12)	3.79
	l	1 : 7.14 : 41.67 : 0.044	0.263 (0.30)	1.03 (0.18)	3.91
$\text{H}_2\text{O} \& \text{Citrate}$	m	1 : 7.14 : 43.48 : 0.040	0.221 (0.31)	3.30 (0.13)	14.93
	n	1 : 7.14 : 38.46 : 0.036	0.310 (0.44)	1.16 (0.19)	3.74
	o	1 : 7.14 : 33.33 : 0.031	0.131 (0.29)	3.88 (0.26)	29.62
	p	1 : 7.14 : 28.57 : 0.027	0.260 (0.64)	2.34 (0.37)	9.00
EtOH	q	1 : 7.14 : 47.61 : 0.027	0.103 (0.36)	3.92 (0.43)	36.98
	r	1 : 7.14 : 47.61 : 0.027	0.241 (0.28)	1.39 (0.25)	5.77
	s	1 : 7.14 : 47.61 : 0.027	0.382 (0.27)	1.04 (0.14)	2.72
	t	1 : 7.14 : 47.61 : 0.027	0.326 (0.39)	0.72 (0.18)	2.21

Table 5.1. Comparison of reaction conditions in molar ratios of tetraethyl ortho silicate : ammonia : water : trisodium citrate dihydrate and resulting average particle diameters, d , and length, L , both with dispersity given in parenthesis calculated from standard deviation over the average diameter $\rho = \sigma/d$ as shown in figure 5.2

tion was then performed on the clean particles. This involved four rounds of centrifugation for 10 minutes at 117g (keeping solids) to remove smaller particles.

High aspect ratio silica rods were synthesized using a similar procedure except the reaction was conducted at a higher temperature, $T = 50^\circ\text{C}$. The reagent amounts were identical to the previously produced rods except for the amount of de-ionized water (9.50 ml).

5.4.3 Preparation of colloidal films

Prior to preparing films of targeted thickness, silica particles were dried in a vacuum oven at 60°C . The dried particles were then dispersed in water to make up known volume fractions:

Series	Label	TEOS / ml	NH ₃ / ml	H ₂ O / ml	citrate / ml	EtOH / ml
NH ₃	a	0.10	0.30	0.20	0.10	1.00
	b	0.10	0.20	0.26	0.10	1.00
	c	0.10	0.10	0.32	0.10	1.00
	d	0.10	0.05	0.35	0.10	1.00
Citrate	e	0.10	0.17	0.23	0.11	1.00
	f	0.10	0.17	0.24	0.10	1.00
	g	0.10	0.17	0.25	0.09	1.00
	h	0.10	0.17	0.26	0.08	1.00
H ₂ O	i	0.10	0.18	0.30	0.08	1.00
	j	0.10	0.18	0.27	0.08	1.00
	k	0.10	0.18	0.25	0.08	1.00
	l	0.10	0.18	0.23	0.08	1.00
H ₂ O & Citrate	m	0.10	0.18	0.24	0.10 (0.18 M)	1.00
	n	0.10	0.18	0.20	0.10 (0.16 M)	1.00
	o	0.10	0.18	0.16	0.10 (0.14 M)	1.00
	p	0.10	0.18	0.12	0.10 (0.12 M)	1.00
EtOH	q	0.10	0.18	0.28	0.10	2.00
	r	0.10	0.18	0.28	0.10	1.50
	s	0.10	0.18	0.28	0.10	1.25
	t	0.10	0.18	0.28	0.10	1.00

Table 5.2. Comparison of reaction conditions in volume of reagents employed in the above reactions (see table 5.1). In all cases the amount of PVP in pentanol (100 g l^{-1}) was kept constant with respect to TEOS at a volume ratio of 100:1 pentanol:TEOS.

$\phi = 0.1, 0.075, 0.05, 0.025$ and 0.0125 of which $100 \mu\text{l}$ of each were deposited onto glass microscope slides by simple drop-casting under ambient conditions, $T = 13^\circ\text{C}$ for $d = 540$ nm and $T = 22^\circ\text{C}$ for other samples. These slides were then contained within petri dishes to enable a steady state of humidity during the drying process.

5.4.4 Material characterization

Samples for SEM imaging for the reaction condition series were prepared by diluting the particle solutions to around 0.5 mg ml^{-1} in ethanol and allowing them to dry onto silicon wafers supported on aluminium stubs with a conductive copper adhesive. SEM imaging was performed on a Zeiss Gemini SEM 500 at 10 kV . Particle films were imaged directly

on the glass microscope slides by fracturing the slides to reasonable dimensions for SEM imaging and supporting them with copper adhesive on aluminium stubs. A long working distance of 8 mm was deployed with an accelerating voltage of 2 kV using the secondary electron detector (SE2) to collect images in order to avoid charging effects.

The absolute (skeletal) density of the silica rods and worms helium pycnometry was measured on dried powder samples using a Micro-meritics Accupyc 1330 Helium Pycnometer.

Film thickness was determined using a Bruker Contour GT-X interferometer with a $5\times$ objective. 10×10 mm sections were measured by stitching with 20% area overlap. The glass slide that samples were deposited on served both as a reference for height = 0 and was useful as a flat reflective surface to align the stage by looking at the interference fringes. The speed and non-destructive nature of this technique made it ideal for our analysis. Large areas were measured to allow us to select regions with even film thickness for the subsequent transport mean free path measurements.

5.4.5 Transport mean free path measurements

A similar procedure was used to perform these measurements as was carried out recently by Syurik *et al.*¹³ The transport mean free path (l_t) of the silica colloid films was determined by performing total transmission and reflectance measurements on films with different thickness. A light source (Ocean Optics HPX-2000) was attached to an optical fiber (Thorlabs FC-UV100-2-SR) via a collimator (Thorlabs) and directed at the sample. The samples (films deposited on glass slides) were clamped and placed in the optical beam path of the light source. The transmitted/reflected light was collected with an integrating sphere (Labsphere) and the signal was acquired by a spectrometer (Avantes HS2048). For total reflection measurements, the signal was normalized with respect to the coating (reference white material – barium sulfate) of the integrating sphere. For total transmission measurement, the signal was normalized with respect to the intensity when no sample was mounted. All measurements were recorded using unpolarized light and an integration $t = 2$ s. Five spectra were taken for each sample and averaged to reduce the signal-to-noise

ratio. All measurements were taken in a dark room in order to reduce interference and background noise.

References

- [1] B. D. Wilts, X. Sheng, M. Holler, A. Diaz, M. Guizar-Sicairos, J. Raabe, R. Hoppe, S. H. Liu, R. Langford, O. D. Onelli, D. Chen, S. Torquato, U. Steiner, C. G. Schroer, S. Vignolini and A. Sepe, *Adv. Mater.*, 2017, 1702057.
- [2] P. Vukusic, B. Hallam and J. Noyes, *Science*, 2007, **315**, 348.
- [3] M. F. Land, *Prog. Biophys. Mol. Biol.*, 1972, **24**, 75–106.
- [4] S. M. Luke, B. T. Hallam and P. Vukusic, *Appl. Opt.*, 2010, **49**, 4246–4254.
- [5] D. S. Wiersma, *Nat. Photonics*, 2013, **7**, 188–196.
- [6] L. McNeil and R. French, *Acta Mater.*, 2000, **48**, 4571–4576.
- [7] H. K. Pulker, G. Paesold and E. Ritter, *Appl. Opt.*, 1976, **15**, 2986–2991.
- [8] G. E. Jellison, L. A. Boatner, J. D. Budai, B. S. Jeong and D. P. Norton, *J. Appl. Phys.*, 2003, **93**, 9537–9541.
- [9] M. Burrelli, L. Cortese, L. Pattelli, M. Kolle, P. Vukusic, D. S. Wiersma, U. Steiner and S. Vignolini, *Sci. Rep.*, 2014, **4**, 6075.
- [10] B. T. Hallam, A. G. Hiorns and P. Vukusic, *Appl. Opt.*, 2009, **48**, 3243–3249.
- [11] C. J. McDonald and M. J. Devon, *Adv. Colloid Interface Sci.*, 2002, **99**, 181–213.
- [12] P. Lepoutre, *Prog. Org. Coatings*, 1989, **17**, 89–106.
- [13] J. Syurik, G. Jacucci, O. D. Onelli, H. Hölscher and S. Vignolini, *Adv. Funct. Mater.*, 2018, 1706901.
- [14] G. Beadie, M. Brindza, R. A. Flynn, A. Rosenberg and J. S. Shirk, *Appl. Opt.*, 2015, **54**, 139–143.

- [15] L. Cortese, L. Pattelli, F. Utel, S. Vignolini, M. Burrese and D. S. Wiersma, *Adv. Opt. Mater.*, 2015, **3**, 1337–1341.
- [16] A. Kuijk, A. Imhof, M. H. W. Verkuijlen, T. H. Besseling, E. R. H. van Eck and A. van Blaaderen, *Part. Part. Syst. Charact.*, 2014, **31**, 706–713.
- [17] M. M. Byranvand, N. Taghavinia, A. N. Kharat and A. Dabirian, *RSC Adv.*, 2015, **5**, 86050–86055.
- [18] M. M. Byranvand, A. N. Kharat, N. Taghavinia and A. Dabirian, *ACS Appl. Mater. Interfaces*, 2016, **8**, 16359–16367.
- [19] A. Kuijk, A. van Blaaderen and A. Imhof, *J. Am. Chem. Soc.*, 2011, **133**, 2346–2349.
- [20] A. Kuijk, D. V. Byelov, A. V. Petukhov, A. Van Blaaderen and A. Imhof, *Faraday Discuss.*, 2012, **159**, 181–199.
- [21] B. Liu, T. H. Besseling, M. Hermes, A. F. Demirörs, A. Imhof and A. van Blaaderen, *Nat. Commun.*, 2014, **5**, 1–8.
- [22] P. Datskos and J. Sharma, *Angew. Chem. Int. Ed.*, 2014, **53**, 451–454.
- [23] R. P. Murphy, K. Hong and N. J. Wagner, *J. Colloid Interface Sci.*, 2017, **501**, 45–53.
- [24] J. Chen, X. Wu, X. Hou, X. Su, Q. Chu, N. Fahrudin and J. X. Zhao, *ACS Appl. Mater. Interfaces*, 2014, **6**, 21921–21930.
- [25] A. F. Routh and W. B. Zimmerman, *Chem. Eng. Sci.*, 2004, **59**, 2961–2968.
- [26] R. E. Trueman, E. Lago Domingues, S. N. Emmett, M. W. Murray and A. F. Routh, *J. Colloid Interface Sci.*, 2012, **377**, 207–212.
- [27] J. P. Gorce, D. Bovey, P. J. McDonald, P. Palasz, D. Taylor and J. L. Keddie, *Eur. Phys. J. E*, 2002, **8**, 421–429.
- [28] E. Akkermans and G. Montambaux, *Mesoscopic Physics of Electrons and Photons*, Cambridge University Press, Cambridge, 2007.

- [29] N. Garcia, A. Z. Genack and A. A. Lisyansky, *Phys. Rev. B*, 1992, **46**, 14475–14479.
- [30] D. Contini, F. Martelli and G. Zaccanti, *Appl. Opt.*, 1997, **36**, 4587–4599.
- [31] S. Caixeiro, M. Peruzzo, O. D. Onelli, S. Vignolini and R. Sapienza, *Appl. Mater. Interfaces*, 2017, **9**, 7885–7890.
- [32] P. D. García, R. Sapienza, J. Bertolotti, M. D. Martín, Á. Blanco, A. Altube, L. Viña, D. S. Wiersma and C. López, *Phys. Rev. A - At. Mol. Opt. Phys.*, 2008, **78**, 1–11.
- [33] T. Svensson, E. Adolfsson, M. Lewander, C. T. Xu and S. Svanberg, *Phys. Rev. Lett.*, 2011, **107**, 1–5.

6

Summary & Outlook

To conclude the work of this thesis a summary for each chapter is given here with a discussion of the potential future research avenues to explore in relation to the findings. This thesis was based upon the transport phenomena that arises from constructing colloids with shape and/or chemical anisotropy. The work was organized into chapters based upon the transport phenomena and material in study.

In **Chapter 2** the surface roughening of poly(styrene) microspheres was performed by a novel method whereby the polymer was deformed whilst packed into an inorganic colloidal matrix. The shape and size of the inorganic colloid could be selected to directly tune the output roughness of the polymer microsphere. Facile removal of the inorganic colloid by weak acid etching in acetic acid allowed recovery of isolated rough microspheres which were assumed to have identical surface chemistry to their smooth counterparts. Subsequently the Brownian motion of roughened particles was compared to ‘smooth’ by 2D particle tracking finding that the no-slip boundary conditions hold and the rough colloid can be modelled well by the STOKES-EINSTEIN-SUTHERLAND relation.

Future work: In extension of this work it would be beneficial to quantify the roughness of the deformed microspheres which as it stands is qualitative only. This is a particularly difficult investigation due to the scale of the particles and asperities (AFM unsuitable due to probability of tip crashing at particle edges) in addition to the insulating nature of the material (tomographic TEM difficult). An analogue of the surface could be made by performing the same roughening procedure on poly(styrene) films. It should then be a simpler task to measure height information with AFM as the roughness extends mostly in the vertical plane due to the initially flat substrate (as opposed to the curved surface of the individual microspheres). This would clearly only serve as an approximation as the curva-

ture of the microspheres surface will impact the roughness particularly as the size of the inorganic colloid becomes larger. It would also be interesting to examine the effect of shear driven flow at these roughened surfaces to further probe the frictional effect of roughening the surface. Finally, the roughening procedure could be optimized to attempt to maximize the produced rough microspheres whilst utilizing less inorganic colloid. Further investigations into potential phase separation of the bi-composite sol upon drying would be helpful in this study.

Chapter 3 extends the work of chapter 2 by introducing a catalytic layer of platinum to one-half of the roughened micro particle hereby affording chemical anisotropy. This asymmetric placement of catalyst allows the particle to propel in hydrogen peroxide solution *via* an auto/self-phoretic mechanism. It was found that roughening of the particle surface with nanoscale features lead to velocities $2\times$ that of their ‘smooth’ relatives. In addition to this it was found that particles with roughened surfaces were more likely to perform circular motions in their propelled trajectories. This was perhaps due to discontinuities in fluid flow about the particle and amplified by the torque of the heavy platinum cap on side of the particle.

Future work: As the work in this chapter builds upon the previous chapter, the improvements suggested there would also be beneficial here. In particular it would be interesting to see if roughness could be tuned so that fluid slip occurs at the particle surface which could lead to much higher propelled velocities. In fact it is possible that slip is already present for our rough colloids with small deformations and that is what contributes to an increase in speed. In order to determine this we would need to decouple the effects of slip and surface reactivity by quantifying both independently. Note that this is a complicated matter which is made worse by the extremely small quantities of particles available for study. A higher yielding synthesis is required to make this feasible. It would also be interesting to perform further studies to elucidate the origin of angular propulsion of the roughened micromotors. Does this effect only happen near the underlying surface where there are potential barriers and restricted fluid flow?

Chapter 4 contains a mechanistic study on the synthesis of ‘matchstick’ shaped silica-metal oxide colloids. The synthesis is presented in two parts with separate characterization: 1. metal oxide synthesis to form matchstick head and 2. silica growth to form matchstick tail. It was found that the produced colloids are highly anisotropic (in shape and chemistry) and that the aspect ratio of matchsticks could be carefully tuned by terminating the reaction at a given time. The dynamics of these colloids were measured by 2D particle tracking and it was found that their auto/self-phoretic response in the presence of hydrogen peroxide was limited due to an encapsulated silica layer around the manganese oxide catalyst. Instead an enhanced diffusion was measured for these particles.

Future work: In order to extend the current work it would be interesting to carry out the initially proposed aspect ratio *vs.* swimming efficiency study. The issue of catalyst accessibility must first be resolved however. Attempts to post-etch the matchstick particles did not expose the manganese oxide without damaging the structure of the particle. A potential fix to this problem could involve the post modification of matchstick particles by grafting and cross-linking polymer from their surface. This layer could then potentially serve as the body of the particle once the silica has been fully etched. The advantage here is that the cross-linking density of the polymer can be tuned by varying the amount of cross-linker, therefore one should have slightly more control of the pore size and thus accessibility to the catalyst. Some initial work has been done here though the complexity of this approach means that additional time and effort is required before the particle is materialized.

In **Chapter 5** some preliminary results from a bio-mimetic approach to designing colloids for white thin films was presented. In this work we took inspiration from the brilliant whiteness of the *Cyphocilus* beetle that arises from a thin ($\sim 5\text{ }\mu\text{m}$) chitinous layer on its shell which is consistent of an anisotropic, filamentous structure. The anisotropic nature of the scattering centres allows for a disordered arrangement, essential for broadband reflection, that would otherwise be difficult to achieve with uniform, spherical scatterers. To find suitable candidate colloids we systemically screened reaction conditions in the synthesis of rod-like silica colloids. Anisotropic ‘rod’ and ‘worm’-like silica colloids of comparable

dimensions to the *Cyphocilus* fibrils were produced which were then assembled into thin films by drop casting. The structure and whiteness have been compared for the ‘rod’ and ‘worm’-shaped colloidal films and it was found that they had similar performance which was slightly worse than the *Cyphocilus* beetle but significantly better than pigments for paper coatings and photonic glasses. To further improve the whiteness we synthesized rods with approximately $2\times$ the aspect ratio of the previous silica colloids that, when assembled into films, lead to lower packing fractions. Some initial results show that these films have much improved performance that rivals the *cyphocilus* beetle. These results suggest that optical crowding may be reducing the whiteness of the lower aspect ratio samples and packing fraction is a critical parameter to consider for optical scattering.

Future work: The author would like to put emphasis here on the fact that the results described in Chapter 5 are all recent and subject to further study. Whilst we are confident that the recent high aspect ratio samples are very promising for their whiteness, we have not yet understood the exact cause. In the current work the diameter is not kept constant between samples and thus with multiple varying parameters it is difficult to determine what is critical to performance. It would be interesting to be able to decouple the size (diameter) and the packing fraction of samples and assess their relative importance. This knowledge can then be directly transferred to the design of new white materials. In addition we would like to begin formulating samples that are more suitable for the coatings industry *i.e.* that contain soft latex binder particles and thickener. We can then determine if these additional components affect performance and assess suitability for a real world application.

A

Additional Characterization

A.1 XPS of amorphous manganese oxide powder

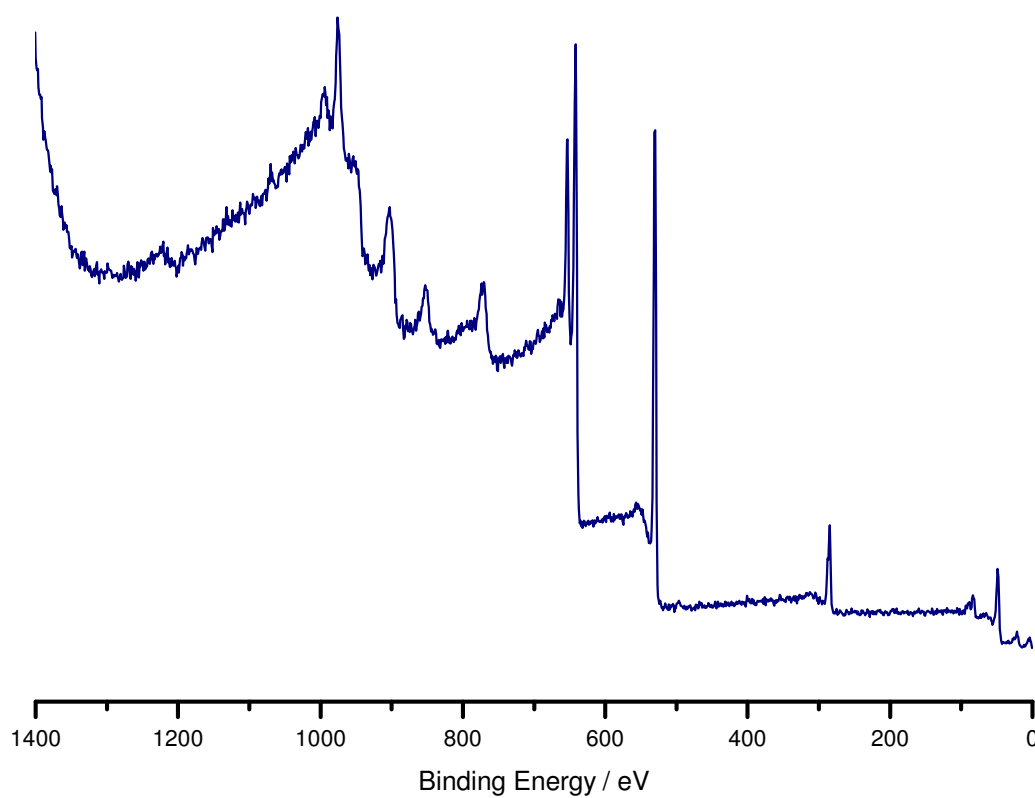


Figure A.1. X-Ray Photoemission Spectroscopy (XPS) survey of dried manganese oxide powder synthesized from part 1 of the ‘matchstick’ particle synthesis detailed in chapter 4.

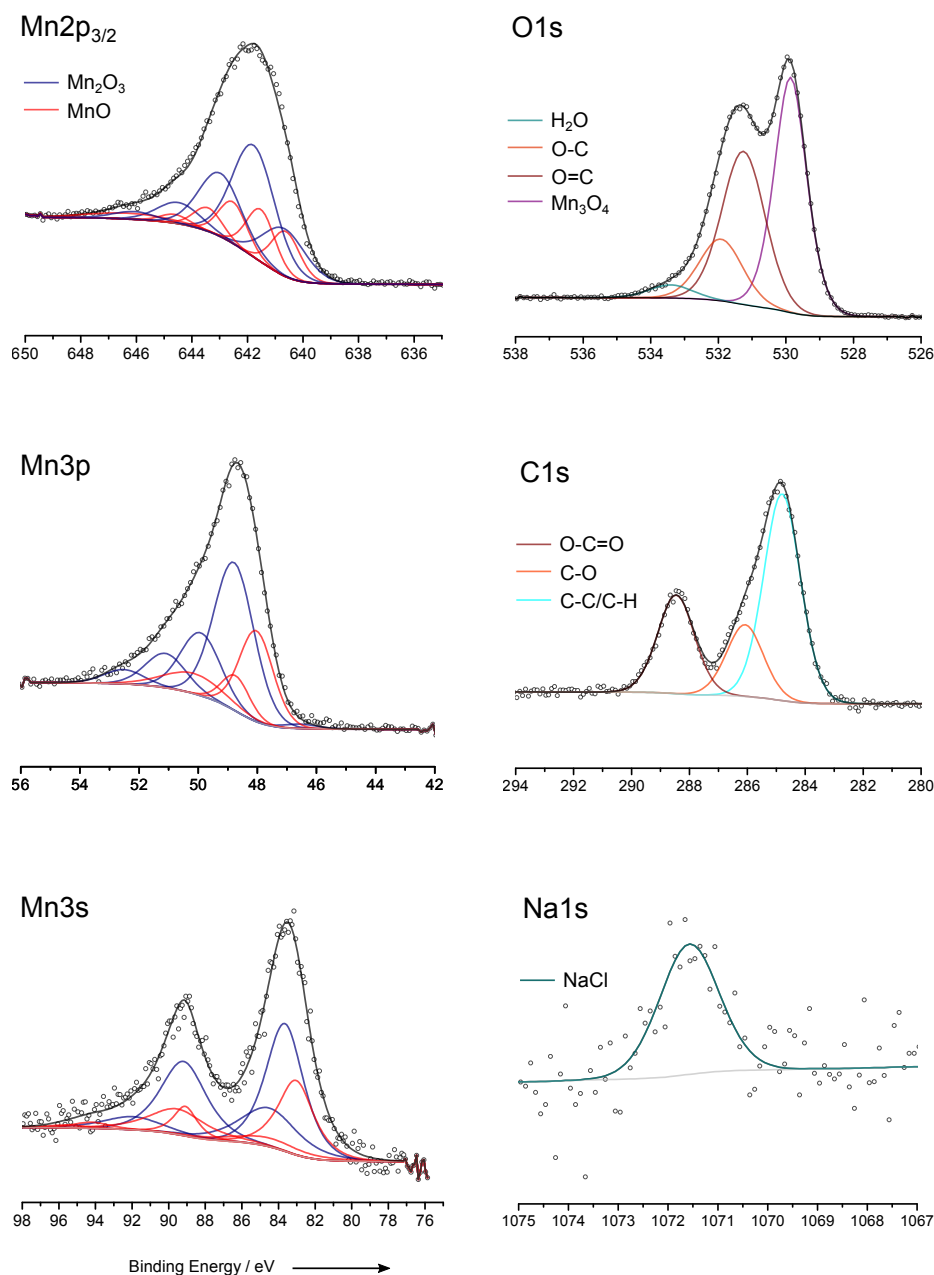


Figure A.2. X-Ray Photoemission Spectroscopy (XPS) traces of dried manganese oxide powder synthesized from part 1 of the ‘matchstick’ particle synthesis detailed in chapter 4. Peak fitting resulted in the assignment of Mn_3O_4 by linear combinations of Mn_2O_3 and MnO as performed by BIESINGER *et al.*¹

Bonding Environment	Binding Energy / eV	% counts	Total / %	
Mn 2p _{3/2} - Mn ₂ O ₃	640.68	12.55	ss Mn ₂ O ₃	66.65
Mn 2p _{3/2} - Mn ₂ O ₃	641.78	29.57		
Mn 2p _{3/2} - Mn ₂ O ₃	642.98	16.82		
Mn 2p _{3/2} - Mn ₂ O ₃	644.48	5.65		
Mn 2p _{3/2} - Mn ₂ O ₃	646.08	2.06		
Mn 2p _{3/2} - MnO	640.62	7.98	MnO	33.35
Mn 2p _{3/2} - MnO	641.52	9.25		
Mn 2p _{3/2} - MnO	642.52	7.36		
Mn 2p _{3/2} - MnO	643.42	4.16		
Mn 2p _{3/2} - MnO	644.62	1.57		
Mn 2p _{3/2} - MnO	646.32	3.03		

Table A.1. Peak fitting of the Mn 2p region

Bonding Environment	Binding Energy / eV	% counts	Total / %	
Mn 3p _{3/2} - Mn ₂ O ₃	48.79	37.40	Mn ₂ O ₃	66.66
Mn 3p _{3/2} - Mn ₂ O ₃	49.92	15.95		
Mn 3p _{3/2} - Mn ₂ O ₃	51.11	8.74		
Mn 3p _{3/2} - Mn ₂ O ₃	52.52	3.64		
Mn 3p _{3/2} - Mn ₂ O ₃	46.57	0.93		
Mn 3p _{3/2} - MnO	48.04	19.42	MnO	33.33
Mn 3p _{3/2} - MnO	48.74	6.26		
Mn 3p _{3/2} - MnO	50.17	7.65		

Table A.2. Peak fitting of the Mn 3p region

Bonding Environment	Binding Energy / eV	% counts	Total / %	
Mn 3s - Mn ₂ O ₃	83.66	28.02	Mn ₂ O ₃	66.67
Mn 3s - Mn ₂ O ₃	84.53	13.07		
Mn 3s - Mn ₂ O ₃	89.19	19.77		
Mn 3s - Mn ₂ O ₃	91.96	4.50		
Mn 3s - Mn ₂ O ₃	94.23	1.31		
Mn 3s - MnO	83.04	15.97	MnO	33.32
Mn 3s - MnO	84.54	3.71		
Mn 3s - MnO	89.09	4.22		
Mn 3s - MnO	89.52	8.74		
Mn 3s - MnO	95.50	0.68		

Table A.3. Peak fitting of the Mn 3s region

A.2 Image thresholds of colloidal silica films

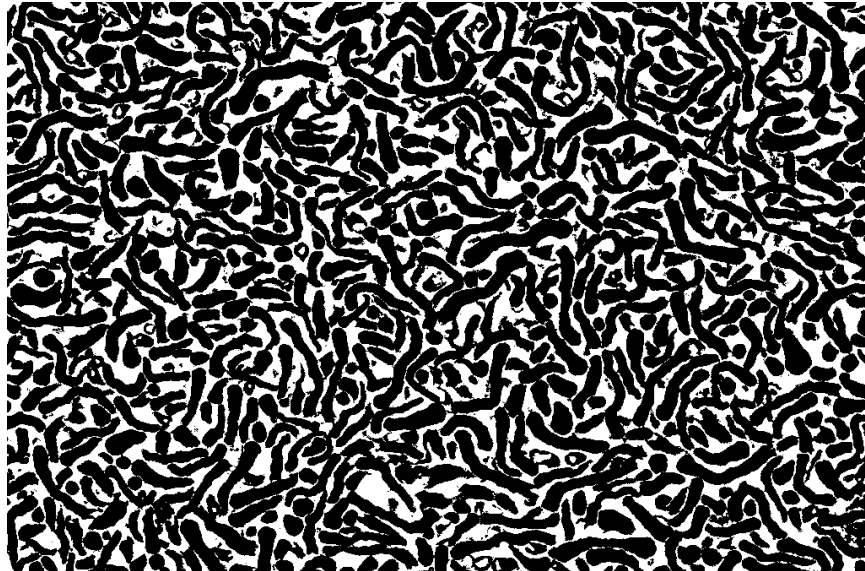


Figure A.3. Binary image created by applying a threshold to the top view image of ‘worm’-like particles in figure 5.6 b) using imageJ’s built in threshold function.

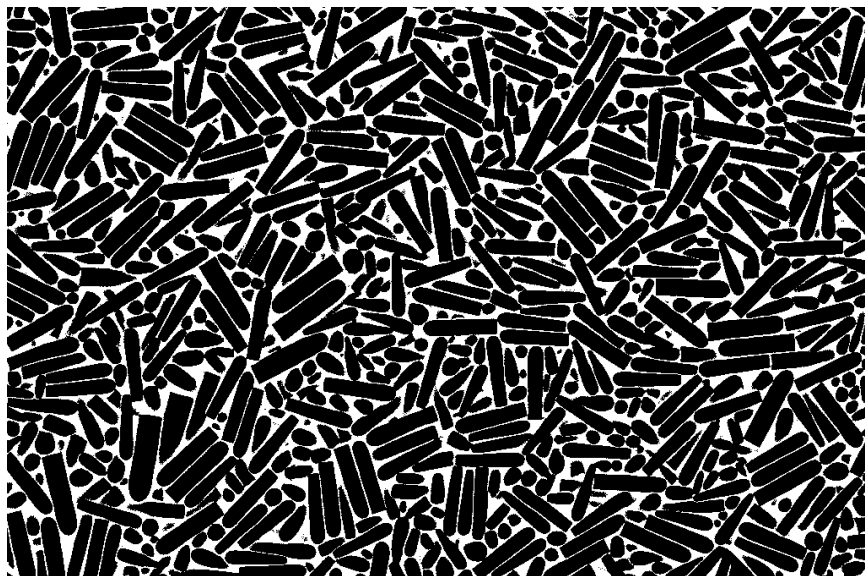


Figure A.4. Binary image created by applying a threshold to the top view image of ‘rod’-like particles in figure 5.7 b) using imageJ’s built in threshold function.



Figure A.5. Binary image created by applying a threshold to the top view image of high aspect ratio ‘rod’-like particles in figure 5.10 b) using imageJ’s built in threshold function.

A.3 Quantification of the extrapolation length for colloidal silica films

In order to rigorously quantify the transport mean free path, l_t , of a sample exhibiting diffuse scattering one must first take into account internal reflections. A portion of the light exiting a sample is reflected back into the sample when it hits with the boundary surface. This effect ultimately influences the distribution of the light paths in a sample. It is within the extrapolation length, z_e , that this effect is encapsulated. We can approximate z_e using the angular distribution of transmitted light using the following equation²:

$$P(\mu) = \mu \frac{z_e + \mu}{\frac{1}{2}z_e + \frac{1}{3}}, \quad (\text{A.1})$$

where $P(\mu)$ and μ are the angular distribution intensity and the cosine of the scattering angle. To obtain $P(\mu)$ the angular resolved transmission data was divided by the total incident light intensity. Fitting the data with equation (A.1) yielded $z_e = (1.55 \pm 0.21)l_t$ (see figure A.6).

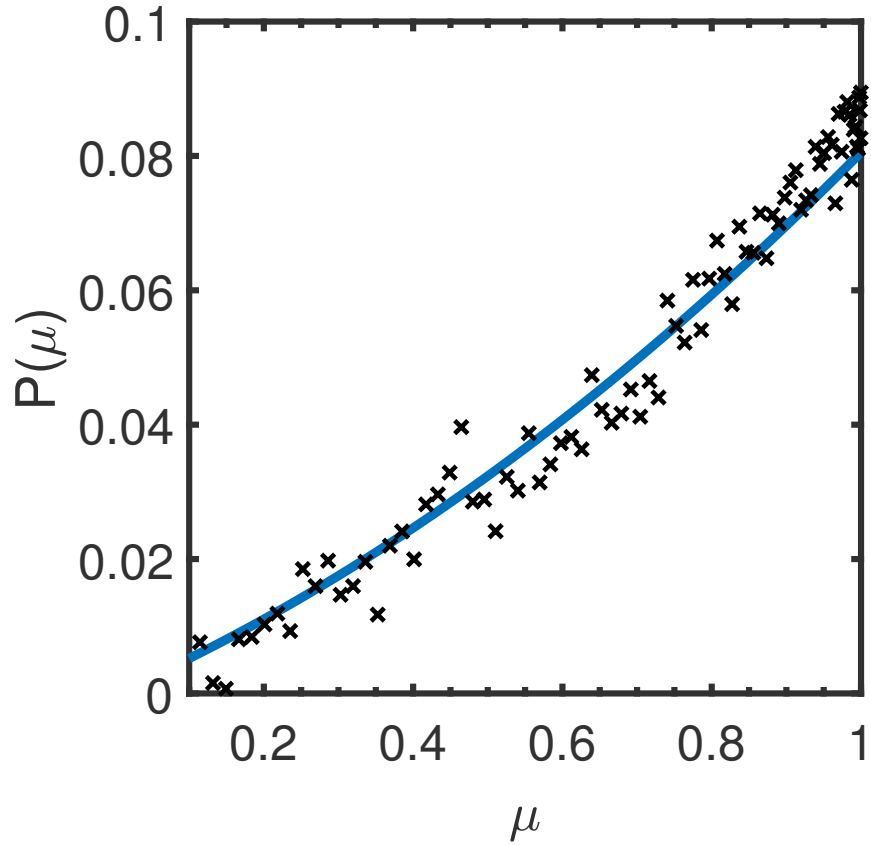


Figure A.6. Approximation of the internal reflections in a ~ 40 μm thick film of silica ‘worm’-like colloids. The angular distribution of intensity, $P(\mu)$, is plotted against the cosine of the scattering angle, μ , and fitted with equation (A.1) (blue line) to extract the extrapolation length, z_e .

B

Supporting Videos

This section details the contents of supporting videos and only functions for the digital version of this thesis. The listed titles are hyperlinked to a file sharing server for video playback.

B.1 SV1 – 2D particle tracking of a rough object

A particle roughened in the presence of cigar-shaped calcium carbonate according to the procedure presented in the chapter 2 is tracked using the Trackmate algorithm. This uses a Laplacian-of-Gaussian filter followed by local maxima searching to find particle centres. The video shows the Brownian motion of such an object and the determination of the particle centre in each frame as highlighted by the purple ring.

B.2 SV2 – Translational to angular propulsion of a rough micromotor

A video recorded at 50 fps shows the transition of a translational to proposed angular propulsion mechanism of a PS-Pt micromotor with large surface deformations (*ld*) dispersed in a 10 vol.% H₂O₂ solution in water. The particle was located near the underlying glass coverslip. This video has been sped up by 4×.

B.3 SV3 – Bubble propulsion of manganese oxide powder

A video of manganese oxide nanoparticle aggregates recorded at 24 fps under a Leica DM 2500M optical microscope operating in bright field with a 10× objective. Manganese oxide powder isolated from stage 1 of the ‘matchstick’ synthesis presented in chapter 4 was

suspended in 10 vol.% H_2O_2 resulting in rapid bubble propulsion. Once all the H_2O_2 had reacted (~ 30 min) a second dose was added and the same effect was observed.

B.4 SV4 – Brownian motion of matchstick shaped colloids

A 30 second 512×512 video recorded at 50 fps showing the Brownian motion of matchstick-shaped colloids.

References

- [1] M. C. Biesinger, B. P. Payne, A. P. Grosvenor, L. W. Lau, A. R. Gerson and R. S. C. Smart, *Appl. Surf. Sci.*, 2011, **257**, 2717–2730.
- [2] M. Vera and D. Durian, *Phys. Rev. E*, 1996, **53**, 3215–3224.